

LOAN COPY: FE
AFWL TECHNICA
KIRTLAND AFB

REF ID: A6474

TECH LIBRARY KAFB, NM

ATMOSPHERIC AEROSOLS: THEIR OPTICAL PROPERTIES AND EFFECTS

A Topical Meeting on Atmospheric Aerosols

Sponsored by

Optical Society of America

and the

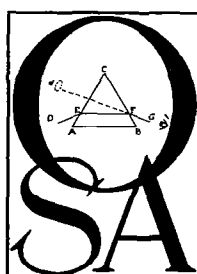
NASA Langley Research Center

Williamsburg, Virginia

December 13-15, 1976

NASA

National
Aeronautics and
Space
Administration



NASA Conference Publications (CP Series) contain compilations of scientific and technical papers or transcripts arising from conferences, workshops, symposia, seminars, and other professional meetings that NASA elects to publish.

The text of these proceedings was reproduced directly from author-supplied manuscripts for publication and distribution prior to opening of the meeting. NASA has performed no editorial review of the papers.



0067339

ATMOSPHERIC AEROSOLS: THEIR OPTICAL PROPERTIES AND EFFECTS

A digest of technical papers presented at the topical meeting on Atmospheric Aerosols:
Their Optical Properties and Effects, December 13-15, 1976, Williamsburg, Virginia

Sponsored by

Optical Society of America
2000 L Street, N.W., Washington, D.C. 20036

NASA Langley Research Center
Hampton, Virginia 23665

NASA
National
Aeronautics and
Space
Administration



For sale by the National Technical Information Service
Springfield, Virginia 22161
Price: \$ 9.50

TECHNICAL PROGRAM COMMITTEE

Franklin S. Harris, Jr.,
NASA Langley Research Center
Hampton, Virginia 23665

Adarsh Deepak
NASA Langley Research Center
Hampton, Virginia 23665

Benjamin M. Herman
University of Arizona
Tucson, Arizona 85721

James D. Lawrence, Jr.
NASA Langley Research Center
Hampton, Virginia 23665

Dale A. Lundgren
University of Florida
Gainesville, Florida 32611

M. Patrick McCormick
NASA Langley Research Center
Hampton, Virginia 23665



TOPICAL MEETING PROGRAM
ATMOSPHERIC AEROSOLS:
Their Optical Properties and Effects
13-15 DECEMBER 1976
WILLIAMSBURG, VIRGINIA

MONDAY, December 13, 1976

8:30 A.M. Opening Remarks, Franklin S. Harris, Jr.
Welcome, Donald P. Hearth, Director,
NASA Langley Research Center

9:00 A.M. PARTICLE CONCENTRATIONS
M. Patrick McCormick, Presider

MA1. Invited Paper: Atmospheric Aerosols and their Optical Properties, K. Bullrich and G. Hanel; Institut fur Meteorologie, Munich.

MA2. Measured and Analytic Size Distributions of Stratospheric Aerosols: A review and Commentary, Franklin S. Harris, Jr., Old Dominion University, and James M. Rosen, University of Wyoming.

MA3. Aerosol Size Distribution Inferred from Spectral Solar Attenuation plus Scattering Measurements, Heinrich Quenzel, Meteorol. Inst. der Universität, Munich.

MA4. A Determination of Aerosol Size Distributions from Spectral Optical Depth Measurements, Michael D. King, Dale M. Byrne, Benjamin M. Herman, John A. Reagan, University of Arizona.

MA5. Airborne Measurements of Particle Size Distribution, Light Scattering, and Turbidity at Different Altitudes, A. J. Alkezweeny and N. S. Laulainen, Battelle-Pacific Northwest Laboratories.

MA6. Coastal Aerosol Measurements, Gary L. Trusty and Thomas H. Cosden, Naval Research Laboratory.

10:45 A.M. SPATIAL DISTRIBUTIONS
R. F. Pueschel, Presider

MB1. Atmospheric Turbidity over the Northern Equatorial Atlantic During the Summer of 1974: The Impact of North African Aerosols, J. M. Prospero, T. N. Carlson, D. Savoie, and R. T. Nees, Rosenstiel School of Marine and Atmospheric Science, University of Miami.

MB2. Occurrence of Dust over Selected Geographical Areas, Glenn B. Hoidale, Richard B. Gomez, and Bobby D. Hinds, Atmospheric Sciences Laboratory, White Sands Missile Range.

MB3. Tethered Balloon-Based Measurements of Aerosol Concentration and Meteorological Parameters, Ronald J. Sentell, Richard W. Storey, and James J. C. Chang, NASA Langley Research Center.

MB4. Continuous Measurements of the Natural Aerosol Size Distribution at Rural, Mountain and Maritime Sites, S. G. Jennings, University of Durham.

MB5. Spatial Concentration of Particulates from Rocket Exhaust Ground Clouds, K. H. Crumbly, R. J. Sentell, R. W. Storey, Jr., and D. C. Woods, NASA Langley Research Center.

MB6. Altitude Profiles of Atmospheric Aerosols Obtained with the Epsilon/AFGL Balloon-Borne Sizing Spectrometer, Henry A. Miranda, Jr., Epsilon Laboratories; and, Frank K. Dearborn, Air Force Geophysics Laboratory.

MB7. Aerosol Tropospheric-Stratospheric Exchange, M. P. McCormick, NASA Langley Research Center; T. J. Swissler, Systems and Applied Sciences; and, W. P. Chu, Old Dominion University.

MB8. Comparison of Airborne Lidar Results with a Physical Model of Stratospheric Aerosols, F. G. Fernald, University of Denver.

MB9. Trend of Twilight Color Ratios and Converted Lidar Data of the Fuego Dust Cloud, Frederic E. Volz, Air Force Geophysics Laboratory.

2:00 P.M. OPTICAL PROPERTIES
Philip B. Russell, Presider

MC1. Aerosols in the Atmosphere: Their Origin and Role in Heterogeneous Processes, A. W. Castleman, Jr., University of Colorado.

MC2. Some Relations Between Aerosol Characteristics at Sea and Meteorological Phenomena, E. J. Mack, U. Katz, R. J. Pillié, and R. J. Anderson, Calspan Corporation.

MC3. Imaginary Index of Refraction and Size Distributions for Atmospheric Aerosols, E. M. Patterson, D. A. Gillette, and E. H. Stockton, National Center for Atmospheric Research.

MONDAY, December 13, 1976 (Continued)

MC4. In-Situ Refractive Index Measurements of Quartz Dust with a CO₂ Laser Spectrophone, C. W. Bruce and R. G. Piñnick, White Sands Missile Range.

MC5. Infrared Extinction of Tropospheric Aerosols: Effluents from a Coal-Fired Powerplant, R. F. Pueschel and P. M. Kuhn, National Oceanic and Atmospheric Administration.

MC6. The Dominance of Tropospheric Sulfate in Modifying Solar Radiation, R. J. Charlson, A. H. Vanderpol, A. P. Waggoner, D. S. Covert, and M. B. Baker, University of Washington.

MC7. Use of Prevailing Visibility Data for Aerosol Studies, N. M. Reiss, R. A. Eversole, and J. J. Mangano, Rutgers University.

3:45 P.M. OPTICAL PROPERTIES II
Diran Deirmendjian, Presider

MC8. Polarization and Scattering by Nonspherical Aerosols, Peter Chýlek, Purdue University.

MC9. Scattering from a Polydispersion of Tumbled Spheroids, David Stein and Gray Ward, University of Florida.

MC10. Scattering Properties of Irregular Dielectric and Absorbing Particles, R. H. Zerull and K. Weiss, Ruhr-Universität.

MC11. Comparison of Extinction and Backscattering Coefficients for Measured and Analytic Stratospheric Aerosol Size Distributions, Thomas J. Swissler, Systems and Applied Sciences; and, Franklin S. Harris, Jr., Old Dominion University.

MC12. Optical Properties of Core-Mantle Particles (Scattering, Polarization, Efficiency Factors), Gerhard Schwefelm, Ruhr-Universität.

MC13. Scattering by Tenuous Aerosols, Charles Acquista, NASA Wallops Island Flight Center.

MC14. Optical Constants for a Meteoric Dust Aerosol Model, E. P. Shettle and F. E. Volz, Air Force Geophysics Laboratory.

MC15. Performance of Differential-Scatter (DISC) Lidar Systems, M. L. Wright and G. Johnson, Stanford Research Institute.

TUESDAY, December 14, 1976

8:30 A.M. In Situ Sampling
Dale A. Lundgren, Presider

TuA1. Invited Paper: Aerosol Measurement Techniques, Dale A. Lundgren, University of Florida.

TuA2. A Doppler Shift Spectrometer for Measurement of Particle Size Distributions, David S. Bright, Natasha K. Neihart, and Ilan Chabay, National Bureau of Standards.

TuA3. Chemical Characterization of Aerosols by Light Scattering, C. C. Gravatt, National Bureau of Standards.

TuA4. Recent Developments in Nephelometers, A. P. Waggoner, N. C. Ahlquist, and R. J. Charlson, University of Washington.

TuA5. Use of Polar Nephelometer Measurements in Determining Aerosol Optical Properties, G. W. Grams and E. M. Patterson, National Center for Atmospheric Research.

TuA6. Portable Transmissometer, H. E. Gerber and R. K. Stilling, Naval Research Laboratory; and, R. G. Buser and R. S. Rohde, U. S. Army Electronics Command.

TuA7. Low Altitude Environmental Aerosol Measurements with an Airborne Particle Morphokinometer, W. M. Farmer and J. O. Hornkohl, Spectron Development Laboratories.

TuA8. Application of Raman Scattering to the Characterization of Atmospheric Aerosol Particles, H. Rosen and T. Novakov, Lawrence Berkeley Laboratories.

TuA9. Measurements of Infrared Properties of Aerosols, John F. Ebersole, David M. Mann, and Conrad M. Gozewski, Aerodyne Research Inc.

11:00A.M. PASSIVE PROBING
James D. Lawrence, Jr., Presider

TuB1. Application of Satellite Image Analysis to Transport and Deposition Studies of Dust Storm Aerosol, William M. Porch and James E. Lovill, Lawrence Livermore Laboratory.

TuB2. Satellite Solar Occultation Measurements SAM II and SAGE, M. P. McCormick, H. B. Edwards, L. E. Mauldin, III, and L. R. McMaster, NASA Langley Research Center.

TUESDAY, December 14, 1976 (Continued)

TuB3. Remote Sensing of Atmospheric Turbidity from Geosynchronous Orbit, P. Koepke and H. Quenzel, Meteor. Institut der Universität, Munich.

TuB4. Some Data from the Skylab Stratospheric Aerosol Limb Experiment, David L. Tingey, Boeing Aerospace Company.

TuB5. Improved Accuracy of Spectral Aerosol Optical Depth Measurements: Interference of Total Ozone, Dale M. Byrne and Michael D. King, University of Arizona.

7:00P. M. ACTIVE PROBING
Richard M. Schotland, Presider

TuC1. Monitoring of Tropospheric Aerosol Optical Properties by Lidar, James Spinhirne, University of Arizona.

TuC2. Comparative Analysis of Red-Blue Lidar and Rawinsonde Data, W. H. Fuller, Langley Research Center; T. J. Swissler, Systems and Applied Sciences; and, M. P. McCormick, NASA Langley Research Center.

TuC3. Determination of the Complex Refractive Index of Aerosol Particles from Bistatic Lidar and Solar Radiometer Measurements, John A. Reagan, Dale M. Byrne, Benjamin M. Herman, and Michael D. King, University of Arizona.

TuC4. Feasibility of Atmospheric Aerosol Measurements with Lidar From Space Shuttle, Ellis Remsberg and G. Burton Northam, NASA Langley Research Center.

TuC5. Scattering of Ultraviolet Radiation by Aerosols in the Lower Atmosphere, M. E. Neer, G. Sandri, and E. S. Fishburne, Aeronautical Associates of Princeton.

TuC6. Design Principles of a Slant Transmissometer for Airport Use, Harold Stewart, Willem Brouwer, and Marion Shuler, HSS Inc.

TuC7. Light Scattering in Water Droplet Fogs, A. I. Carswell, J. S. Ryan, and S. R. Pal, York University.

TuC8. Light Scattering as a Measure of Aerosol Concentration, Jiri, Motycka, University of Toronto.

TuC9. Temporal-and Spatial-Frequency Spectra for Atmospheric Aerosols, M. J. Post and R. L. Schwiesow, National, Oceanic and Atmospheric Administration.

TuC10. Field Comparison of Optical Particle Counters, Edward E. Hindman II, Naval Weapons Laboratory.

TuC11. Atmospheric Aerosol Data from Circum-solar Telescope Measurements, D. F. Grether, A. J. Hunt, and M. Wahlig, Lawrence Berkeley Laboratory.

WEDNESDAY, December 15, 1976

8:30A.M. MODELING I
Benjamin M. Herman, Presider

WA1. A Comprehensive Aerosol Growth Model, Ronald L. Drake, Batelle, Pacific Northwest Laboratories.

WA2. H_2SO_4 Gas Phase Concentration in the Stratosphere, Patrick Hamill, NASA Ames Research Center.

WA3. Gas Phase Chemistry in the Ames Stratospheric Model, R. C. Whitten, NASA Ames Research Center; and, R. P. Turco, R and D Associates.

WA4. A Model of the Stratospheric Sulfate Aerosol, R. P. Turco, R and D Associates, and P. Hamill, O. B. Toon, and R. C. Whitten, NASA Ames Research Center.

WA5. A Steady State One Dimensional Model of the Stratospheric Aerosol, J. M. Rosen, D. J. Hoffman, and P. Singh, University of Wyoming.

WA6. Data Inversion for Spacecraft Solar Occultation Experiments in the Near IR, UV, and Visible Region, W. P. Chu, Old Dominion University; T. J. Swissler, Systems and Applied Sciences; and, M. P. McCormick, NASA Langley Research Center.

WA7. The Effect of Horizontal Rayleigh Air Mass Models upon Evaluation of Stratospheric Aerosol Optical Depth Remote Sensing Measurements from Earth Orbit, Gregory L. Matloff, New York University.

WA8. Analytical Modeling Of Aerosol Size Distribution, Adarsh Deepak, Old Dominion University.

10:30A.M. MODELING II
Robert S. Fraser, Presider

WA9. Approximate Determination of Aerosol Size Distributions, Michael A. Box and Shui-yin Lo, University of Melbourne.

WA10A. Inversion of Multispectral Extinction Data - The Anomalous Diffraction Approximation, Michael A. Box and Bruce H. J. McKellar, University of Melbourne.

WA10B. Approximations to Aerosol Extinction Michael A. Box, Shui-yin Lo, Bruce H. J. McKellar, and Michael Reich, University of Melbourne.

WA11. Concerning the Retrievability of Aerosol Size Distribution Parameters from Remote Sensing Experiments, W. A. Pearce and R. W. L. Thomas, EG&G/Washington Analytical Services Center, Inc.

WA12. On the Extraction of Extinction Coefficients Profiles from Sun Photometer Measurements, Alistair B. Fraser, The Pennsylvania State University.

WA13. The Sensitivity of Zenith Twilight Polarization to Stratospheric Aerosol Particle Concentration, D. Q. Wark and L. L. Stowe, National Oceanic and Atmospheric Administration.

WA14. On Aerosol Property Discrimination Through Sky Polarization Measurements, Robert W. L. Thomas and William A. Pearce, EG&G/Washington Analytical Services Center; and, A. C. Holland, NASA Wallops Flight Center.

WA15. Radiative Transfer in Rural, Urban, and Maritime Model Atmospheres, Eric P. Shettle, Air Force Geophysics Laboratory.

1:15P.M. AEROSOL EFFECTS
Alan P. Waggoner, Presider

WB1. Influence of Aerosol Particles on Thermal Properties of the Upper Atmosphere, G. W. Grams, National Center for Atmospheric Research; and, G. Fiocco and A. Mugnai, Instituto di Fisica, Rome, Italy.

WB2. Influence of Airborne Particles (Aerosols) on the Earth's Radiation Balance, Ruth A. Reck, General Motors Corporation.

WB3. Stratospheric Aerosols and Climatic Change, Owen B. Toon and James B. Pollack, NASA Ames Research Center.

WB4. Effects of Aerosol Particles on Visibility, Atmospheric Pollution, Radiation Budget, and Climate, Kurt Bullrich and Reiner Eiden, Johannes Gutenberg-Universität.

WB5. Application of Directly Measured Aerosol Radiative Properties to Climate Models, R. E. Weiss, R. J. Charlson, A. P. Waggoner, M. B. Baker, D. S. Covert, D. Thorsell, and S. Yuen, University of Washington.

WB6. Laser Beam Broadening in Aerosol Media, Adarsh Deepak, Old Dominion University.

WB7. Multiwavelength Visible and IR investigations of Atmospheric Aerosols, Arne Hagard, Bertil Nilsson, Hans Ottersten, and Ove Steinwall, National Defense Research Institute, Stockholm, Sweden.

WB8. Atmospheric Albedo Changes Measured in the Mt. Sutro Tower Aerosol and Radiation Study, Philip B. Russell and Edward Uthe, Stanford Research Institute.

3:15P.M. RADIATIVE TRANSFER
William M. Irvine, Presider

WC1. Invited Paper: Multiple Scattering in Thick Layers, H. C. van de Hulst, Rijksuniversiteit Leiden.

WC2. Invited Paper: Review of Radiative Transfer Methods in Scattering Atmospheres, Jacqueline Lenoble, Université des Sciences et Techniques, France.

WC3. Extending Radiative Transfer Models by Use of Bayes' Rule, Cynthia Whitney, C. S. Draper Laboratory.

WC4. An Improved Diffusion Approximation to Radiative Transfer in Atmospheres and Clouds, W. E. Meador and W. R. Weaver, NASA Langley Research Center.

WC5. A Solution to the Radiative Transfer Equation Employing a Semi-Analytic Integration over Optical Depth, Benjamin M. Herman, University of Arizona.

WC6. Radiative Transfer for Imaging Purposes, Bruce W. Fowler, US Army Missile Command.

WC7. Earth-Atmosphere Albedo Relationships for Realistic Atmospheres, Robert E. Turner, Environmental Research Institute of Michigan.

WC8. Analysis of Radiative Properties of Warm Clouds at Infrared Wavelengths, Richard D. H. Low and Richard B. Gomez, White Sands Missile Range.

Atmospheric Aerosols and Their Optical Properties

by K. Bullrich and G. Hänel

Institut für Meteorologie, Johannes Gutenberg-Universität,
Mainz, FR Germany

Abstract: Measured properties of atmospheric aerosol particles are presented. They must be known to compute the optical effects of the aerosols. Results of calculations are described.

Summary: To describe radiative properties of particulate matter suspended in the atmosphere the following parameters must be known: a) aerosol size frequency distribution (Fig. 4), b) complex refractive index (Fig. 2,3 and Table 1). These properties strongly depend on the relative humidity. Reasons are condensation of water vapor with increasing and evaporation of water with decreasing relative humidity. Humidity effects are illustrated on the Figures 1,2,5,6 and 7. The model computations are based on the presuppositions of thermodynamic equilibrium and of Mie-theory.

Literature:

- (1) K. Andre (1976). Diplomarbeit, Institut für Meteorologie, Johannes Gutenberg-Universität, Mainz
- (2) K. Fischer (1971). Contrib. Atm. Phys. 43, 244-254
- (3) K. Fischer and G. Hänel (1972). "Meteor" Forschungsergebnisse B 8, 59-62
- (4) K. Fischer (1973). Contrib. Atm. Phys. 46, 89-100
- (5) G. Hänel (1968). Tellus 20, 371-379
- (6) G. Hänel (1976). Advances in Geophysics 19, 73-188
- (7) G. Hänel and W. Blättner (1976). Unpublished results.
- (8) C. Junge and R. Jaenicke (1971). Aerosol Science 2, 305-314

Table 1: Mean complex refractive indices $n_o - ik_o$ of samples of dry aerosol particles at the wavelength of light 0.6 μm (references in brackets).

n_o	k_o	Description
1.59	-	Mainz, 8-22 Jan., 1966 (5)
1.55	-	Mainz, 3-12 May 1966 (5)
1.51	-	Mainz, 12-17 May 1966 (5)
1.64	-	Mainz, 17-20 and 23-24 May 1966 (5)
1.63	-	Mainz, 6-10 June 1966 (5)
1.64	-	Mainz, 30 June - 5 July 1966 (5)
1.55	-	Mainz, 27 Aug.-2 Sept. 1966 (5)
1.55	-	Mainz, 8-9 Sept. 1966 (5)
1.56	-	Mainz, 9-14 Sept. 1966 (5)

Table 1 - continued

n_o	k_o	Description
1.62	0.054	Mainz, average, Summer 1966 (2, 6)
1.55	0.047	"Meteor", 13-16 April 1969 (Model 3), (3)
1.56	0.011	"Meteor", 16-25 April 1969 (3)
1.55	0.050	Mainz, 16-17 Jan. 1970 (4, 6)
1.50	0.015	Hohenpeissenberg, Bavaria, FRG, 18 June - 27 Aug. 1970 (Model 6), (4, 6)

List of Figures:

Fig. 1: Ratio $r(f)/r_o$ of the particle volume equivalent radii at relative humidity f and in dry state versus relative humidity for a clean air aerosol (Hänel 1976, Model 6).

Fig. 2: Mean bulk density ρ and mean complex refractive index $n-ik$ versus relative humidity f for a clean air aerosol (Hänel 1976, Model 6).

Fig. 3: Mean mass absorption index k_o/ρ_o versus wavelength λ of light of dry aerosol particles of different size ranges and of corresponding dry precipitation residues for a clean air aerosol (Andre 1976). Dusselbach is located in the western part of the FR Germany. o = dry state.

Fig. 4: Schematic diagram of the particle size frequency distributions of different types of aerosols (after Junge and Jaenicke 1971). N = total particle number per cm³, r = particle volume equivalent radius.

Fig. 5: Ratios $\delta_e(f)/\delta_{eo}$, $\delta_s(f)/\delta_{so}$, $\delta_a(f)/\delta_{ao}$ of extinction, scattering, and absorption coefficients and ratio $Q(f)/Q_o$ of the total geometrical cross section of the volume equivalent spheres versus relative humidity f for a maritime aerosol (Hänel 1976, Model 3). E = extinction, S = scattering, A = absorption, o = dry state.

Fig. 6: Phase function of a clean air aerosol (Model 6) at different relative humidities f versus scattering angle (Hänel and Blättner 1976).

Fig. 7: Degree of polarization of a clean air aerosol (Model 6) at different relative humidities f versus scattering angle (Hänel and Blättner 1976).

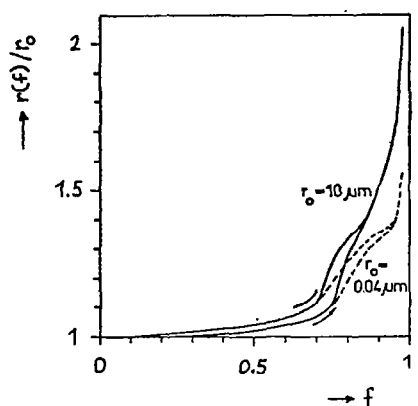


Fig. 1

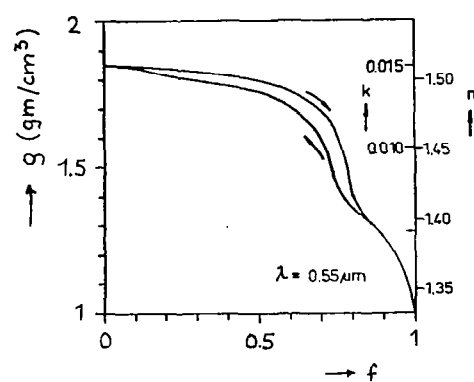


Fig. 2

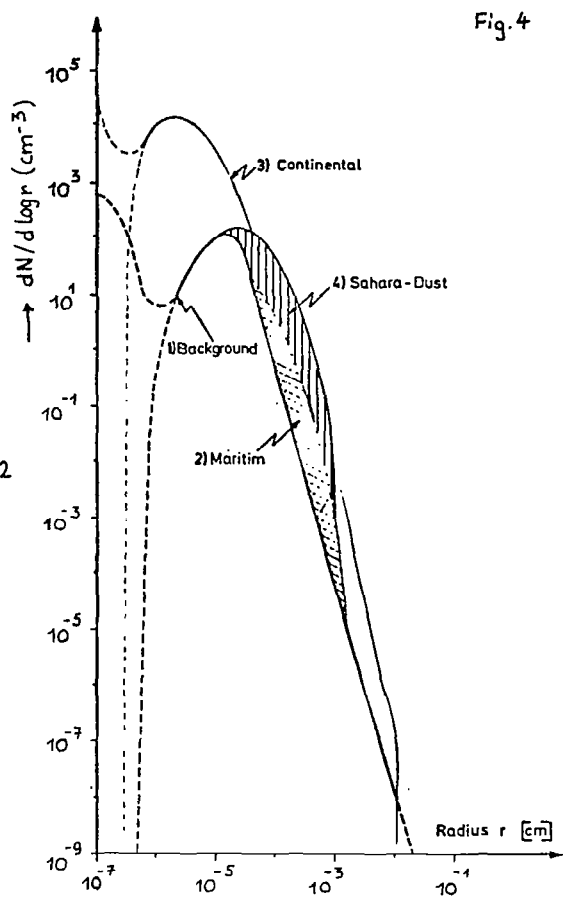


Fig. 4

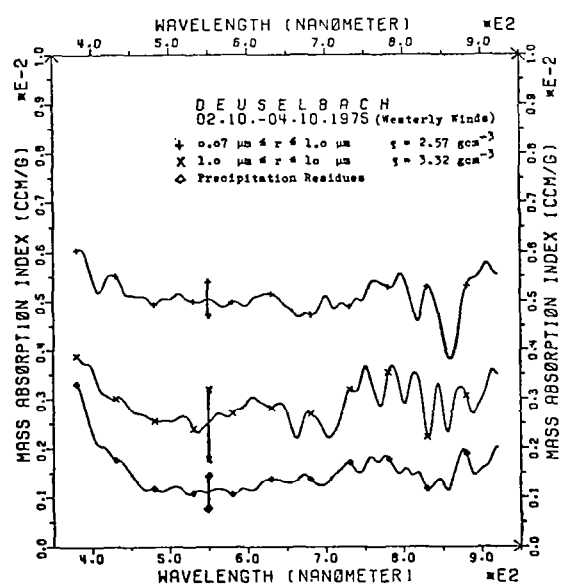
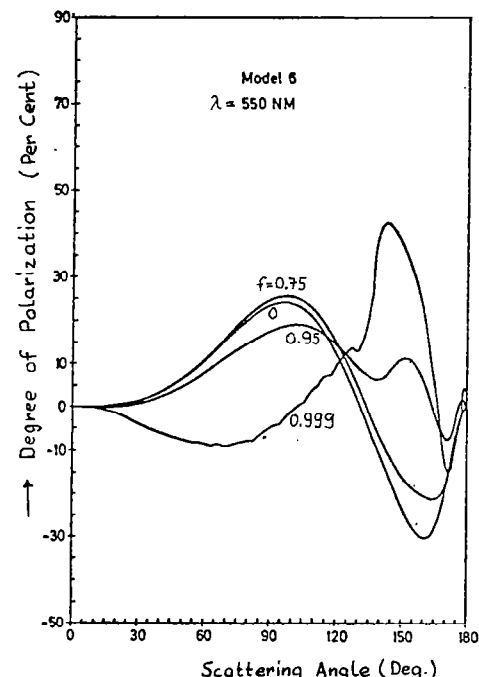
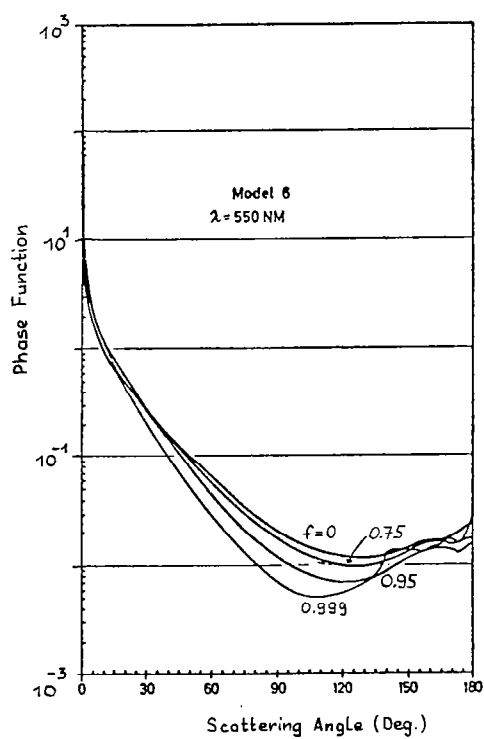
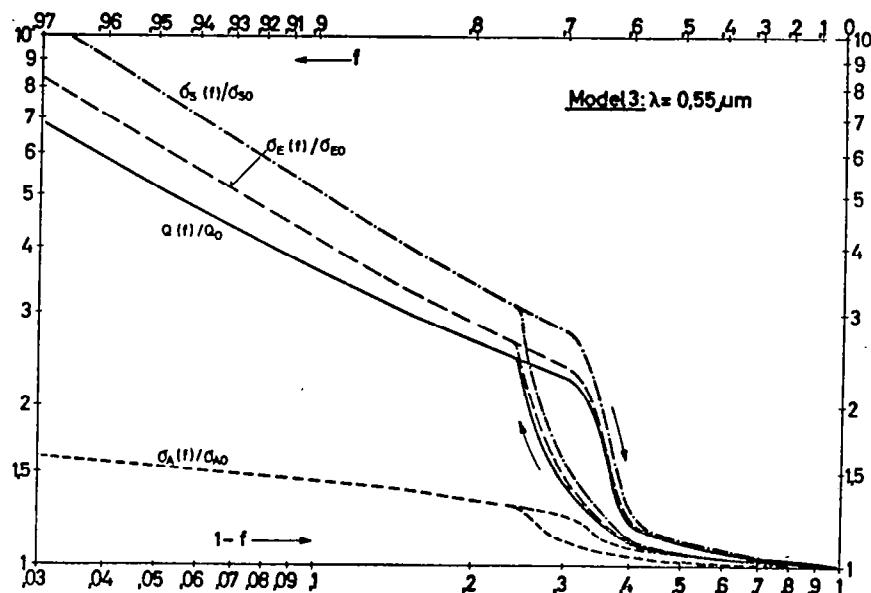


Fig. 3



Measured and Analytic Distributions of Stratospheric Aerosols: A Review and Commentary

Franklin S. Harris, Jr., Old Dominion University, Norfolk, Virginia 23508
James M. Rosen, University of Wyoming, Laramie, Wyoming 82070

The measured size distribution of the stratospheric aerosol is becoming a highly sought after yet elusive quantity. Its reliable measurement is relatively difficult. The size distribution is required in optical models for radiation transfer calculations and interpretation of measurements obtained from spacecraft require accurate optical models to utilize the basic data. A detailed knowledge of the particle size distribution is also fundamental to the development of an aerosol formation model in the stratosphere. The purpose of this paper is to review critically and compare relevant size distribution measurements to eliminate those data or portions thereof that are not in the mainstream, and present a consensus of the present state of knowledge of the stratospheric aerosol size distribution.

As a basis for comparison we have chosen the integral size distribution $N(r)$, the number of particles per cm^3 with radius equal to or greater than r . Thus not only can a comparison of the shape of the size distribution be made, but also of the absolute values. Unless the absolute values as determined from a particular measurement are within reason the sample is not necessarily representative and consequently the resulting size distribution shape is highly suspect. In the past most reviewers have assumed the measured size distributions were representative and simply normalized the absolute values so that an easy comparison of the curve shapes could be made (see for instance, Toon and Pollack, 1976). This procedure is obviously questionable and produces highly misleading impressions. The basic data to be considered in this paper is presented in Figure 1 and can be divided into two main groups--that obtained from impactors and that obtained from photoelectric particle counters. Although this figure gives an overall impression that there is a mainstream of agreement there are some alarming discrepancies.

The present state of knowledge of the stratospheric aerosols is based almost entirely on information gained through the use of impactors. This is an old and often used technique for the collection of solid particles but its application to the sampling of the volatile particles of the stratosphere (H_2SO_4) should be given much more attention by those who use it. Once the particles are removed from their environment in which they are in equilibrium with H_2SO_4 and H_2O vapor they can in general be expected to change size considerably through evaporation or absorption of more water. Thus there is not necessarily a straight forward relation between the particle's in situ size and its size as seen under the microscope in the laboratory. In spite of this, most experimenters using impactors to collect stratospheric samples have, without experimental justification, assumed that the in situ size is the same as it appears under the microscope. One of the major discrepancies between the sets of data shown in Figure 1 is the concentration of particles at $1 \mu\text{m}$ radius as suggested by the impactor measurements of Mossop, Junge, et al., Ivlev, and Ferry and Lem, when compared to the much lower and we believe more realistic values obtained by the Wyoming group, and Brownlee, et al. The latter group used impactors designed to collect only large particles and these particles were found to be predominantly solid Al_2O_3 from rocket engines. Thus there is little uncertainty in this case concerning the size of the particles. Since most of the data in Figure 1 under Brownlee, et al., was collected by Ferry, we have one experimenter reporting a 4 orders

of magnitude discrepancy in his own data at 1 μm radius. One possible explanation of this discrepancy is that the size of the largest particles determined in the laboratory by Ferry and Lem is about three times larger than the actual *in situ* values. Since the problems of the Ferry and Lem data are not unique to most of the impactor results shown in Figure 1 we feel that this general technique of sampling the volatile stratospheric aerosol is not reliable. One notable exception to the previously mentioned impactor results illustrated in Figure 1 is the work of Bigg. In this case the H_2SO_4 particles were made to react chemically with a substrate on the collecting surface and the reaction zone was then related to the size of the original particle. This appears to represent a considerable improvement in the technique of impactor sampling of volatile particles. Another problem associated with impactor sampling is the sometimes low and generally unknown collection efficiency of small particles ($r \geq 0.1 \mu\text{m}$). Some authors make a correction for the collection efficiency and others do not. This effect along with natural fluctuations is probably responsible for most of the scatter in the data for radii less than 0.3 μm . The data of Mossop and Friend show a very low total concentration and therefore do not meet our criteria as being representative samples.

The other type of data illustrated in Figure 1 were gained from photoelectric particle counters. These types of instruments are sometimes looked upon with suspicion because they cannot always be uniquely calibrated. However for particle radii less than 0.25 μm the instruments quoted in this work can be quite respectably calibrated (Pinnick and Hofmann, 1973) and certainly have the potential of producing accurate size measurements of the volatile stratospheric aerosol. Although the agreement between the two groups using photoelectric particle counters is not bad, in view of the similarity of the instruments the agreement should be much better. The size distributions of Miranda and Dulchinos, and Miranda, et al. seem to be unrealistically steep for the largest particles that they observed. Their measured concentration for these sizes is almost 3 orders of magnitude below that reported by Ferry and Lem. The counter used by this group, unlike the Wyoming counter, has to our knowledge never been environmentally tested to determine the counting efficiency vs. altitude. The concentration of the smallest particle size reported by the Wyoming group was obtained with a photoelectric cn counter (Rosen and Hofmann, 1975). Although the size of these particles is not at all well known, it is of minimal importance in this region of the size distribution. Other measurements of the very small particle concentration in the stratosphere by Käselau (1974) support the measurements of the Wyoming group.

The concentration measurements made at both extremes of the size distribution all seem to be quite consistent and provide valuable bounds for assessing the experimental data in the middle region of Figure 1. In addition these bounds are extremely valuable for fitting analytic size distributions to the experimental data. Figure 2 shows some of the many size distributions that have been used and suggested by various researchers. Several of these curves (Wyoming, Zold, aged volcano) are reasonably good fits to the "mainstream" of the measurements and have been used successfully to predict some of the observed optical properties of the stratospheric aerosol as well as the mass loading (Pinnick, et al., 1976; Toon and Pollack, 1976). It should be remembered, however, that all the measurements presented in Figure 1 are thought to represent quiet conditions not perturbed by a recent volcanic eruption.

Conclusion: It is extremely difficult if not impossible to determine accurately *in situ* particle size of the volatile stratospheric aerosol using a simple impactor technique. In regions where the size distribution is steep, this deficiency becomes very serious and is, we feel, responsible for many of the apparent discrepancies in Figure 1. The photoelectric counter method yields much better information concerning the size of the particles but an inaccurate knowledge of their counting efficiency as a function of altitude causes some uncertainties in the measured concentrations. The concentration of particles in both the large and size extremes provides very useful limits for assessing the credibility of various mid-range measurements as well as providing boundary conditions for analytic fits to the data. This work was partially supported under NASA Grant NSG 1245.

References:

Bigg, E. K., 1975: Stratospheric particles. *J. Atmos. Sci.*, 32, 910-917.

Brownlee, D. E., Guy V. Ferry and D. Tomandl, 1976: Stratospheric aluminum oxide. *Science*, 191, 1270-1271.

Deirmendjian, D., 1973: On volcanic and other particulate turbidity aerosols. *Adv. Geophys.*, 16, 267-296.

Ferry, Guy V., and Homer Y. Lem, 1974: Aerosols at 20 km altitude. *Environmental Impact of Aerospace Operations in the High Altitude Second International Conference*, July 8-10, 1974, San Diego, California, American Meteorological Society, Boston, pp. 27-32.

Friend, James P., 1966: Properties of the stratospheric aerosol. *Tellus*, 18, 465-473.

Ivlev, L. S., 1975: personal communication on results at Rylsk. See J. M. Rosen, N. T. Kjome and D. J. Hofmann, *Bull. Am. Meteor. Soc.*, 57, 225.

Junge, C. E., C. W. Chagnon, and J. E. Manson, 1961: Stratospheric aerosols. *J. Meteor.*, 18, 81-108.

Käselau, K. H., 1974: Measurements of aerosol concentration up to a height of 27 km. *Pure Appl. Geophys.*, 112, 877-885.

Miranda, Henry A., Jr., and John Dulchinos, 1975: Balloon measurements of stratospheric aerosol size distribution following volcanic dust incursion. AFCRL-TR-75-0518. Aug.

Miranda, Henry A., Jr., John Dulchinos, and Henry P. Miranda, 1973: Atmospheric balloon aerosol particle counter measurement. Epsilon Laboratories, Inc., Bedford, Massachusetts, AFCRL-TR-73-0700 (Nov.)

Mossop, S. C., 1964: Volcanic dust collected at an altitude of 20 km. *Nature*, 203, 824-827.

Murphy, C. H., and J. S. Kim, 1975: The importance of stratospheric aerosols in determining twilight transmission functions. *Ann. Geophys.*, 31, 395-400.

Pinnick, R. G., and D. J. Hofmann, 1973: Efficiency of light-scattering aerosol counters, *Appl. Opt.*, 12, 2593-2597.

Pinnick, R. G., J. M. Rosen and D. J. Hofmann, 1976: Stratospheric aerosol measurements III, Optical model calculations, *J. Atmos. Sci.*, 33, 304-313.

Rosen, J. M., and D. J. Hoffmann, Balloon-borne measurements of condensation nuclei report #CN-3 of the Atmospheric Physics Group, University of Wyoming, Laramie, Wyoming (submitted for publication).

Shettle, Eric P., and Robert W. Fenn, 1975: Models of atmospheric aerosols and their optical models. AGARD Optical Propagation in the Atmosphere, 27-31 Oct., Lynby, Denmark. Conference Proc., CP-183, pp. 2-1 to 2-16.

A DETERMINATION OF AEROSOL SIZE DISTRIBUTIONS FROM
SPECTRAL OPTICAL DEPTH MEASUREMENTS

M. D. King¹, D. M. Byrne², B. M. Herman¹, J. A. Reagan³

The University of Arizona
Tucson, AZ 85721

¹ Institute of Atmospheric Physics

² Optical Sciences Center

³ Electrical Engineering Department

A solar radiometer has been used at the University of Arizona in order to monitor the directly transmitted solar irradiance at selected wavelengths throughout the day. From values of total optical depth obtained from this type of measurement, it is possible to correct for molecular scattering and ozone absorption and thus obtain values of aerosol optical depth (King and Byrne, 1976). The spectral optical depth values are produced through attenuation by aerosols and are primarily determined by the aerosol size distribution. The spectral optical depth measurements have been successfully inverted in order to obtain a columnar size distribution for over 40 days thus far. The present investigation indicates a correlation between the character of the inversion result and the type of spectral optical depth values which are measured.

In theory, the integral equation relating size distribution to aerosol optical depth, designated τ_a , can be written as

$$\begin{aligned}\tau_a(\lambda) &= \int_0^\infty \pi r^2 Q_t(\lambda, r, m) \int_0^\infty n(r, z) dz dr \\ &= \int_0^\infty \pi r^2 Q_t(\lambda, r, m) n_c(r) dr\end{aligned}$$

where n represents the columnar size distribution as a function of radius, r , and Q_t is the extinction efficiency factor from Mie theory. In practice, the integral on the right hand side is replaced by a sum over coarse intervals in r , each of which is composed of several sub-intervals as described by Herman *et al.* (1971). The method of inversion used here is a linear inversion with second derivative smoothing constraint as described by Twomey (1963).

Figure 1 shows the result for 29 August 1975 in which the spectral optical depth measurement follows very nearly the power law with a corresponding Junge or two-slope type size distribution. The solid line on the $\log \tau_a$ versus $\log \lambda$ plot indicates how the inverted size distribution reproduces the measurements. The three different size distribution results correspond to different Junge distribution initial guesses indicating a relative insensitivity to the initial guess except in the radii range where no information exists.

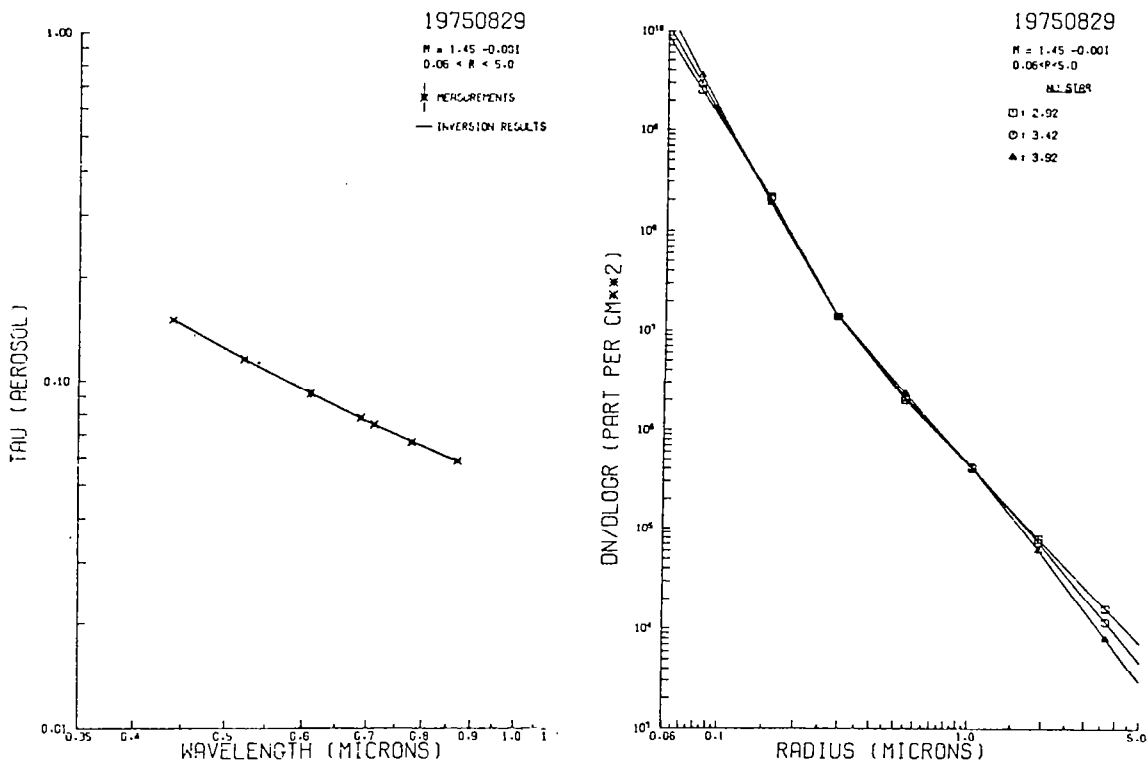


Figure 1. Observed optical depth and estimated size distribution for 29 August 1975 at Tucson, Arizona.

In cases in which the optical depth versus wavelength shows negative curvature, i.e., the optical depth decreases rapidly with both increasing and decreasing wavelength, we observe size distribution results indicating a log-normal type of behavior. This is due to the absence of both small and large particles as suggested by the $\log \tau_a$ - $\log \lambda$ plot.

Figure 2 shows just such a case for 24 October 1975. Note the good agreement in distribution function for the three Junge distribution initial guesses. The inversion procedure is clearly capable of perturbing the initial guess as required.

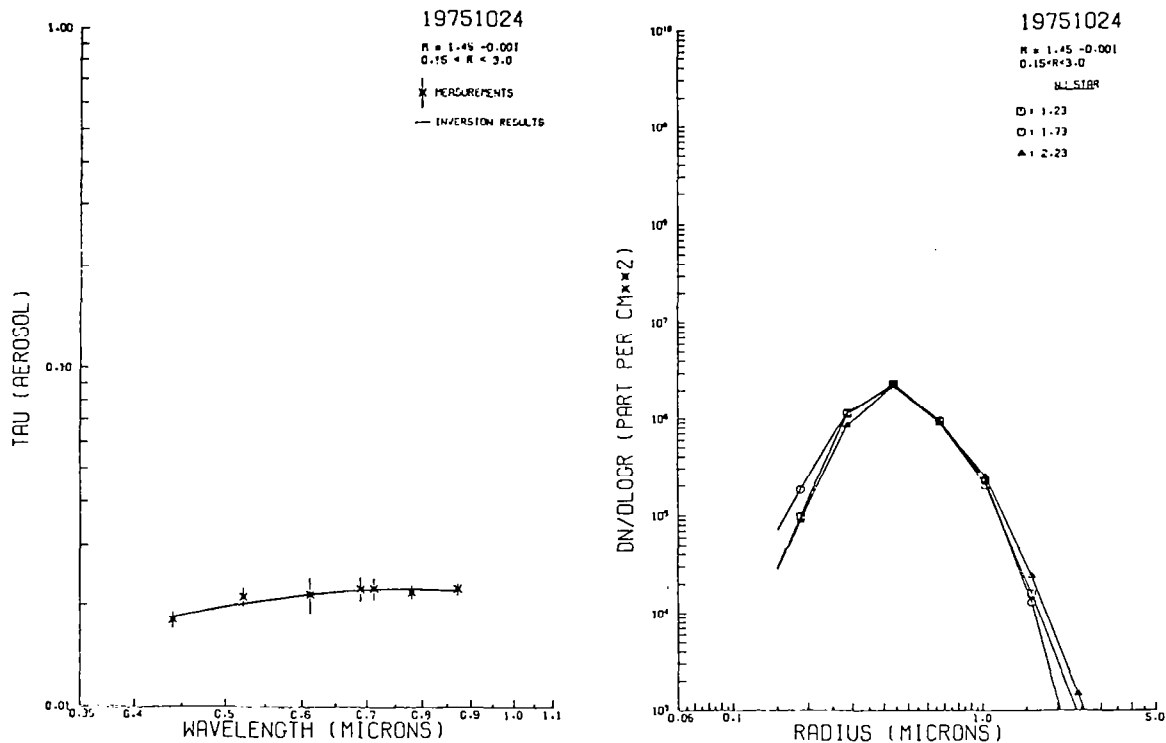


Figure 2. Observed optical depth and estimated size distribution for 24 October 1975 at Tucson, Arizona.

Perhaps the most interesting distribution type which we have observed is one for which the spectral optical depth values show positive curvature becoming the most pronounced at the largest wavelengths. Such a data type is exhibited in Figure 3 for 15 March 1976. We have observed this data type often enough to be of significance and it always yields size distributions with an apparent source of large particles. This could easily be described as constituting a Junge plus a log-normal size distribution.

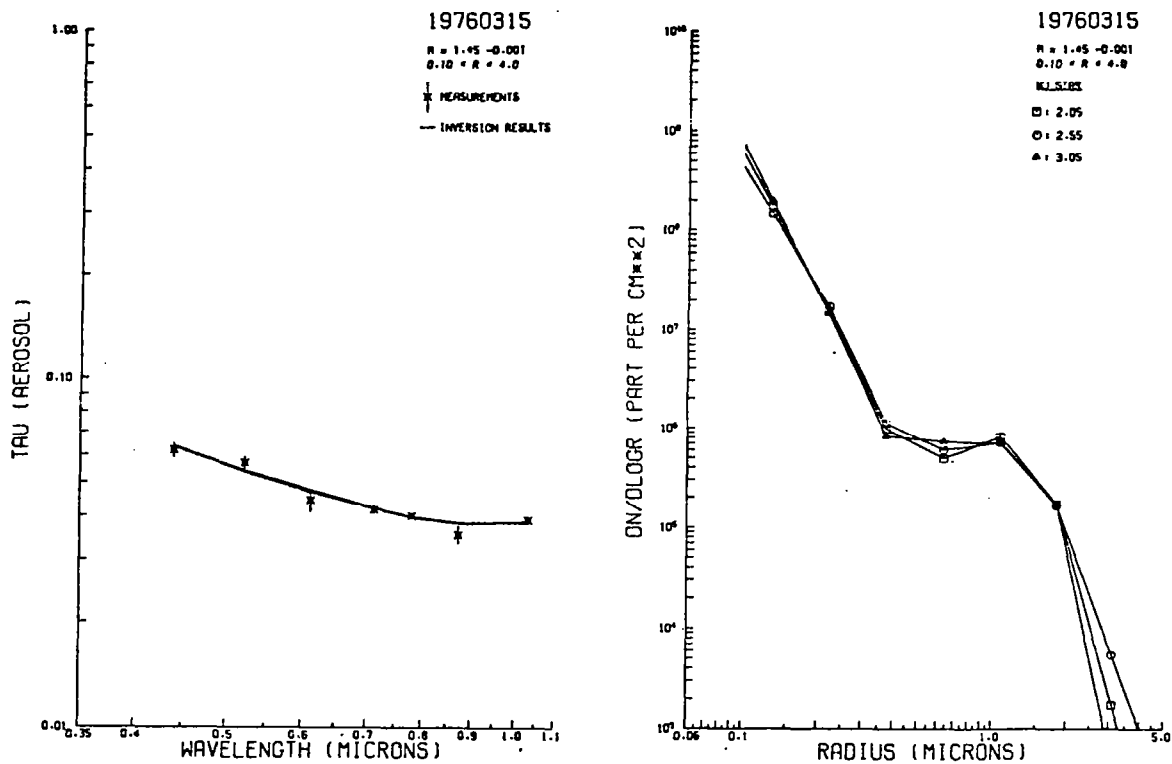


Figure 3. Observed optical depth and estimated size distribution for 15 March 1976 at Tucson, Arizona.

References

Herman, B. M., S. R. Browning, and J. A. Reagan, 1971: Determination of aerosol size distributions from lidar measurements. *J. Atmos. Sci.*, **28**, 763-771.

King, M. D., and D. M. Byrne, 1976: A method for inferring total ozone content from the spectral variation of total optical depth obtained with a solar radiometer. To be published in *J. Atmos. Sci.*, **33**.

Twomey, S., 1963: On the numerical solution of fredholm integral equations of the first kind by the inversion of the linear system produced by quadrature. *J. Assoc. Comput. Mach.*, **10**, 97-101.

AIRBORNE MEASUREMENTS OF PARTICLE SIZE DISTRIBUTION,
LIGHT SCATTERING AND TURBIDITY AT DIFFERENT ALTITUDES

by

A. J. Alkezweeny and N. S. Laulainen
Battelle-Pacific Northwest Laboratories,
Richland, Washington 99352

Simultaneous measurements of particle size distributions, light scattering extinction coefficients and turbidity (aerosol optical depth) over the Pacific Northwest were made in June 1976 using an instrumented DC-3 aircraft. The particle size distributions were measured in the range of 0.01 to 5 μm with an electrical aerosol analyzer (Liu, et al., 1975) and a Royco Optical Sensor, Model 220. The optical sensor was interfaced with a 15-channel pulse height analyzer and printer. Aerosol light scattering data were obtained with an MRI integrating nephelometer, Model 1562 (Ahlgren and Charlson, 1967). A multiwavelength sunphotometer was employed to measure solar intensities in 5 wavelength bands; only the turbidities derived from the channel at $\lambda = 500 \text{ nm}$ were used in this study.

Data were collected at different altitudes from ground-level to 10,000 ft. MSL. Aerosol extinction coefficients were derived from sunphotometer turbidity measurements using the relationship,

$$b = \Delta\tau/\Delta h$$

where $\Delta\tau$ is the difference between turbidities measured at h and $h + \Delta h$. The integrating nephelometer measured aerosol scattering extinction coefficient, b_{scatt} , directly at wavelength $\lambda = 525 \text{ nm}$. For comparison, aerosol extinction coefficients were calculated from the measured size distributions at each altitude using tabulated Mie extinction efficiencies $Q(\alpha_i, n)$ for refractive index $n = 1.6 - 0i$ and a wavelength of $\lambda = 500 \text{ nm}$ from the expression

$$b = \sum_i Q(\alpha_i, n) \Delta S(D_{p_i}) \cdot \frac{10^{-6}}{4}$$

where $\alpha_i = \pi D_{p_i} / \lambda$ is the size parameter and $\Delta S(D_{p_i})$ is the measured particle surface area ($\mu\text{m}^2/\text{cm}^3$) in the geometric mean particle diameter size class D_{p_i} . The summation is over all size intervals from about 0.04 to 5 μm .

Figure 1 shows the particle volume distributions measured over the Tri-Cities, Sunnyside, and Seattle, Washington. It can be seen that the size distributions are bi-modal with a peak at 0.1 - 0.2 μm particle diameter and a second peak greater than 1 μm . According to Whitby (1973), the submicron mode is characteristic of the polluted atmosphere while the second mode is caused by mechanically produced aerosol such as resuspension and sea spray; there is no interaction between the two modes. The latter can be seen easily by comparing the distributions from Sunnyside and Seattle. Sunnyside is a small community in Eastern Washington with no major sources of pollution in contrast to the large metropolitan city of Seattle, where many sources exist. Since the first mode is a result of chemical reactions, it is expected that the peak of this mode should be higher for Seattle than for Sunnyside. On the other hand, the second mode is not related to the pollution level and

therefore the two locations ought to have similar values. Actually, the peak of the second mode at Sunnyside is higher than Seattle, indicating resuspension of dust as a possible cause. Over the Tri-Cities on June 8, there was a temperature inversion between 5000 and 6000 ft. MSL, resulting in a reduction in concentration of all particle size classes above the inversion. Similar effects were observed in St. Louis in 1975 by the authors (Alkezweeny and Laulainen, 1976).

Comparison of the calculated aerosol scattering extinction coefficients using a refractive index of 1.6 and the measured extinction coefficients obtained with the integrating nephelometer and the sunphotometer are shown in Figure 2. In all cases, the calculated values are smaller than the measured values. The poor agreement between measured and calculated extinction was also found for the data obtained over St. Louis during August 1975, even when a substantial imaginary aerosol refractive index was included in the calculations. In many cases, the extinction coefficients derived from the sunphotometer measurements are larger than those obtained with the nephelometer, which measures only aerosol light scattering, while the sunphotometer optical depths contain both light scattering and absorption by the aerosol. Although the measured and calculated b_{scatt} do not agree, the two quantities are well correlated. A correlation coefficient of 0.93 was determined for this set of data. Such behavior was also found by Ensor, et al., (1972), for Los Angeles aerosol. The error in the aerosol extinction coefficients derived from the sunphotometer turbidity measurements is very large in a clean air case because of instrumental resolution and it is consequently difficult to compare them with the nephelometer and calculated values.

On the basis of these limited data and those obtained by the authors at St. Louis, it is not practical to derive particle size distributions from multiwavelength sunphotometer measurements alone; the situation is particularly poor for clean air case.

This paper is based on research performed under U. S. Energy Research and Development Administration Contract E(45-1):1830.

References:

1. Ahlquist, N. C., and R. J. Charlson, "A new instrument for evaluating the visual quality of air," J. Air. Poll. Control Assoc., 17, 467-469, 1967.
2. Alkezweeny, A. J., and N. S. Laulainen, "Simultaneous aerosol size distributions and turbidity measurements over a metropolitan area," Pacific Northwest Laboratory Annual Report for 1975 to the USERDA Division of Biomedical and Environmental Research. Part 3, Atmospheric Sciences, 202-205, 1976.
3. Ensor, D. S., R. J. Charlson, N. C. Ahlquist, K. T. Whitby, R. B. Husar, and B. Y. H. Liu, "Multiwavelength nephelometer measurements in Los Angeles smog aerosol. 1. Comparison of calculated and measured light scattering," J. Coll. Interf. Sci., 39, 242-251, 1972.
4. Liu, B. Y. H., and D. Y. H. Pui, "On the performance of the electrical aerosol analyzer," J. Aerosol Sci., 6, 249-264, 1975.
5. Whitby, K. T., "On the multimodal nature of atmospheric aerosol size distributions," Presented at VII International Conference on Nucleation, Leningrad, U.S.S.R., September, 1973.

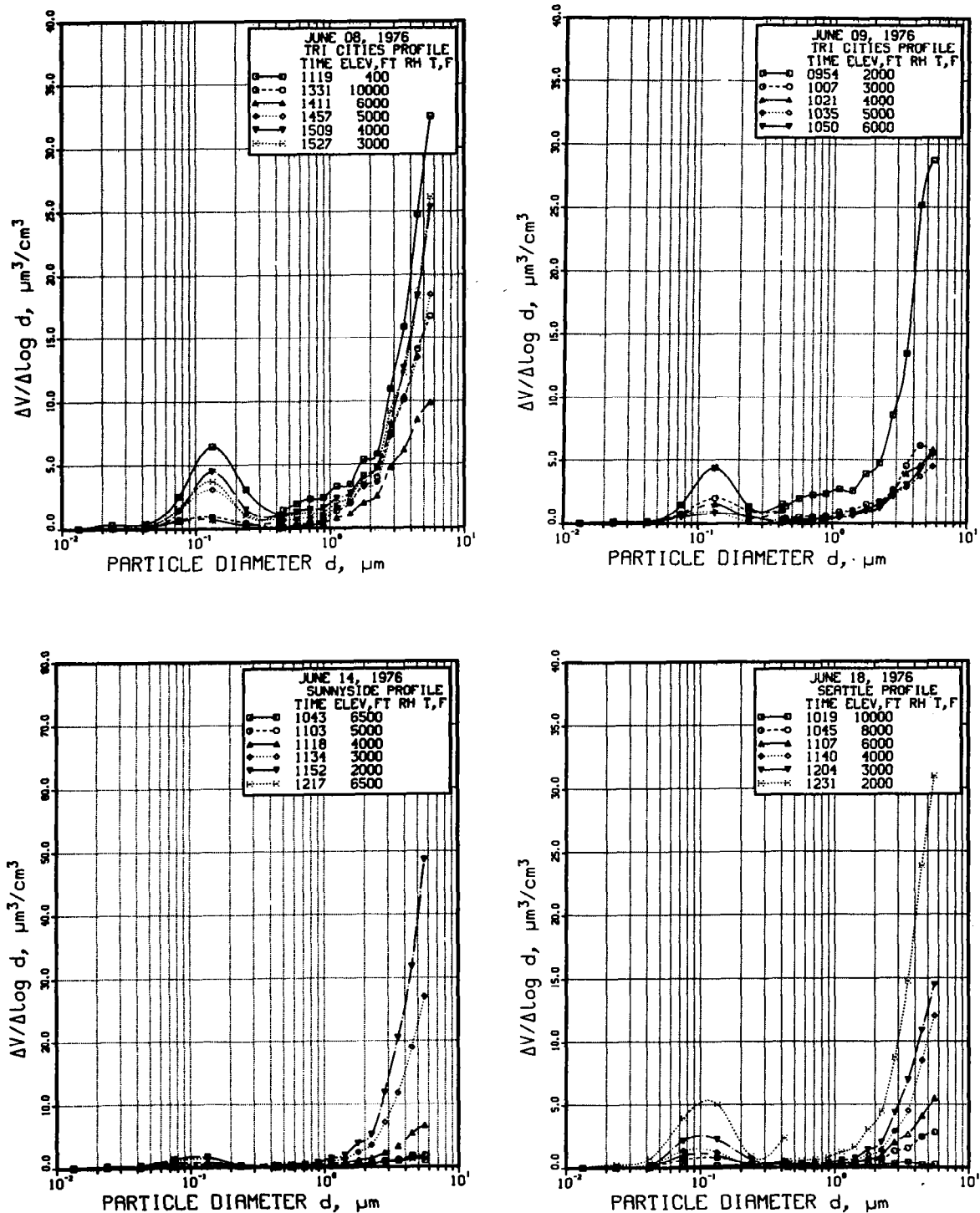
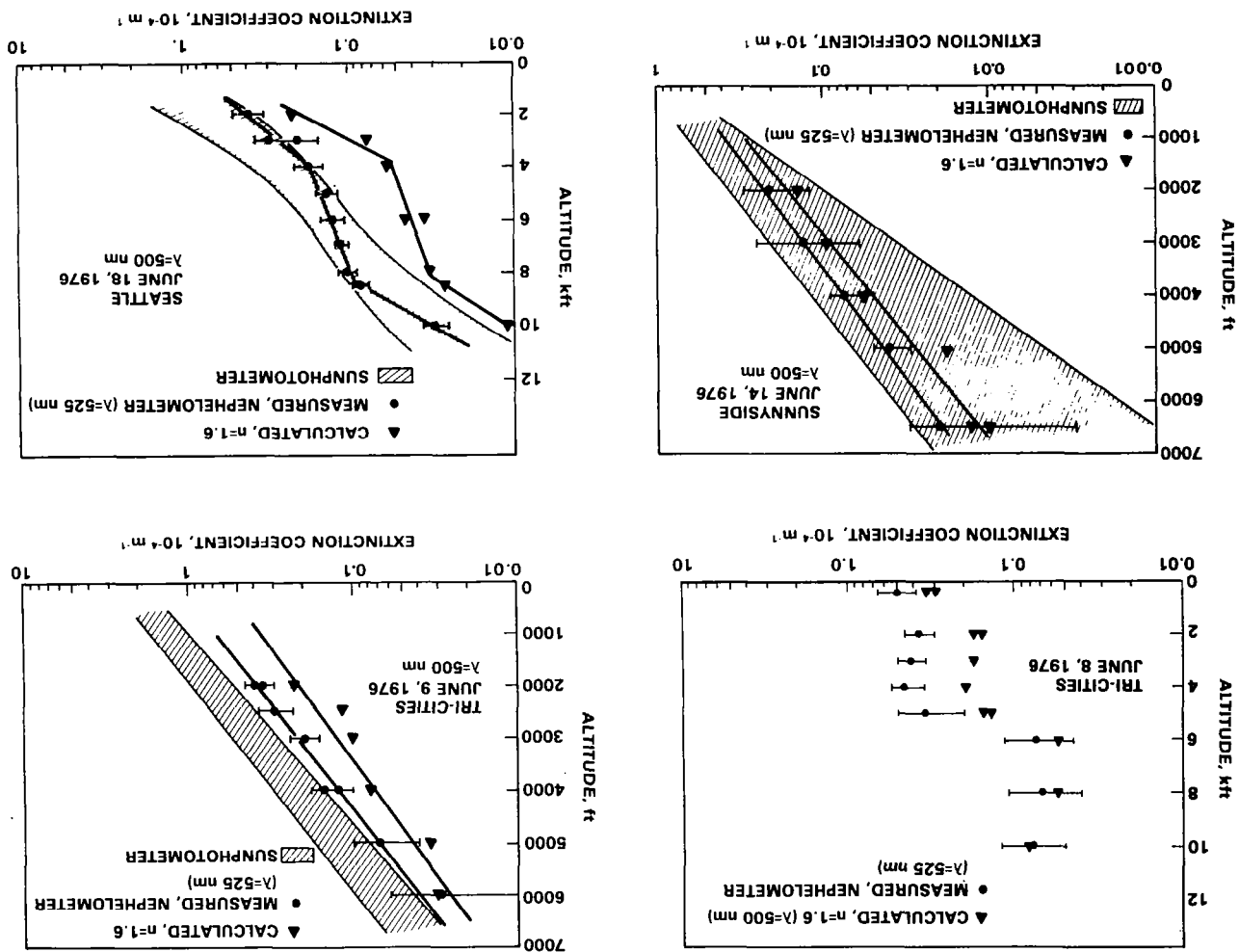


Figure 1. AEROSOL VOLUME DISTRIBUTIONS

Figure 2. Calculated and Measured Extinction as a Function of Altitude.



Coastal Aerosol Measurements

Gary L. Trusty[†]
and
Thomas H. Cosden

As a supplement to a series of atmospheric laser transmission measurements, a system was designed and constructed which would allow site measurements of aerosol distributions and other related parameters. Figure 1 depicts, schematically, the mobile laboratory configuration. It is a self-powered vehicle containing all of the electronics and two towers for mounting sensors at distances up to 38 meters from the main unit.

For simplification of data reduction, all the meteorological information, as well as the particle sizing information, are stored on one magnetic tape.

Figures 2, 3 and 4 show representative data for three locations on the days noted in 1975. For those data only the ASASP (Active Scattering Aerosol Spectrometer Probe) was in use. This unit is represented in Fig. 1 as the probe covering the size range 0.1 to 4 μ radius. The data from those three locations are plotted as $\frac{dN}{dr}$ vs. r . The peaks near 0.7 μ are believed to be machine dependent due to a double valued sizing sensitivity curve as described by Knollenberg and Luehr.¹

Figure 5 shows aerosol data taken in Trinidad, California during an occurrence of patchy fog. Note that in that figure the second aerosol counter of Fig. 1 has been added, thus extending the size range to beyond 20 μ diameter. Figure 5 is also plotted slightly differently than the others. Here the ordinate is $N(cm^{-3})$, i.e., the number of particles larger than the corresponding abscissa reading. This difference in presentation was made to allow easier comparisons with other optical particle counters in use at the Trinidad site. A particle counter comparison plot is shown in Figure 6. A detailed report describing the Trinidad measurement will be presented elsewhere.²

Other types of output capable of being produced from the aerosol van data are given in Fig. 7. There is shown an example of the variation of aerosols due to cloud modulation of solar radiation. Other observations of this phenomenon are discussed in Ref. 3. These results show emphatically the necessity of proper sampling procedures.

All the other meteorological variables are also available in a format similar to that in Fig. 7, viz. as a function of time of day. Cross correlations between aerosol and meteorological parameters are routinely done.

[†]Authors are at Naval Research Laboratory, Washington, D. C. 20375

The above results are all from point source measurements. To study the spatial distribution of aerosol fields, which is extremely important for most operations involving optical transmission, the system described in Fig. 8 is now being instrumented.

References

1. Knollenberg, R. G., and Luehr, R., Open Cavity Laser "Active" Scattering Spectrometry from 0.05 to 5 Microns. Particle Measuring Systems Report, Boulder, Colorado.
2. Participants were: NWC; Edward Hindman (coordinator of the effort) and Raymond Kelso: DRI; James Hudson and Fred Rogers: NRL; (PMS) Gary Trusty and Thomas Cosden, (Royco) William Hoppel and James Fitzgerald.
3. Kapustin, V. N., et al; Izv., Atmospheric and Oceanic Physics, Vol. 10, No. 12, 1974.

MOBILE LABORATORY

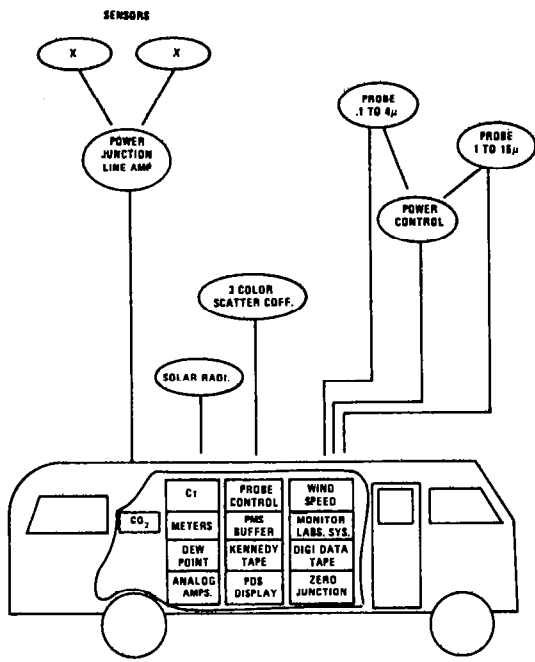


Fig. 1

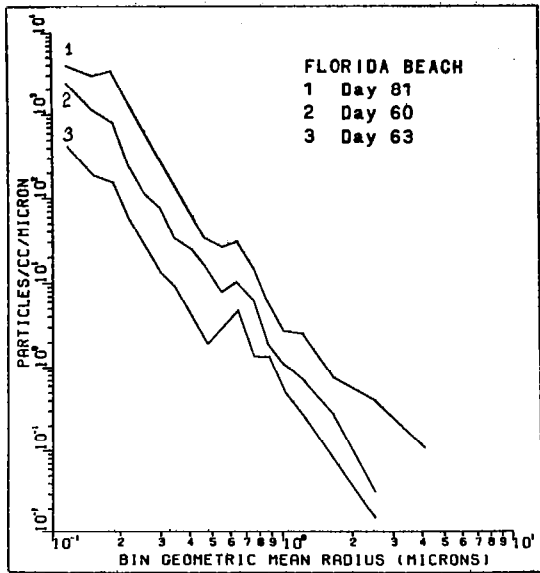


Fig. 2

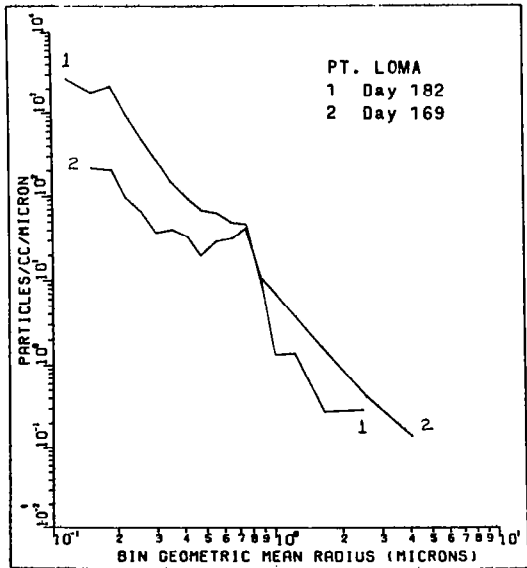


Fig. 3

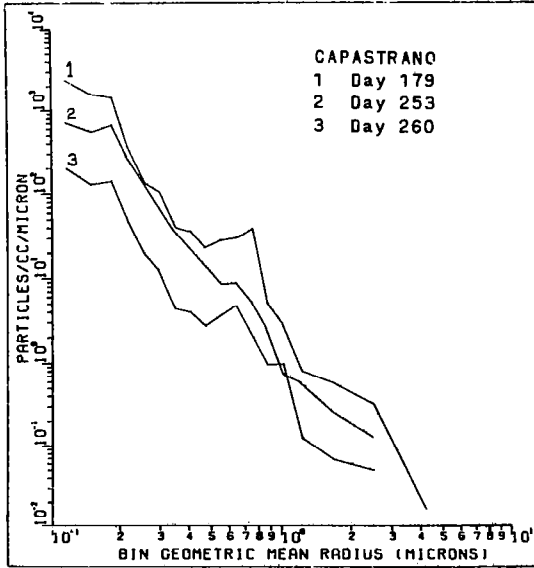


Fig. 4

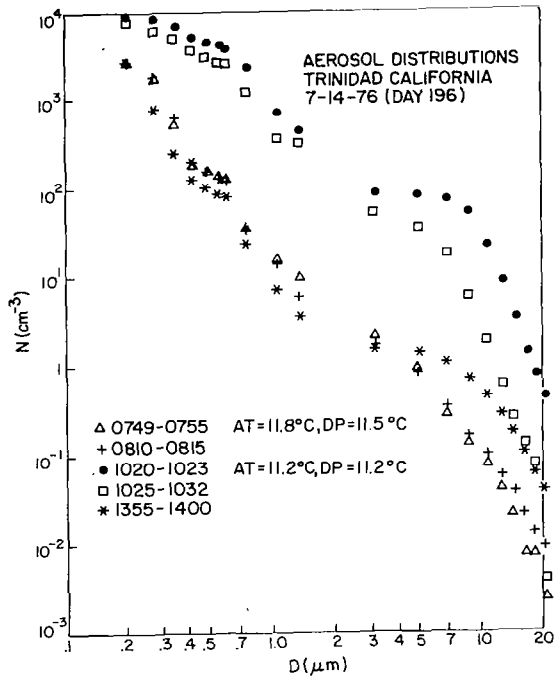


Fig. 5

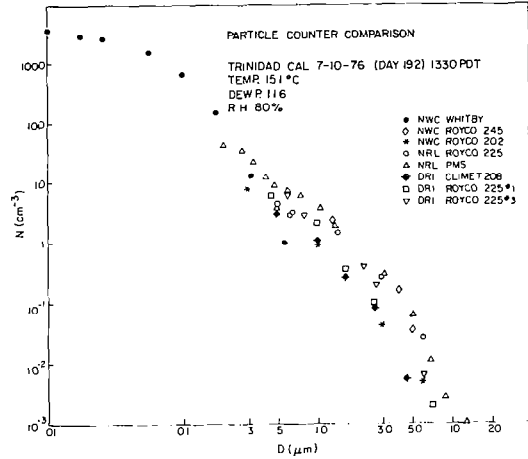


Fig. 6

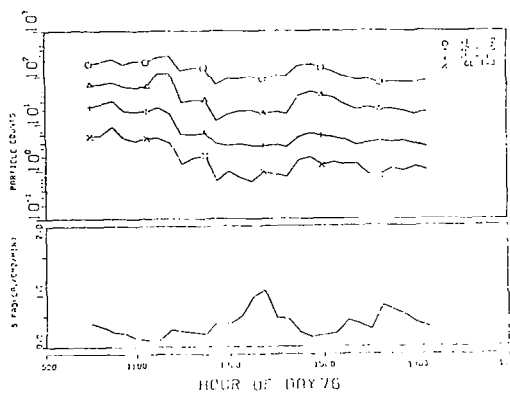
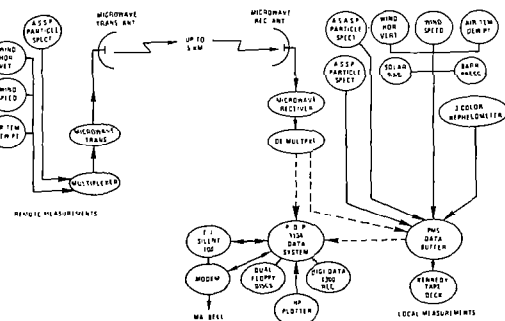


Fig. 7



AEROSOL MEASUREMENT SYSTEM

Fig. 8

Atmospheric Turbidity over the Northern Equatorial Atlantic during
the Summer of 1974: the Impact of North African Aerosols

J.M. Prospero, T.N. Carlson*, D. Savoie and R.T. Nees
Rosenstiel School of Marine and Atmospheric Science
University of Miami
4600 Rickenbacker Causeway
Miami, Florida 33149

*Department of Meteorology
Pennsylvania State University
University Park, Pennsylvania

Introduction

Studies of the aerosols in the atmosphere of the equatorial North Atlantic and the Caribbean have shown that the principal component of the aerosol is mineral dust which originates from the arid and semiarid regions of West Africa (Carlson and Prospero, 1972; Prospero and Carlson, 1972). These studies have shown that there is a very pronounced seasonal periodicity in the dust concentration in the tradewinds, the maximum concentration occurring during the summer. Another trend which has become evident is the dramatic increase in dust load which occurred during the last several years, especially 1973 and 1974. This increase coincided with the most severe portion of the extended drought that afflicted North Africa in the early seventies.

These high mineral aerosol concentrations are attributable to large scale dust outbreaks which occur along the coast of Africa, mostly between 15° and 25° N. These outbreaks result in markedly hazy conditions over the entire equatorial northern Atlantic and the Caribbean; the movement of the dust outbreaks across the Atlantic can be readily followed by means of satellite photographs.

In this paper, we report on atmospheric turbidity measurements made in a network in the Northern Equatorial Atlantic in a three month period during the summer of 1974 as a part of GATE (Global Atmospheric Research Program Atlantic Tropical Experiment). Measurements were made with Volz sun photometers at two wavelengths, 500nm and 880 nm. The land stations were: Dakar, Senegal; Sal Island, Cape Verde Islands; Barbados, West Indies; Miami, Florida, and Bermuda. Also, measurements were made from eight ships distributed across the Atlantic between the equator and 20° N.

Results and Discussion

The monthly mean turbidities at Sal, Barbados and Miami are shown in Table 1. The daily values of the Volz turbidity at 500nm and of α are plotted in Figures 1, 2 and 3. Also presented in these figures are the daily average mineral aerosol concentrations ($\mu\text{g m}^{-3}$) at each station as determined by filter collections.

The mean turbidities at Sal are high--they are comparable to those of a large industrialized city. The mean turbidities decrease with increasing distances from the coast of Africa westward across the Atlantic. This is most clearly seen in Figure 4 which presents the mean monthly turbidity (500nm) for all land and ship stations during July.

The high turbidities are obviously related to the presence of mineral aerosols emerging from the coast of Africa. However, the turbidity is not highly correlated with the dust concentrations as measured at sea level. The mean turbidities (500nm) for the entire experimental period were (Prospero *et al.*, 1976): Sal, 0.290; Barbados, 0.122, and Miami, 0.097. The mean mineral aerosol concentrations were, respectively: 29.8, 20.5

and $8.08 \mu g m^{-3}$; the mean sea-salt aerosol concentrations were 22.7, 20.6 and $6.96 \mu g m^{-3}$. This lack of correlation is attributable, in part, to the fact that the dust transport occurs mainly in a meteorologically defined layer having a base at 1.5 to 2 km and at top at 5 to 7 km. Also, the concentration of particles in the optically important portion of the aerosol size distribution ($< 1 \mu$) may not be highly correlated with the concentration of larger particles which make up the bulk of the aerosol mass (Savoie and Prospero, 1976).

The fact that the turbidity at Sal seldom fell below 0.200 suggests that North Africa was a relatively constant source of optically active aerosol material during the experiment.

The Angstrom wavelength exponent, α , was low at Sal and Barbados, 0.390 and 0.265 respectively. Error analysis suggests that the difference in α values is not significant. These low alphas, and the attendant neutral extinction, suggest that the Junge size distribution parameter, β , is close to two. This is in agreement with size distribution measurements made by Savoie and Prospero (1976) who found that the normalized geometric mean particle-number size distribution for three major dust outbreaks passing over Sal had $\beta = 2.02 \pm 0.29$ in the size range 0.5 to 1.0μ diameter. In contrast, non-arid region aerosols have α values in the range 3 to 3.5 which should yield β values of 1 to 1.5. Alpha values in this range are seen in Miami during those periods when Saharan aerosols are not present; conversely, there is a tendency for low α 's to obtain when Saharan air parcels are in the area. The persistence of low α 's in Barbados and Miami in the presence of Saharan air parcels is consistent with the size distribution measurements at these locations; although the mean β 's for the size range $0.5 - 1 \mu$ were somewhat higher than that at Sal, the differences were not significant and the combined mean for all three stations was 2.18 ± 0.13 (Savoie and Prospero, 1976). Low α values appear to be a characteristic feature of air masses over, or emanating from, arid regions (Roosen *et al.*, 1973).

REFERENCES

Carlson, T.N., and J.M. Prospero, 1972. J. Applied Meteorology 11, 283-297.

Prospero, J.M., and T.N. Carlson, 1972. J. Geophys. Res. 77, 5255-5265.

Prospero, J.M., R.T. Nees and D. Savoie, 1976. Atmospheric aerosol measurements during GATE. Univ. Miami Tech. Rept. TR76-5.

Roosen, R.G., R.J. Angione and C.H. Klemcke, 1973. Bull. Amer. Meteor. Soc. 54, 307-316.

Savoie, D., and J.M. Prospero, 1976. Bull. Amer. Meteorol. Soc., 57, 145.

MEAN TURBIDITIES AT LAND STATIONS

	July			August			September			GATE		
	B_{500}	B_{880}	α Days	T_{500}	T_{880}	α Days	T_{500}	T_{880}	α Days	T_{500}	T_{880}	α Days
Sal Island	0.325	0.278	0.311 24	0.291	0.234	0.414 22	0.253	0.200	0.445 11	0.290	0.237	0.390 57
Barbados	0.137	0.123	0.250 29	0.139	0.120	0.318 30	0.091	0.087	0.226 25	0.122	0.110	0.265 84
Miami	0.118	0.077	0.880 25	0.095	0.060	0.893 27	0.079	0.045	0.986 24	0.097	0.061	0.920 76

MB1-3

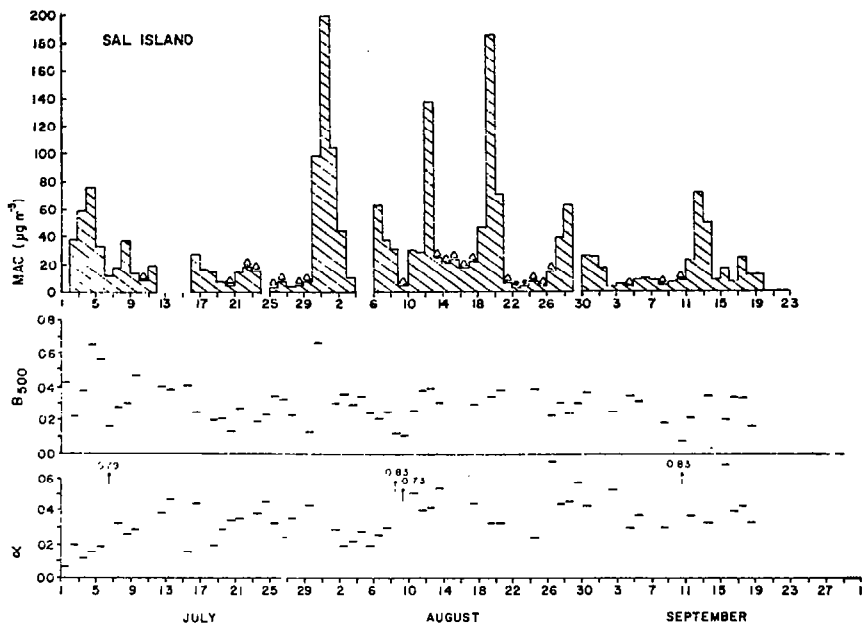


Figure 1

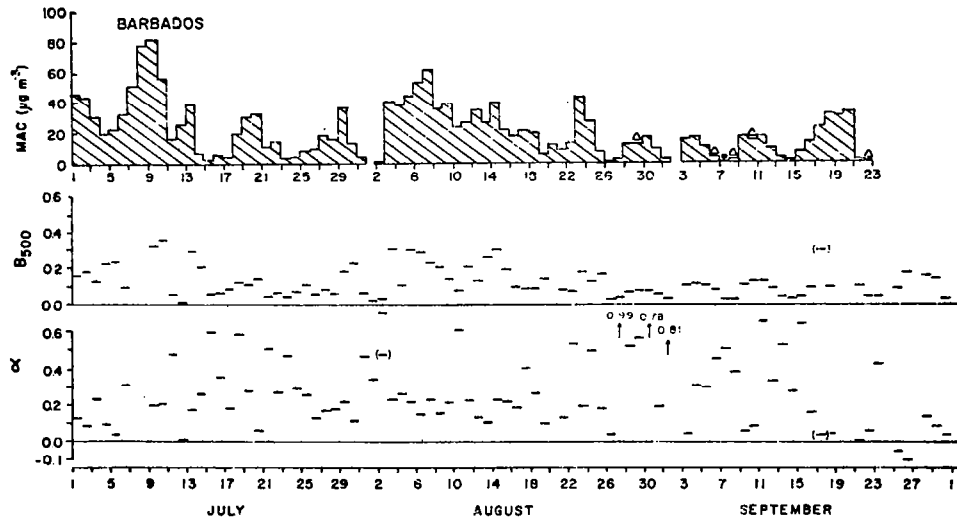


Figure 2

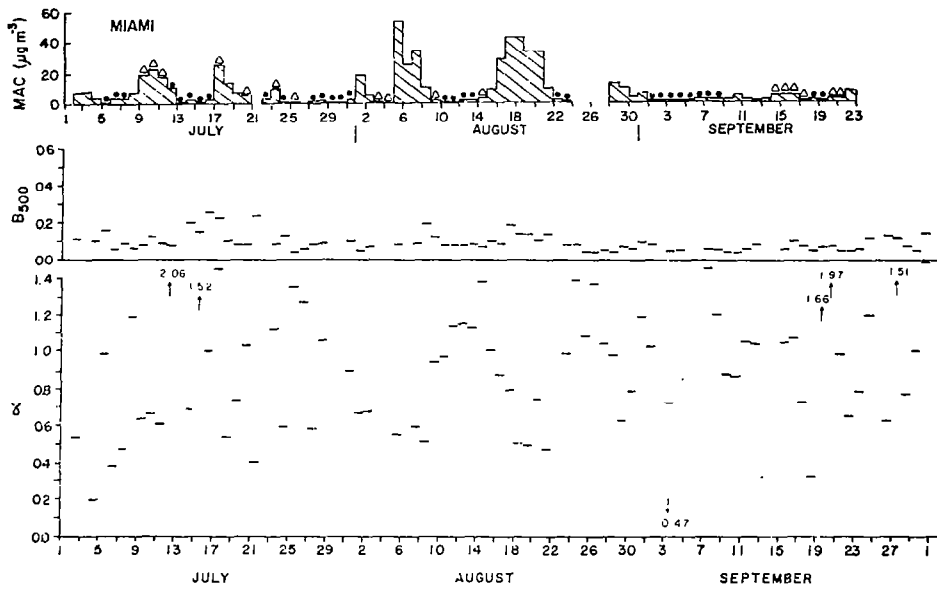


Figure 3

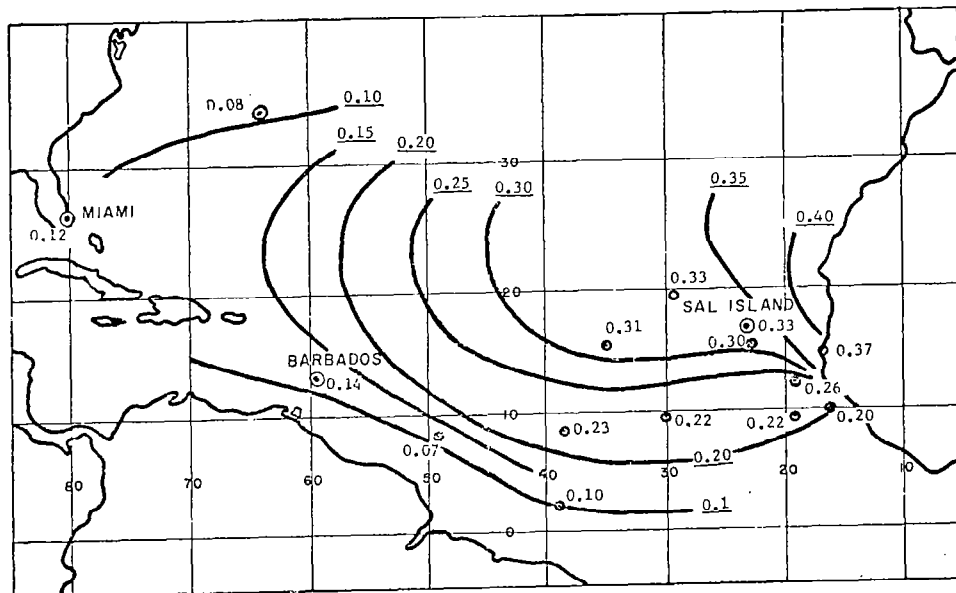


Figure 4

OCCURRENCE OF DUST OVER SELECTED GEOGRAPHICAL AREAS

Glenn B. Hoidal, Richard B. Gomez, and Bobby D. Hinds
Atmospheric Sciences Laboratory
US Army Electronics Command
White Sands Missile Range, New Mexico 88002

INTRODUCTION

Atmospheric dust contributes to air pollution and presents serious difficulties in the operation and maintenance of mechanical and electrical equipment. Moreover, atmospheric dust is a limiting factor in the increasing utilization of systems which depend on the atmospheric propagation of electromagnetic energy. To assess the potential impact of naturally occurring atmospheric dust in these areas, questions arise as to the likelihood of reduced visibilities as a function of time of the day and month of the year and as to the likelihood of that condition lasting for a specified period of time.

To answer these questions, the Atmospheric Sciences Laboratory (ASL) analyzed the hourly surface weather observations from two stations in south-central New Mexico and, through ETAC,* the 3-hourly surface weather observations from 650 worldwide stations. The results of these analyses are being published in a series of four reports.^{1,2,3,4} The purpose of this letter is to indicate the availability of these data and provide a synopsis of the content of each of the four parts.

In the series of four reports, two categories of reduced visibilities are treated, blowing dust and dust storm. Blowing dust will refer to horizontal visibilities of less than 11 km and dust storm will refer to horizontal visibilities of less than 1 km.

SYNOPSIS

The data presented in Reference 1 are based mostly on surface weather observations taken at the White Sands Weather Station (WSWS) and the Holloman Weather Station (HWS). Although the stations are only 62 km apart, observations spanning a 14-year period reveal that the HWS experiences over twice as many occurrences of blowing dust and almost six times as many dust storms as the WSWS.

Tabulated data are presented on the diurnal variation of the probability of occurrence of blowing dust by month and on the probability of occurrence of selected durations of blowing dust by month for both sites. These data are supported by tabular listings of each individual occurrence of blowing dust and dust storms for the respective periods of record. As a point of reference, it might be noted that for the HWS the probability of occurrence of blowing dust reaches its highest values of 8-9% during the late afternoon in March and April.

*The United States Air Force, Air Weather Service, Environmental Technical Applications Center.

In addition, published data on the propagation effect, refractive index, composition, number concentration, and size distribution of atmospheric dust over south-central New Mexico are summarized in an appendix by means of 30 annotated references.

Reference 2 covers 18 stations in the Middle East, 72 stations in the Near East, and 45 stations in North Africa. Each of the 135 tables provides information on the probability of occurrence of both blowing dust and dust storms as a function of time of the day and month of the year and on duration factors applicable to both categories of reduced visibilities. Illustrative of the 135 tables is that for Kuwait (Table I).

The number for a given hour, month, and dust condition represents the likelihood of occurrence of that dust condition. For example, the 40 at 0900 hours in August for blowing dust corresponds to a 40% chance of blowing dust being observed at 0900 hours in August. The percent likelihood of one of the visibility conditions lasting for a certain period of time at a specified hour and month equals the duration factor times the relevant occurrence. For example, the likelihood of the visibility being less than 11 km for at least 6 hours beginning at 0900 Local Standard Time (LST) in August at Kuwait is 20% ($0.50 \times 40\%$).

Previously published climatological data on the occurrence of dust over the three geographical areas are summarized in an appendix by means of 24 annotated references.

Reference 3 presents tabulated data for Russia on the probability of occurrence and on the duration factors, similar to Reference 2, for a total of 214 stations.

Much climatological data on the occurrence of atmospheric dust over the USSR have been published previously. Unfortunately, these articles are widely dispersed in the literature and are usually not available in English translation. Through the US Army Foreign Science and Technology Center, 12 selected articles have been translated into English. The complete translations of these articles are included in an appendix.

Comparisons between the data presented in these translations and the data presented in Reference 3 should be approached with caution, primarily because of differences in terminology. Broadly speaking the Russian "dust storm" is equivalent to the "blowing dust" of this four-part series.

Dusty conditions are most intense in Kazakhstan in a broad belt extending from the Caspian Sea north-northeast to Pavlodar. Reduced visibilities due to dust are most likely to occur in late spring and early summer.

Reference 4 encompasses the remainder of the ETAC data. Tabulated data on the probability of occurrence and on the duration factors for 45 stations with blowing dust occurring at least 3.7 days per year (1%) are presented. These tables span Angola (2 stations), Australia (1), China (1), Italy (1), Mali (13), Mauritania (11), Mexico (4), Niger (5), North Korea (1), Peru (2), South Korea (1), Spanish Sahara (2), and Venezuela (1).

TABLE I. Occurrence of dust at Kuwait, Arabia (1949-1968).

Hour (LST)	Diurnal variation by month (%)												Hours (≥)	Duration Factor
	J	F	M	A	M	J	J	A	S	O	N	D		
Dust storms (visibility <1 km)														
00				1	2	1	1			1			1	1.00
03		1			1	1		1					3	0.58
06		1			1	1			1		1		6	0.33
09	1	1	1	3	1	1	3	1	1		2		9	0.11
12	2	1	3	3	2	6	8	2	1	1	3		12	0.03
15	1	2	3	3	3	7	7	3	2		3		24	
18	1	1	4	3	3	7	6	3	2		2			
21			1	1	1	2	2							
Avg	1	1	1	2	2	3	3	1	1	*	1			
Blowing dust (visibility <11 km)														
00	8	4	18	9	12	27	26	17	7	5	4	4	1	1.00
03	7	2	16	10	14	10	17	6	2	3	3	3	3	0.74
06	8	7	20	16	26	13	23	9	13	7	3	3	6	0.50
09	13	15	31	32	43	51	47	40	14	16	8	6	9	0.31
12	17	23	41	37	45	57	49	44	21	23	10	19	12	0.22
15	20	26	37	24	33	41	34	33	15	15	7	16	24	0.03
18	17	23	41	30	41	54	50	42	27	17	7	13		
21	8	9	23	10	20	38	36	30	16	7	5	5		
Avg	13	14	29	21	30	37	35	28	15	13	6	9		

*Denotes percent occurrence greater than zero but less than 0.5.

Blank spaces denote no observed occurrence.

Among the 45 stations is Khotan, China. This station, located in the southwestern corner of the Takla Mekan Desert, exhibited the highest probability of occurrence of blowing dust of any of the 650 stations surveyed. From March through August the probability averaged 41% and showed remarkably little diurnal variation.

In addition, there were 257 stations (in 35 countries) which did not meet the occurrence criterion of at least 3.7 days per year. For these stations, a summary is given which includes the mean annual number of days with blowing dust and dust storm, but there is no breakdown as to diurnal variation and duration factors.

AVAILABILITY

Any report, or the entire series of reports, will be available by writing to this command or may be requested through the National Technical Information Service.

REFERENCES

¹B. D. Hinds, R. F. Kimberlin, III, and G. B. Hoidale, "Boundary Layer Dust Occurrence. I. Atmospheric Dust over the White Sands Missile Range, New Mexico Area," ECOM-DR-75-2, Atmospheric Sciences Laboratory, US Army Electronics Command, White Sands Missile Range, NM (AD A 010 335), April 1975.

²B. D. Hinds and G. B. Hoidale, "Boundary Layer Dust Occurrence. II. Atmospheric Dust over the Middle East, Near East, and North Africa," ECOM-DR-75-4, Atmospheric Sciences Laboratory, US Army Electronics Command, White Sands Missile Range, NM (AD A 022 637), December 1975.

³B. D. Hinds and G. B. Hoidale, "Boundary Layer Dust Occurrence. III. Atmospheric Dust over Russia," in press, Atmospheric Sciences Laboratory, US Army Electronics Command, White Sands Missile Range, NM.

⁴B. D. Hinds and G. B. Hoidale, "Boundary Layer Dust Occurrence. IV. Atmospheric Dust over Selected Geographical Areas," in press, Atmospheric Sciences Laboratory, US Army Electronics Command, White Sands Missile Range, NM.

TETHERED BALLOON-BASED MEASUREMENTS OF AEROSOL CONCENTRATION
AND METEOROLOGICAL PARAMETERS

Ronald J. Sentell, Richard W. Storey
NASA Langley Research Center, M/S 475, Hampton, VA 23665

James J. C. Chang
Systems and Applied Science Corp., Riverdale, MD 20840

Ground-level measurements of the diurnal trends in aerosol concentration have shown a consistent excursion in the early morning.¹ This excursion appears to be independent of anthropogenic sources, and suggests a fumigation type phenomena associated with the dynamic micrometeorology.² To study this potential relationship, tethered balloon-based measurements, to 400 meters altitude, were taken at Wallops Flight Center on June 29, 1976, of aerosol concentration (3 size channels), temperature, humidity, wind speed, and pressure. These measurements consisted of 12 profiles covering a 4-hour period, beginning at sunrise. These data clearly show a relationship between aerosol concentration and the dynamic meteorology.

The tethered balloon system, developed by Dr. James M. Rosen at the University of Wyoming, consists of a 42-cubic meter, helium-filled, class "C" balloon, a 16-kilogram instrument package, and a ground station. The balloon can be parked at a fixed altitude or moved up and down continuously at a maximum rate of 0.5 meters per second. The ground station consists of a wench mounted on a flat-bed trailer, a fair-lead pulley mounted at ground level about 25 meters from the wench, an antenna dish, and electronics in a laboratory located on the trailer.

The instrument package consists of a sizing aerosol counter, thermistors for temperature and humidity measurements, a cup anemometer for horizontal wind speed, and a pressure transducer. The aerosol counter is a forward-scattering type with maximum collection efficiency at 25⁰ and utilizes two photomultipliers with coincidence circuits to minimize noise.³ Discriminators are calibrated to size aerosols in the ranges \geq 0.3-micrometer diameter, $>$ 0.5-micrometer diameter, and $>$ 3.0-micrometer diameter, referenced to polystyrene spheres.^{3,4} Three thermistors are mounted in a 6.1-centimeter diameter cylinder with sun shields and are aspirated at 9 centimeters per second. One thermistor has a time constant of 1 second, and two thermistors (wet bulb-dry bulb) have a time constant of 10 seconds. A wick covers one thermistor and is attached to a water reservoir. The wet bulb-dry bulb thermistors were calibrated to obtain a psychometric constant for the particular geometry and aspiration used, and the measurements should be accurate to ± 2 percent.⁵ All thermistors were calibrated to $\pm 0.01^{\circ}$ C, and equations were fitted to the calibration data with residuals at least this good. The cup anemometer is a 3-cup type using a dc generator, and has a starting threshold of 0.36 meters per second, a distance constant of 2.26 meters, and an accuracy of ± 1 percent. The pressure sensor consists

of a membrane mounted in an open-ended capsule with strain gages attached. With temperature compensation, the sensor is accurate to ± 0.1 millibar, giving an altitude resolution of approximately ± 1 meter.

The output from each sensor is converted to a frequency and placed on a carrier to modulate a 1680 megahertz transmitter. All data are telemetered continuously and in parallel to a ground receiver. Data are recorded on FM tape, and voltage levels are plotted in real time on X-Y plotters (altitude versus variable). Real-time plotting is necessary to insure that the sensors are functioning properly, and to locate inversion layers which may be of interest for further study. After each project, the FM tapes are transcribed to digital tapes for computer processing. A special interface circuit has been designed and built for the transcription to insure no loss in accuracy in data transcription. Frequency-to-digital conversion is accurate to 1 part in 20,000. Computer software has been developed for data analysis, listing, and plotting.

Results of the experiment are shown in figures 1, 2, 3, and 4. In all the data presented, 1-second averages are taken. Even though this averaging period may be inappropriate for obtaining a mean profile, especially for wind speed, both the mean and variance of each profile can be approximated by inspection of the data. To summarize a large volume of data, three profiles out of the twelve measured are presented where the largest changes occurred in aerosol concentration. For the 4-hour measurement period, the aerosol profiles are nearly constant with altitude to about 400 meters, with the exception of a smaller concentration near the ground early in the morning. The changes in concentration are shown in figure 1. In going from 5:44 a.m. to 6:49 a.m., an increase occurs in aerosol concentration with a larger increase in the smaller aerosols. Also, the concentration near the ground increases to a greater extent until a nearly constant profile is observed. Aerosols in the size range 3.0-micrometer diameter are not shown due to their low abundance and an inadequate averaging time. At 8:38 a.m., a decrease occurred in the concentration. Temperature profiles are shown in figure 2. The progression goes from a positive lapse rate to 100 meters and isothermal upward at 5:44 a.m. to strictly isothermal at 6:49 a.m. to nearly adiabatic at 8:38 a.m. Also, a buildup of a turbulent-like structure from the ground is noted. This same type of turbulent-like buildup is seen in wind speed, figure 3. The mean wind speed progresses from nearly logarithmic to nearly constant with altitude. Changes in relative humidity are shown in figure 4. After sunrise, the humidity decreases near the ground.

Aerosol dynamics in the lower troposphere are observed on a small time scale to be closely related to the meteorological dynamics. As the temperature profile progresses from very stable to stable to adiabatic, as the mean wind speed goes from nearly logarithmic to nearly constant with altitude, and as the humidity near the ground decreases after sunrise, the aerosol concentration increases and then decreases. In the early morning, the aerosol

concentration within the lowest 100 meters follows the changing temperature structure in this same layer. When a completely isothermal profile is reached, the entire vertical distribution of aerosol increases. Due to a lack of data on the boundary layer, a question still exists on whether aerosols are transported up or down. Measurements are planned which will cover a longer time period and a higher altitude.

REFERENCES

1. Storey, R. W.; Sentell, R. J.; Woods, D. C.; Smith, J. R.; and Harris, F. S., Jr.: Atmospheric Particulate Measurements in Norfolk, Virginia. NASA TM X-3285, 1975.
2. Williamson, S. J.: Fundamentals of Air Pollution. Addison-Wesley Publishing Co., 1973.
3. Pinnick, R. G.; Rosen, J. M.; Hofmann, D. J.: Measured Light-Scattering Properties of Individual Aerosol Particles Compared to Mie Scattering Theory. Applied Optics, Vol. 12, No. 1, Jan. 1973, pp. 37-41.
4. Pinnick, R. G.; Hofmann, D. J.: Efficiency of Light-Scattering Aerosol Particle Counters. Applied Optics, Vol. 12, No. 11, Nov. 1973, pp. 2593-2597.
5. Bindon, H. H.: A Critical Review of Tables and Charts Used in Psychrometry, Vol. 1 of Humidity and Moisture, Robert E. Ruskin, ed., Reinhold Publishing Corp., 1965, pp. 3-15.

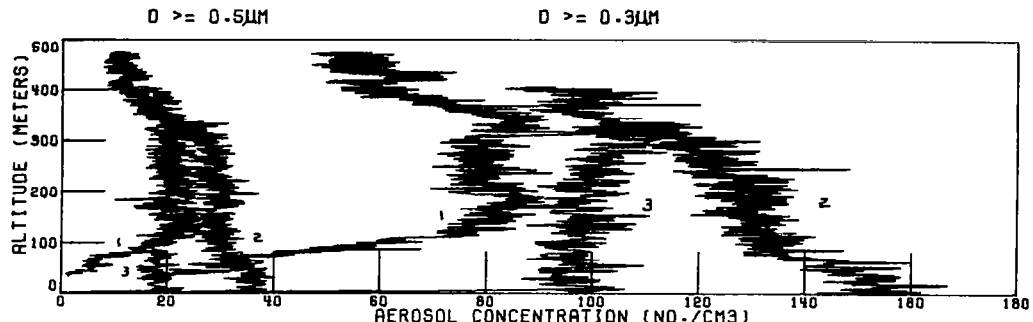


FIGURE 1. AEROSOL PROFILES FOR (1) 05:44AM-06:00AM.
(2) 06:49AM-07:02AM. (3) 08:38AM-08:54AM. DATE: 6/29/76.

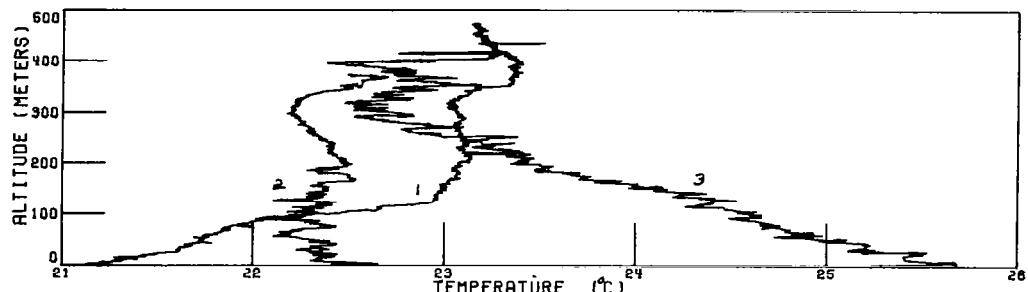


FIGURE 2. TEMPERATURE PROFILES FOR (1) 05:44AM-06:00AM.
(2) 06:49AM-07:02AM. (3) 08:38AM-08:54AM. DATE: 6/29/76.

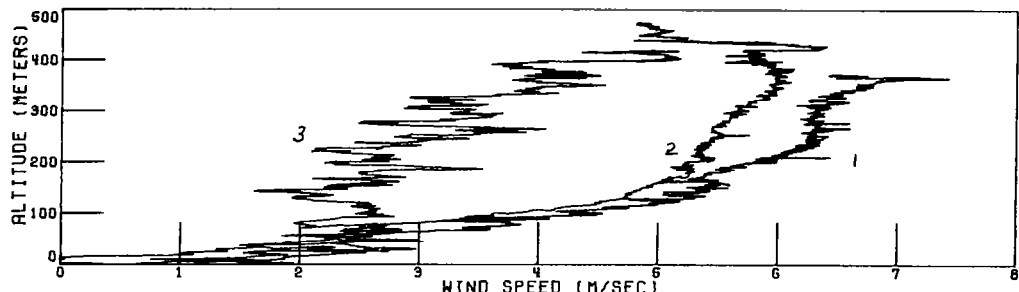


FIGURE 3. WIND SPEED PROFILES FOR (1) 05:44AM-06:00AM.
(2) 06:49AM-07:02AM. (3) 08:38AM-08:54AM. DATE: 6/29/76.

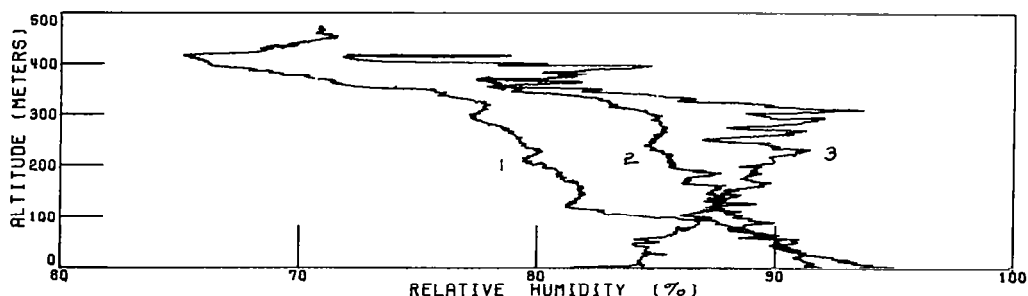


FIGURE 4. HUMIDITY PROFILES FOR (1) 05:44AM-06:00AM.
(2) 06:49AM-07:02AM. (3) 08:38AM-08:54AM. DATE: 6/29/76.

CONTINUOUS MEASUREMENTS OF THE NATURAL AEROSOL SIZE DISTRIBUTION
AT RURAL, MOUNTAIN, AND MARITIME SITES

BY: S.G. JENNINGS, Department of Physics, University of Durham, Durham, U.K.

Although particle size distribution measurements have been made now for some years, few continuous measurements extending over periods of days or longer have been published. In the following summary, measurements are presented of the natural aerosol size distribution in the radius range 0.25 up to 5.0 micrometres using a calibrated Royco model 225 optical particle counter. Continuous measurements¹ were made at Durham Observatory 2 km SSW of Durham City with a population of 27,100 inhabitants in the North East of England over a 49 day period from July 21st to September 8th 1975. Results are also presented of particle size distribution measurements taken at a remote mountain field station at Great Dun Fell, 832 msl on the Northern Pennine Range, Westmorland and at Ardnamurchan Lighthouse situated at the most westerly point of the British Isles. Calculations are presented of the effect of relative humidity on the extinction coefficient due to measured and model sea salt particle distributions and that of model aerosol particle distributions of ammonium sulphate, recognized to be an important constituent of continental atmospheric aerosols.

It was found that the diurnal variation of the natural aerosol particle size distribution in the size range from 0.25 up to 1.5 micrometres in radius is distinctive in that it assumes a shape which is approximately an inverse relation to that normally measured for the submicrometre Aitken particle distribution². The maximum number concentration occurs for all size categories with the exception of the largest sized category at the approximate period from 0200 to 0800, local time, whilst the afternoon period is characterized by a distinct minimum. This trend is also reflected in the measurements made at the remote site of Great Dun Fell. This inverse relation largely concurs with measurements obtained by Marple et al.³ on aerosol sampled at Harbor Freeway, Los Angeles as shown in figure 1.

The use of probability paper, on which the cumulative frequency distribution of particle size over all size categories measured at the 3 sites, is plotted indicates clearly that the particle number concentrations follow closely a log-normal distribution in each case. The results of the cumulative distribution for five selected particle size ranges is shown in figure 2 for the atmospheric aerosol sampled at Durham Observatory.

The particle size distribution for the Durham, Great Dun Fell and Ardnamurchan sites follows the shape of a Junge log-radius type distribution reasonably closely with slopes β equal to 3.04, 2.74 and 1.72 respectively. The distributions show that the number concentration over the radius intervals is an order of magnitude lower at the mountain site of Great Dun Fell than at Durham Observatory. The relatively lower slope for the maritime aerosol averaged over 7 days continuous measurements agrees quite closely with the size distribution of chloride particles measured by Metnieks⁴ off the West Coast of Ireland.

A rare opportunity of obtaining the background level of aerosol particle production at a period of minimum anthropogenic activity was achieved by monitoring the particle concentration over a 21 day continuous sequence which included the Christmas period. The particle size distribution was continuously measured at the remote mountain station at Great Dun Fell from December 15th 1975 to January 6th 1976. The period from 0000 hours on December 25th until 0000 hours on December 27th was considered to represent accurately the period of least activity during the year, when particle production from man-made sources such as vehicular traffic and industrial pollutants is at a minimum level. This predicted pattern is confirmed by the result in figure 3 where the average value of particle size concentration for the days December 25th and 26th is compared with the overall average for the 21 day period.

A correlation analysis was carried out on the July-September measurements at Durham observatory. A relatively high negative correlation coefficient was obtained between the wind speed and the particle concentration. As shown in Table 1. A scatter diagram of wind speed in knots, (X), versus the particle concentration for the size category 0.25-0.35 micrometres yielded a line of regression of

$$Y = -0.0588 X + 0.8953$$

where $Y: \log_{10}(\text{particle concentration})$. The decrease in particle concentration with increase in wind speed occurred for all size categories examined and may be attributed to an increase in humidity as also reflected by the positive correlation between the parameters shown in Table 1.

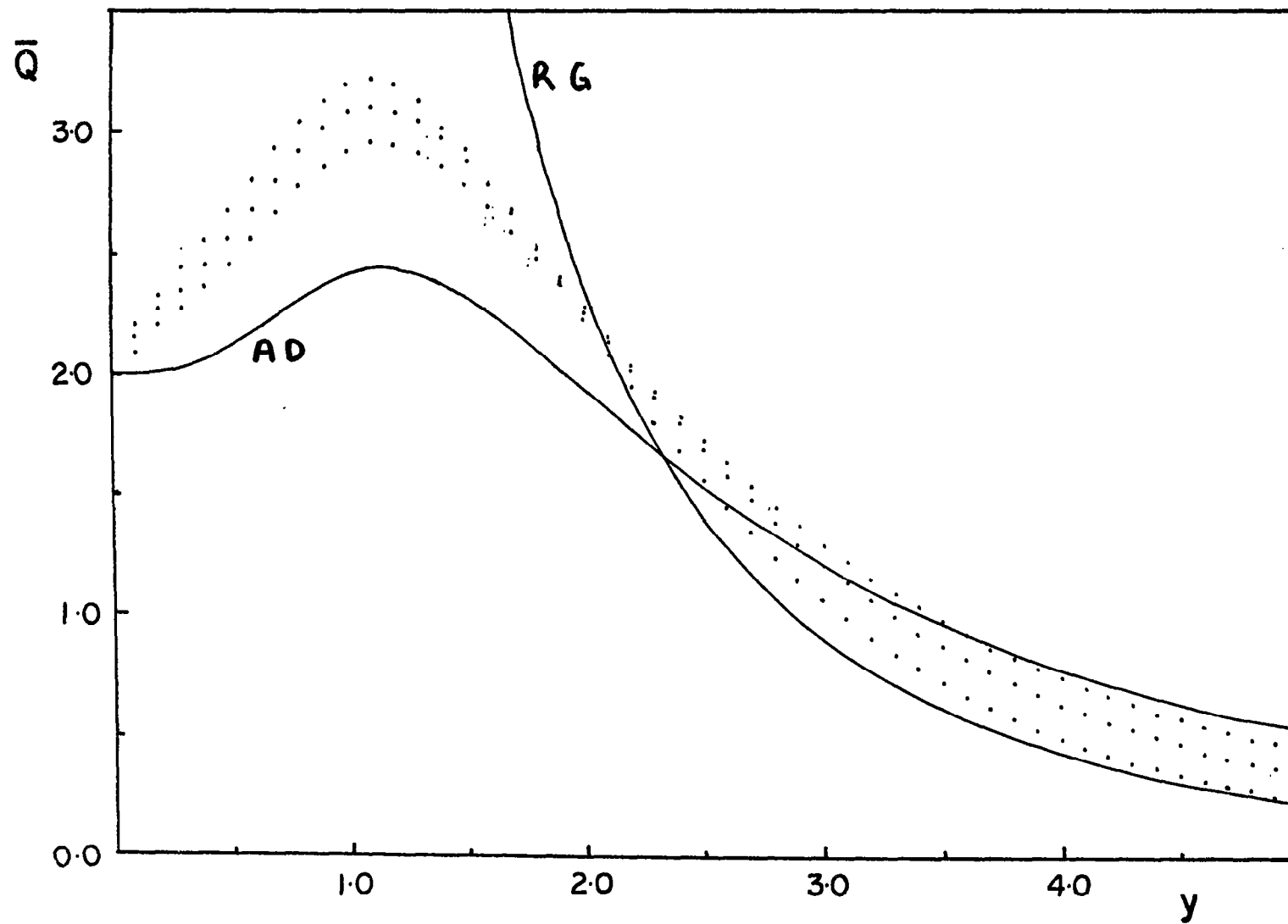
The effect of relative humidity in the extinction coefficient of a mono-disperse aerosol size distribution of sodium chloride and ammonium sulphate particles over a range of dry particle mass from 3×10^{-17} gm to 3×10^{-4} gm was examined. Approximations for the scattering area ratio were based on the equations derived by Deirmendjian⁵ and Penndorf⁶. The variation of refractive index with humidity was considered by means of linear approximation equations which gave good agreement with tabulated results. Selected values of extinction coefficient for three values of relative humidity of 80, 95 and 99 per cent over a wide range of particle dry mass is shown in Table 2(a). It can be seen from Table 2(b) that aerosol particles of sodium chloride are more efficient than ammonium sulphate particles in reducing visibility.

Computations of the extinction coefficient due to selected particle size distribution for sodium chloride are shown in figure 4. It can be seen that a Junge distribution possessing a slope β of -3 causes the largest extinction for values of humidity greater than about 94 per cent. The sea spray aerosol has approximately the same effect upon visibility as a Junge distribution of sodium chloride in the radius range 0.1 to 1.0 micrometres up to a value of humidity of about 90 per cent and the Junge distribution exceeds that due to the sea spray distribution by an average value of 35 per cent over the relative humidity range between 90 and 99 per cent. The computations for sodium chloride suggest that the extinction coefficient increases with the steepness of the slope of the logarithmic radius particle size distribution.

This work was supported by means of a research contract with the U.S. Government, through the European Research Office.

References

1. Jennings S.G. and Elleson, R.E., 1976. "Nature Aerosol Size Distributions in the 0.25-5.0 Micrometre Radius Range". Submitted to Atmospheric Environment.
2. Jennings, S.G., 1975. "Measurements of the Number Concentration of Aitken Nuclei at Mountain and Rural Sites". Jnl. de Rech. Atmos., 11, pp. 59-66.
3. Marple, V.A., Sverdrup, G.M., and Whitby, K.T. (1976). Private Communication.
4. Metnieks, A.L. 1958. "The Size Spectrum of Large and Giant Sea-Salt Nuclei Under Maritime Conditions". Geophysical Bulletin No. 15, Dublin Institute for Advanced Studies.
5. Deimendjian, D. (1969). "Electromagnetic Scattering on Spherical Poly-dispersions". Elsevier, New York-London-Amsterdam.
6. Penndorf, R.B. (1962). "Scattering and Extinction Coefficients for Small Absorbing and Non-Absorbing Aerosols". J. Opt. Soc. Am. 52. pp. 896-904.



MB4-4

MB-5 Spatial Concentrations of Particulates from Rocket Exhaust Ground Clouds

K. H. Crumbly; R. J. Sentell; R. W. Storey, Jr.; D. C. Woods; NASA Langley Research Center, Hampton, Virginia 23665

The Langley Research Center has been involved for the past three years in a program to measure spatial concentrations of particulates left behind as effluents during the launch of large solid rocket motor boosters.

This paper summarizes results of particulate measurements from launches conducted at NASA's Kennedy Space Center. The particulates originate from ground stabilized clouds which are composed of launch effluents, debris, dirt, and tower coolant water. These clouds are heated from the burning process and thus become buoyant moving upward rapidly after a launch until they reach a stabilization height determined by prevailing meteorologic conditions. The stabilized height is usually achieved by the cloud within five minutes after the booster firing, at which point it is carried along by the prevailing wind at the stabilized altitude. Stabilization heights for clouds measured during this program have ranged from 1.1 km to 2.0 kilometers, the lower altitudes being more predominant in the winter and fall and the higher altitudes during the spring and summer. As the cloud moves, it diffuses and is dissipated in the troposphere.

The measurements reported here result from a downward diffusion of debris and effluent from the cloud as it moves over the instrument measuring station.

The instrument used to measure the suspended particulate was a 47 mm diameter membrane filter oriented for a horizontal flow of about 28 liters per minute held in a plastic holder. Most of the instruments were run for a period of 20 to 25 minutes. The unused filters are opened in a class 100 clean room where they are indexed and weighed following which they are individually placed in petri dishes for transport to the Kennedy Space Center. There the filters are loaded in a holder and covered by a plastic bag until launch time. Some 15 to 30 filter instruments are deployed for each launch in a network downrange from the launch pad and in the direction of the prevailing winds. After exposure, the filter membranes were removed from the holder and placed in petri dishes for transport back to the Langley Research Center where they are reweighed after being stabilized to the pre-weighing humidity and temperature conditions.

Five launches are discussed in this paper with the corresponding movement of the stabilized ground cloud plotted along with the mass loadings as determined by the filter weighing.

Table 1 of this summary lists by launch date the distance of each measurement station from the launch pad in kilometers, the azimuth in degrees from north and the mass loading in micrograms per cubic meter. The measurements vary from launch to launch and no consistent pattern is seen from the Table. The effluent seems to be randomly dispersed indicating that small turbulent eddies are dispersing the cloud as it travels over the different measuring stations.

TABLE 1--SPATIAL CONCENTRATIONS OF EFFLUENTS FROM ROCKET EXHAUSTS

February 1974			May 1974			May 1975			August 1975			September 1975		
Km	°N	μgm/M ³	Km	°N	μgm/M ³	Km	°N	μgm/M ³	Km	°N	μgm/M ³	Km	°N	μgm/M ³
0.5	57	146	0.6	64	-	2.7	175	81	1.2	86	50	3	248	148
0.5	73	138	0.6	77	24	3.0	160	35	1.2	86	76	3.1	243	95
0.6	30	444	0.6	88	125	5.0	165	92	2.2	335	-	3.2	238	21
0.6	41	76	0.7	106	9	5.5	170	43	2.6	333	-	3.2	315	-
0.6	92	432	0.7	117	149	5.9	166	72	2.9	332	-	3.3	306	-
0.6	102	178	0.7	52	107	6.0	175	29	3.1	91	50	3.4	235	139
0.7	113	150	0.9	125	248	6.8	179	58	3.1	91	36	3.5	301	91
0.8	122	64	0.9	39	-	6.8	170	65	3.2	331	-	3.8	261	262
0.9	8	174	0.9	33	48	6.9	165	172	3.4	306	179	3.8	295	13
0.9	127	534	1.0	133	709	7.1	175	57	3.5	303	94	7.3	264	122
1.0	131	414	1.0	26	220	7.6	165	91	3.6	301	180	7.3	262	99
1.1	134	375	1.1	138	197	8.0	164	125	3.6	330	-	7.5	257	7
			1.1	21	-	8.2	170	109	3.7	299	50	7.5	254	54
			1.2	17	-	8.3	184	66	3.8	296	50	7.6	252	72
			1.2	142	-	8.7	164	92	3.8	297	58	8.9	295	196
			1.4	12	28	9.0	174	51	4.0	329	48	9.1	297	-
			1.4	145	1215	9.1	180	48	4.1	291	144	9.4	300	134
			1.5	10	116	9.4	170	43	4.2	290	353	9.6	302	113
			1.5	148	384	9.7	163	38	4.3	289	345	9.8	304	450
			1.8	5	66	10.4	184	20	4.5	287	40	9.9	310	349
			2.1	2	163	10.5	180	61	4.6	301	-	10.1	307	101
						11.3	175	55	4.6	285	-	10.2	308	60
						12.5	169	70	7.8	306	37	10.5	307	44
						12.5	177	55	5.1	308	7	11.0	305	73
						12.6	183	56	5.4	313	-	11.3	304	160
						12.7	158	78	5.7	316	-	11.7	303	434
						13.0	174	66	6.0	339	254	12.0	302	228
						13.0	163	105	6.0	339	13	12.4	301	238
						13.9	180	-	6.3	28	308	12.8	300	41
						13.9	183	71	6.3	28	162	13.2	298	56

ALTITUDE PROFILES OF ATMOSPHERIC AEROSOLS OBTAINED
WITH THE EPSILON/AFGL BALLOON-BORNE SIZING SPECTROMETER

Henry A. Miranda, Jr.

Frank K. Dearborn

Epsilon Laboratories, Inc. 4 Preston Court, Bedford, MA 01730

This paper presents the results of a rather sophisticated in-situ stratospheric balloon-borne sizing spectrometer which has been under more or less continued development by Epsilon Laboratories during the past several years with the support of Dr. Robert Fenn and associates at Air Force Geophysics Laboratories. To date four successful flights have been conducted at Holloman AFB, New Mexico: Three in May of 1973 and the fourth in January of 1975, a few months after the Fuego volcanic eruption of mid-October of 1974, with an improved system. To our knowledge, these data represent the first successful balloon-borne operation of such a device capable of accurately sizing particles down to the 1/4 micron diameter regime.

The size distributions obtained were of a somewhat unusual and unexpected character, as will be seen. Because of this and also because the size distribution of particulates in the atmosphere has important implications bearing upon the interpretation of ground-based Lidar and other types of nephelometric measurements, as well as upon stratospheric nucleation/sublimation phenomena, the validity of the data has been a subject of intense scrutiny on our part.

The device is a two channel forward scattering instrument in which particles are gently sampled and caused to transit an internal sensing gap under laminar flow conditions. The gap is illuminated by a HeNe laser beam properly shaped to provide uniform illumination ($\pm 10\%$, approximately) across the flow field, which is cylindrically symmetrical about the sampling flow tube axis. The light scattered by the particles as they are illuminated is collected by two separate annular apertures centered at 10° and 30° respectively, and an appropriate pair of field stops image a 1mm diameter interaction zone within the sensing gap.

Meticulous care is taken to ensure that the resulting pulse heights are accurately measured. Special signal processing hardware has been employed for this purpose including threshold circuits which track the respective DC background levels in each channel and a pair of peak detection circuits which are both gated on whenever the signal exceeds the threshold level in either channel. This latter circuit inspects the signals in both channels for a period of 60 μ seconds following the instant that the threshold in either channel is crossed, and provides outputs proportional to the peak values of both channels to the digitizing circuitry.

The pulse height signals are digitized and recorded on magnetic tape in a format compatible with an IBM 370/158 computer so that the tape can be fed directly to the latter for processing. The on-board processing system accepts signals over a four-decade range extending from 10^{-8} ampere to 10^{-4} ampere. Based upon an absolute calibration utilizing Rayleigh scattering from the interaction zone volume ($\sim 1\text{mm}^3$), it has been ascertained that the minimum detectable pulse height corresponds to about 100 photocathode electrons. Hence particle size detection limits are set by noise in background levels, and not by counting statistics per se.

The software embodies a variety of diagnostic and auxiliary data reduction routines and printouts. The main data reduction program accepts the laser power measurement, the flowrate measurement, the background level and the raw digitized pulse heights for both channels as its main inputs. A separate software threshold value is set automatically for both channels on every record.

(i.e., once every 20 seconds), based upon the respective background distributions determined separately for each record by means of a special background level sampling circuit and logic function. After rejecting any pulses which do not appear simultaneously in both channels (i.e., do not exceed both software threshold levels), a histogram of aerosol sizes is generated for any desired set of records. The histogram is divided into 91 adjacent bins of 0.01μ diameter width.

Because of the above measures, the sizing precision (i.e., resolution) is within $\pm 0.01 \mu$. This has important implications on the determination of size distribution slopes, as will be seen. The accompanying figure depicts the output of a set of calibration runs with Dow Corning polystyrene latex spheres of several different sizes treated as though they were unknown particles by the software. The diameters of each set are shown above the arrows at the top of the figure. The second peak accompanying the 0.234μ particles is believed to be associated with the presence of the nebulizing fluid, which appears to assume increasing dominance for smaller particles (note the small hump in the tail of the 0.357μ distribution).

The sizing accuracy of this instrument is of course less than its precision, being limited by the uncertainty in index of refraction. We have ascertained that, over the region between 1.33 and 1.6, the uncertainty is $\pm 10\%$.

The flight data (consisting of several sets of altitude profiles of aerosol concentration for selected sizes, from 0.25μ up, in $1/2$ micron increments) are too numerous for such a brief presentation as this, its presentation here would take up space better devoted to summarizing the salient features of the results:

- The departure from constant mixing ratio, except for a restricted range of particle size and altitude, appears to be the rule rather than the exception. In general smaller sized particles tend to fall off less strongly, and larger particles more strongly, than the atmospheric density.
- A shoulder which tends to be size-dependent, is clearly in evidence. In general this shoulder resides at higher altitudes for smaller particles, a feature which is in qualitative agreement with what might be expected.
- A general similarity in sub-structure is perceived in all sets.

Offsetting these general overview features are distinct differences:

- the suggestion of an extensive high altitude peak of smaller particles (i.e., less than 0.35μ diam), on one of the 1973 flights
- a sharp peak at about 20 Km observed on the downleg portion of another of the 1973 flights, especially for particles less than 0.4μ

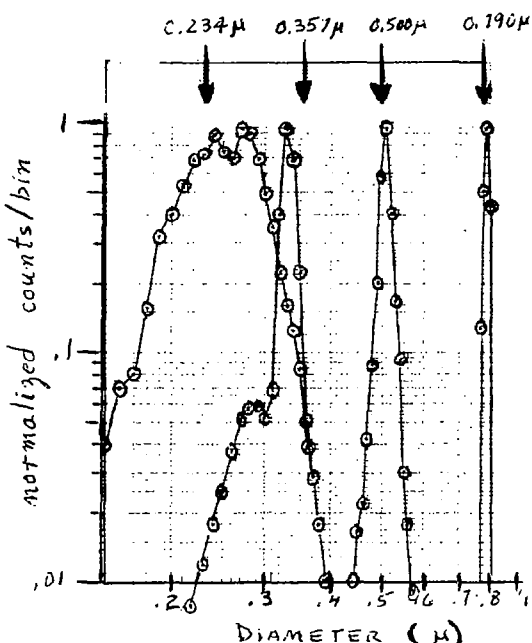


Fig. 1 Measured size distributions of several monodisperse polystyrene latex calibration particles treated as unknowns, plotted on Log/Log format.

- the double peak (at 19 Km and at 14 Km) characterizing the volcanic incursion
- the differences in the absolute concentration in the shoulder between two flights for which the shoulder is clearly in evidence

That these differences are not easily ascribable to balloon wake effects was shown by a set of size distributions collected during a vertical "jog" effected during the last flight in order to investigate this question.

A general feature of considerable significance is the exceedingly steep slopes found throughout. With some notable exceptions beyond the scope of this summary discussion, most of the distributions can be characterized by an inverse power log size distribution D^{-a} , with a -values ranging from 6 to more than 16. This is illustrated in the selected distributions shown here, which were taken from the 1975 flight data.

The steepness of the observed size distributions has significant implications with regard to correlation with Lidar signal returns. For a Lidar operating at 6943 Å, and for particles having a typical index of refraction of 1.5 - 0.01i, the convolution with a D^{-6} distribution reveals that roughly 2/3 of the signal return arises from particles less than 0.35 μ diameter. Since many of the observed size distributions are even steeper than D^{-6} , it would seem that the measurement of small particles is of vital concern for correlation with Lidar measurements.

Of even greater concern for any and all applications is the necessity to ensure that the cut-off characteristics of any instrument utilized to measure particle concentrations be sharp, particularly on the small-size end of its throughput passband, in order to prevent serious contamination of the measurement at any given size by erroneous information from smaller sizes. Because of this, it is very likely that aerosol size distributions measured in the past with instrumentation having relatively "soft" cut-off characteristics may have been subject to this deficiency.

As is the case with any convolution, when the cut-off slope is not substantially steeper than the slope of the size distribution against which it is pitted, the resulting "measured" slope will be much less steep than the actual slope under investigation. For example, when dealing with a D^{-6} slope, the cut-off characteristics should be at least D^{-9} or greater in order to ensure proper fidelity. On the other hand, if the cut-off characteristic is less steep than the slope of the size distribution, then the convolution function diverges and the integral value is determined by the concentration of the smallest particles present. Under these conditions the "measured" value for the assigned sizing bin will clearly be much higher than the actual concentration for that bin.

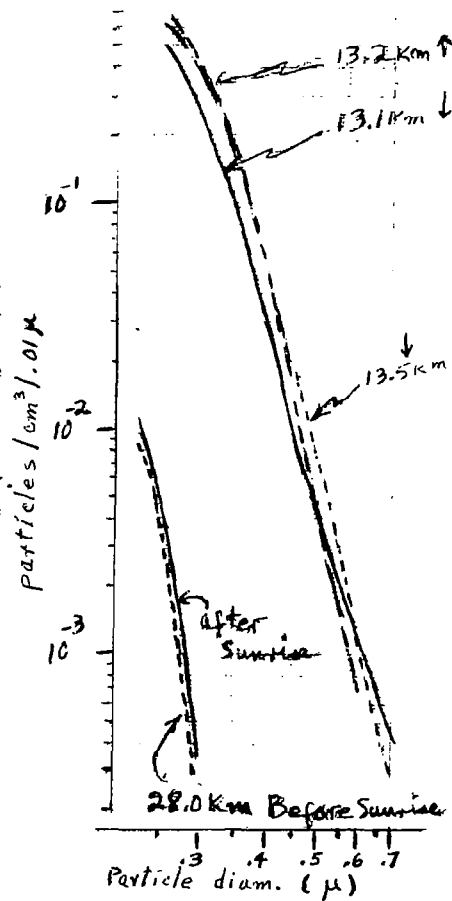


Fig. 2 Selected size distributions showing the steepness of the slopes.

The system response to a monodisperse set of particles bears a one-to-one relationship with the analogous passband of a filter, and can be viewed in exactly the same light. Recalling the calibration data shown in Fig. 1 it is seen that our instrument displays an exceedingly high resolution in relation to other instrumentation of which we are aware, and is thereby particularly well suited to dealing with steep slopes. Specifically, the cut-off characteristics represented by these calibration data have been ascertained to be as steep as D^{+20} or better, down to about 0.3μ diameter at least. This is more than sufficient to ensure that particle size distributions having slopes as high as D^{-16} or so, are accurately represented as such.

Slopes approaching this steepness have been encountered in the data collected and presented here, as noted previously. We have been unable to discover serious deficiencies in our instrumentation despite an intensive effort in this regard. In view of these facts it would perhaps be useful to perform a critical examination of the instrumentation used to collect the extant data in terms of this specific parameter. The simplest diagnostic that can be used for this purpose is a plot of the size distribution obtained with monodisperse calibration particles treated as unknowns.

Finally, two sunrise dwell experiments (one at 20 Km in 1973 which had been reported elsewhere previously, (Ref 1), and the second at 27 Km in 1975) were conducted to examine an aerosol nucleation hypothesis advance by Friend, et. al. (Ref 2), whereby a complex series of chemical reactions involving photooxidation of SO_2 plays a key role. The results of both these experiments (one of which, namely the 1975 experiment, is shown in Figure 2 on the previous page), indicate that no discernable difference is evident before and after sunrise. These results may be useful in establishing an upper limit for the phenomenon once other elements of the complex theory will have been better established.

References:

- 1 Miranda, H. A., Jr., and Fenn, R., "Stratospheric Aerosol Sizes", *Geophys. Res. Lett.*, 1, 201, (1975)
- 2 Friend, J. P., Leifer, R., and Tichon, M., "On the Formation of Stratospheric Aerosols", *J. Atmos. Sciences*, 30, 465, (1973)

Aerosol Tropospheric-Stratospheric Exchange

McCormick, M. P., Langley Research Center, NASA, Hampton, Va. 23665
 Swissler, T. J., Systems and Applied Sciences, Riverdale, Md. 20840
 Chu, W. P., Old Dominion University, Norfolk, Va. 23508

Stratospheric aerosol data over a two-year period have been taken with the NASA-LRC 48-inch Ruby Lidar System. This paper will summarize these measurements by examining the time variation of the stratospheric aerosol layer as observed over Hampton, Virginia. The data are presented in terms of the time history of the peak aerosol backscattering ratio (Figure 1) and the integrated aerosol backscattering for various layers of the stratosphere (Figure 2). The peak aerosol backscattering ratio is defined as: $\text{Max } (R(Z)-1.0)$, where $R(Z)$ is the lidar backscattering ratio defined as the ratio of the total backscattering (aerosols + molecules) to molecular backscattering. This ratio is experimentally determined from the measured lidar signal profile and from local rawinsonde measurements at Wallops Island, Virginia (120 km N. E. of the lidar system). The integrated aerosol backscattering is defined as

$$\int_{h_1}^{h_2} (R(Z)-1.0) * f_m(z) dz$$

where h_1 and h_2 are given heights in the stratosphere and, $f_m(z)$ is the molecular backscattering function derived from the rawinsonde data. This integral has been normalized to the value obtained from the lidar data of October 10, 1974 and is subsequently defined as the normalized column density.

Both the peak aerosol backscattering and the normalized column density demonstrate the initial rapid increase in the dust layer after the eruption of the volcano de Fuego in October 1974. Subsequently, both show decay in the winter-spring months of 1974-1975, and by the summer of 1975 the aerosol layer has decreased considerably from the maximum values observed in early January.

Possible processes for the removal of particles from the stratosphere are: (i) Seasonal variations in the height of the mean tropopause level; (ii) Mean meridional circulation and transport; (iii) Large scale eddy diffusion and transport; and (iv) Particle sedimentation. Mechanism (i) has been discussed previously by Hofmann et al. (1975) while (ii) and (iii) have been examined by Reiter (1975). Models for the residence times of stratospheric aerosols due to sedimentation have been discussed by Hunten (1975).

Throughout the summer and fall of 1975 relatively little change occurred in the aerosol layer, indicating stability and lack of significant decay. For this time period processes (i) through (iii) are not thought to be significant. In the following winter and spring months, the lidar data again showed considerable variation in aerosol content and by March 1976 the normalized column density values have returned to their early October 1974 values.

The effect of seasonal variation in the integrated aerosol back-scattering can be examined by dividing the stratosphere into three layers: (1) A layer from the tropopause up to 15 km - a region where periodic variations have been observed in the winter-spring aerosol profiles; (2) the layer between 15 and 22 km where the maximum aerosol concentration is observed; and (3) the stratospheric layer from the tropopause to 28 km.

The aerosol content of the 15 - 22 km layer appears to be the dominant factor in the total integrated backscattering curve up to 1976. The behavior of this layer demonstrates the build-up of the aerosols immediately after the volcano, the initial weekly fluctuations that were observed, and the subsequent decay to values representative of pre-Fuejo conditions. After the initial injection, the sharp variations that appear in the total integrated amount are coincident with the large increases of the aerosols in the lower layer (tropopause to 15 km). These variations are coincident with the lowering of the tropopause whether due to seasonal adjustments or due to large scale turbulent mixing processes. By the summer and fall of 1976, the 15 - 22 km layer has decayed to values of the normalized column density that are no longer the dominant contributor to the total integrated amount. The added effect of aerosols from the lower stratospheric layer are now comparable.

Decay rates have been calculated for the peak aerosol back-scattering and the normalized column density curves. These rates are variable depending on the season and the elapsed time from the last major volcanic eruption. Generally, the summer to fall period is stable, while rapid decay of the stratospheric aerosol occurs over the late winter to early spring period. In North America, the mixing of air masses of different origin is at its peak during this time period. This activity has been estimated by Reiter (1975) to be responsible for 20% of the total stratospheric air mass exchanged with the troposphere in one year. Variations in the height of the mean troposphere between winter and spring seasons have also been estimated by Reiter (1975) to be responsible for roughly 10-15% of the total variation of the stratospheric air masses. The lidar data for the stratosphere over Hampton, Virginia shows that during the late winter and early spring a significant cleansing of the stratospheric dust occurs. For both winter to summer periods of 1975 and 1976, we observed an approximate 40% decrease in the integrated aerosol backscattering, which is in good agreement with the postulated cleansing mechanisms. The decrease of the total stratospheric

aerosol column density over a one-year period from January 1975 to January 1976 is approximately 65%. This is also in relative agreement with Reiter's estimate (1975) of 73% annual outflow of stratospheric air mass over the northern hemisphere. This outflow of stratospheric air mass over the northern hemisphere includes stratospheric-tropospheric exchange from eddy diffusion, Hadley cell circulation and transport into the southern hemisphere, and through seasonal adjustments in the mean tropopause levels.

References

D. J. Hofmann, J. M. Rosen, T. J. Pepin and R. G. Pinnick (1975) Stratospheric Aerosol Measurements I: Time Variations at Northern Latitudes, *J. Atmos. Sci.* 32, 1446-1456.

D. Hunten (1975) Residence Times of Aerosols and Gases in the Stratosphere, *Geophys. Res. Lett.* 2, 26-28.

E. R. Reiter (1975) Stratospheric-Tropospheric Exchange Processes, *Rev. Geophys. Space Phys.* 13, 459-474.

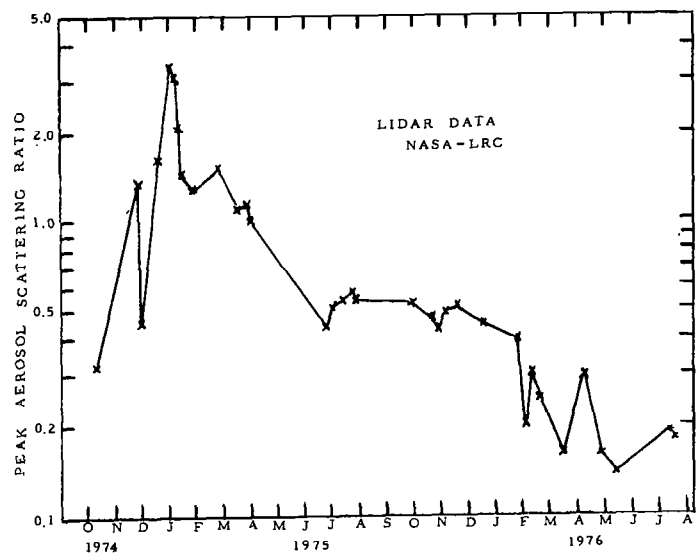


Figure 1. Time Variation of the Peak Aerosol Backscattering Ratio, (R-1), From October, 1974 to July, 1976

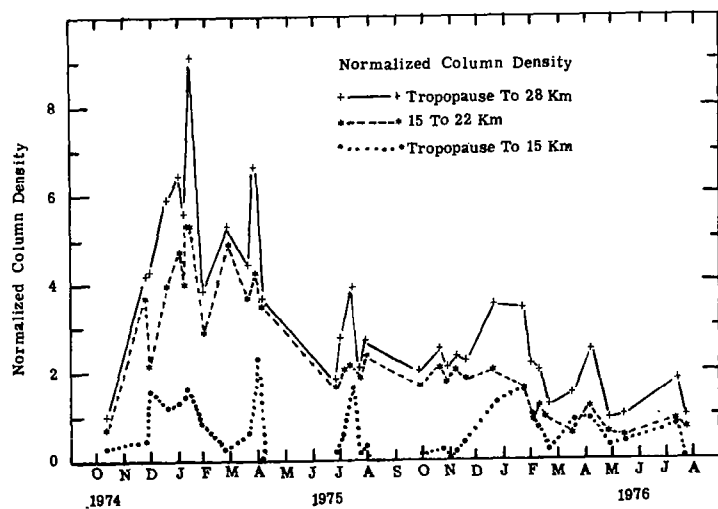


Figure 2. Time Variation of the Normalized Column Density For Given Heights From October, 1974 to July, 1976

Comparison of Airborne Lidar Results with a Physical Model
of Stratospheric Aerosols

F. G. Fernald
Department of Physics and Astronomy
University of Denver, Denver, Colorado 80208

INTRODUCTION

The stratospheric aerosol layer is often referred to as the stratospheric dust layer, which fosters the concept of a layer containing a suspension of relatively inert solid particles of irregular shape. Under such an impression, variations in the stratospheric aerosol loading are tied almost entirely to transport phenomena (including injection and removal processes) affecting the stratosphere. Hamill, Toon and Kiang (1976a) have recently proposed a physical model of the stratospheric aerosols which emphasizes the physics of droplets that are approximately 75% sulfuric acid in water. Hamill, Toon and Kiang's paper is especially important for it strongly projects the droplet nature of these H_2SO_4 aerosols, showing that they will tend to grow and shrink through condensation and evaporation in response to their stratospheric environment.

The 1973 airborne lidar experiment (Fernald et al., 1975; Fernald and Schuster, 1976) emphasized the correlation between the synoptic scale stratospheric circulation and observed patterns in the distribution of stratospheric aerosol scattering ratio without providing a rigorous explanation of the observed correlations. The physical aerosol model proposed by Hamill, Toon and Kiang provides the basis for a new examination of the results from the airborne lidar experiment.

DISCUSSION OF THE LIDAR EXPERIMENT

During the winter and early spring of 1973, the National Center for Atmospheric Research and the Climatic Impact Assessment Program within the Department of Transportation supported an airborne lidar experiment over a considerable portion of the Northern Hemisphere. Features that consistently appeared in the data were (1) the upward displacement of the aerosol maximum in the vicinity of upper tropospheric troughs, and (2) the appearance of relative maxima in aerosol scattering ratio in the vicinity of upper tropospheric cols and ridges. A re-examination of the experimental data shows that these aerosol maxima were located in the vicinity of stratospheric temperature minimas. Thus, the heretofore unexplained features can be simply ascribed to the fact that aerosol maxima tend to occur at temperature minima as predicted when the physical aerosol model was incorporated into a one-dimensional model of the stratospheric aerosol layer (Hamill et al., 1976b; Hamill et al., 1976c).

Examples appear in Figure 1 for the 10 April 1973 flight between Goose Bay, Labrador and Keflavik, Iceland and in Figure 2 for the 17 April 1973 flight between Washington, D.C. and Albuquerque. On 10 April 1973 a deep

trough was centered over Labrador (left hand edge of Figure 1) with a ridge of high pressure over Iceland (right hand edge). The layer of maximum scattering ratio (delineated by the heavy contours) sloped from 22.0 km over Labrador to 20.5 km over Iceland. Within the lower stratosphere the aerosols show a horizontal gradient from a scattering ratio of 1.04 over Labrador to a maximum of 1.16 over Iceland. Temperature contours (light lines) show relatively warm air above the tropospheric trough over Labrador with an accompanying upward displacement of the level of minimum temperature. Relatively cool air resides in the stratosphere above the high pressure ridge over Iceland. A similar correspondence between temperature and aerosol scattering ratio can be observed in Figure 2.

SUMMARY AND CONCLUSIONS

The appearance of a good physical model of stratospheric aerosols has shown the importance of cloud physics phenomena which act, along with transport processes, to modify the stratospheric aerosol distribution. Hamill, Toon and Kiang (1976a) have called for experimental verification of their model. While the cursory examination of lidar results performed here can not be construed as such an effort, it does show that the model is consistent with the experimental lidar observations. Such a model will greatly enhance the value of remote stratospheric sensing for the effects of variations in the aerosol refractive index and size distribution on the aerosol's optical scattering properties can now be rigorously investigated. The model provides the framework in which the elements of future stratospheric aerosol experiments such as satellite measurements, lidar observations, in situ sampling and meteorological observations can be analyzed.

REFERENCES

Fernald, F. G., F. G. Schuster, E. F. Danielsen and D. G. Deaven, 1975: Synoptic scale variability in the distribution of stratospheric aerosols as revealed by airborne lidar. Optical and Quantum Elec. 7, 141-145.

Fernald, F. G. and B. G. Schuster, 1976: Wintertime 1973 airborne lidar measurements of stratospheric aerosols. To be published in J. Geophys. Res.

Hamill, P., O. B. Toon and C. S. Kiang, 1976a: A physical model of stratospheric aerosol particles. Submitted to J. Atmos. Sci.

Hamill, P., R. P. Turco, O. B. Toon, R. C. Whitten and C. S. Kiang, 1976b: A one-dimensional model of the stratospheric aerosol layer. Submitted to Geophys. Res. Letters.

Hamill, P., P. B. Russel and G. M. Walker, 1976c: Estimate of gas phase sulfuric acid concentration in the stratosphere. Submitted to Nature.

TREND OF TWILIGHT COLOR RATIOS AND
CONVERTED LIDAR DATA OF THE FUEGO DUST CLOUD

Frederic E. Volz

Atmospheric Optics Branch, AFGL, L. G. Hanscom AFB, MA 01731

The stratospheric dust veil which after the Fuego eruptions in Guatemala during October 1974 spread over the northern hemisphere caused widely noticed purple twilight skies until about February 1975 (Meinel and Meinel, 1975; Volz, 1975).

Here results of continued monitoring by twilight photometry at Puerto Rico, New Mexico and New England will be reported and semi-quantitatively compared to lidar data from Mauna Loa, Hawaii (Fegley and Ellis, 1975a, b), Hampton, Virginia (Remsberg and Northam 1975), Boulder, Colorado (Fernald and Frush, 1975), Stanford, California (Russel et al, 1976) and Japan (Fujiwara et al, 1975). Also consulted were dust sonde profiles from Laramie, Wyoming (Hofman and Rosen, 1975) and searchlight profiles from New Mexico (Elterman, 1976). The comparison is based on model calculations of twilight color ratio amplitudes by using typical observed layer profiles.

Model Twilight Calculations

A Monte Carlo type computer program, which includes atmospheric refraction and scattering and polarization by aerosols (see Blattner et al, 1974) was used to calculate sky radiation at $\lambda 0.5$ and $0.7\mu\text{m}$ and color ratios $\lambda 0.70/\lambda 0.50$. Here, of prime consideration is the color ratio amplitude (CRA), that is the peak CR at $4-5^\circ$ solar depression normalized to the CR at sunset. This normalization has mainly been introduced to successfully account for large surface turbidity in observations. Otherwise, CR changes are caused mainly by intensity changes at the longer wavelength. As in the measurements, the view angle is 20° above the horizon in the solar azimuth.

Calculations were based on typical layer profiles observed by lidar. A moderate surface turbidity, and a constant background aerosol mixing ratio between 4 km and the layer, were assumed. CRA's as function of increasing aerosol optical thickness τ_A in these layers are shown in Fig. 1b. Up to $\tau_A \sim 0.02$, the CRA's grow with about the square root of τ_A for the narrower layer A and B, and are largest for the narrow 19 km layer. After saturation at $\tau_A \sim 0.03$, the CRA decreases due to overwhelming extinction of the incident solar radiation on the daylight side of the layer. Still wider layers (Model C) as typically used by Blattner and Wells (1973) result in slower growth. Also, higher background mixing ratios (0.1 and 0.2 respectively in Model A' and A'') reduce color ratios considerably. It should be noted, that λ^{-1} scattering (as assumed here) by fine sulphate type aerosol or λ -independent scattering by coarse volcanic dust make little difference. Since aerosol scattering functions are to be known only for scattering angles around 24° , uncertainties in size distribution

and refractive index are not critical.

These results show that medium volcanic turbidity ($\tau_A \approx 0.03$) in a narrow layer causes the CRA to increase with the square root of τ_A , but also that a detailed knowledge of the layer profile and of background turbidity below the layer are necessary to assess observed CRA's.

Relation between Lidar Data and Color Ratio Amplitudes

The lidar data provide, in principle, the pertinent parameters for their conversion to τ_A and twilight CRA's. If the lidar data are given as ratio R_h of observed backscatter to Rayleigh backscatter as function of height, then

$$\tau_A(\lambda 550 \mu\text{m}) = f b_r b_A^{-1} \int \tau_{rh} (R_h - 1) dh$$

$f \approx 1.27$ relates the quantities on the right hand side ($\lambda 700$, Ruby laser) to the visual wavelength. τ_r is the Rayleigh extinction coefficient, and $b_r = 0.12 \text{ sr}^{-1}$ is the ratio of backscatter to extinction of air molecules (τ_r), and likewise b_A for aerosol. Preferred theoretical values of b_A yield for the main Fuego period $\tau_A \approx 0.02$ to (Russel et al, 1976a) 0.04 which seem too high: solar radiation at Mauna Loa (Fegley and Ellis, 1975b) and Sac Peak, N.M., gives values < 0.01 , that is we assume $b_r = 0.026 \text{ sr}^{-1}$.

The such defined τ_A -values have in Fig. 2d(r.h. ordinate) been plotted for all available lidar data. The l.h. ordinate gives twilight CRA's as function of τ_A based on the early, narrow Mauna Loa lidar profiles assuming twilight model A with a background aerosol mixing ratio of 0.05 below the layer as suggested by the Panama dust soundings of 1972/73 by Rosen and Hofman (1974).

The lidar data of the first few Fuego months seem to be in general agreement with the twilight data (Fig. 2, a-c), especially in the lack of changes with latitude apart from delayed arrival in New England. However, Fuego aerosol in mid latitudes often was distributed over a greater altitude range, and aerosol background below the layer might have been larger so that CRA's would have been expected to be lower.

The day to day scatter of the twilight CRA's is believed to be mainly caused by cloud conditions (especially cirrus) at and below the horizon: any lift of the grazing solar rays depresses the CRA. In "good" volcanic twilights, the change of color ratio with solar depression was not always the same, thus indicating variations of the aerosol distribution. However, this hardly affected CRA's. Only the envelope of the CRA's should therefore be considered as undisturbed.

Trends during 1975 and 1976

Beginning in March 1975, the lidar data show abatement of the volcanic layer

corresponding to a residence time of about 6 months (Fig. 2d). The dip in spring 1975 and 1976 in the twilight data from Sac Peak and New England is a common, yet difficult to explain, twilight feature. The latest New England CRA's are still slightly higher than shortly before the Fuego eruption. This is even more true at Sacramento Peak and Puerto Rico, although the falloff by early 1976 coincides well with the virtual disappearance of the dust layer in the Hawaii lidar data.

Of the recently added twilight stations, that at Samoa (13S) shows strong twilights comparable to those of the early Fuego period, while those from Australia (34S) are quite weak for the season.

References

Blättner, W. G., H. G. Horak, D. G. Collins and M. B. Wells, *Applied Optics* 13, 534-547, 1974.

Blättner, W. G., and M. B. Wells: *Monte Carlo Studies of Sky Radiation.* Report AFCRL-TR-73-0613, 1973.

Elterman, L., *Applied Optics*, 15, 1113, 1976.

Fegley, R. W., and H. T. Ellis, *Geophys. Res. Letter* 2, 139, 1975a.

Fegley, R. W., and H. T. Ellis, *Applied Optics* 14, 1751, 1975b.

Fernald, F. G., and C. L. Frush, *EOS Transact., Am. Geophys. Union*, 56, 366, 1975.

Fujiwara, M., T. Itabe, and M. Hirono, *Rep. Ionos. Space Res. Japan*, 29, 74-78, 1975.

Hofmann, D. J., and J. M. Rosen, *EOS Transact.*, 56, 995, 1975.

Meinel, A. B., and M. P. Meinel, *Science* 188, 477, 1975.

Remsberg, E. E., and G. B. Northam, *EOS Transact., Atm. Geophys. Union*, 56, 365, 1975.

Russell, P. B., R. D. Hake, Jr., and W. Viezee, *Quant. Jnl Roy. Met. Soc.* 102, 619-639, 1976a.

Russell, P. B., R. D. Hake, Jr., and W. Viezee, *preprint IAMAP Symp. on Radiation in the Atmosphere*, Garmisch-Partenkirchen, Germany, 1976b.

Volz, F. E., *Science*, 189, 48-50, 1975.

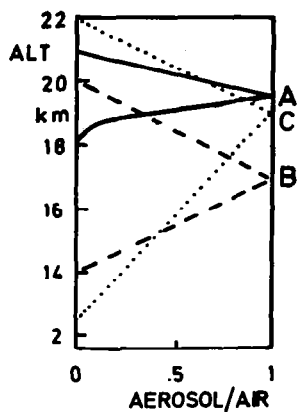


FIG.1 a

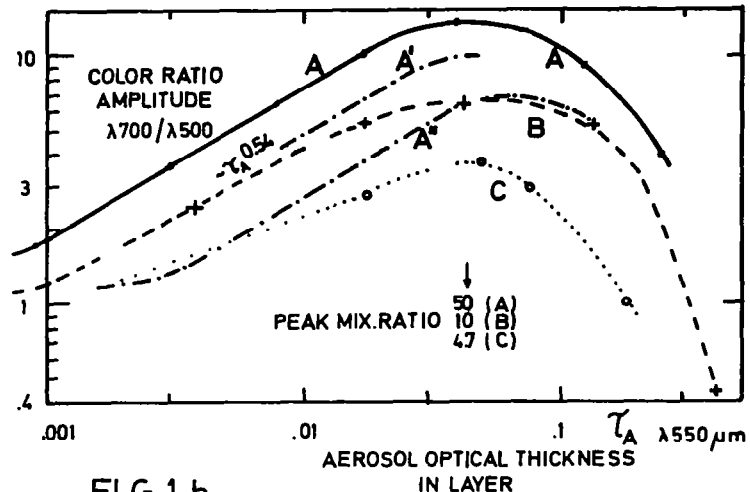


FIG.1 b

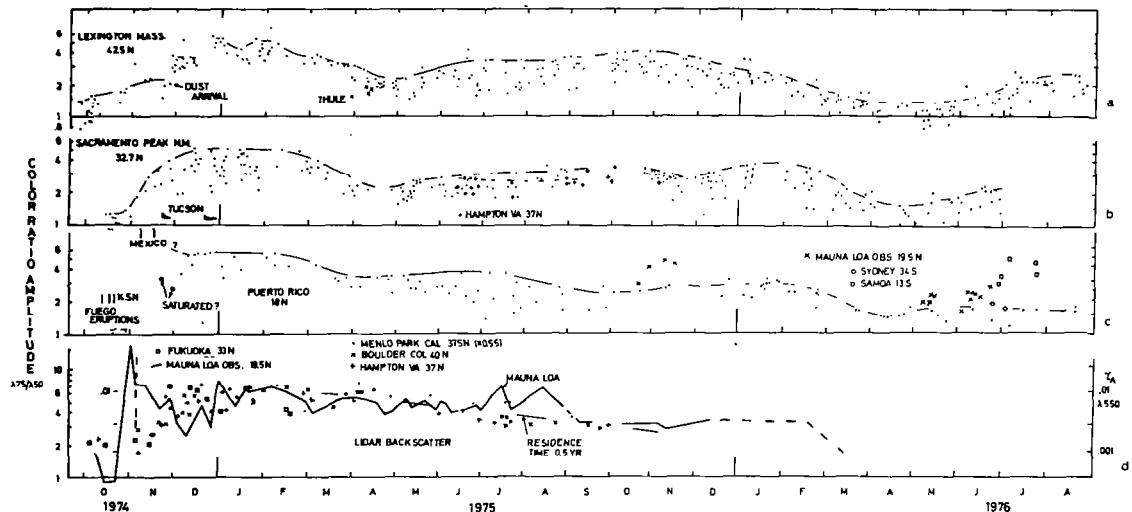


FIG.2

Fig. 2(a-c): Amplitude of twilight color ratio (750/500) at 42N, 33N, and 18N. (d) Lidar aerosol backscatter after the Fuego volcanic eruption from several locations, scaled to twilight color ratio amplitudes according to model calculations (Fig. 1).

Aerosols in the Atmosphere: Their Origin
and Role in Heterogeneous Processes

A. W. Castleman Jr.
CIREs
University of Colorado/NOAA
and
Department of Chemistry, University of Colorado
Boulder, Colorado 80309

The existence of globally distributed persistent aerosol layers in the upper atmosphere has been known for about two decades, but the mechanisms responsible for their formation are not well known. A major fraction of the aerosols in the stratosphere, and a large fraction in the troposphere, are comprised of sulfur bearing compounds. In the vicinity of the mesopause, noctilucent clouds appear occasionally; condensation on pre-existing particles, as well as nucleation about ion clusters involving such ions as Fe^+ , have been proposed as possible processes contributing to their formation.

We have undertaken laboratory studies to establish the rates of SO_2 oxidation and subsequent steps in the formation of H_2SO_4 aerosols, and these are reported in this paper. Both optical and in situ measurements of sulfate aerosols in the stratosphere are shown to correlate with volcanic activity, but there is always considerable time-lag in the attainment of maximum concentration. The

delay times are consistent with the chemical processes responsible for their formation on the basis of the laboratory data given.

Data pertaining to the clustering of molecules about ions of atmospheric interest have been measured in the laboratory, and the role of ion clustering in noctilucent cloud formation will be discussed. Calculations have been done to establish the role of aerosols in heterogeneous processes, and these results will also be presented.

Some Relations Between Aerosol Characteristics at Sea and Meteorological Phenomena.

E. J. Mack, U. Katz, R. J. Pillie, and R. J. Anderson, Calspan Corporation
Box 235, Buffalo, NY 14221

Observed relationships between total aerosol concentration, CCN activity, spectra, aerosol chemistry, visibility, and conventional meteorological variables will be summarized.

Imaginary Index of Refraction and Size Distributions
for Atmospheric Aerosols

E. M. Patterson, D. A. Cillette, B. H. Stockton

National Center for Atmospheric Research*
P. O. Box 3000
Boulder, Colorado 80303

Accurate modeling of the optical effects of aerosols requires, among other knowledge, accurate knowledge of both the mean optical properties and mean size distributions, as well as a measure of the variation in these quantities for the various classes of aerosols that make up the total atmospheric aerosol burden. We have measured optical properties for a variety of aerosols using diffuse reflectance techniques (Lindberg and Laude, 1974; Patterson et al, 1976). For certain classes of aerosols, e.g., soil derived aerosols, we have been able to compare our results with some optical properties inferred on the basis of scattering measurements (Grams et al, 1974), thus providing a comparison of the techniques used to determine these results.

We have also measured size distributions for a number of cases in which soil derived aerosols are a component of the tropospheric aerosol. Our measurements and those of a number of other investigators show a remarkable similarity in results. Apparent differences are seen in a number of cases to be the result of differing measurement techniques.

I. Visible Optical Properties

We have measured the imaginary index of refraction as a function of wavelength for several aerosols; some preliminary results are shown in Figure 1. Indices were determined using an integrating sphere technique in which the total diffuse reflectance of a mixture of aerosol and white standard is measured. If the total reflectance of the standard has been previously measured and if the optical properties of the standard are known, application of the Kubelka-Munk theory allows a determination of absorption properties of the aerosol, from which the imaginary index of refraction as a function of wavelength may be calculated.

Two measurements of the imaginary index of refraction of Saharan aerosols are shown in Figure 1. The Canary Islands sample was collected on Tenerife during the GATE program using a high volume filter sampler located on the ground. The sample was a characteristic brown color

*The National Center for Atmospheric Research is sponsored by the National Science Foundation.

typical of Saharan dust aerosols. The mid-Atlantic sample was collected aboard the German vessel, "Meteor", as part of a sampling program during 1973; the sample was collected approximately 600 km west of Sal Island. The measurements appear to be consistent even though they were taken in different seasons and different years. The fact that the shipboard measurements are slightly lower than the Tenerife sample may be due to the presence of sea salt in the aerosol collected aboard the ship.

For comparison we have also shown two measurements of the imaginary index of refraction calculated from soil samples using the prototype polar nephelometer (Grams et al, 1974) and the compact polar nephelometer (Grams et al, 1976). The measured value of $n_{IM} = 0.005$ at 500 nm was determined for soil derived aerosols in a rural area of Texas (Grams et al, 1974). The measured value of $n_{IM} = 0.0055$ at 633 nm is the result of some preliminary analysis of Saharan dust aerosols measured aboard the NCAR Electra aircraft during the GATE program. Although the error bars are large due to the preliminary nature of the analysis, the mean value determined is in agreement with our laboratory measurements for the Saharan aerosol samples. The Texas data is also in agreement but is slightly lower than the Saharan dust values.

We have also shown results of measurements sampled of volcanic ash from the Fuego volcano in Guatemala. This Fuego ash has a significantly greater absorption at all wavelengths measured than does the soil aerosol. The imaginary index of refraction of this volcanic material appears to be high enough so that relatively small quantities of the volcanic material in the predominantly sulfuric acid-water stratospheric aerosol could lead to significant absorption.

II. Size Distribution for Tropospheric Aerosols

We have made several measurements of the size distribution for tropospheric aerosols under conditions ranging from near duststorm conditions to background conditions at a number of locations. In many of these, soil derived aerosols are a major component of the distribution. A general distribution for these aerosols is shown in Figure 2 from Patterson and Gillette (1976). Three modes are apparent: Mode A appears to be the mode most characteristic of soil derived aerosols and is produced by a process of sandblasting. Mode B, consisting of larger particles, appears to be characteristic of the original soil distribution and is important only in cases of heavy aerosol loading. Mode C, although seen in measurements of soil derived aerosols, does not appear to be characteristic of the soil derived aerosol but appears to consist of a global background aerosol.

When plotted on a $dV/d \log r$ or a $dS/d \log r$ representation both our size distributions and those of a number of other investigators appear to be very similar, and the modes may be described with parameters of very similar values. The differences in the measurements may in many cases be attributed to differences in the techniques used to measure size distributions.

We would like to thank Herr Lothar Schütz and Dr. Ruprecht Jaenicke for making the sample from the "Meteor" available.

References

Grams, G. W., I. H. Blifford, Jr., D. A. Gillette and P. B. Russel, 1974: Complex index of refraction of airborne soil particles, J. Appl. Meteor., 13, 459-471.

Grams, G. W., A. J. Dascher, and C. M. Wyman, 1975: Laser polar nephelometer for airborne measurements of aerosol optical properties, Optical Eng., 14, 85-90.

Lindberg, J. D. and L. S. Laude, 1974: Measurement of the absorption coefficient of atmospheric dust, Appl. Opt., 13, 1923-1927.

Patterson, E. M., D. A. Gillette, and G. W. Grams, 1976: The relation between visibility and the size-number distribution of airborne soil particles. J. Appl. Meteor., 15, 470-478.

Patterson, E. M., C. E. Shelden, B. H. Stockton, 1976: Kubelka-Munk optical properties of a barium sulfate white reflectance standard. Appl. Opt., in press.

Patterson, E. M. and D. A. Gillette, 1976: Commonalities in measured size distributions for aerosols having a soil derived component, manuscript in preparation.

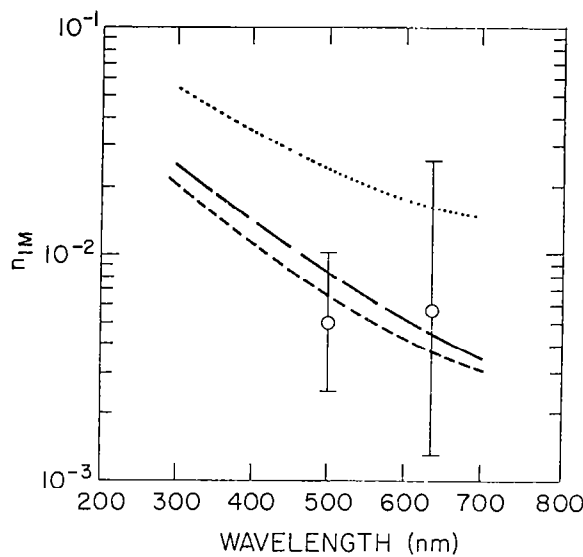


Figure 1.

Diffuse reflectance measurement of the imaginary index of reaction for several aerosols: Saharan aerosol from Tenerife (— — —), Saharan aerosols from the "Meteor" (— - - -), and volcanic ash from Fuego (.....). Polar nephelometer measurements (o) are shown for Texas aerosols (500 nm) and Saharan aerosols (633 nm).

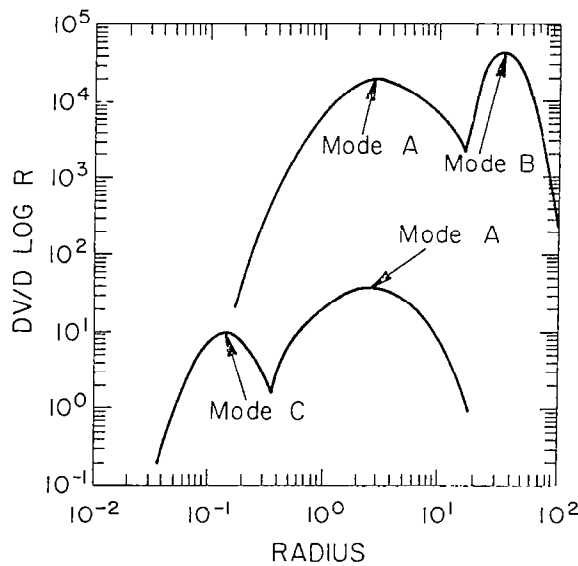


Figure 2.

Two typical size distributions for aerosols having a soil derived aerosol component. The upper curve is characteristic of conditions of heavy aerosol loading in the atmosphere, and the lower curve is characteristic of light aerosol loading.

In-Situ Imaginary Refractive Index Measurements
of Quartz Dust with a CO₂ Laser Spectrophone

by

C. W. Bruce and R. G. Pinnick

Atmospheric Sciences Laboratory
White Sands Missile Range, New Mexico
88002

Measurements of the imaginary refractive index of polydispersions of quartz dust in the 9.2-10.7 μm spectral region are presented. The measurements are derived from simultaneous absorption and particle sizing and counting measurements on laboratory-prepared dust samples of quartz dispersed in a 1 m^3 chamber. The particulate absorption measurements were accomplished with a CO₂ cw acoustical spectrophone by subtracting out gaseous absorption from the total gaseous-plus-particulate absorption signal. Particle sizing and counting was done with a light-scattering particle counter combined with electron microscope measurements of dust filter samples. Total particulate mass loading determined from the measured size distributions together with the particulate absorption measurements are used to infer particle imaginary refractive index. Comparison of the results with existing measurements on quartz is given.

INFRARED EXTINCTION OF TROPOSPHERIC AEROSOLS
EFFLUENTS FROM A COAL-FIRED POWERPLANT

R.F. Pueschel and P.M. Kuhn
National Oceanic and Atmospheric Administration
Atmospheric Physics and Chemistry Laboratory
Boulder, Colorado 80302

1. INTRODUCTION

Knowledge about the infrared (IR) optical aerosol properties is important to (1) evaluate the climatological effects of aerosols and (2) correct radiometric measurements taken from aircraft and satellites. In order to determine transmissivities in the IR window (8 - 14 μm wavelengths) we measure brightness temperatures with a radiometer so that the effects of aerosol on IR radiative transfer are reflected in these measurements. In the following we discuss such measurements for the effluents of the Four Corners Powerplant near Farmington, N.M. The IR extinction coefficient results directly from the temperature measurements. A comparison of the in situ measurement of the extinction coefficients with Mie computations for simultaneously measured aerosol size distributions results in an estimate of the IR absorption index for this particular aerosol.

2. EXPERIMENTAL

2.1 Radiation Measurements

The basic instrument is a Barnes Model PRT-5 8-14 μm Precision Radiation Thermometer. This completely portable, non-contact, direct reading instrument was operated from an aircraft to measure the effective equivalent blackbody temperature of the power plant's cooling lake both with and without the plume intercepted.

Consider in Fig. 1 the radiometric observation of a smoke layer of thickness Δz by examining the power budget at the top of the aerosol layer, denoted by the level symbol 1. The arrows indicate the direction of propagation of the radiant power, dashed arrow shafts indicating transmission and solid shafts indicating emission or reflection. In each case we refer to the vertical component of power transfer.

The radiant power balance at the top of the aerosol layer may be written (Davis, 1971; Kuhn, 1970) as

$$N_2^\uparrow = T_{\Delta\nu} N_1^\uparrow + (1.0 - T_{\Delta\nu}) N_A^\uparrow + R_{\Delta\nu} N_2^\downarrow \quad (1)$$

where N_2 , N_1 and N_A are the radiances ($\text{watts cm}^{-2} \text{ ster}^{-1}$) at the top, the bottom and within the aerosol layer, respectively. $T_{\Delta\nu}$ is the transmission of the aerosol layer in the spectral interval $\Delta\nu$. $R_{\Delta\nu}$ is the reflection in the spectral interval $\Delta\nu$. Radiances N_2 and N_1 are measured with the PRT 5 radiometer directly. Radiance N_A is the difference between N_2 and N_1 . N_A can also be calculated from independent temperature measurements within the plume with the emissivity resulting from the radiance measurements.

Neglecting the terms containing the reflectivity $R_{\Delta\nu} = 0.03$ (Davis, 1971) equation (2) may be rewritten to give transmissivity as

$$\tau_{\Delta\nu} = \frac{N_2^\uparrow - N_A^\uparrow}{N_1^\uparrow - N_A^\uparrow} \quad (2)$$

Beer's law permits us to state that

$$\tau_{\Delta\nu} = \exp(-K_{\Delta\nu} \Delta z) \quad (3)$$

where $K_{\Delta\nu}$ is the optical thickness, $K_{\Delta\nu}$ is the bulk total extinction coefficient (per unit length) and Δz is the plume thickness.

The heating rate experienced by a layer of air due to the absorption of aerosol particles may be expressed as

$$\frac{\partial T}{\partial z} = - \frac{\pi}{\rho c_p} \frac{\Delta N}{\Delta z} = \frac{\pi}{\rho c_p} \cdot \frac{(N_2 - N_1)}{\Delta z} \quad (4)$$

where ρ and c_p denote the air density and specific heat at constant pressure, respectively.

2.2 Aerosol Analysis

2.2.1 Aerosol Elemental Composition

Aerosols were collected on 0.1 μm pore size nucleopore membranes for size, shape and elemental composition analysis. Individual particle analysis was performed utilizing the combined techniques of scanning electron microscopy and energy-dispersive X-ray analysis. It was found that the flyash aerosol typically exists of spherical particles. Their elemental composition is dominated by Si which is present in every particle analyzed to date, followed by Al, found in 80% of all particles, Mg (50%), S (50% and Cl (30%).

The basic structure of all silicates, and the one that determines their index of refraction, is the silicon-oxygen tetrahedron $[\text{SiO}_4]^{4-}$. The silicate class embraces the largest number of minerals with optical constants very close to those of quartz. The scattering index, n^1 , (real part of the complex index of refraction) of stable silicates have values around 1.6. This value was assigned to the flyash aerosol as its bulk scattering index.

An estimate for the absorption index n^2 (imaginary part of the complex index of refraction) will be given later in this discussion after Mie calculations based on measured size distributions has been performed.

2.2.2 Aerosol Size Analysis

The aerosol mass as function of particle size was measured in the plume with a 10-cascade Quartz Crystal Microbalance (Chuan, 1974). Such a real-time and in-situ measurement is very desirable for the rapid assessment of particulate mass concentration. Figure 2 shows the mass concentration, $\Delta M / \Delta \log D$ in micrograms per cubic meter, as function of particle diameter D (μm) from one measurement. From this measured mass distribution we can construct the particle number density via

$$n(D) = \frac{\Delta N}{\Delta \log D} = \frac{6}{\rho \pi D^3} \frac{\Delta M}{\Delta \log D} \quad (\text{m}^{-3}) \quad (5)$$

This particle density function $n(D)$ has been inserted into the IR radiance extinction formula

$$K = \frac{1}{4} \int_{D_1}^{D_2} Q_{\text{EXT}} \pi D n(D) dD \quad (6)$$

approximated by

$$K = \frac{1}{4} \sum_{D_{\text{min}}}^{D_{\text{max}}} Q_{\text{EXT}} \pi D n(D) \Delta D \quad (7)$$

to calculate an extinction coefficient that can be compared with the one deduced from radiometric measurements. The various efficiency factors, Q , in equations (6) and (7) can be calculated from Mie theory (Van de Hulst, 1957) for the desired range of particle sizes D and refractive indices $n = n^1 - i n^2$.

3. RESULTS AND DISCUSSION

Table 1 shows the relevant radiometric plume properties. The transmissivity, τ , is calculated from the measured radiance by means of equation (3). The extinction coefficient, K , follows from τ by means of equation (5) for an observed plume thickness of 200 meters. The cooling rate, $\frac{dT}{dx}$, was calculated from the measured effective radiances N , integrated over one hemisphere, by means of equation (4).

Information about IR transmissivities, τ , and IR extinction coefficient, K , are indispensable for solutions of the radiative transfer equations. The effect of aerosols on the transfer of IR radiation has been treated theoretically in the past (e.g. Ackerman et al., 1976). Aerosol model distributions were assumed in these treatments. Measurements of the type described here, taking into account the existing aerosol distributions, are indispensable to verify the model calculations.

Another property relating to the IR effects of aerosols is its absorption index n'' . An estimate of n'' is possible by comparing measured (equation 3) with calculated (equation 7) extinction coefficients. Figure 3 shows the calculated extinction coefficients as functions of the absorption index, n'' , for a constant scattering index $n' = 1.60$. The spread in the data is due to variations in the measured particle mass distributions. Also shown in Fig. 3 is the IR extinction coefficient that was deduced from the IR radiance measurements. The range of intercept of the two measures of the IR extinction is the range of the absorption index that can be assigned to the flyash aerosol. It can be seen that n'' has been determined within the limits $0.6 < n'' < 0.9$. It is due mainly in uncertainties in the aerosol size distribution measurement that at present this value cannot be resolved with more accuracy.

On the basis of the measurements it appears likely that an aerosol layer trapped below an inversion may act to strengthen the inversion by cooling from the top of the aerosol layer. This in turn would increase the aerosol concentration below the inversion by preventing the lifting or destruction of the inversion.

It is being realized that the established IR effects of plume effluents are noticeable on the local or regional scale at the most. However, in light of planned new power plant constructions and operations it would appear important now to combine IR cooling rates for power plant effluents with solar radiation heating calculations to complete the radiation budget for regional atmospheres.

4. SUMMARY AND CONCLUSIONS

We have demonstrated that *in situ* radiometric measurements on power plant plume effluents lead to realistic IR extinction coefficients for the window (8-14 μm) spectral region. The results can be used to calculate IR heating or cooling rates, and to correct temperature measurements from aircraft and satellites.

Comparisons of the measured extinction coefficients with Mie calculations for measured aerosol size distributions result in values of the absorption index. Our measurements show that the IR absorption index for the plume effluents is comparable in magnitude to those determined by Volz (1973) for ammonium sulfate. It is, however, appreciably higher than what we found for a desert and an urban aerosol (Pueschel and Kuhn, 1975).

We propose that the findings on IR transfer are combined with measurements or calculations of the effects of stack effluents or short wave radiation so that the climatic impact of increased power plant operations can be evaluated.

LIST OF REFERENCES

Ackerman, T.P., K.N. Liu and C.B. Leovy, 1976: Infrared Transfer in Polluted Atmospheres, J. Appl. Meteor., 15, 28-35.

Chuan, R.L., 1974: Application of an Oscillating Quartz Crystal to measure the Mass of Suspended Particulate Matter, in Analytical Methods Applied to Air Pollution Measurements, Ann Arbor Science Publishers, Inc., Ann Arbor, Mich.

Davis, P.A., 1971: Applications of an Airborne Ruby Lidar during a BOMEX Program of Cirrus Observations, J. Appl. Meteor., 10, 1314-1323.

Kuhn, P.M., 1970: Airborne Observations of Contrail Effects on the Thermal Radiation Budget, J. Atmos. Sci., 27, 937-942.

Pueschel, R.F. and P.M. Kuhn, 1975: Infrared Absorption of Tropospheric Aerosols: Urban and Rural Aerosols of Phoenix, Arizona, J. Geophys. Res., 80, 2960-62.

Van de Hulst, H.C., 1957: Light Scattering by Small Particles, 453 pp., J. Geophys. Res. 77, 1017-1031.

Volz, F.E., 1973: Infrared Optical Constants of Ammonium Sulfate, Sahara Dust, Volcanic Pumice and Flyash. Appl. Optics, 12, 564-568.

Table 1: IR optical and related properties of effluents in the plume of the Four Corners coal-fired power plant.

Transmissivity $\tau=0.82 \pm 0.01$ Plume Thickness $\Delta z=200 \text{ m}$ Extinction Coeff. $K=0.99 \pm 0.04 \text{ km}^{-1}$ Cooling Rate $\Delta T/\Delta t=0.64 \pm 0.1^\circ \text{C/hr}$

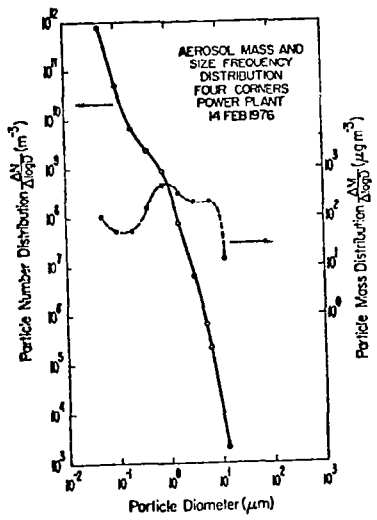
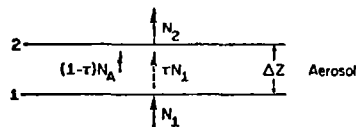


Figure 2: Aerosol size and mass frequency distribution of a flyash aerosol.

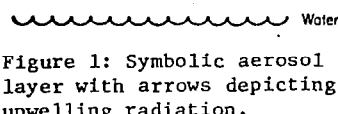


Figure 1: Symbolic aerosol layer with arrows depicting upwelling radiation.

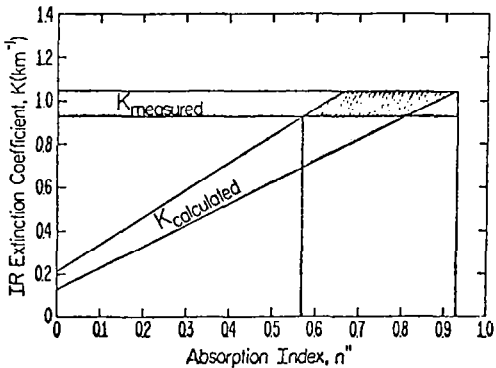


Figure 3: Calculated IR extinction coefficient as function of the aerosol absorption index, compared with the measured IR extinction coefficient.

CHARLSON, R.J., VANDERPOL, A.H., WAGGONER, A.P., COVERT, D.S., BAKER, M.B.
Department of Civil Engineering, University of Washington, Seattle, WA 98195 USA

The Dominance of Tropospheric Sulfate in Modifying Solar Radiation

Introduction Atmospheric measurements in eastern United States and northern Europe have shown that sulfate compounds are often the dominant component of the submicrometer aerosol particle mass on a regional or 1000 km scale in the boundary layer. Thus, they have a large effect on light scattering and turbidity. These sulfates have been identified as H_2SO_4 , $(NH_4)HSO_4$, $(NH_4)_3H(SO_4)_2$, $(NH_4)_2SO_4$ though they probably exist as intermediate mixtures as well. Measurements of light scattering and molecular properties of regional sulfate aerosols are reviewed here.

Physical and Chemical Aerosol Properties Particle size distribution measurements made over the past seven years (1,2) have shown that for atmospheric aerosols in general and also for regional sulfate aerosols the particulate mass is bimodally distributed above and below about $2\mu m$ in locations not immediately influenced by combustion sources. A typical example of this bimodal distribution is illustrated in Fig. 1.

Although the oxidation mechanisms by which sulfate aerosol is formed are not well quantified, power plant SO_2 plume data show that sulfate aerosols form and grow rapidly into the accumulation mode between $0.05\mu m$ and $2.0\mu m$ in diameter (4), Fig. 2. Typically 80% to 90% of the particulate sulfate mass is found in this mode and 40% to 50% or more of the total mass of the accumulation mode is sulfate as one of the compounds identified above (5,6,7,9). A comparison of particle light scattering cross section per unit volume as a function of particle diameter (illustrated in Fig. 3) with the bimodal size distribution shows that light scattering by aerosols is controlled by the accumulation mode aerosol mass. It follows that particulate sulfates as the major compounds of this mode are the chemical species which dominate light scattering.

As a result particulate light scattering coefficient, b_{sp} , is highly correlated with accumulation mode aerosol volume and is also correlated with aerosol sulfate mass (5,10) as shown by data illustrated in Figs. 4 and 5 respectively.

Nephelometric Measurement of Aerosol Chemistry Integrating nephelometers (11, 12) which measure b_{sp} can be used as a monitor of accumulation mode aerosol or aerosol sulfate mass. Two techniques involving nephelometry have been developed which provide in situ information on the molecular form of regional sulfate aerosol. The first, a humidity controlled nephelometer, humidograph (7,14), measures b_{sp} as a function of relative humidity, RH, from 30% to 90% which is presented as a graph of the ratio $B(RH) \equiv b_{sp}(RH)/b_{sp}(30\%)$ versus RH (humidogram). The second, a thermal analysis technique will be discussed elsewhere in these proceedings (14). A third nephelometric technique, measurement of hemispheric backscattering, b_{bsp} , (17) presented here as the ratio $R \equiv b_{bsp}/b_{sp}$, has yielded data which is correlated with the molecular form of sulfate aerosols.

Chemical identification with the humidograph is made by observation of the shape of the $B(RH)$ curve as the humidity of the aerosol sample flow through the nephelometer is varied from 30% to 90% with or without the addition of NH_3 at ppm levels. A deliquescence step, or increase in B by a factor of 1.5 to 2, in the ambient aerosol humidogram at 80% RH is indicative of $(NH_4)_2SO_4$. A change in the humidogram from hygroscopic behavior, monotonic increase with RH, for the ambient aerosol to deliquescent behavior for the ambient aerosol plus NH_3 is an indication of acid sulfate species, H_2SO_4 and/or $(NH_4)HSO_4$. Fig. 6a,b,c,d illustrates examples of the types of humidograms which have been observed and

the molecular information which has been derived. The humidograph has been operated for ten weeks at three locations in midwest United States. Sites, times and molecular information are summarized in Table 1. The Tyson, Mo. and Milford, Mich. sites are located 40-50 km outside of metropolitan areas (St. Louis and Detroit). The Hall Mt. site is about 200 km northwest of Little Rock, Ark., and 400-500 km from any metropolitan area, e.g., St. Louis, Kansas City, Dallas-Fort Worth. SO_2 emission in a 100 km grid surrounding Hall Mt. are on the order of 10^{-9} to 10^{-8} gm/m²/sec and 100 to 1000 times greater at the other sites (19). The percentages in the table and the magnitude of the deliquescence steps observed in the humidograms show that at each site sulfates dominated the accumulation mode, light scattering aerosol. The distinguishable molecular forms of the sulfate aerosol persisted on the order of hours to days, characteristic of the time scale of synoptic motions in the atmosphere. For the 1973 Tyson data the molecular form of the aerosol has been shown to be associated with the 72 hr trajectory of the aerosol (16). These data suggest that the Midwest sulfate aerosol is an extensive system covering spacial scales of 1000 km. It is hypothesized that the molecular form is dependent on air mass composition and history and that these are determining factors in controlling mechanisms of production and modification of SO_4^{2-} which are as yet only qualitatively understood.

Data on the backscatter-total scatter ratio, R, measured at Tyson in 1973 are illustrated in Fig. 7. The bimodality of R has been found to be related to the occurrence of the molecular form of the sulfate aerosol as determined by the humidograms. This difference in R is consistent with Mie calculations of the scattering coefficient for refractive indices of H_2SO_4 and $(\text{NH}_4)_2\text{SO}_4$ (1.40 and 1.53 respectively) (17). Within reasonable limits variation of the size distribution and introduction of an imaginary part of refractive index coefficient (0.01 to 0.03) had little effect on the qualitative sense of calculated R values.

Turbidity Data Turbidity data gathered in the U.S. in rural areas (18) are illustrated in Fig. 8a. Turbidity as defined here is due exclusively to aerosol particles. The data show an average annual turbidity of about 0.15 over a $(1000 \text{ km})^2$ area on the eastern U.S. which is much greater than that due to Rayleigh scattering or ozone absorption. A similar region of turbidity is expected to exist over Europe. Rural sulfate data for eastern U.S. (19) are shown in Fig. 8b. The region of high turbidity coincides with the region of high sulfate. Calculations (20) indicate that at these levels turbidity is controlled by the sulfate aerosol in the boundary layer. These data are consistent with nephelometer and humidograph measurements in the same area in both magnitude and extent.

Conclusions An integrated analysis of size distribution and chemical data from several sources indicates that sulfate in particulate matter dominates the accumulation mode, optically important aerosol a large fraction of the time in the eastern U.S. and northern Europe. Levels of turbidity and light scattering are controlled by the presence of this sulfate aerosol. The ratio R and the increase in aerosol scattering at high RH are determined by the molecular form of the aerosol through refractive index and hygroscopic growth. A discussion of the role of particulate sulfur compounds in the radiative climate of the earth has been presented by Bolin and Charlson (20). The sources of these aerosols are not well quantified. If anthropogenic contributions to the atmospheric sulfur budget are large compared to natural sources, trends may become apparent in data such as are presented here. This overall analysis points out that it is possible and worthwhile to investigate the role of an individual class of substances as it affects aerosol scattering properties and solar radiation.

References

1. Whitby, K.T., et al., 1972, *J. Coll. and Interface Sci.*, 39, 240.
2. Whitby, K.T., 1974, Modeling of Multimodal Aerosol Distributions, presentation at Gesellschaft für Aerosolforschung, Bad Soden, FRG.
3. Wilson, W.E. et al., 1976, Sulfates in the Atmosphere, presented at 69th Air Poll. Control Assn. meeting, Portland, Oregon.
4. Whitby, K.T. et al., 1974, Preprints of 171st Am. Chem. Soc. meeting, New York, p. 49. Wilson, W.E. et al., 1976, General Motors Sulfate Dispersion Experiment, presented at 69th Air Poll. Control Assn. meeting, Portland, Ore.
5. Husar, J.D. et al., 1976, Preprints of 171st Am. Chem. Soc. meeting, New York, p. 90. Mascias, E.S. and Husar, R.B., 1976, *Fine Particles*, Academic Press, New York, p. 536.
6. Dzubay, T.G. and Stevens, R.K., 1976, *X-ray Fluorescence Methods for Analysis of Environmental Samples*, Ann Arbor, Ann Arbor Science Publishers (submitted for publication).
7. Charlson, R.J. et al., 1975, *Atm. Environ.*, 8, 1257.
8. Brosset, C., 1976, Preprints of 171st Am. Chem. Soc. meeting, p. 19.
9. Brosset, C., Andréasson, K. and Ferm, M., 1976, *Atm. Environ.*, 9, 631.
10. Waggoner, A.P. et al., 1976, *Nature*, 216, 120.
11. Beutrell, R.G. and Brewer, A.W., 1949, *J. Sci. Instr.*, 26, 357.
12. Charlson, R.J. et al., 1969, *J. Air Poll. Control Assn.*, 19, 937.
13. Covert, D.S. et al., 1972, *J. Appl. Meteor.*, 11, 968.
14. Husar, R., 1976, Determination of Ambient H_2SO_4 and its Ammonium Salts by Thermal Analysis, Symposium on Radiation in the Atmosphere, Garmisch, FRG.
15. Electric Power Research Institute document, EPRI EC-125, 3, 1976.
16. Vanderpol, A.H. et al., 1975, *Science*, 190, 570.
17. Bhardwaja, P.S., 1976, The Backward Scattering Ratio of Atmospheric Aerosols, Ph.D. dissertation, Univ. of Washington, Seattle, WA, USA. Bhardwaja, P.S. et al., 1976, Backward Hemispheric Scattering Ratio of Atmospheric Aerosols and its Relation with their Refractive Index, Symposium on Radiation in the Atmosphere, Garmisch, FRG.
18. Finklea, J., private communication, 1974, EPA-NASN data.
19. Flowers, F.C., McCormick, R.A., Kurfis, K.R., 1969, *J. Appl. Meteor.*, 8, 955.
20. Bolin, B. and Charlson, R.J., 1976, *Ambio*, 5, 47.
21. Hidy, G.M., ed, 1975, ACHEX, Final Report to State of California Air Resources Board, Vol. 3, p. 30.

Table 1: Percentage of observations categorized as acid SO_4^{\equiv} and $(NH_4)_2SO_4$

site, time	% acid SO_4^{\equiv}	% $(NH_4)_2SO_4$
Tyson, Mo., 21-27 Sept 1973 88 humidogram pairs	77%	22%
Tyson, Mo., 11-26 Sept 1975 750 humidogram pairs	39%	60%
Milford, Mich., 29 Sept-14 Oct 1975 656 humidogram pairs	12%	73%
Hall Mt., Ark., 4 Nov-4 Dec 1975 1444 humidogram pairs	30%	57%

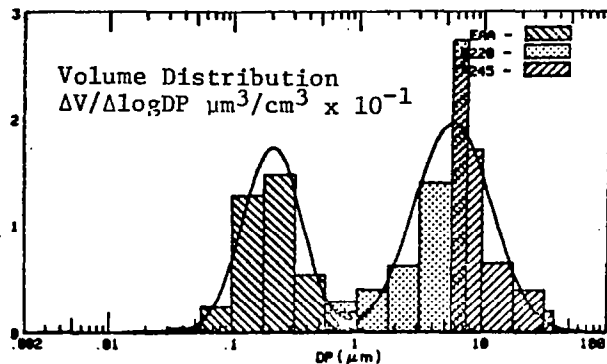


Fig. 1

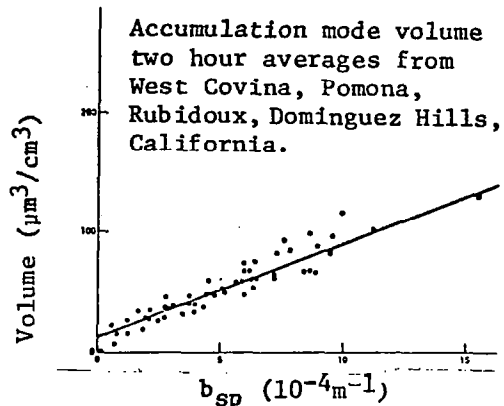


Fig. 4

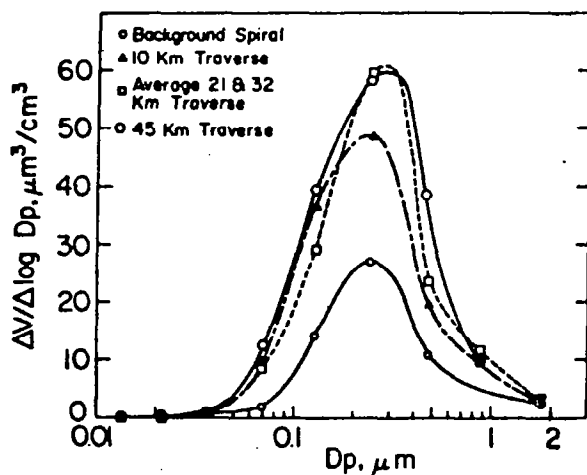


Fig. 2

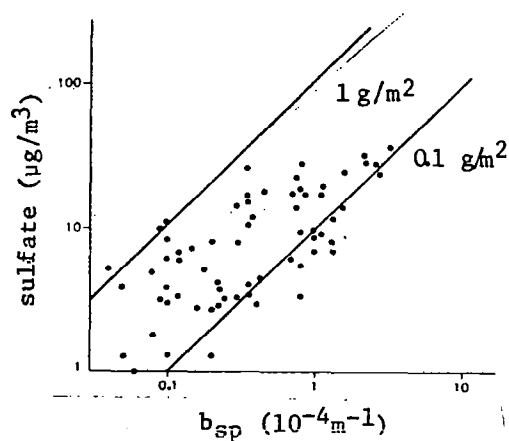


Fig. 5

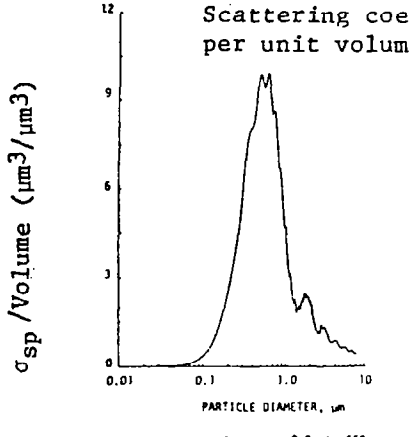


Fig. 3

Fig. 1. Typical E. U.S. aerosol size distribution [Milford, Michigan, 13 Oct 1975 (3)].
 Fig. 2. Power plant, SO_2 , plume aerosol size distribution [Labadie, Mo., 14 Aug 1974 (4)].
 Fig. 3. Light scattering coefficient per unit volume,
 Fig. 4. Correlation of accumulation mode aerosol volume unit with b_{sp} (21).
 Fig. 5. Aerosol sulfate concentration, $[\text{SO}_4^{2-}]$, and nephelometer data, b_{sp} , for aircraft flights in rural Sweden. A comparison of b_{sp} and $[\text{SO}_4^{2-}]$ shows a correlation of 0.73 for all flights. The limits of $[\text{SO}_4^{2-}]/b_{sp}$ (g/m^2) shown by solid lines are consistent with chemical and physical aerosol data and Mie scattering calculations (10).

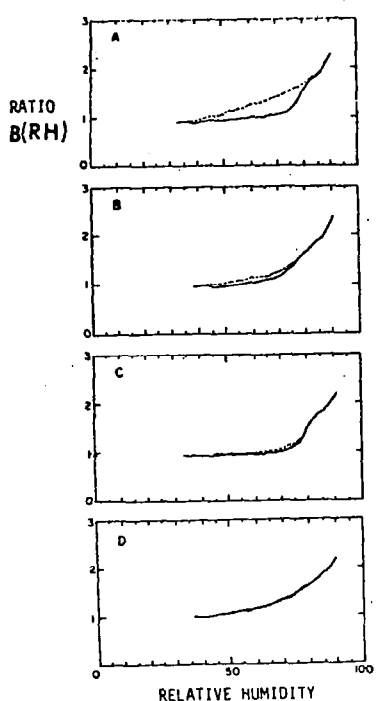


Fig. 6

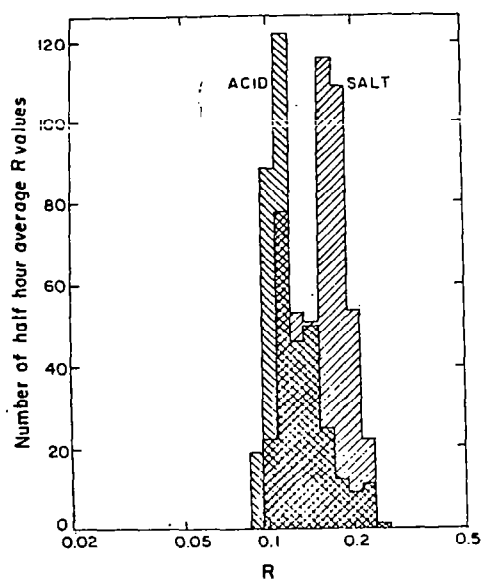


Fig. 7

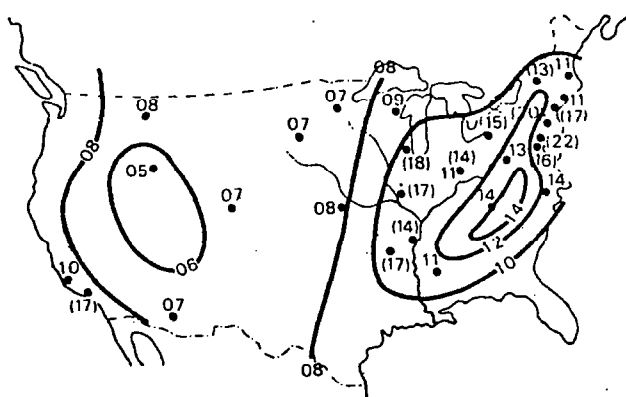


Fig. 8a

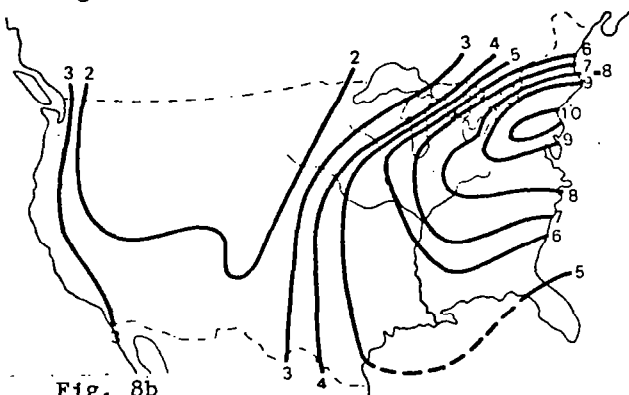


Fig. 8b

Fig. 6. Categorization of molecular form from humidograms. Dashed curve is ambient humidogram; solid curve is with addition of NH_3 .
 a. Monotonic (hygroscopic) curve; NH_3 caused inflection (deliquescent) at 80% RH; categorized as acid $\text{SO}_4^{=}$ aerosol. b. Slightly deliquescent curve; NH_3 caused enhancement of deliquescence; categorized as acid $\text{SO}_4^{=}$.
 c. Strongly deliquescent curve; NH_3 caused little change; $(\text{NH}_4)_2\text{SO}_4$. d. Monotonic curve unaffected by NH_3 ; non-sulfate.

Fig. 7. Histogram of measured half hour average R values separated according to acid or salt according to humidogram data.

Fig. 8 a. Annual average rural turbidity, B, in the United States, 1961-1966, after Flowers et al (20). Urban values are in parentheses [Unit 10^2 (air mass) $^{-1}$].

b. Annual average rural SO_4^{2-} concentration $\mu\text{g}/\text{m}^3$, for the United States, U.S. Environmental Protection Agency data.

Use of Prevailing Visibility Data for Aerosol Studies

N. M. Reiss, R. A. Eversole and J. J. Mangano

Department of Meteorology and Physical Oceanography
Cook College, P. O. Box 231
Rutgers University--The State University of New Jersey
New Brunswick, N. J. 08903

Introduction.

Numerous studies have been done which utilize transmissometer data to obtain information as to the optical properties of aerosols. Most investigators avoid using prevailing visibility observations that are taken routinely at airports and at other meteorological observing stations on an hourly basis, in that such observations are thought to be subject to large errors. Stations that observe prevailing visibility are, however, much more numerous than those with transmissometer data, and their observations often extend through many years. Furthermore, prevailing visibility records are available on computer tapes from the National Weather Records Center, and thus lend themselves readily to numerical processing.

It is the purpose of this paper to discuss the nature of the prevailing visibility observations, and the reduction of the data to usable form. An example will be given of the use of reduced prevailing visibility data.

Observations of Prevailing Visibility.

The Federal Meteorological Handbook No. 1 - Surface Observations (FMH1) defines "visibility" as "the greatest distance at which selected objects can be seen and identified", and "prevailing visibility" as "the greatest visibility equalled or exceeded throughout at least half the horizon circle which need not necessarily be continuous." In taking an observation, the observer typically refers to a map in polar coordinates, centered on his station, upon which the locations of any number of "selected objects" such

as tall buildings, mountains and water towers are plotted.

Table 1 gives "reportable" values of visibility for meteorological stations. These figures represent the accuracy that is officially desired for prevailing visibility reports. In practice, the reports are never given with greater accuracy than this (e.g., $17\frac{1}{2}$ miles), but, particularly in the case of high visibilities that are not operationally significant, are often given with considerably less accuracy. When the prevailing visibility is less than seven miles, regulations require that an obstruction to visibility must be reported (e.g., rain, fog or haze), although obstructions may also be reported at higher visibilities. The effect of this regulation is to stimulate some observers to report "seven miles" as the prevailing visibility whenever the visibility is greater than or equal to seven miles. A similar effect is found when the visibility exceeds the distance of the farthest visibility marker. In such a case, the distance of the marker is often used, rather than the best estimate of the actual value. Even numbers and numbers evenly divisible by five are also greatly favored. The net result is a frequency distribution of visibilities that shows huge artificial peaks at these preferred values. Table 2 gives an example.

Table 1. Reportable Visibility Values (miles). (After FMH1)

Increments of Separation (Miles)						
1/16	1/8	1/4	1/2	1	5	
0	3/8 1 1/4	2	2 1/2	3 10	15	
1/16	1/2 1 3/8	2 1/4	3	4 11	20	
1/8	5/8 1 1/2	2 1/2		5 12	25	
3/16	3/4 1 5/8			6 13	30	
1/4	7/8 1 3/4			7 14	35	
5/16	1 1 7/8			8 15	40	
3/8	1 1/8 2			9	etc.	

Adjustment of Visibility Data.

In adjusting the visibility data, it is assumed that two types of error are present. The first is the unavoidable inaccuracy in observation, which is assumed to be random. The second is the error due to the effects discussed above. In the latter case, which occurs only at high visibilities, it is assumed that the observer has a bias toward recording lower values than are actually occurring. It is further assumed that the visibilities are log-normally distributed.

A cumulative probability distribution is computed. As shown in Figure 1, the distribution follows a log-normal pattern fairly well, except at high visibilities, where the observer bias begins to appear. A best-fit log-normal curve is fitted to the points lying below about seven miles and extrapolated to higher visibilities. The curve does become asymptotic at very high visibilities, due to the ubiquitous effects of Rayleigh scattering, but this does not have any great effect at moderate visibilities.

The straight line in Figure 1 allows one to obtain prevailing visibility statistics, while minimizing the effect of observer bias.

Table 2.
Daytime Visibilities at
Atlantic City, N. J.
(1949 - 1973)

Visibility (miles)	Frequency of Observation
0	3
1/16	9
1/8	5
3/16	2
1/4	18
5/16	0
3/8	5
1/2	17
5/8	3
3/4	29
1	51
1 1/8	0
1 1/4	8
1 3/8	0
1 1/2	79
1 5/8	0
1 3/4	3
2	114
2 1/4	1
2 1/2	118
3	467
4	639
5	932
6	876
7	1680
8	1448
9	243
10	4095
11	9
12	1755
13	1
14	0
15	3503
20	2
≥ 25	3

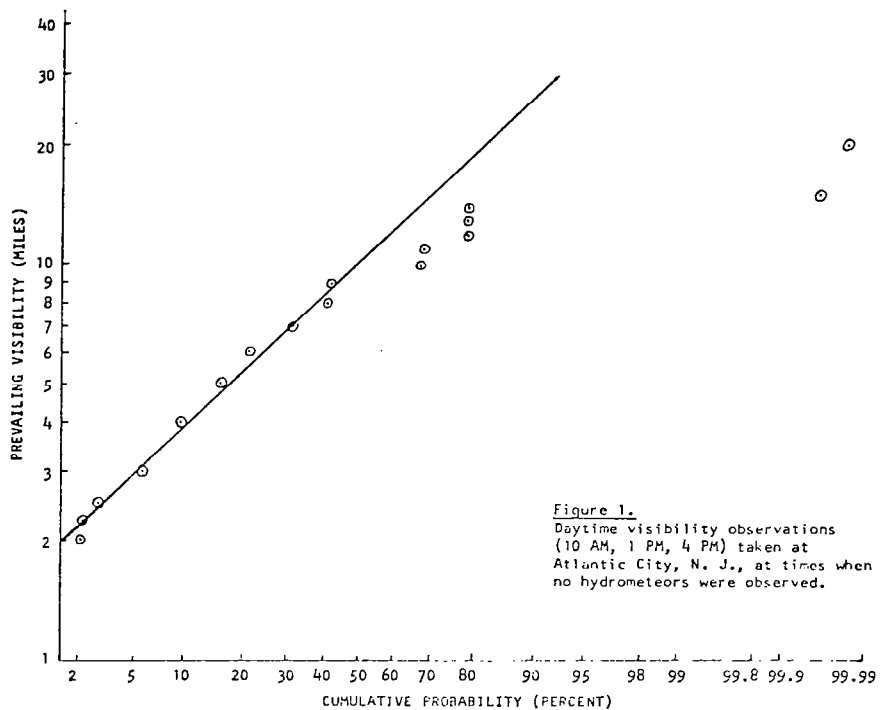


Figure 1.
Daytime visibility observations
(10 AM, 1 PM, 4 PM) taken at
Atlantic City, N. J., at times when
no hydrometeors were observed.

Use of Prevailing Visibility Data.

We are presently investigating the use of prevailing visibility data as a surrogate variable for observations of mass concentrations of total suspended particulates (TSP). There are hazards involved in this, in that visibility is related not only to TSP, but also to relative humidity and to the optical properties of the particles. As an initial step, we are examining data for locations where simultaneous TSP, wind, prevailing visibility and relative humidity observations are available. Data are being stratified by relative humidity and wind direction, in an effort to obtain a signature, associated with a given TSP source region, that relates particulate concentration to visibility and relative humidity.

References.

Federal Meteorological Handbook No. 1 - Surface Observations. U. S. Dept. of Commerce, Washington, D. C.

Polarization and Scattering
by Nonspherical Aerosols

Petr Chýlek
 Department of Geosciences
 Purdue University
 West Lafayette, Indiana 47907

Let us write electric vectors \vec{E}_i and \vec{E}_s of an incoming and scattered radiation in the form

$$\vec{E}_i = \begin{pmatrix} E_{i\perp} \\ E_{i||} \end{pmatrix} \quad (1a) \quad \vec{E}_s = \begin{pmatrix} E_{s\perp} \\ E_{s||} \end{pmatrix} \quad (1b)$$

where symbols \perp and $||$ denote the perpendicular and parallel components of a corresponding vector with respect to the scattering plane. We define the scattering matrix

$$A = \begin{pmatrix} A_{11} & A_{12} \\ A_{21} & A_{22} \end{pmatrix} \quad (2)$$

by the relation $\vec{E}_s = A \vec{E}_i$. (3)

In the general case of the scattering by an arbitrarily shaped particle all matrix elements A_{jk} are nonzero and they are functions of the scattering angle, particle's shape, size, orientation and material.

If the scattering particles are spherical, the scattering matrix is diagonal. Consequently, if the incoming electromagnetic plane wave is linearly polarized then the radiation scattered into the forward or backward direction has the same polarization as the incoming wave. In other words, no depolarization occurs. This fact is often used for an active remote sensing¹⁻⁴ of clouds or aerosol layers to derive information concerning the shape of cloud or dust particles. The remote sensing data are usually interpreted in the way that if the backscattered radiation has the same polarization as incoming radiation particles are assumed to

be spherical and if the backscattered radiation is partially depolarized particles are assumed to be nonspherical.

We want to point out that the theory of the light scattering by spherical particles does not imply the above interpretation of backscattering data. From the diagonality of the scattering matrix for spherical particles only follows that if the depolarization of the backscattered radiation occurs then the scattering particles are not spherical. However, no change of the polarization does not imply necessarily spherical particles. The reason being that the sphericity of the scattering particles is only sufficient but not necessary condition for diagonality of the scattering matrix. Therefore, even if the state of polarization of backscattered and incoming radiation is the same particles still can be nonspherical.

Let the scattering process on an arbitrarily shaped particle in a definite orientation with regard to the scattering plane be described by the scattering matrix \mathbb{A} [Eq. (2)]. Then the scattering process on a particle that is obtained by reflecting the original one with respect to the scattering plane is described by the scattering matrix \mathbb{A}^1 given by ⁵

$$\mathbb{A}^1 = \begin{pmatrix} A_{11} & -A_{12} \\ -A_{21} & A_{22} \end{pmatrix}. \quad (4)$$

If the scattering particle has a reflectional symmetry with respect to the scattering plane (particle is identical with its mirror image with respect to the scattering plane), then the scattering matrices \mathbb{A} and \mathbb{A}^1 have to be identical which is possible only if

$$A_{12} = A_{21} = 0. \quad (5)$$

Thus the scattering matrix of an arbitrarily shaped particle possessing a reflectional symmetry with respect to the scattering plane is a diagonal matrix. Therefore, such

a particle will not cause a depolarization of an incident linearly polarized electromagnetic wave provided an electric vector of an incident wave is in the direction perpendicular or parallel to the scattering plane. There are obviously infinite numbers of possible shapes that satisfy the above condition (reflectance symmetry with respect to the scattering plane) and all of them in appropriate orientation with respect to the scattering plane do not depolarize the incoming radiation. The Fig. 1 shows few examples of such particles.

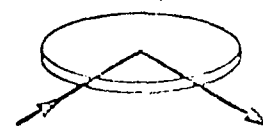
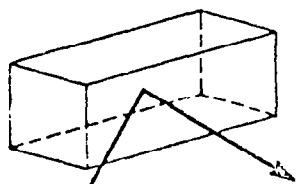
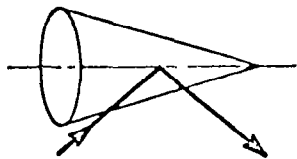
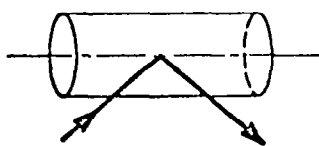
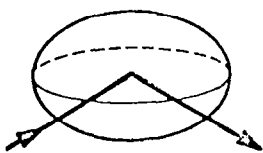
In the case of the forward and backward scattering any plane containing the incoming beam is a scattering plane. Consequently no depolarization will occur if the scattering particle has a reflectional symmetry with respect to an arbitrary plane through the direction of an incoming beam. From this follow that no depolarization in the forward or backward direction will occur if the scattering particle has a rotational symmetry with the axis of rotation oriented parallel to the direction of an incoming beam.

Thus cylinders, spheroids, cones and all other rotationally symmetric shapes (see Fig. 2 for a few examples) with rotational axis parallel to the incoming radiation will not cause the depolarization of the backscattered radiation and consequently they cannot be distinguished from spherical particles by the means of depolarization.

References

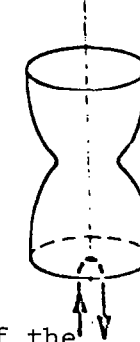
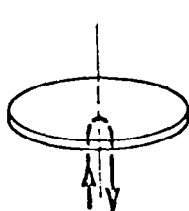
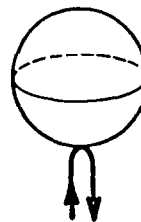
1. R.C. Boston, *J. Appl. Meteor.* 9, 717-720 (1970).
2. R.M. Schotland, K. Sassen and R. Stone, *J. Appl. Meteor.* 10, 1011-1017 (1971).
3. K.N. Liou and H. Lahore, *J. Appl. Meteor.* 13, 257-263 (1974).
4. K. Sassen, *J. Appl. Meteor.* 13, 923-933 (1974).
5. H.C. Van de Hulst, Light Scattering by Small Particles, Wiley 1957.

Figure 1



Few examples of particles causing no depolarization of an incoming linearly polarized electromagnetic plane wave with electric vector either perpendicular or parallel to the scattering plane.

Figure 2



Few examples of particles causing no depolarization of the radiation scattered into the backward direction.

SCATTERING FROM A POLYDISPERSION OF TUMBLED SPHEROIDS

David Stein and Gray Ward
Department of Physics and Astronomy
University of Florida
Gainesville, Florida

The atmospheric aerosol is modeled as a polydispersion of spheroids with index of refraction $m = m_r - i m_i$ and oversize distribution $N(r) = N_0 / [1 + (r/a)^p]^r$ to fit bistatic lidar data.

Bistatic LIDAR data can be fitted reasonably well over most of the angular range using a spherical particle model for the atmospheric aerosol [1]. However, near backscatter nonspherical particle effects are noticeable. Better fits are obtained when the atmospheric aerosol is modeled as a polydispersion of spheroids.

The phase functions for electromagnetic scattering from tumbled prolate and oblate dielectric spheroids were calculated by a perturbation technique [2,3]. The random orientation was taken into account by averaging the perturbation function over all possible orientations of the particle relative to the propagation and polarization vectors of the incident beam.

It is found that tumbled polydispersions of prolate and oblate spheroids of varying axial ratios give rise to curves of intensity and polarization versus scattering angle that differ from that from spheres. A tumbled spheroid gives a different scattering pattern than an equivalent sphere, and this difference is not eliminated by having a wide range of particle sizes. The difference is most pronounced in the angular range 160° - 180° .

References

1. Gray Ward, K.M.Cushing, R.D.McPeters, and A.E.S. Green, Applied Optics 12:11, 2585-2592 (Nov. 1973).
2. Victor A. Erma, Phys. Rev. 179:2, 1238-1246 (1969).
3. A.F. Stevenson, J. Appl. Phys. 24:9, 1134-1142 (1971).

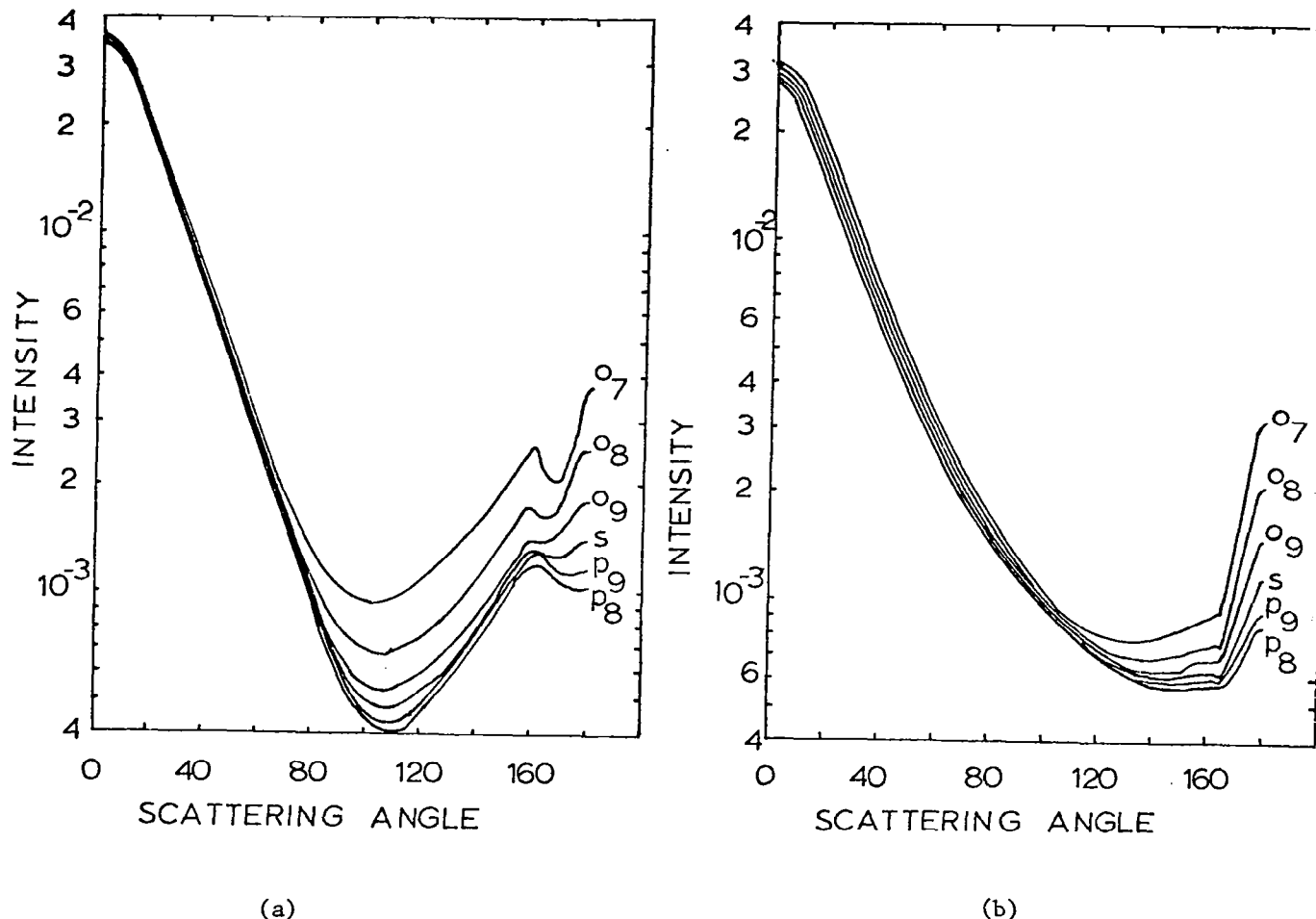


Figure 1. This is the scattered intensity polarized (a) parallel to and (b) perpendicular to the scattering plane. The incident radiation is polarized at 45° to the scattering plane. Curves are shown for oblate spheroids of axial ratios of 0.7, 0.8, and 0.9; for a sphere; and for prolate spheroids of axial ratios of 0.9 and 0.8. The particles are tumbled and averaged over a typical size distribution with $\nu=3.5$, $a = 0.05 \mu\text{m}$, and $m = 1.50-i0.005$.

ZERULL, R.H. and WEISS, K.

Bereich Extraterrestrische Physik, Ruhr-Universität Bochum, FRG.

Scattering Properties of Irregular Dielectric and Absorbing Particles

The results presented in this paper are derived from microwave analog measurements^{1,2}.

1. Irregular Dielectric Particles

As many results are published elsewhere^{1,2}, scattering properties of irregular dielectric particles are illustrated here by only one typical example. Fig. 1 includes a picture of "convex" and "concave" particles and their averaged scattering functions σ_1 and σ_2 for unpolarized incident radiation, compared to a polydisperse mixture of spheres in the same size interval $5.9 \leq a \leq 17.8$. Base for comparison is the volume of the particles. For particles with convex boundary theoretical predictions concerning the averaged geometrical cross-section and the reflected part of the radiation can be made, not so for "concave" ones (see van de Hulst³). The diffraction pattern, to the extent that it could be measured, is nearly identical for the irregular bodies and the mixture of spheres. For larger scattering angles, by contrast, the curves deviate strongly from one another. The intensity in the middle range of angles is markedly higher for irregular particles (maximally by a factor of 5), where the scattering intensity of the "concave" bodies is still clearly above that of the "convex" ones. Contrary to spheres the run of σ_1 and σ_2 is very similar for "convex" and "concave" bodies, as

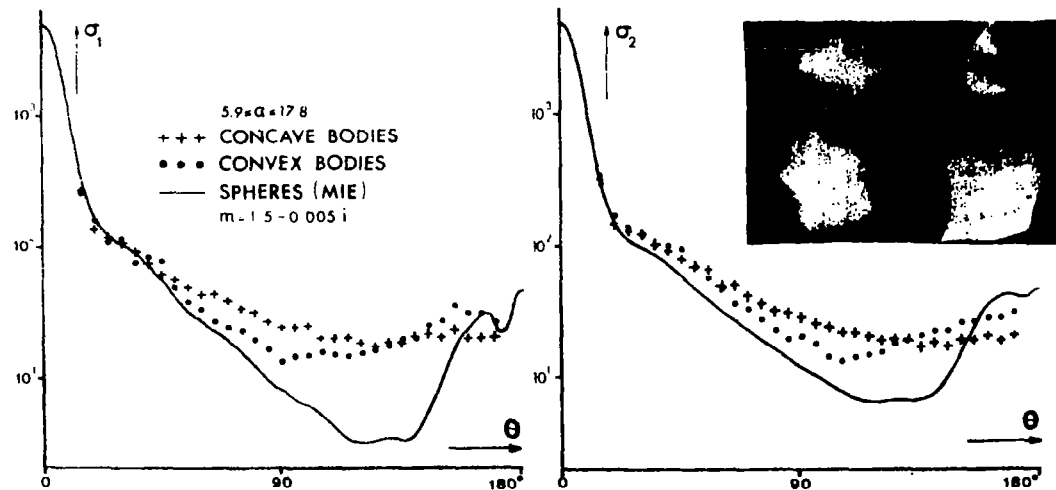


Fig. 1: Scattering functions of irregular particles via Mie-theory.

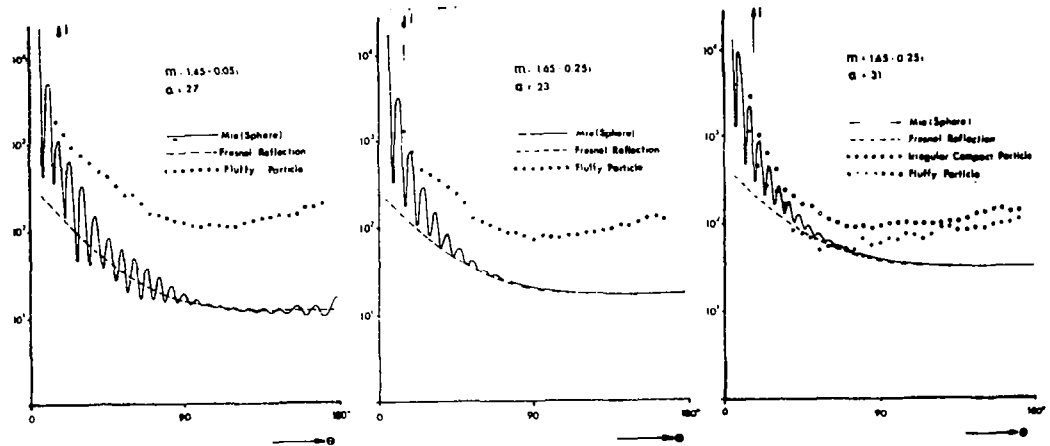


Fig. 4: Total intensity scattered by monodisperse mixtures of irregular absorbing particles

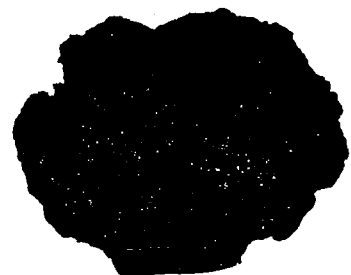
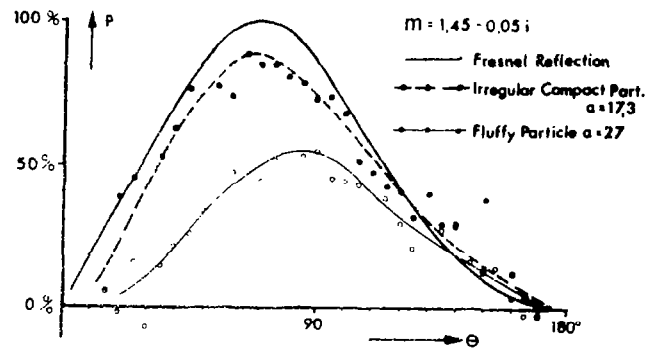


Fig.2: Typical "compact" absorbing particle

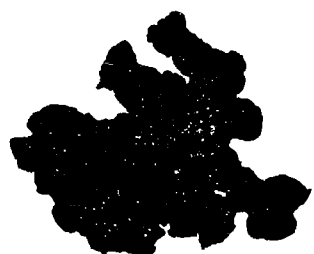
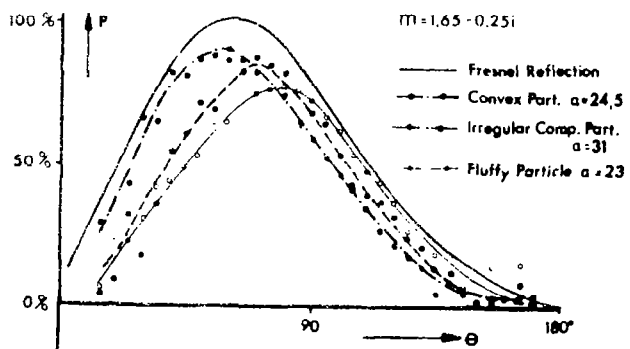


Fig. 5: Polarization by monodisperse mixtures of irregular absorbing particles

Fig.3: Typical "fluffy" absorbing particle

well. This indicates, that the polarization behaviour of the irregular particles is nearly neutral. A clear difference in the three courses can furthermore be recognized in the back-scattering region: in contrast to the strong rise of back-scattering, typical for mixtures of dielectric spheres, the "convex" bodies here exhibit only a small rise, whereas the "concave" ones scatter nearly isotropic in this range.

2. Irregular Absorbing Particles

Typical irregular absorbing particles treated in this section are shown in Fig. 2 and 3. The particle in Fig. 2 is compact, whereas the particle in Fig. 3 has a "fluffy" shape, consisting of many smaller particles in loose arrangement. The scattering results of absorbing particles are illustrated by plotting the total intensity i and the degree of linear polarization P , considering monodisperse mixtures. In Fig. 4 the total scattered intensity of 4 different mixtures of irregular absorbing particles are compared to Mie calculations and Fresnel reflection curves for spheres of equal volume.

The intensity level is increased for both refractive indices, especially vivid in the case of fluffy particles. Most striking is the further enhancement towards backscattering. This is probably due to additional external reflections of refracted rays by outstanding parts of an irregular particle, by which in particular scattering towards the medium range of angles is weakened.

As different sizes are considered in the polarization diagrams of Fig. 5, to avoid confusion the results are compared to Fresnel reflection curves only. For both grades of absorption the positive peak of polarization, which is due a distinct minimum of i_2 , is obviously flattened and shifted towards 90° by irregular particles, especially in the case of fluffy shapes.

Literature

- 1) R.H. Zerull, Mikrowellenanalogieexperimente zur Lichtstreuung an Staubpartikeln, Bundesminister für Forschung und Technologie FB-W 73-18 (1973)
- 2) R.H. Zerull and R.H. Giese, in Planets, Stars, and Nebulae studied with Photopolarimetry, p. 901 University of Arizona Press, Tucson (1974)
- 3) H.C. van de Hulst, Light scattering by small particles, John Wiley, New York (1957)

Comparison of Extinction and Backscattering Coefficients for Measured And Analytic Stratospheric Aerosol Size Distributions, Thomas J. Swissler, Systems and Applied Sciences, Riverdale, MD 20840; and, Franklin S. Harris, Jr., Old Dominion University, Norfolk, VA 23508

Using several measured and modeled size distributions for stratospheric aerosols in the 18-20 km layer, extinction and backscattering coefficients were computed for several wavelengths and refractive indexes.

OPTICAL PROPERTIES OF CORE-MANTLE PARTICLES

G. Scheweim

(Ruhr-Universitäts Bochum, Bereich Extraterrestrische Physik, F.R.G.)

According to the scattering theory by Gütter, Aden and Kerker [1,2] the intensity of radiation of wavelength λ scattered by a spherical particle is given by

$$I = I_0 \frac{\lambda^2}{4\pi^2} \left(\frac{i_1 + i_2}{2} \right)$$

where i_1 and i_2 are proportional to the electric field components polarized vertical and parallel to the direction of observation. I_0 is the intensity of the incident light.

i_1 and i_2 are defined as

$$i_1 = |s_1|^2 = \sum_{n=1}^{\infty} \frac{2n+1}{n(n+1)} [a_n \pi_n + b_n \tau_n]^2$$

$$i_2 = |s_2|^2 = \sum_{n=1}^{\infty} \frac{2n+1}{n(n+1)} [a_n \tau_n + b_n \pi_n]^2$$

The amplitude function a_n and b_n are complex numbers and are functions of the wavelength λ , the size parameter v of the particle and the complex refractive index:

$$a_n = \frac{[\psi\psi]_{n,\alpha}^{\prime} \cdot [\chi\psi]_{n,v}^{\prime} - [\chi\psi]_{n,\alpha}^{\prime} \cdot [\psi\psi]_{n,v}^{\prime}}{[\psi\psi]_{n,\alpha}^{\prime} \cdot [\chi\zeta]_{n,v}^{\prime} - [\chi\psi]_{n,\alpha}^{\prime} \cdot [\psi\zeta]_{n,v}^{\prime}}$$

$$b_n = \frac{[\psi\psi]_{n,\alpha}^{\prime\prime} \cdot [\chi\psi]_{n,v}^{\prime\prime} - [\chi\psi]_{n,\alpha}^{\prime\prime} \cdot [\psi\psi]_{n,v}^{\prime\prime}}{[\psi\psi]_{n,\alpha}^{\prime\prime} \cdot [\chi\psi]_{n,v}^{\prime\prime} - [\chi\psi]_{n,\alpha}^{\prime\prime} \cdot [\psi\zeta]_{n,v}^{\prime\prime}}$$

where the brackets stand for products and sums of the Riccati-Bessel functions [3].

The efficiency factors for extinction, scattering and absorption can be derived, analogous to the case of a homogeneous spherical particle

$$Q_{ext} = \frac{2}{\nu^2} \sum_{n=1}^{\infty} (2n+1) \operatorname{Re} (a_n + b_n)$$

$$Q_{sca} = \frac{2}{\nu^2} \sum_{n=1}^{\infty} (2n+1) (|a_n|^2 + |b_n|^2)$$

$$Q_{abs} = Q_{ext} - Q_{sca}$$

The scattering functions were calculated using a modified recursion for the Riccati-Bessel functions based on Miller [4]. A detailed description of the computer program can be found in Giese, Schwehm, Zerull [5].

Calculated Scattering Functions

With the above mentioned computer program the following scattering functions for single-particles were calculated.

m_{core}	m_{mantle}	α	ν	Material
a) 1.27-1.37i	1.33	10	10.5(0.5)25	iron-ice ($\lambda \sim 440 \mu\text{m}$)
b) 2.46-1.45i	1.33-0.06i	5	5.5(0.5)10	graphite-ice ($\lambda \sim 440 \mu\text{m}$)
c) 1.48-2.36i	1.33-0.06i	5	5.5(0.5)10	graphite-ice
d) 1.27-1.37i	1.5	5(0.2)14.8	15	iron-silicate
e) 1.5	1.5-0.1i	5(0.1)19.9	20	
f) 1.27-1.37i	1.7	5(0.2)14.8	15	iron

m_{core} = refractive index core

m_{mantle} = refractive index mantle

α = size parameter core = $\frac{\text{radius}}{\text{circumference}}$

ν = size parameter mantle

As for the application the scattering of polydisperse mixtures of particles is of much more interest, a variety of models with different size distributions and parameters have been investigated.

A polydisperse mixture of particles is a sample of many single particles with the same refractive index, but different radii. The averaged scattering functions σ_1 , σ_2 of a mixture

of particles with size parameters $v_1 \leq v \leq v_2$ and the size distribution law

$$n(v) \cdot dv = \text{const} \cdot f(v) \cdot dv$$

is defined as

$$\sigma_j = \frac{\int_{v_1}^{v_2} i_j(v, \theta) \cdot f(v) \cdot dv}{\int_{v_1}^{v_2} f(v) \cdot dv}; \quad j = 1, 2.$$

where the indices $j = 1, 2$ denote the perpendicular and parallel polarized radiation. $n(v)$ is the number of particles per volume, of which the size parameters are in the interval dv around v , and $f(v)$ is the size distribution functions.

Calculated Scattering Functions of Mixtures of Particles

Interval of size parameters $v_1 \div v_2$	Refractive Indices m_{core}	m_{mantle}	$1/q$
1 1.0 \div 10.0	1.5	1.5-0.1i	1.01(0.01) 1.1(0.05) 1.8(0.2) 4
2 10.0 \div 60.0	1.5	1.5-0.1i	1.01 \div 6
3 10.0 \div 60.0	1.27-1.37i	1.5	1.01 \div 4
4 10.0 \div 60.0	2.456-1.421	1.33	1.2 \div 4

$1/q$ = ratio of size parameter core to size parameter mantle

The numbers in brackets show the stepwidth with which the parameters have been varied. An example of the dependence of the scattering of mixtures of particles on the ratio of particle radius to core radius is given in Fig. 1.

For small particles ($v \leq 1$) the scattering function and the polarization is for all models of particle similar to Rayleigh-scattering. In the region $1 < v < 2$ the polarization strongly depends on the inner structure of the particle, i.e. whether the core is absorbing or dielectric or whether the mantle is absorbing.

For particles in the region $4 < v < 40$ we get for all calculated models the same dependence on the ratio q . If $q \leq 0.2$ the optical properties of the core-mantle particle are totally

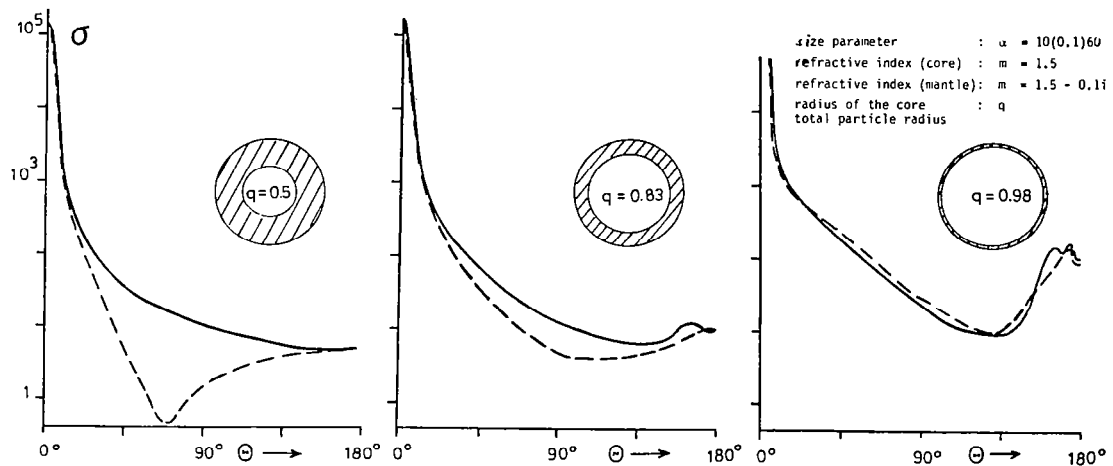


fig. 1: Light scattering functions of mantle-core particles

defined by the material of the mantle. These results agree with the results given by Fenn and Oser [6] which were derived for a different model.

Recently we calculated the efficiency factors for extinction, scattering and absorption taking into account the wavelength dependence of the refractive index of the particle material and integrating over the whole spectrum of a given radiation source, e.g.

$$\bar{Q}_a = \int Q_{\text{abs}}(\lambda) F_{\odot} \lambda d\lambda$$

where we found the expected result, that the absorption efficiency and consequently the temperature of particle is even much more affected by the composition than the scattering function.

- [1] Güttsler, A., 1952: Ann. Phys. 11, 65
- [2] Aden, A.L. and Kerker, M., 1951: J.Appl.Phys.22, 601
- [3] Kerker, M., 1969: The Scattering of Light and other Electromagnetic Radiation, Academic Press, New York
- [4] Miller, C., 1949: BAAS, Bessel-Functions-Part II, Cambridge U.P., Cambridge, 10, p. XVII
- [5] Giese, R.H.; Schwehm, G. and Zerull, R., 1974: Grundlagenuntersuchungen zur Interpretation extraterrestrischer Zodiakallichtmessungen und Lichtstreuung von Staubpartikeln verschiedener Formen, BMFT-Forschungsbericht W 74-10
- [6] Fenn, R.W. and Oser, H., 1965: Appl.Optics 4, 1504

SCATTERING BY TENUOUS AEROSOLS

by

Charles Acquista*
 NASA Wallops Flight Center
 Wallops Island, VA 23337

When confronted with situations in which aerosol scattering is significant, it is common practice to treat the scatterers as if they were spheres in order to apply the results of Mie theory. However, recent experiments¹ on the scattering properties of real aerosols show that they behave quite differently from spheres. Since a large class of atmospheric aerosols can be considered to be tenuous (i.e., interact weakly with the incoming radiation), it is reasonable to use a perturbation scheme to model their scattering properties.

Shifrin² derived an integrodifferential equation for the effective electric field when an arbitrarily shaped particle is illuminated by the plane wave $E_0 \exp(ik \cdot r)$:

$$E_{\text{eff}}(r) = E_0 e^{ik \cdot r} + \alpha(k^2 + \text{grad div}) \int U(r') E_{\text{eff}}(r') \cdot \\ \cdot G(r, r') d^3 r' + \frac{4}{3} \pi \alpha U(r) E_{\text{eff}}(r).$$

Here α is the polarizability

$$\alpha = \frac{3(m^2 - 1)}{4\pi(m^2 + 2)} ,$$

G is the Green's function of the Helmholtz equation

$$G(x, y) = \frac{\exp(ik|x-y|)}{4\pi|x-y|} ,$$

and U is a scattering potential defined by

$$\begin{aligned} U(r) &= 1 \text{ if } r \text{ is inside the scatterer} \\ &= 0 \text{ if } r \text{ is outside the scatterer.} \end{aligned}$$

The integrodifferential equation can be changed into a pure integral equation by applying a Fourier transform, using the convolution theorem, and then inverting the transform. The end result is

$$\begin{aligned} \mathbf{E}_{\text{eff}}(\mathbf{r}) &= \mathbf{E}_0 e^{i\mathbf{k} \cdot \mathbf{r}} + \frac{\alpha}{(2\pi)^6} \iint e^{i\mathbf{p} \cdot \mathbf{r}} g(\mathbf{p}) \mathbf{u}(\mathbf{p}') \cdot \\ &\quad \cdot \left[k^2 \mathbf{e}_{\text{eff}}(\mathbf{p}-\mathbf{p}') - \mathbf{p} (\mathbf{p} \cdot \mathbf{e}_{\text{eff}}(\mathbf{p}-\mathbf{p}')) \right] d^3p d^3p', \end{aligned}$$

where g , u and \mathbf{e}_{eff} are the Fourier transforms of G , U and \mathbf{E}_{eff} . Constructing a power series for \mathbf{E}_{eff} in terms of the small parameter α , we solve this equation by the method of successive iterations. In the first iteration we obtain

$$\mathbf{E}_{\text{scat}}^{(1)}(\mathbf{r}) = \frac{\alpha k^2}{r} e^{i\mathbf{k} \cdot \mathbf{r}} \mathbf{E}_{0\perp} \mathbf{u}(\hat{\mathbf{k}} - \mathbf{k}),$$

for the effective scattered field far from the scatterer. Here $\hat{\mathbf{k}}$ is the wave vector for the scattered radiation, and $\mathbf{E}_{0\perp}$ is the component of \mathbf{E}_0 perpendicular to $\hat{\mathbf{k}}$. When u is computed for spheres, disks and ellipsoids, we find that $\mathbf{E}_{\text{scat}}^{(1)}$ is identical to the Rayleigh-Gans approximation.

In the second iteration, we find

$$\begin{aligned} \mathbf{E}_{\text{scat}}^{(2)}(\mathbf{r}) &= \mathbf{E}_{\text{scat}}^{(1)}(\mathbf{r}) + \frac{\alpha^2 k^2}{2\pi^2} \frac{e^{i\mathbf{k} \cdot \mathbf{r}}}{r} \int \frac{u(\mathbf{q} + \hat{\mathbf{k}}) \mathbf{u}(\mathbf{q} + \mathbf{k})}{\mathbf{q}^2 - \mathbf{k}^2} \cdot \\ &\quad \cdot \left\{ \left(\frac{2}{3} \mathbf{k}^2 + \frac{1}{3} \mathbf{q}^2 \right) \mathbf{E}_{0\perp} - (\mathbf{q} \cdot \mathbf{E}_0) \mathbf{q}_\perp \right\} d^3q. \end{aligned}$$

These approximations for the scattered field can be evaluated for arbitrarily shaped and oriented particles. In fact, the transform of the scattering potential, u , is the sole carrier of information about the scatterer. Since u is readily obtainable for particles of different shapes (disks, cylinders, ellipsoids, rectangular solids, etc.), we can use these approximations to model experiments on the scattering properties of real aerosols. In particular, several features of the polar nephelometer experiments of Holland and Gagne¹ can be explained with this theory. In the nephelometer experiment, a beam of partially polarized light illuminates a gas jet carrying particles of a known size and composition. The Stokes parameters of the scattered light are measured at different scattering angles in order to determine the scattering matrix, S_{ij} . (This matrix relates the Stokes parameters of the incident and scattered radiation.³) The elements of the scattering matrix can be obtained theoretically from the scattered field. For example, using the second iteration, we obtain

$$\begin{aligned}
 S_{11} &= k^2 r^2 \frac{I_{\text{scat}}}{I_0} \\
 &= \alpha^2 k^6 u^2 (\hat{k} \cdot \hat{r}) \left(\frac{1 + \cos^2 \beta}{2} \right) + \frac{\alpha^3 k^6}{\pi^2} u (\hat{k} \cdot \hat{r}) \cdot \left\{ (2k^2 + q^2) \left(\frac{1 + \cos^2 \beta}{6} \right) - \right. \\
 &\quad \left. \cdot \int \frac{u(q + \hat{k}) u(q + \hat{r})}{q^2 - k^2} \cdot \left\{ (2k^2 + q^2) \left(\frac{1 + \cos^2 \beta}{6} \right) - \right. \right. \\
 &\quad \left. \left. - \frac{q^2}{2} \sin^2 \theta (1 - \cos^2 \phi \sin^2 \beta) + \frac{q^2}{8} \sin 2\theta \sin 2\beta \cos \phi \right\} d^3 q. \right.
 \end{aligned}$$

Even when very simple models are used for the scatterers, (e.g., monodisperse randomly oriented thin disks), we find that this theory gives much closer agreement to the experiment than Mie theory (for spherical scatterers).

References

*This work was performed while the author held an NRC-NASA Resident Research Associateship.

1. A. C. Holland and G. Gagne, Appl. Optics 9, 1113, (1970).
2. K. S. Shifrin, "Scattering of Light in a Turbid Medium," Moscow: 1951 (NASA Technical Translation TT F-477, 1968).
3. H. C. van de Hulst, "Light Scattering by Small Particles," New York: 1957.

OPTICAL CONSTANTS FOR A METEORIC DUST AEROSOL MODEL

E. P. Shettle and F. E. Volz

Atmospheric Optics Branch, Air Force Geophysics Laboratory
L. G. Hanscom AFB, Bedford, MA 01731

INTRODUCTION: The major component of the upper atmospheric aerosols is generally considered to be meteoric dust, e.g. see Newkirk and Eddy (1964) or Rosen (1969). Meteoric or cometary dust also form some of the layers occasionally observed in the upper atmosphere. Poultney (1972 & 1974) has related the Lidar observations (through 1970) of layers in the upper atmosphere to either cometary sources of micrometeoroid showers or noctilucent cloud observations. Divari et al. (1973) have related observations of increased brightness of the twilight sky to the Orionid meteor shower. To determine the scattering and absorption properties of the aerosol it is necessary to know their size distribution and refractive index.

REFRACTIVE INDEX: The reflectance R of a material is related to its refractive index through Fresnel's equation for normally incident light:

$$R = \frac{(n-1)^2 + k^2}{(n+1)^2 + k^2} \quad (1)$$

where n and k are respectively the real and imaginary parts of the refractive index. Using classical dispersion and representing each reflection feature by a damped harmonic oscillator the complex index of refraction can be written (see Spitzer and Kleinman, 1961; or Lipson and Lipson, 1969).

$$n^2 - k^2 = A_0 + \sum_j \frac{2 A_j (\nu_j^2 - \nu^2)}{(\nu_j^2 - \nu^2)^2 + \gamma_j^2 \nu^2} \quad (2a)$$

$$nk = \sum_j \frac{A_j \gamma_j \nu}{(\nu_j^2 - \nu^2)^2 + \gamma_j^2 \nu^2} \quad (2b)$$

Where ν_j is the frequency of the j th oscillator, A_j is the oscillator strength, and γ_j is the damping constant or band width. Solving the pair of equations (2a) and (2b) and substituting into Eq. (1) R can be expressed in terms of the oscillator parameters.

The reflectance was measured for a mixture chondrite dust (which represents the major type of meteorite incident on the earth), using procedures described elsewhere (Volz, 1972 and 1973). The measurements covered the spectral region 2.5 to 40 microns (250 to 4000 cm^{-1}). A 9 oscillator model was fitted

to these measurements, using a nonlinear least-squares optimization of equations (1) and (2) with resulting parameters as in Table 1.

Table 1

DISPERSION PARAMETERS FOR METEORIC DUST

j	A_j	ν_j (cm^{-1})	γ_j (cm^{-1})
0	1.5154	-	-
1	37,041.	150.	100.
2	29,309.	337.5	84.97
3	27,417.	405.4	58.47
4	50,014.	511.5	83.97
5	8,375.	611.2	39.36
6	6,029.	730.3	71.14
7	80,913.	882.2	94.17
8	69,390.	995.5	166.6
9	991,307.	2,313.6	2,321.

Oscillator No. 1 with ν_1 and γ_1 held fixed at 150 and 100 during the least-squares procedure, was introduced in an attempt to correctly model the properties near 40 microns where they are poorly constrained by the limited measurements.

METEORIC DUST AEROSOL MODEL

The size distribution to represent the meteoric dust aerosols is similar in shape to a model developed by Farlow & Ferry (1972), with two important differences. First, the present model has proportionately more smaller particles and second, the number densities for all size ranges are several orders of magnitude larger than in Farlow & Ferry's model. These differences are consistent with rocket observations in the upper atmosphere (e.g. see Soberman & Hemenway, 1965; Farlow & Ferry, 1972; the summary of rocket data by Lindblad et al., 1973). This size distribution is represented by a log normal size distribution with $r_o = 0.03$ micron and $\sigma = 0.5$.

The normalized attenuation coefficients shown in Figure 1 are based on Mie theory calculations using this size distribution and the meteoric dust refractive index data. The refractive index for wavelengths less than 2.5 microns is based on an extrapolation of the dispersion equation using the parameters in Table 1. The Reflectance measurements are currently being extended into the visible.

The normalization of the attenuation was chosen to simplify comparisons with other aerosol models which have been developed at AFGL (Shettle & Fenn, 1976). Typical values for the extinction coefficient at 0.55 microns range from

$\sim 10^{-5}$ km $^{-1}$ near 40 km to $\sim 10^{-9}$ at 100 km, with uncertainties of a factor of 10.

Layers in the upper atmosphere have been observed (Poultney, 1972 & 1974) where the extinction coefficients are none than 2 orders of magnitude greater than the typical values indicated above.

REFERENCES

Divari, N. B., Yu. I. Zaginailo, and L. V. Koval'chuk (1973): "Meteoric Dust in the Upper Atmosphere;" Solar System Res., 7, 191-196. (Translated from Astronomicheskii Vestnik 7, 223-230).

Farlow, N. H. & G. V. Ferry (1972): "Cosmic Dust in the Mesosphere;" Space Res., 12, 369-380.

Lindblad, B. A., G. Arinder and T. Wiesel (1973): "Continued Rocket Observations of Micrometeorites;" Space Res., 13, 1113-1120.

Lipson, S. G. & H. Lipson (1969): Optical Physics, pp. 308-310, Cambridge University Press.

Newkirk, Jr., G. & J. A. Eddy (1964): "Light Scattering by Particles in the Upper Atmosphere;" J. Atmos. Sci., 21, 35-60.

Poultney, S. K. (1972): "Laser Radar Studies of Upper Atmosphere Dust Layers and the Relation of Temporary Increases in Dust to Cometary Micrometeoroid Streams;" Space Research, 12, 403-421.

Poultney, S. K. (1974): "Times Locations and Significance of Cometary Micrometeoroid Influxes in the Earth's Atmosphere;" Space Res., 14, 707-708.

Rosen, J. M. (1969): "Stratospheric Dust and its Relationship to the Meteoric Influx;" Space Sci. Rev., 9, 58-89.

Shettle, E. P. & R. W. Fenn (1976): "Models of the Atmospheric Aerosols and their Optical Properties" in AGARD Conference Proceedings 183, Optical Propagation in the Atmosphere, Lyngby, Denmark, 27-31 October 1975.

Soberman, R. K. & C. L. Hemenway (1965): "Meteoric Dust in the Upper Atmosphere;" J. Geophys. Res., 70, 4943-4949.

Volz, Frederic E. (1972)b: "Infrared Refractive Index of Atmospheric Aerosol Substance," Appl. Opt., 11, 755-759.

Volz, Frederic E. (1973): "Infrared Optical Constants of Ammonium Sulfate, Sahara Dust, Volcanic Pumice, and Flyash," Appl. Opt., 12, 564-568.

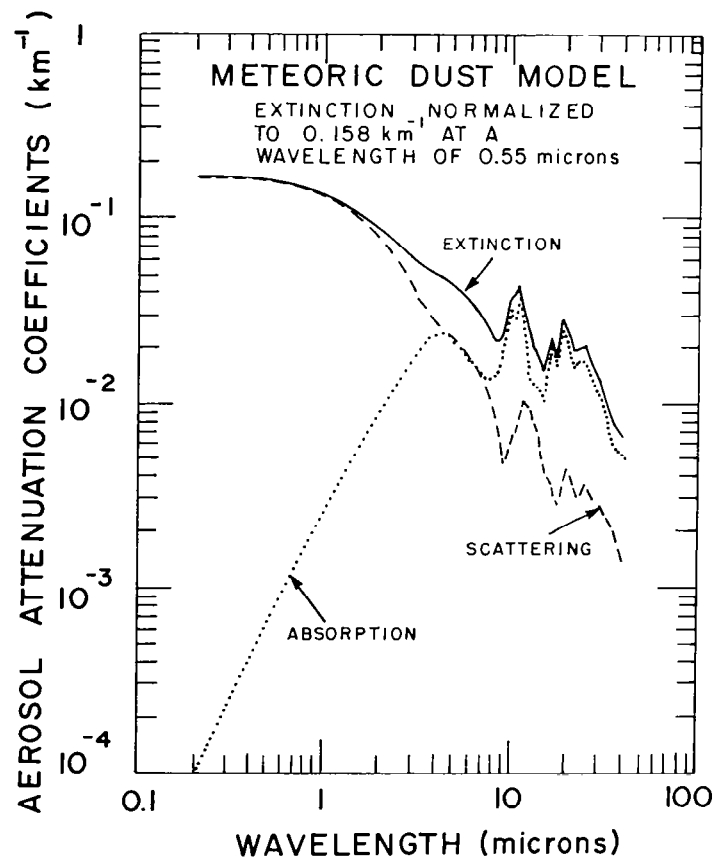


FIGURE 1

PERFORMANCE OF DIFFERENTIAL-SCATTER
(DISC) LIDAR SYSTEMS

M.L. Wright and G. Johnson
Stanford Research Institute
Menlo Park, California 94025

ABSTRACT

A remote-sensing system capable of determining the chemical composition of atmospheric aerosols would be desirable for reducing the cost of long-term measurements, especially in the stratosphere, and for avoiding some of the difficulties encountered in aerosol sampling systems. A differential-scatter (DISC) lidar system uses characteristic differences in the infrared backscatter spectra of aerosols to identify the chemical composition of the aerosol. Recent studies of backscatter spectra for stratospheric aerosols have shown that substantial amplitude variations occur over relatively narrow wavelength ranges (Ref. 1). Figure 1 shows typical backscatter spectra for several different stratospheric aerosols. This differential backscatter is the mechanism by which a DISC lidar system determines the composition of stratospheric aerosols.

Backscattered signals received by an actual DISC lidar system are affected not only by the differential aerosol backscatter but also by the gaseous attenuation of the atmosphere and by changes in the lidar system. The selection of lidar system parameters to provide optimum performance for measurements on a specific aerosol must take into account

all of these factors. The use of the computer with the Modular Atmospheric Propagation Program (MAPP) to select these parameters is described for applications to stratospheric aerosol measurements. Initial calculations indicate that a portion of the H_2SO_4 concentration range of stratospheric aerosols can be measured by the DISC technique.

Multiple operating wavelengths are necessary in order to discriminate among the backscatter spectra produced by the various constituents in a stratospheric aerosol. The optimum number of wavelengths and the optimum location for each of these wavelengths is dependent on the characteristics of the actual lidar system, the atmosphere through which the optical signals must propagate, and the expected range of variation in constituents in the stratospheric aerosol. Present work primarily concerns a ground-based CO_2 lidar system. For this system, the optimum number of wavelengths and their locations were determined for a variety of stratospheric aerosol models representing a range of different constituents and different constituent concentrations. This selection process is treated as a pattern recognition problem because the system makes decisions among various stratospheric aerosol models by choosing the model backscatter spectrum that best fits the observed experimental data.

The theoretical basis for the DISC system and a description of the line-selection process were described earlier (Refs. 2 and 3) and will be reviewed briefly. This paper concentrates on the level of system performance that would be obtained in DISC system measurements. Several performance measures are considered, and an example of the system performance that can be expected is presented.

DISC lidar systems are useful for various aerosol measurements in both the stratosphere and troposphere. For example, the DISC technique could be used for measuring the sulfuric acid content of

aerosols emitted by power plants, refineries, and automobile catalytic converters. If time permits, a brief presentation will be given for these and other applications of the DISC technique.

REFERENCES

1. D.S. Colburn and J.B. Pollack, "Infrared Backscatter Spectra for Differentiation of Stratospheric Aerosol Composition," presented at the Seventh International Laser Radar Conference, Stanford Research Institute, Menlo Park, California, November 4-7, 1975.
2. M.L. Wright, J.B. Pollack and D.S. Colburn, "DISC--A Technique for Remote Analysis of Aerosols by Differential Scatter," presented at the Seventh International Laser Radar Conference, Stanford Research Institute, Menlo Park, California, November 4-7, 1975.
3. M.L. Wright, J.B. Pollack, and D.S. Colburn, "Remote Analysis of Aerosols by Differential Scatter (DISC) Lidar Systems," presented at the Eighth Materials Research Symposium, National Bureau of Standards, Gaithersburg, Maryland, September 20-24, 1976.

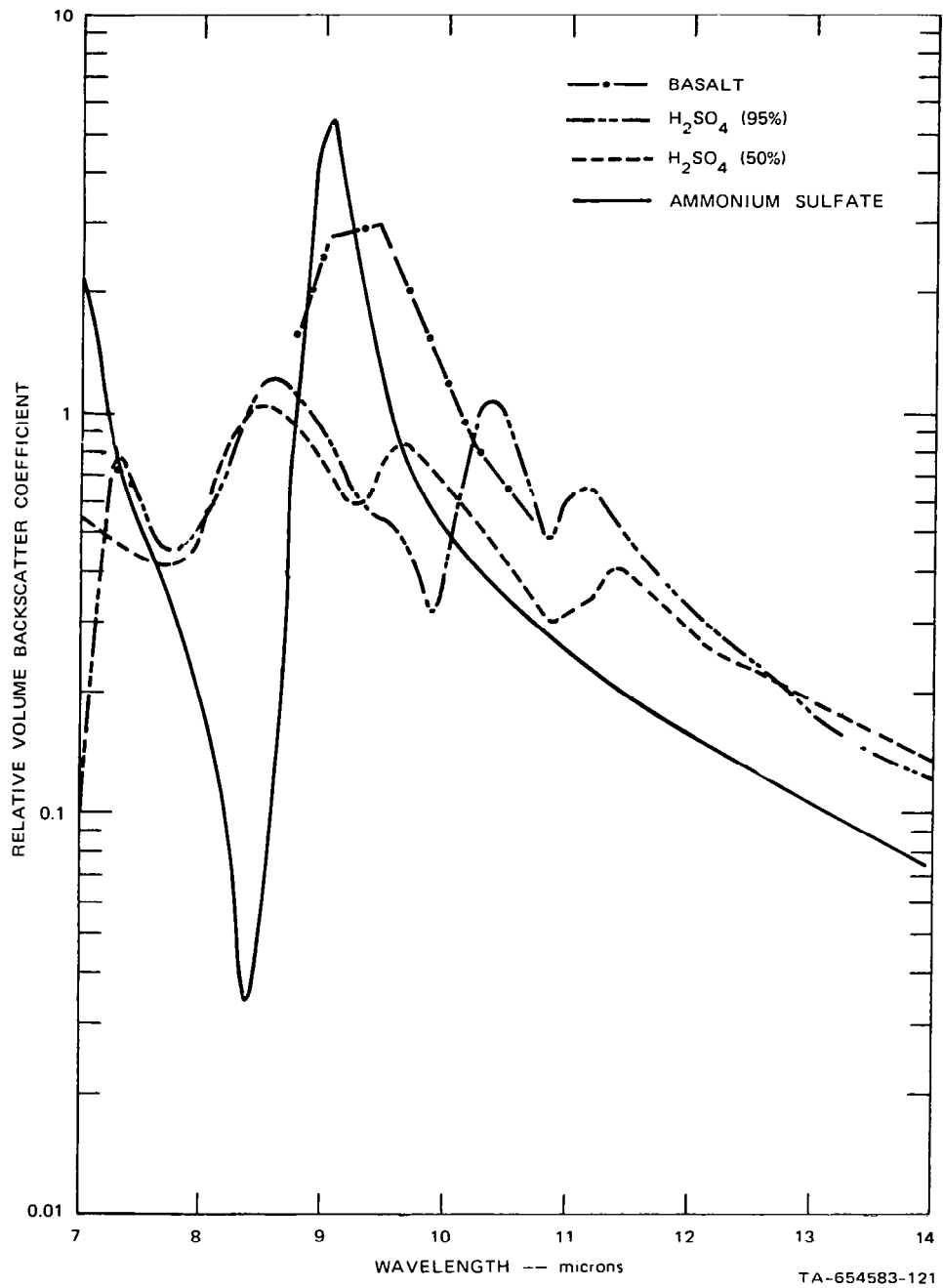


FIGURE 1 RELATIVE BACKSCATTER FOR SEVERAL ATMOSPHERIC AEROSOLS

Aerosol Measurement Methods
by
Dale A. Lundgren
Environmental Engineering Sciences Department
University of Florida
Gainesville, Florida 32611

Fine particle measurement has been an important discipline to many areas of science and industry, and the topic of many excellent books. Articles on the techniques and importance of particle size distribution measurements date back to about 1900. Industries such as paint pigment manufacturers and flour millers have been affected by particle size distribution since their beginnings.

Particle size distribution can be measured in a powder or an aerosol. Measurement in an aerosol differs from that in a powder in several ways and for several reasons. Powders consist of relatively large particles (normally 1 to 1000 μm diameter) with large quantities of material available for the particle size measurement (1 gram or greater quantities). Aerosols, however, involve much smaller particles covering a wider size range (0.001 to 100 μm diameter) with much smaller quantities of particulate mass available for an analysis (often 1 milligram or less).

Measurement of the particle size distribution of an aerosol by instrumental techniques is the topic area of this discussion which is intended as an overview for those who use or anticipate using commercially available instrumentation to study, measure, monitor, or analyze particle size distribution or size fractionated samples of an aerosol. Four specific techniques, based upon the inertial, optical, electric mobility, and diffusional properties of gas borne particles, are covered:

- 1) Inertial classification (including centrifuges, cyclones, and inertial impactors)
- 2) Light-scattering particle counters (single-particle optical counters)
- 3) Electric aerosol analyzers (electric mobility analyzers)
- 4) Condensation nuclei counters - diffusion batteries (combined for size analysis)

These four techniques are essentially the only methods a researcher has to study the particle size dependent properties of an aerosol such as formation, condensation/evaporation, or coagulation. As such, they form the basis for discussion.

Sieving, sedimentation, elutriation, simple air classification and some air permeability and surface area techniques used for

size measurement of powders are not directly applicable to aerosol measurement and are excluded from discussion here. These methods of size classification are discussed in books by R.D. Cadle (1955), C. Orr and J.M. Dallavalle (1959), G. Herdan (1960), L. Silverman, C.E. Billings and M.W. First (1971), T.T. Mercer (1973), R. Dennis (1976) and others.

Microscopy, both light and electron, is equally useful in the measurement of both powders and aerosols and is very basic to the calibration of other measurement techniques and to the description of particle shape. No measurement instrument is more important, useful or versatile than the light microscope. Similar comments can be made about the relatively complicated electron microscope and scanning electron microscope (SEM). Microscopy is not discussed although a basic knowledge of microscopy and an understanding of its uses and limitations is assumed. Several of the books referred to above consider microscopy and there are several specific texts on the subject. These works also discuss the techniques and problems of aerosol sampling and sample preparation for viewing.

Inertial Classification

Inertial classification devices separate particles out from a gas stream and do not, by themselves, measure aerosol concentration or size distribution. This means that gas borne particles are fractionated, or removed from a gas stream, in an aerodynamic size dependent manner for subsequent analysis of the known size particulate fraction. Size fractionated samples containing many particles are obtained in this manner, with the analysis being done on the gross sample and not normally on single particles.

Aerodynamic diameter classification devices include gravitational sedimentation chambers, air elutriators, aerosol centrifuges, cyclones and inertial impactors. Sedimentation chambers and air elutriators are frequently used for size-fractionation of aerosolized powders or dusts but not often for ambient concentration aerosol sampling.

Centrifuges

Aerosol centrifuges are mechanical devices which involve a rapidly spinning body through which an aerosol sample is flowing at a constant controlled rate. They are capable of size-separating smaller particles because a very high centrifugal force can be applied to the particles of interest. High rotational speed centrifuges work best in the general size range from about 0.1 to 1.0 μm (aerodynamic) diameter. Classification is also accomplished in similar air centrifuges with much higher flowrates, used by various industries to coarse fractionate powders in the 5 to 50 μm size range; these devices are not used for normal

aerosol concentrations.

Cyclones

Cyclones are similar to centrifuges in that they rely upon centrifugal force for particle separation. Cyclones, however, are simpler mechanical devices which rely upon a rapidly spinning air stream inside a fixed housing for the separation force, as opposed to the mechanically complicated rapidly spinning body of a centrifuge. Particle size classification is not as clear (or sharp) in an air sampling cyclone, with an optimum particle size classification range of from 3 to 30 μm (aerodynamic) diameter. Cyclones are especially useful as pre-collectors for other aerosol size measurement devices.

Inertial Impactors

Several impaction stages connected in series are normally referred to as cascade impactors. These impactors are intermediate between cyclones and centrifuges in both mechanical complexity and particle size classification, being optimally suited to the 0.5 to 5 μm (aerodynamic) diameter size range. Through the use of very small dimensions and very high gas velocities, the lower size limit can be decreased to perhaps 0.2 μm ; conversely, through the use of very large dimensions, low velocities and high gas flowrates, the upper size limit can be increased to perhaps 50 μm . If it were not for operational problems, cascade impactors could be ideal classification devices because theoretically they can cover a very broad particle size range.

Aerosol centrifuges, cyclones and inertial impactors are all devices which collect out (or remove) gas borne particles in a size dependent manner. These samples of particulate matter are then available for subsequent chemical or physical analyses. In general, these devices are not aerosol monitors and are not intended for in situ particle size distribution measurement. One technique to automate the readout of these devices involves the use of piezoelectric crystal sensors. B.Y.H. Liu's book (1976) as well as the works referenced earlier discuss the uses and limitations of these inertial classification devices.

Light Scattering Particle Counters

Single particle optical counters provide a very different or supplementary method of aerosol measurement. These are in situ particle size distribution monitors which do not collect out an aerosol sample, except subsequent to the measurement. The basic measurement parameter is the amount of light scattered by a particle. This particle is then assigned an "optical" size which is equal to the actual size of a spherical calibration particle which scatters an equal amount of light (as measured by

the instrument photosensitive detector).

All commercial light scattering particle counters have the same principle of operation. Each assumes that μm size particles flow single file, in a narrow beam, through a constant density light beam and scatter off a fraction of the light in a known, reproducible manner. Mie theory allows light scattering calculations for certain types of particles; therefore, the response or performance of an optical particle counter is predictable. A known fraction of the scattered light is collected and measured through a system of mirrors or lenses by a light sensitive device, usually a photomultiplier tube. The number and height of these pulses is electronically converted to a particle number and particle size. Combined with a known and controlled air flow-rate this data easily converts to a particle concentration and size distribution. This above principle of operation was first described about 25 years ago with several corporations now manufacturing devices.

There are certain problems commonly associated with all optical particle counters, namely: light source stability, lens system distortion, imperfect particle size resolution, improper particle counting, optical system contamination causing noise, multi-valued light scattering vs. particle size response, light scattering dependence upon index of refraction, multi-particle scattering causing coincidence errors, particle size dependent sampling losses and poor unit to unit reproducibility. Optical particle counters are, however, frequently used to detect and measure gas borne particles because the instrumental technique is rapid, continuous, non-destructive, and can be easily automated. This benefit of real time measurement of particle size distribution can outweigh the method limitations.

Although optical counters have been primarily used in clean environments, they can be adapted to fairly dirty environments. Again, there is an optimum particle size range for these devices; most operate best for particles between 0.5 and 5.0 μm diameter. Other models or modifications work well over either a slightly lower or higher size range with no theoretical upper limit, and a lower limit of perhaps 0.1 μm for the most sophisticated laboratory units. This class of counters fulfills a very important function in the aerosol measurement field for the in situ monitoring of number concentration in a preselected size interval or intervals. Real time response and the lack of a directly competitive method make the optical sensors extremely valuable and the topic of numerous papers in this meeting. Further information is contained in the books referred to earlier and listed in the bibliography.

Electrical Aerosol Analyzer

The electrical aerosol analyzer is a device especially suited to the in situ measurement of particle size distribution below the range of the optical counter. Size separation is obtained because the electric mobility of a gas borne particle in an electric field is a function of particle size. This device collects the aerosol during measurement, but is not just an aerosol sampler. Rather, it is a rapid response (several minutes), aerosol size distribution monitor with good size measurement capability over the general 0.01 to 0.5 μm (electrical) diameter size range. The electrical aerosol analyzer determines the electric mobility of an unknown particle in a known electric field and then assigns a diameter to the unknown particle equal to the diameter of a known size calibration particle having an equal electric mobility.

There are three basic parts to the electric analyzer: a diffusion charger section which places a known, reproducible charge on each aerosol particle; a mobility analyzer section which collects out charged particles having a mobility greater than a pre-set value (corresponding to particle sizes smaller than a corresponding value); and an electrometer section which collects out and measures the current flow from the remaining charged particles.

The diffusion charger exposes the incoming aerosol to a controlled concentration of positive gas ions for a known time, thereby allowing the particles to acquire a charge level which depends only upon particle size. The mobility analyzer (of circular geometry) brings the charged aerosol in around a central core of clean air where the charged particles are attracted to a central collection rod carrying a controlled level, negative voltage. Particles with low mobility (larger size) do not migrate to the collection rod before leaving the collection section. Instead, they pass onto a high efficiency collection filter which removes them, causing a positive electrostatic charge to accumulate and leak off through an electrometer, indicating a current flow. In a number of programmed steps, the collecting rod voltage is varied to produce a known particle size classification. Currents are read either manually or through an automated system, and converted to particle number concentration data which can then be used to determine particle size distribution. Air flow rates, voltages and charging section currents are carefully controlled in a known, reproducible manner.

Although the first instrument to measure the mean size of an aerosol electrically was built over 50 years ago, it was only three years ago that a successful commercial electrical aerosol monitor was available. This recently modified analyzer, introduced in 1973, is a greatly improved version of an earlier, commercially available model introduced in 1967. Development

work on this first unit began at the University of Minnesota's Particle Technology Laboratory in 1963. Whenever a submicron size aerosol needs to be monitored, this instrument is probably applicable. Further details are found in several of the books referenced.

Condensation Nuclei Counter - Diffusion Battery

As the name implies, a condensation nuclei counter (C.N.C.) is a device to count the number of nuclei which serve as condensation sites for a supersaturated vapor, normally water. The counting can be done manually, as it was in early devices (and still is in some units), or automatically by measuring the light extinction caused by the liquid droplets formed in the condensation process. These devices are capable of sensing or counting particles greater than about $0.005 \mu\text{m}$ (diffusional) diameter. This lower detectable particle size is somewhat uncertain but certainly within the 0.001 to $0.01 \mu\text{m}$ diameter range, depending upon the composition of the particles and the instrument operating conditions (such as degree of supersaturation). C.N.C.'s are capable of particle size distribution measurements to a limited extent. If several fractions of a stable aerosol are sensed at different supersaturations and a count recorded for each sample, then the differences in number will indicate the number of particles in a calculated size interval.

The main advantage of the C.N.C. is its ability to sense or detect rapidly smaller particles at lower concentrations than can be detected by any other device or method. It also serves as a sensing or counting device for other methods of particle size classification, namely, the diffusion battery, a device which preferentially removes the very smallest particles first because of a higher diffusion coefficient.

A diffusion battery is a set of circular or rectangular cross section tubes through which an aerosol stream flows. Several of these cells are normally mounted in series and the aerosol stream deflected through various combinations of these cells to produce the differential removal as a function of particle size. A C.N.C. is used at the output of a diffusion battery to provide a readout or measurement of the particle number concentration. In this combination a particle size distribution device is achieved which works well over the 0.01 to $0.1 \mu\text{m}$ diameter range even for low aerosol concentrations. This range can be extended almost 5 fold in both directions. Above $0.3 \mu\text{m}$ other techniques (optical particle counters) work far better. Below $0.01 \mu\text{m}$ the C.N.C. is the only device capable of detecting low aerosol concentrations. This separation technique, therefore, has definite applications down to a theoretical lower limit of perhaps $0.002 \mu\text{m}$ diameter. Several of the referenced books consider the design and operation of this technique.

Aerosol Measurement Literature Sources

Many books have been published that specifically relate to the field of aerosol measurement. Several of them discuss the related problems of aerosol sampling (a representative sample is necessary in order to obtain a meaningful measurement), aerosol generation (necessary for proper instrument calibration), particle statistics (including presentation of data and calculation of measurement error), aerosol physics (physical laws governing the motion and interaction of gas borne particles) and aerosol chemistry (formation, reaction and composition of particles).

One book, now in press and edited by D.A. Lundgren, M. Lippmann, F.S. Harris, Jr., W.E. Clark and W.H. Marlow, will soon be published on the specific topic, Aerosol Measurement. It is intended to be a complete text on the basic principle, mechanical operation, calibration, data gathering procedures, data interpretation, instrument limitations and specific applications for each of the four instrumental techniques discussed in this paper. For further information, the books referenced above have been annotated in a short bibliography following this discussion.

Annotated Bibliography

Cadle, R.D., 1955: Particle Size Determination. Interscience Publishers, Inc., 303 pp.

Principle topics covered are particle statistics, sampling, optical and electron microscopy, sieve analysis, sedimentation, elutriation and surface area measurements (powders). Light scattering is also considered.

Dennis, R., Ed., 1976: Handbook on Aerosols. National Technical Information Service, TID-26608, 142 pp. Subjects discussed are aerosol generation, aerosol dynamics, optical properties, aerosol sampling and particle size measurement. Extensive reference lists are included for each subject as well as a bibliography of aerosol books and periodicals containing aerosol articles.

Herdan, G., 1960: Small Particle Statistics. Butterworth and Company, Ltd., 418 pp.

A complete treatment of particle statistics. This work also considers sample preparation and sizing by microscope, gravitational and centrifugal sedimentation (in liquids), surface area measurement methods and general information on powders. Some aerosol measurement discussion.

Liu, B.Y.H., Ed., 1976: Fine Particles. Aerosol Generation, Measurement, Sampling and Analysis. Academic Press, 837 pp. Proceedings of the 1975 Symposium on Fine Particles. Contains numerous articles on aerosol generation, aerosol sampling, aerosol measurement and analysis.

Lundgren, D.A., M. Lippmann, F.S. Harris, Jr., W.E. Clark and W.H. Marlow, Eds., In Press: Aerosol Measurement. University of Florida Press.

Detailed coverage of four specific aerosol measurement techniques: inertial classification (centrifuges, cyclones and impactors), light scattering particle counters, electric aerosol analyzers, and condensation nuclei counters together with diffusion batteries. Numerous articles on each topic cover basic principle, mechanical operation, calibration, data gathering procedures, data interpretation, instrument limitations and specific application.

Mercer, T.T., 1973: Aerosol Technology in Hazard Evaluation. Academic Press, 394 pp.

Comprehensive text on aerosol generation, sampling and measurement. General discussion of aerosol properties, particle statistics, aerosol sampling for size and concentration measurement, instruments for aerodynamic, optical, electrical and other size measurements, respirable samplers and production of test aerosols.

Orr, C., Jr. and J.M. Dallavalle, 1959: Fine Particle Measurement. Academic Press, 394 pp.

Topics included are microscopy, particle statistics, sieving, sedimentation, inertial classification, light scattering, surface area measurement by flow resistance, gas adsorption and liquid-phase sorption, and pore size measurement (powders).

Silverman, L., C.E. Billings and M.W. First, 1971: Particle Size Analysis in Industrial Hygiene. Academic Press, 317 pp. Complete coverage of particle sampling and size analysis for both powders and aerosols. Review of sampling instruments, size analysis by optical, electron and scanning electron microscopy. Discussion of all common particle sizing apparatus (both manual and automatic), particle statistics and application areas.

A Doppler Shift Spectrometer for Measurement
of Particle Size Distributions

David S. Bright, Natasha K. Neihart, and Ilan Chabay
Analytical Chemistry Division
National Bureau of Standards
Washington, D. C. 20234

Summary

An instrument has been developed for measuring the size distributions of aerosols above 1 μm radius by determining their settling velocities and light scattering characteristics. Absolute measurements of size are obtainable for homogeneous spherical particles of known density and index of refraction.

This spectrometer [1] measures the particles while dispersed in air, thus, liquid particles are measured as easily as solid particles. The size distribution is measured in real time with many particles present in the scattering volume. The radii of the particles are measured independently of the scattered light intensity which, for spheres, is a complicated function of radius, wavelength, index of refraction and scattering angle. This calculated function (Mie scattering) is used with the experimental data as an inherent means of determining true particle size. The polarization properties, narrow lines at several specific wavelengths, and the angular resolution (0.1°) of the spectrometer render it suitable for basic studies of the light scattering properties of particles other than homogeneous spheres.

Spheres of a given density and radius fall at a velocity given by the Stokes-Cunningham law. Laser light (single line, single mode), scattered out of the horizontal incident beam (Figure 1) and Doppler shifted by the falling particles, is mixed with light with no Doppler shift, scattered from the windows of the sample chamber. The signal from the

photomultiplier tube (PMT) in the vertical scattering plane thus contains beat frequency components which are proportional to the falling velocities. The intensities of these components can be related by Mie scattering theory to the numbers of particles of the corresponding sizes. Particle radii below 1 μm cannot be measured at present because the instantaneous velocities due to Brownian motion are comparable to the falling velocities.

Particles are produced by a Berglund-Liu vibrating orifice generator [2]. To sample the aerosol stream, a valve arrangement first allows the stream to flow through a one-meter glass tube above the scattering chamber, and then seals the particle chamber (Figure 2). The particles are now free to settle down into the scattering chamber. The time for the tube to clear varies from several minutes for large particles to several hours for small particles. The light scattered from the particles is collimated by pinholes (Figure 1) before reaching the PMT. The AC signal from the PMT is passed through a filter and amplifier to a spectrum analyzer. The resultant curves of light intensity vs particle radius are then normalized by the appropriate Mie light scattering table.

Particles of dioctyl phthalate from 0.5 to 20 μm radius can be generated. The light intensity distributions (intensity vs radius or frequency) for monodisperse aerosols appear as peaks whose widths reflect combinations of the width of the particle size distribution, the broadening of the Doppler signal due to Brownian motion of the particles, and the resolution of the instrument. The relative contributions of each of these factors varies with particle size.

Polydisperse aerosols are made by sweeping the driving frequency of the Berglund-Liu particle generator. Light-intensity distributions from these aerosols are characterized

by the peaks of the Mie scattering function. The radii corresponding to these peaks along with the corresponding Doppler frequencies serve as two independent absolute measures of particle size.

Bands of light due to the Mie scattering phenomenon can be observed with a vertical light beam illuminating a mono-disperse aerosol stream. The maxima and minima of the scattered light vs scattering angle have been experimentally related to particle size for particles down to 0.5 μm radius. An advantage of this technique is that the particles can be observed within seconds after they are generated, allowing the investigation of rate of evaporation of solvent from the particles. It also serves as an independent means of determining size for the same sample measured by the Doppler shift instrument.

References

1. Gollub, J. P., Chabay, I., and Flygare, W. H., *Applied Optics* 12, 2838-2842 (1973).
2. Berglund, R. N. and Liu, B. Y. H., *Environmental Science and Technology* 7, 147-153 (1973).

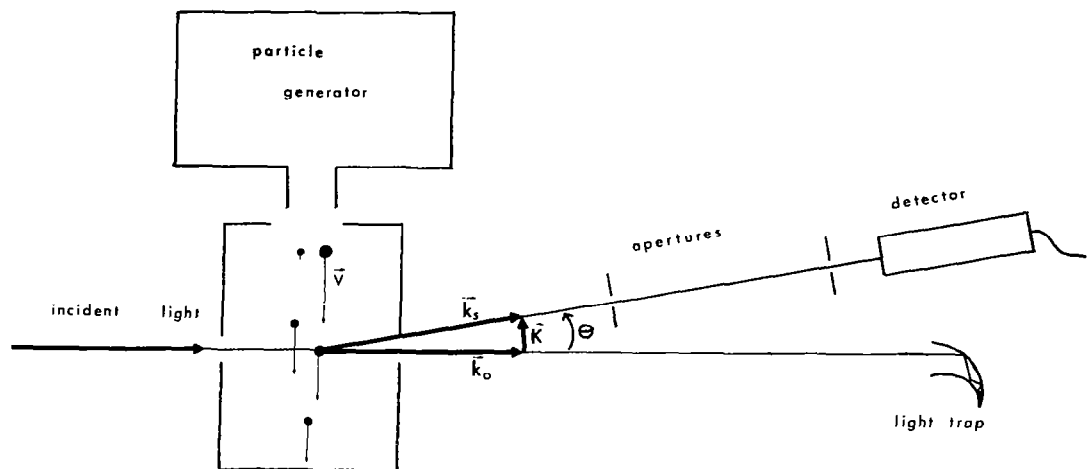


Figure 1

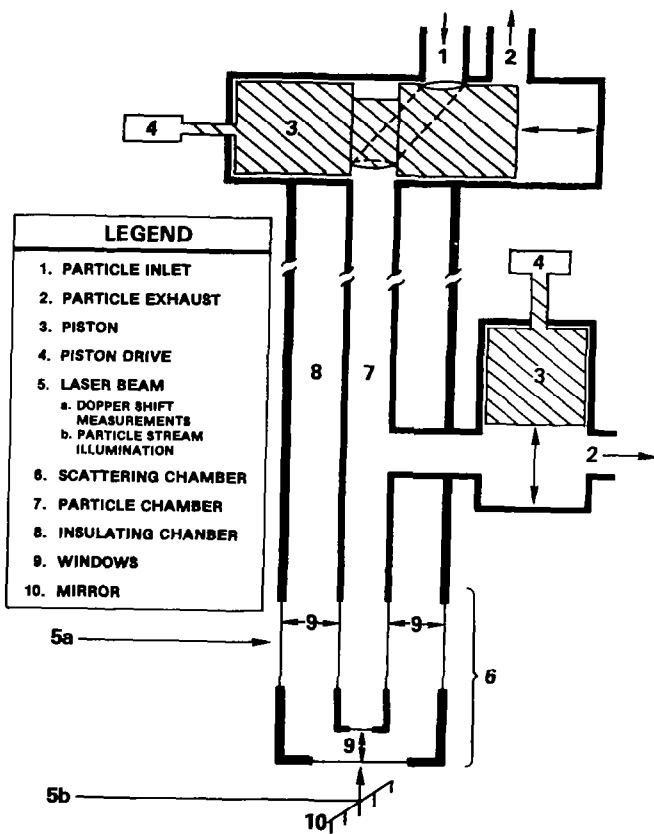


Figure 2

CHEMICAL CHARACTERIZATION OF AEROSOLS
BY LIGHT SCATTERINGC. C. Gravatt
Analytical Chemistry Division
National Bureau of Standards
Washington, D. C. 20234

This paper will describe a new light scattering method for the chemical characterization of particulate matter. Specifically, it is possible by this method to distinguish carbon, absorbing, and metal containing particles from other materials, and in some instances to distinguish among various types of carbon containing and metallic particles. This technique can be applied either to the characterization of individual particles or to aerosols containing many particles, and applications in both areas will be discussed. In many situations some degree of chemical characterization of aerosols would be advantageous, and the present technique is especially attractive since it can be accomplished without the collection and subsequent chemical analysis of a sample.

The following is a brief introduction to the important optical parameters to be used in this paper. The index of refraction will be represented as

$$m - n - ik \quad (1)$$

with real component n and imaginary component k . Consider a beam of light of intensity, i_0 , and wavelength, λ_0 ,

traveling in the direction given by a unit vector, k_0 , and scattered by a sample at 0. A ray scattered in the direction given by unit vector, k , is measured to have intensity, i , by a detector located a distance R from the sample. The scattering angle, θ , is the angle between the directions defined by k_0 and k . The scattering plane is that plane containing the sample and the unit vectors k and k_0 . For this paper it is also necessary to define the state of polarization of the incident radiation and the following notation will be adopted. If the polarizer is oriented such that the direction of polarization is in the scattering plane, then the scattered radiation is represented by $i_{//}$. If it is oriented such that the direction of polarization is normal to the scattering plane then the scattered radiation is represented by i_{\perp} .

SINGLE PARTICLE CASE

A single particle is located at 0 and the scattered intensities, $i_{//}$ and i_{\perp} , are measured as a function of θ . In order to investigate the effect of index of refraction on the scattering behavior of particulates, the scattering curves ($i_{//}$ and i_{\perp} vs. θ) have been calculated for a wide range of indices of refraction and particle size using a modification of the procedure given by Dave. From a comparison of a number of these scattering curves a certain pattern was noticed; specifically, that the $i_{//}$ curves for

materials with $k = 0$ differed markedly from those for materials with $k > 0$ over the angular range from $\theta = 30^\circ$ to $\theta = 90^\circ$. A more complete analysis of this effect has shown that the angular region from $\theta = 40^\circ$ to $\theta = 70^\circ$ for $i_{//}$ is extremely sensitive to the magnitude of the k value of the particle index of refraction and can be used for chemical characterization of the particles.

There are a number of possible applications of a single particle chemical characterization instrument as described above and several will be discussed. These involve applications in air pollution, coal mining, and industrial plant monitoring.

MULTI-PARTICLE CASE

In this section the chemical characterization technique will be extended to a device that monitors an aerosol containing many particles rather than measuring a single particle at a time. The application to be discussed in detail is a smoke detector but several additional applications will be presented.

The optical configuration of the instrument is as follows. The light source is either an incandescent bulb or a medium pressure mercury arc. The incident light system is of straightforward design and produces a reasonably well collimated, linearly polarized beam of uniform intensity

approximately 1 cm² in cross section. The scattered light detector system in the plane of polarization has an aperture of approximately $\pm 15^\circ$ centered at 55° and employs a photodiode-op-amp combination as the light detector. The output of this detector is relatively large for an aerosol containing non-absorbing particles and is relatively small for an aerosol containing a large number of carbon-like particles.

There is also a second scattered light detector system normal to the plane of polarization centered at an angle of 90° with an aperture of $\pm 10^\circ$. This system also uses a photodiode-op-amp combination as the light detector. The output of this detector is a quantity approximately proportional to the total number of particles in the beam, independent of whether they are absorbing or not. The output of the instrument is the ratio of the two detector outputs.

The actual response of the smoke detector was measured for a number of aerosol samples. It was shown that the instrument is effective in distinguishing fire-produced aerosols and other types of absorbing materials from non-absorbing aerosols. Results of these measurements will be presented.

Recent Developments in Nephelometers

By A. P. Waggoner, N. C. Ahlquist, R. J. Charlson
 University of Washington, Seattle, Washington 98195

Abstract

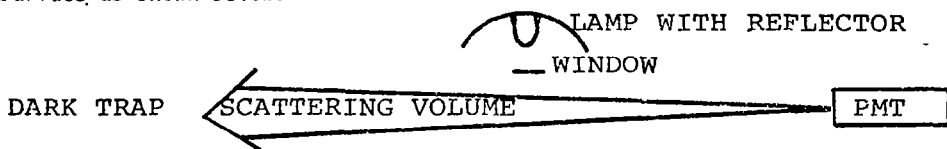
Recent developments have greatly increased the sensitivity and zero stability of multiwavelength nephelometers to the point where they are appropriate for measuring background aerosol properties.

Description of 4 Wavelength Nephelometer

The 4-Wavelength Nephelometer is an instrument that measures the scattering portion of the extinction coefficient due to particles. The instrument was designed at the University of Washington and produced under license by MRI of Altadena, California.

Optical Description

Sample air is drawn into an enclosed volume and illuminated by light from a diffusing milk window. The window is illuminated by a quartz-halogen incandescent lamp located outside of the sample chamber. The intensity of illumination from the window has a $\cos \theta$ dependence, where θ is the angle from normal to the diffuser surface. A photomultiplier tube views a small solid angle (about 1.5 degrees) parallel to but not intersecting the diffuser surface as shown below.



The field of view of the PM tube is defined by an optical system consisting of holes in baffle plates. No glass surfaces are used.

This geometry (1) provides integration over the aerosol scattering Phase function, $\beta(\theta)$ to measure the scattering extinction coefficient due to particles, b_{sp} .

$$b_{sp} = \int \beta(\theta) d\Omega = 2\pi \int^{\pi} \beta(\theta) \sin \theta d\theta$$

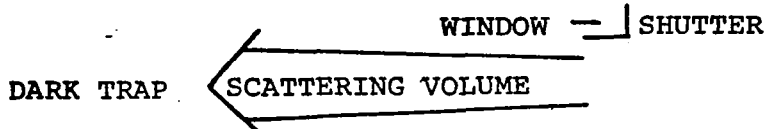
The amount of light on the PM tube is proportional to the scattering extinction coefficient of molecules and particles within the scattering volume. This allows the instrument to be calibrated using the Rayleigh scattering coefficient of particle free gasses such as CO_2 and Freon-12 (CCl_2F_2).

The range of the integration does not include 0° to 7° or 170° to 180° . Detailed analysis (2,3,4) for a variety of aerosol size distributions have concluded that the errors due to the finite angular integration are of order 10% for the usual low RH aerosol and the instrument reading is 0.5 of actual b_{sp} for large particle aerosols such as fogs and dust storms.

In this instrument, optical interference filters are used to allow measurements in four wide band channels (70 nm bands centered on 450, 550, 700 and 840 nm) and one narrow channel (5 nm band centered on 500 nm). The five filters are located in a filter wheel located immediately in front of the PM tube. The filter wheel rotates at 20 RPM and scattering in each wavelength is measured every three seconds. The rotation can be stopped on a selected filter for improved signal to noise ratio.

The narrow 500 nm optical channel can be used for more accurate calibration using Freon-12 as a reference scattering standard. The narrow optical bandwith reduces uncertainty as to the effective wavelength for the Freon-12 reference Rayleigh scattering gas. Other optical filters could be used to provide any desired response within the region ~ 400 nm - 850 nm set by lamp emission and photo-cathode quantum efficiency.

A modification has been made on the optical system of one nephelometer to allow measurement of an aerosol optical parameter related to albedo. When a black surface is illuminated by a zenith sun, the albedo per unit thickness of a single scattering aerosol layer can be determined by integrating the aerosol phase function over the backward hemisphere of scattering angle. A partial shutter, shown below, can change the angle of integration so that the scattered intensity is proportional to the backward hemisphere aerosol scattering extinction coefficient.



Electronic Description

The low intensity light scattered onto the photomultiplier photocathode is detected by photon counting techniques. The output current from the PMT consists of DC leakage currents, small pulses from electrons thermally emitted by the dynodes and large pulses from electrons emitted by the photocathode. The amplifier and discriminator detect these large pulses and produce one output pulse for each electron from the photocathode. The pulses are from photons incident on the photocathode and dark current (thermal emission of electrons). The signal during the period when a filter is passing light is the sum of dark counts plus counts due to light.

The light is from: (1) scattering by particles, (2) Rayleigh scattering by the gas molecules, (3) scattering off the interior surfaces of the instrument. The signal detected when the instrument is filled with clean particle free air is the instrument background and is the sum of counts due to dark current, Rayleigh scattering and wall scattering. When the instrument is filled with ambient air, the detected light will increase because scattering by aerosol particles increases the light incident on the photocathode. A digital subtraction of the ambient count minus the clean air count is used to detect the signal due to aerosol particles. An additional signal, that due to scattering by a white (BaSO_4) painted wire, is used to stabilize the instrument calibration against drifts in lamp color and brightness, filter transmission and photo-tube sensitivity.

The instrument accumulates counts in three 64 bit memories for each wavelength. The first, clean air, is accumulated when the instrument is filled with filtered ambient air. Next a painted wire, (calibrate 1) is inserted into the scattering volume and counts are accumulated. Finally, the calibrate object is withdrawn and a valve is opened allowing ambient air into the instrument. Now, ambient air counts are accumulated into the third set of memories.

Clean air counts are subtracted from calibrate and ambient counts giving two digital words proportional to calibrate object and particle brightness. Both counts are converted to analog voltages proportional to the log of the number of counts and log calibrate is subtracted from log ambient. This difference, the log of the ratio of particle scattering to calibrate object brightness, is added to a voltage set by the master calibrate control to generate the output signal. (As the output is log, an addition to the output is a multiplicative constant.) This calibration is made using Freon-12, CCl_2F_2 , as a standard.

An analog output is provided for each of four wavelengths proportional to the log of b_{sp} covering the range 10^{-7} to 10^{-2}m^{-1} .

Performance

The signal is obtained by subtracting clean air photon counts from ambient air. In clean conditions, these two numbers approach each other and the noise in the signal is $\sqrt{2}$ times the noise or statistical fluctuations on clean air

counts. The noise in counts per second N , with an averaging time T , a counting time fraction of A and a background count rate of B is given by:

$$N = \sqrt{\frac{2B}{AT}}$$

The value of A is 0.5 for operation on a single filter and 0.05 for operation on all four filters.

The value of N is multiplied by a factor F that relates b_{sp} to count rate.

The useable sensitivity will depend on lamp brightness, filter center wavelength and bandwidth, photo-tube quantum efficiency and dark count rate and averaging time. Measured values for B and F for serial number 106 are listed below:

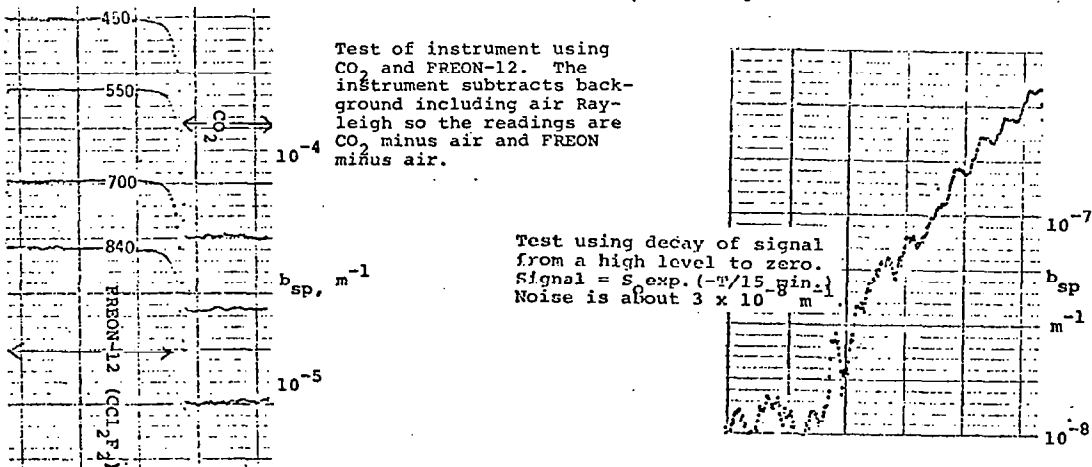
Wavelength	B	F
450	2.2KHZ	3.23×10^{-8} /HZ
550	6.1KHZ	8.20×10^{-9} /HZ
700	12.2KHZ	3.69×10^{-9} /HZ
840	6.1KHZ	6.54×10^{-9} /HZ

The calculated noise in b_{sp} for each wavelength for averaging times of 10 seconds, 2 and 15 minutes, all filters operated, are listed below:

Wavelength	Time		
	10 S.	2 Min.	15 Min.
450	3×10^{-6}	1×10^{-6}	3.2×10^{-7}
550	1.2×10^{-6}	3.5×10^{-7}	1.3×10^{-7}
700	8×10^{-7}	2.3×10^{-7}	8.4×10^{-8}
840	1×10^{-6}	2.8×10^{-7}	1×10^{-7}

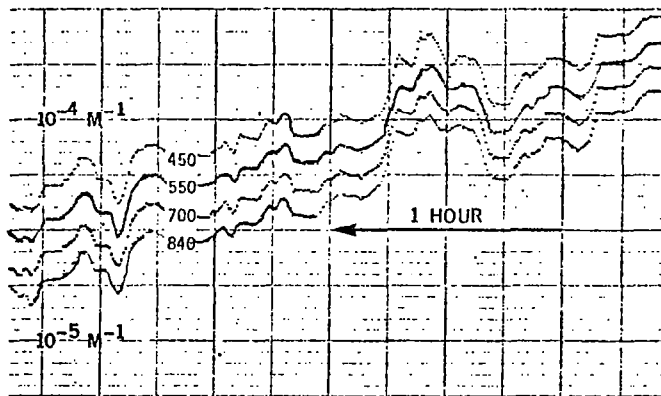
For operation on a single wavelength, the noise is reduced by about a factor of three.

These calculated noise levels have been verified in two tests. In the first, the instrument was operated on all four wavelengths, 2 min. averaging time and filled with CO_2 and Freon-12. The measured value of b_{sp} (of CO_2 minus air) at 840 nm was $3.8 \pm 0.3 \times 10^{-8} \text{ m}^{-1}$, in agreement with calculated noise. In the second test, the instrument was operated on a single wavelength, 700 nm, with a 15 min. averaging time. A large signal was loaded into ambient memory and then the instrument was filled with filtered air. The signal will decay to zero and at some point the instrument noise will randomize the data trace. The trace is shown below and the noise is about $3 \times 10^{-8} \text{ m}^{-1}$ as previously calculated.

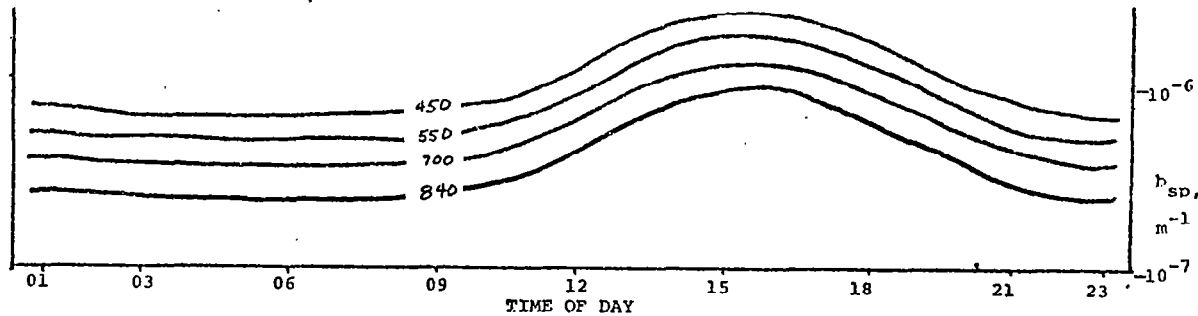


Data

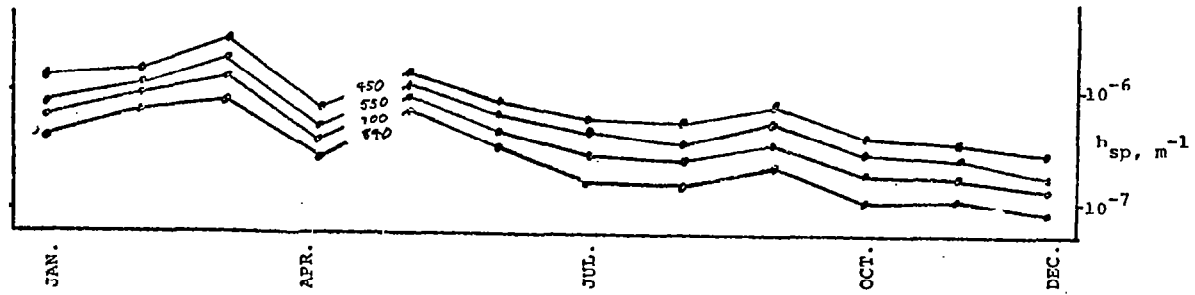
Shown below are samples of atmospheric measurements. The values of b_{sp} at various wavelengths show a high degree of correlation with the usual wavelength dependence of b_{sp} given by $\lambda^{-0.5}$ to $\lambda^{-2.0}$. Mean values of $b_{sp}(550 \text{ nm})$ are twice to four times Rayleigh scattering in rural continental U.S. measurements. At Mauna Loa, $b_{sp}(550\text{nm})$ during 0300-0400 hours ranges from 1% to 5% of Rayleigh scattering.



Typical measurements of particle scattering extinction coefficient, b_{sp} , at four wavelengths (450, 550, 700 and 840 nm). During the period of measurement in urban Seattle, the 550 nm b_{sp} ranged from $1.4 \times 10^{-5} \text{ m}^{-1}$ to $2.2 \times 10^{-4} \text{ m}^{-1}$ and the wavelength dependence of b_{sp} was almost constant at $\lambda^{-1.4}$.



AVERAGE b_{sp} AS A FUNCTION OF TIME OF DAY, MAUNA LOA, 1974



MONTHLY 03-04 HRS. b_{sp} FOR 1974 MEASURED AT MAUNA LOA ORS. DATA TAKEN BY DR. R. RODHAIN, NOAA

$\lambda = 530 \text{ nm}$. UNITS OF 10^{-4} m^{-1} . 63% OF ALL DATA POINTS FALL BETWEEN $b_{sp}(\text{LOW})$ and $b_{sp}(\text{HIGH})$

TABLE 1. LIGHT SCATTERING

LOCATION	b_{sp} (AVERAGE)	b_{sp} (LOW)	b_{sp} (HIGH)
TYSON	0.76	0.3	0.89
MILFORD	0.44	0.16	0.56
HALL MT.	0.4	0.22	0.56

USE OF POLAR NEPHELOMETER MEASUREMENTS IN DETERMINING AEROSOL OPTICAL PROPERTIES

G. W. Grams and E. M. Patterson
 National Center for Atmospheric Research*, Boulder, Colorado 80303

A prototype laser polar nephelometer¹ was constructed and used to measure the optical properties of airborne soil particles in the atmospheric boundary layer at the 1.5-m level near Big Spring, Texas, during the latter part of May 1972. A smaller version of the polar nephelometer, suitable for installation on a pressurized aircraft, was subsequently developed² to obtain data on aerosol optical properties for studies of the effects of aerosol layers on the global climate. This compact nephelometer has been mounted on the NASA CV-990 jet aircraft and on the NCAR Electra aircraft during a number of field measurement programs, and it has been used in laboratory studies of the effects of nonsphericity on particle scattering functions.

The general features of the laser polar nephelometer are illustrated in Figure 1. The system was designed for operation in a pressurized aircraft cabin by using outside air ducted through a 5-cm diameter airflow tube. The sample volume is that which is common to the intersection of a collimated linearly polarized helium-neon laser beam and the detector field-of-view within

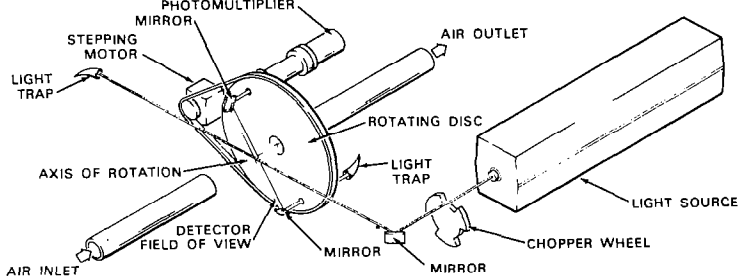


Figure 1. Schematic illustration of the laser nephelometer.

the airflow tube. Scattered-light intensity measurements are made at scattering angles from 15° to 165° with reference to the direction of propagation of the light beam. Pulses provided by digital circuits control a stepping motor which sequentially rotates the detector by pre-selected angular increments (5° is used in normal operation).

The scattering phase function data taken with the compact polar nephelometer have been analyzed in two ways. In the first, Mie theory has been used to calculate a value for the imaginary refractive index of the aerosol particles when the size distribution parameters and the real refractive index are known. In the second mode of analysis, the scattering phase function for particles with

*The National Center for Atmospheric Research is sponsored by the National Science Foundation.

known optical properties is studied in order to determine the changes from Mie theory that occur when the particles are not spherical.

An example of the first type of analysis is shown in Figure 2 which shows some data obtained with the compact nephelometer on the Electra aircraft during the GATE program in 1974. Simultaneous particle-size data were

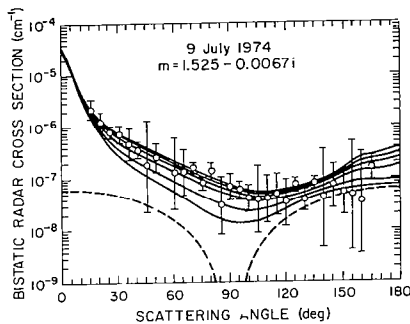


Figure 2. Comparison between observed polar scattering diagrams (circles with error bars) and those calculated for observed aerosol size-number distributions and a variety of complex refractive index values (solid lines). See text for more details.

obtained from real-time measurements made with a single-particle optical counter and from laboratory analyses of particle samples collected by an aerosol impactor. Values of the angular variation of the scattered-light intensity are calculated by applying Mie scattering theory to the observed size distribution functions and assuming different values of the complex index of refraction of the particles. Calculated values are then compared with data on the actual variation of the scattered-light intensity obtained with the polar nephelometer. The most probable value of the complex refractive index is taken to be that which provides the best fit between the experimental light-scattering data and the parameters calculated from the observed size distribution function. In Figure 2, the solid curves are calculated values of scattered-light intensity for various assumed values of the refractive index; in all cases, the real part is 1.525 and the imaginary part is (from top to bottom) 0, 0.005, 0.01, 0.02 0.05, and 0.1. The refractive index value determined to have the best fit for real part 1.525 is shown at the top of the graph. Dotted lines represent contributions to the scattered-light intensity due to air molecules.

We have employed the second method of analysis in laboratory studies of scattering by nonspherical particles. These studies have been carried out in collaboration with P. Chýlek of Purdue University and R. Pinnick of the White Sands Missile Range. The work has led to a method³ for calculating light scattering by irregular randomly oriented particles which yields results that are in good agreement with experimental data. The starting point in the development of this method was an observation that the glory--a strong enhancement of scattering in the backward direction--occurs only in scattering by spherical particles⁴. Consequently, the mechanism that produces the glory exists only if the particles are spherical, and it does not exist if particles are of irregular shapes. According to van de Hulst⁵, the glory is caused by surface waves. Chýlek had previously shown⁶ that surface waves are also responsible for the "ripple structure" in the normalized extinction cross section, and that there is a one-to-one correspondence between the surface waves and the partial-wave resonances in the Mie amplitude functions; consequently, he proposed that the first-order correction for nonsphericity of scattering particles should be the removal of the partial-wave resonances. We carried out a series of experi-

mental studies³ to help establish the procedure for removing the resonances by relatively simple modifications to the standard Mie calculations. Under controlled laboratory conditions, we generated aerosol particles with known refractive index and with sizes comparable to those normally observed in the earth's atmosphere. We measured scattering phase functions for various types of particles with the polar nephelometer. Particle shapes and size distributions were documented by means of scanning electron microscope photographs of particles collected onto Nuclepore filters. Using the known data on refractive index and particle size distribution, we then compared these experimental results with results obtained by Mie calculations and with results obtained by the nonspherical approximation. Figure 3 illustrates the major results of the intercomparisons between measured and calculated phase functions. We obtained almost exact agreement between experimental data and the Mie calculations for the case of spherical particles, as shown in Figure 3a. For nonspherical particles, we could obtain good agreement between measurements and calculations using the modified Mie theory, as shown in Figure 3c. However, it was often not possible to get close fits

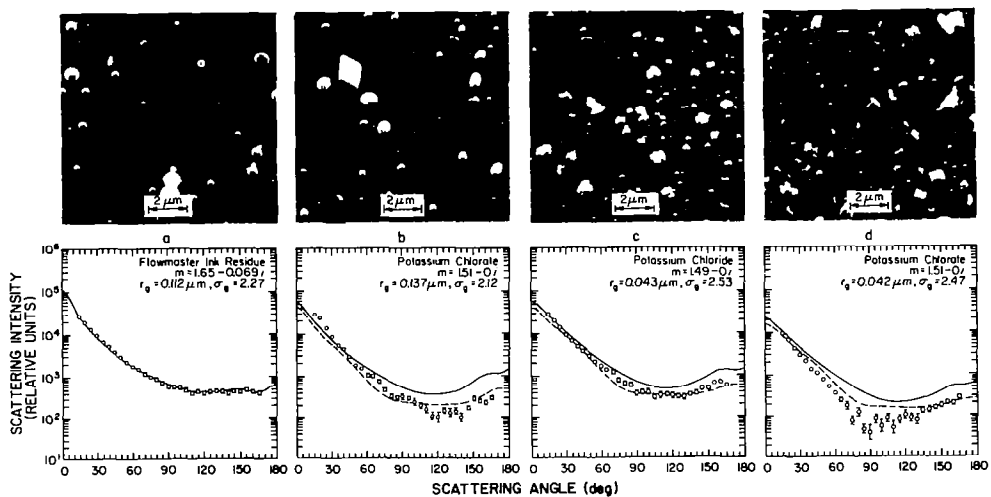


Figure 3. Comparison of angular scattering patterns measured with the polar nephelometer (circles with error bars) with those calculated by Mie theory (solid lines) and the modified Mie theory (dashed lines). Particle composition and complex refractive index are identified on each scattering diagram; each diagram also contains the geometric mean radius r_g and geometric standard deviation σ_g for log-normal size distributions obtained by determining the radii of spheres of equal cross section for several thousand particles from scanning electron microscope photographs. Examples of such photographs are presented above the scattering diagrams to illustrate their respective particle shapes.

between the measured and calculated angular scattering patterns when the distribution of particle shapes included an appreciable fraction of particles with one dimension longer than the others, as illustrated by the ellipsoids in Figure 3b and the irregular particles in Figure 3d. We suspect that such an aerosol may result in preferentially oriented particles, thereby violating a basic assumption of random particle orientation.

Our data on the light-scattering properties of the particles in the Saharan dust layer obtained during the 1974 GATE program are currently being analyzed using Mie theory and the modified Mie theory described above. We plan to complete our analysis of this data by the end of 1976. In addition to the refractive index results, we will be able to provide additional data on a variety of other optical properties used in studies of the effects of aerosols on the earth's radiation balance. This would include data on such parameters as single-scattering albedos, backscattered fractions, and scattering phase functions for the particles in the Saharan dust layer.

References

1. Grams, G. W., I. H. Blifford, Jr., D. A. Gillette, and P. B. Russell, Complex index of refraction of airborne soil particles, J. Appl. Meteor., 13, 459-471, 1974.
2. Grams, G. W., A. J. Dascher, and C. M. Wyman, Laser polar nephelometer for airborne measurements of aerosol optical properties, Optical Engineering, 14, 85-90, 1975.
3. Chýlek, P., G. W. Grams, and R. G. Pinnick, Light scattering by irregular randomly oriented particles, Science, 193, 480-482, 1976.
4. Hansen, J. E., and L. D. Travis, Light scattering in planetary atmospheres, Space Sci. Rev., 16, 527-610, 1974.
5. van de Hulst, H. C., Light Scattering by Small Particles. John Wiley, New York, 470 pp., 1957.
6. Chýlek, P., Partial-wave resonances and the ripple structure in the Mie normalized extinction cross section, J. Opt. Soc. Am., 66, 285-287, 1976.

GERBER, H.E. and STILLING, R.K.

Naval Research Laboratory, Washington, D.C. 20375, USA

BUSER, R.G. and ROHDE, R.S.

U.S. Army Electronics Command, Fort Monmouth, NJ 07703, USA

Laser Transmission Through Concentrated Aerosol

1. INTRODUCTION - A portable transmissometer was developed which simulates atmospheric transmission lengths on the order of 1 Km. These lengths were achieved over a folded path of 20 m by introducing atmospheric aerosol in which the dispersed phase was concentrated centrifugally up to two orders of magnitude. This summary describes the design and performance of the concentrator and gives results of some initial laser propagation measurements through the concentrate.

2. INSTRUMENTATION - A schematic of the aerosol concentrator is shown in Fig. 1. Ambient aerosol flows at V_1 (liters/min) into the inlet manifold 5 and along a concentric annulus formed by a solid outer cylinder 1 at rest and a porous inner cylinder 2 rotating at high speed. Suction (V_3) applied to the hollow shaft 4

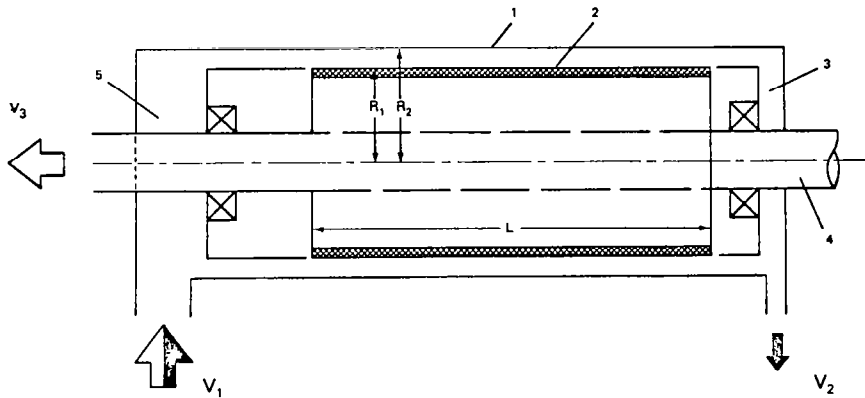


Fig. 1 - Schematic of aerosol concentrator (explanation in text).

causes the dispersion medium to pass through the porous cylinder and into the shaft. Since the radial velocity of the aerosol is comparable to that of the inner cylinder near its surface, aerosol particles move radially outward due to the centrifugal force in addition to their motion along the annulus. The particles reach their highest concentration at the end of the annulus near the outlet manifold 3 where they are drawn off at V_2 which is typically set equal to $0.02 V_1$. With no particle losses in the annulus the concentration increase of the aerosol particles is simply V_1/V_2 .

The inner cylinder consists of seamless sintered stainless steel which has uniform porosity and a tensile strength which is sufficient to withstand the centrifugal force of 25,000 rpm ($L=30\text{cm}$, $R_1=4.4\text{cm}$). The pores cover 1/5 of the cylinder's surface and average $25\text{ }\mu\text{m}$ in diameter.

The concentrate is drawn through the transmission cell which consists of a slab-like vertical chamber 200cm x 20cm x 3 cm. Mirrors at each end step the laser beam through the chamber to give the 20 m path length. Baffles placed along the inner walls minimize wall reflections, and clean air flushes the lower mirror to prevent particle deposition. Attenuation in the filled cell can be measured for optical thicknesses greater than 0.1, and Zuev et al. (1967) showed that the Bouguer law describes the attenuation for thicknesses up to 25 for a similar transmissometer.

3. EXPERIMENTAL RESULTS - The proper simulation of the 1 Km atmospheric transmission path requires that the aerosol particles which significantly affect attenuation pass through the concentrator without losses. Figure 2 shows the results of measurements made to test that requirement for a rpm of 8000. Atmospheric particles were used in all the tests except in one test where 1.090 μm monodisperse latex particles were used. The concentration was measured with a Royco particle counter in the flow entering 5 and leaving 4, membrane filters were used to collect the latex particles. The concentration factor was expected to be 50 with flow rates of $V_1=4$ liters/min and $V_2=200$ liters/min.

The cutoff in the concentration factor for small particles for the case $\Delta R = R_2 - R_1 = 0.6\text{cm}$ is in the position expected by calculating the particle size for which the centrifugal sedimentation velocity equals the mean suction velocity into the porous cylinder. Particles with smaller sedimentation velocities are lost into the pores. The decrease for large particles is at a smaller particle size than expected. This

cutoff is a result of inertial impaction losses on the outer cylinder due to turbulence in the annulus as verified by hot-wire anemometry. The turbulence, found at all rpm values even though the uniform suction on the porous cylinder should have stabilized the flow much above the rpm corresponding to the critical Taylor's number for no suction (see Schlichting, 1968)), was probably due to the surface of the cylinder rotating significantly off-axis at one end.

The inner cylinder was placed in a larger container with an effective ΔR of 2.4cm and was again tested at 8000 rpm. The decrease of losses for larger particles shows that fewer impacted on the walls, and the shift of the lower cutoff to larger particle sizes suggests that the boundary layer moving with the cylinder was much thinner than in the previous case. The loss at

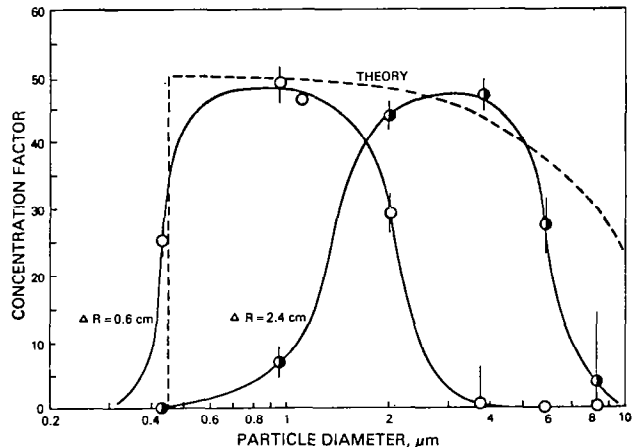


Fig. 2 - Concentration enhancement as a function of particle size.

the lower cutoff was now more consistent with the suction rate into individual pores than with the mean suction rate. The theoretical curve is from Davies (1966) for "stirred settling" losses in a chamber of size R_1 and L .

The attenuation of $0.6328 \mu\text{m}$ laser radiation through the transmissometer is shown in Fig. 3 as the cell is filled with concentrated ambient aerosol and then is flushed with ambient aerosol ($\Delta R=2.4\text{cm}$, 8000 rpm). The estimated curve was calculated from the attenuation coefficient α obtained from the estimated 40 Km visual range. Figure 4 shows the attenuation through an oil

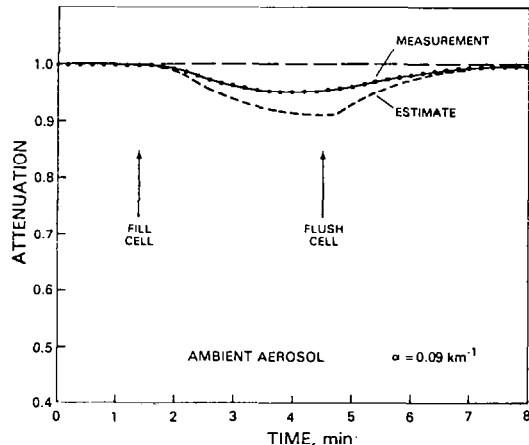


Fig. 3 - Attenuation through concentrated atmospheric aerosol.

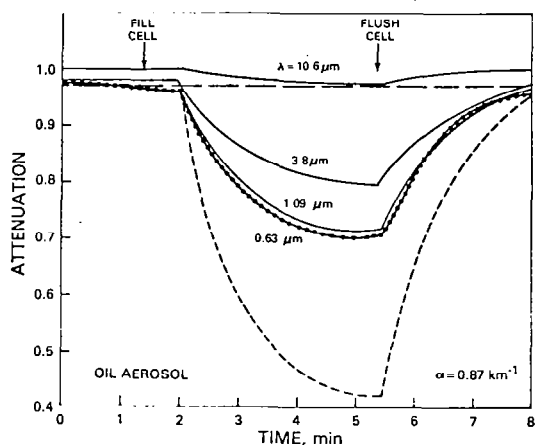


Fig. 4 - Attenuation through concentrated oil aerosol.

aerosol for which α was measured in the laboratory. The curves for other values of λ were calculated using the size distribution of the oil droplets and their scattering efficiency factors for the refractive index of 1.50. In both examples the transmissometer gave about 1/2 the attenuation at $0.6328 \mu\text{m}$ which was expected for the concentration factor of 50.

4. CONCLUSIONS - We have demonstrated the feasibility of simulating long atmospheric transmission lengths in a portable cell filled with concentrated aerosol particles. Current progress to increase surface coverage of smaller pores on the rotor and improved rotor concentricity promises to significantly increase the particle size range which is concentrated without significant losses.

5. REFERENCES -

- Davies, C.N., 1966: Deposition from moving aerosols. Aerosol Science, Ed. C.N. Davies, Academic Press, NY, 393-446.
- Schllichting, H., 1968: Boundary-Layer Theory, McGraw Hill, NY pp. 748.
- Zuev, V.E., M.V. Kabanov and B.A. Sabel'ev, 1967: The limits of applicability of the Bouguer law in scattering media for collimated light beams. (English Translation). Izv. Atm. and Oceanic Phys., 3, 724-732.

LOW ALTITUDE ENVIRONMENTAL AEROSOL MEASUREMENTS
WITH AN AIRBORNE PARTICLE MORPHOKINETOMETER

W. M. Farmer and J. O. Hornkohl
Spectron Development Laboratories, Inc.
P. O. Box 861, Tullahoma, TN 37388

SUMMARY

"Particle Morphokinetometer" describes the combined optical and electronic systems of an instrument designed to simultaneously measure particle size and velocity. These measurements are obtained from light scattered from an interference pattern generated by a laser interferometer which is similar in configuration to those used for differential Doppler laser velocimeter systems. The velocity is determined by measuring the IF signal frequency of the light scattered from the interference pattern, while particle size is determined by either a measurement of the signal shape or by measuring the magnitude of the signal amplitude.

The SDL Particle Morphokinetometer has been successfully operated from an airborne helicopter platform in Phoenix, Arizona. Data were obtained on six different flights and under a variety of environmental conditions, including day and nighttime operation. Both velocity and particle size distributions were obtained at two different positions relative to the aircraft and time resolved particle size distributions and relative number density measurements were obtained for both horizontal and vertical sample flights. The relative number density measurements are shown in Figures 1 and 2. The horizontal sample (Figure 1) revealed number density variations as large as two or three for path differentials as small as 0.4 kilometers and the relative number

density was observed to vary by factors of as much as 100 for a flight path approaching 10 kilometers. The vertical sample (Figure 2) which was taken during early morning hours revealed a very shallow inversion layer existing between 15 and 30 meters. The relative number density in the inversion layer was observed to be about 100 times that measured above it. The particle size distribution observed in this inversion layer was nearly the same as that observed on the ground. In-flight measured mean particle sizes ranged between 50 to greater than 75 microns in diameter while the measured velocity of the sample space was found to be 12.5 ± 4.9 meters per second at a distance of approximately 65 cm from the edge of the aircraft.

Some of the particle size data obtained by the instrument is believed to be questionable because of the smallness of the standard deviation of the size distributions and lack of slopes in the wings of the distribution. It was consistently observed that particle sizes on the ground covered a much broader spectrum than those observed when airborne. A major operational problem found in the instrument was the rejection of signal noise resulting from background sunlight. The interference filter used in these measurements had too broad a passband and required operation of the instrumental threshold at a level believed to be too high to adequately detect the smaller particles which scattered poorly. Nevertheless, the trend of observing only the large particle sizes when airborne proved to be a consistent effect whether the instrument was operated at night or during bright sunlight. Since the ground base measurements were made near a major city street, a possible explanation for this difference is the grinding action of automobile tires.

The results of this paper were obtained under Contract DA-6-99-2294A with the U. S. Environmental Protection Agency.

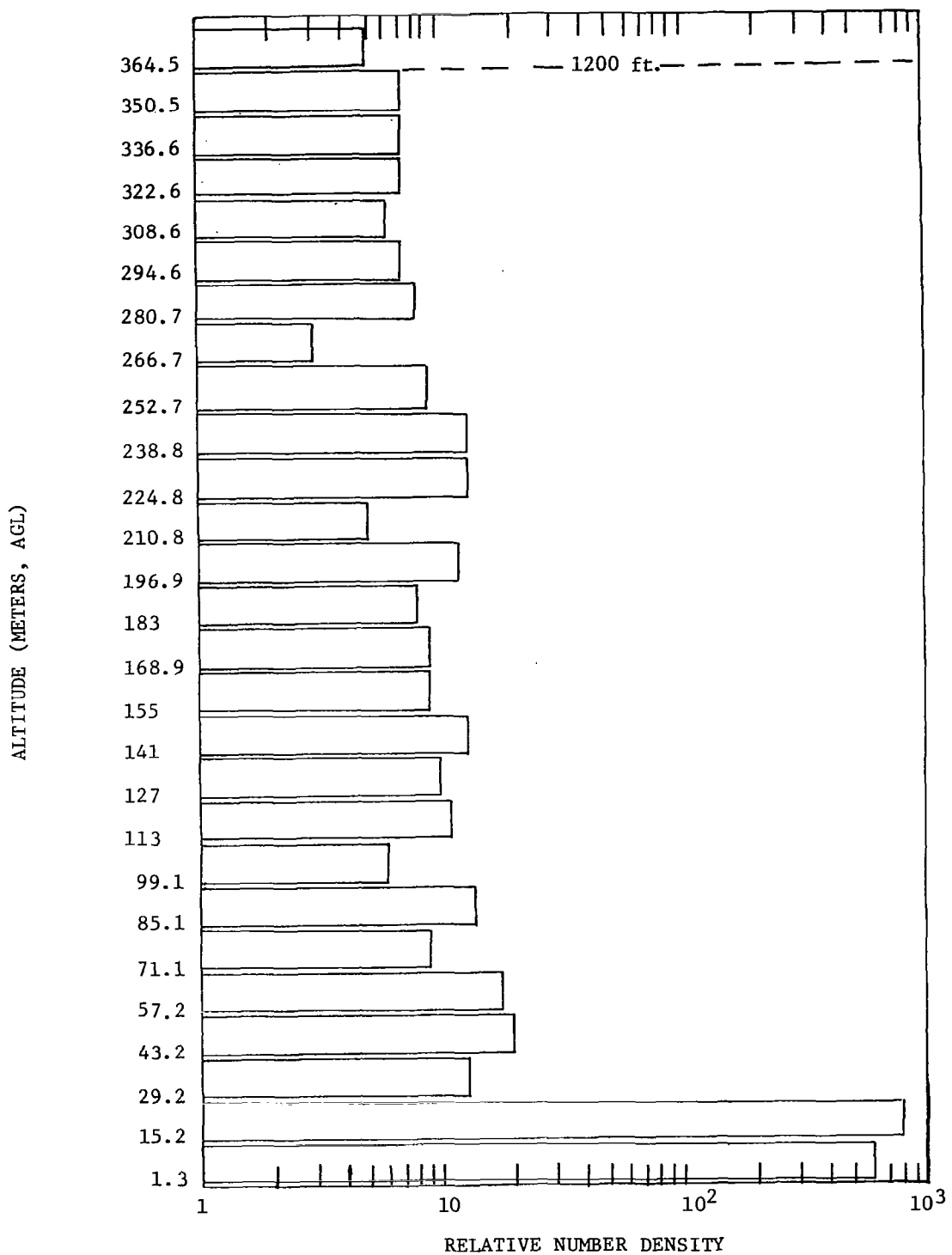


Figure 1. November 24, Flight 2. Return to airport. Descent from 1200' AGL altitude at 250'/min. rate. Relative number density distribution over 12.7 m altitude increment for a vertical sample path.

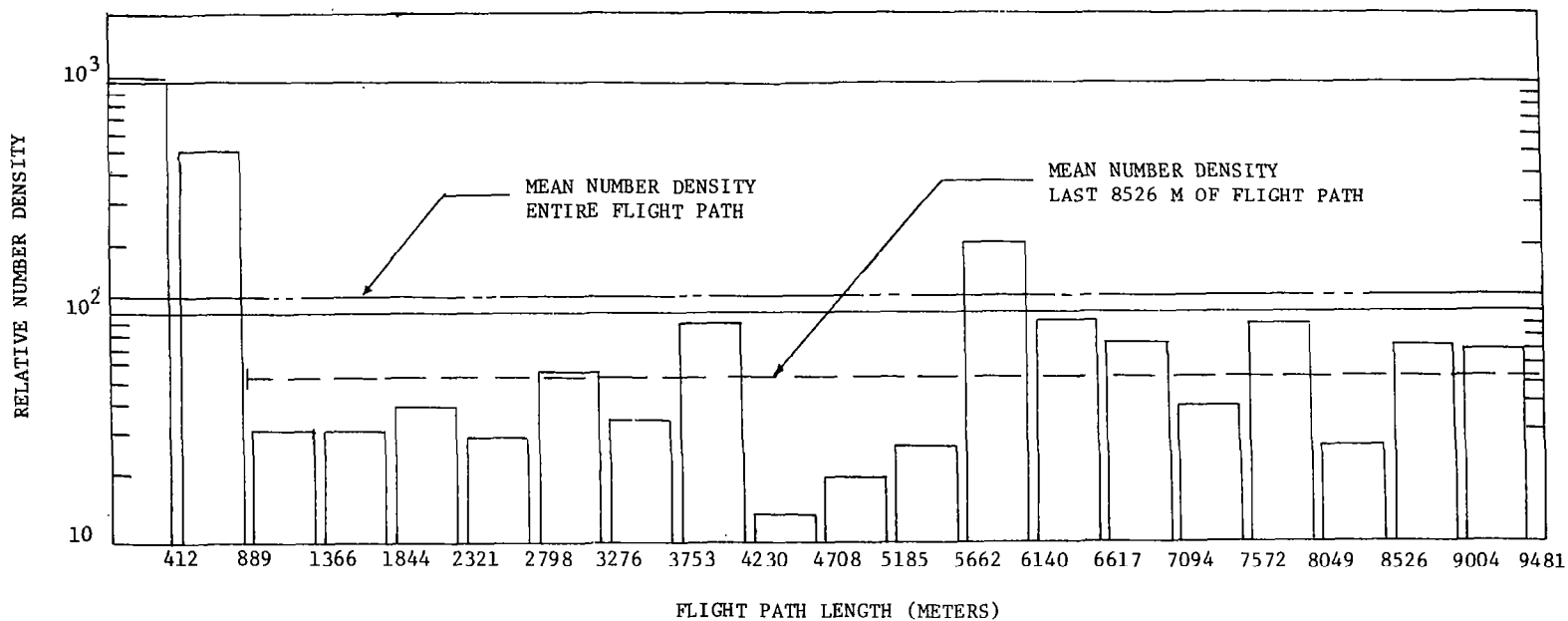


Figure 2. November 25, Flight 2. Track 11 (Glendale), Altitude Is 500' AGL. Relative Number Density Distribution Over 412 m Distance Increments For A Horizontal Sample Path.

APPLICATION OF RAMAN SCATTERING TO THE CHARACTERIZATION
OF ATMOSPHERIC AEROSOL PARTICLES

H. Rosen and T. Novakov

Lawrence Berkeley Laboratory, University of California, Berkeley CA 94720

Airborne particulates play a major role in the air pollution problem. They are responsible for acid rain, reduced visibility, and, in certain size ranges, are deposited in the lungs where they can cause a variety of adverse health effects. Considerable effort has been expended in the analysis of these particulates. Such techniques as wet chemistry, X-ray fluorescence, infrared spectroscopy, and ESCA have been used rather extensively. Yet there are still great uncertainties as to the chemical form and origin of many of the particulate species. In this paper we would like to report on our preliminary studies to explore the feasibility of characterizing particulate pollutants by means of Raman spectroscopy. We believe that this is the first attempt to apply this spectroscopic technique in this area of research. The samples studied were, among others, diesel exhaust particles, automobile exhaust particles (unleaded fuel, no catalytic converter), and several ambient air samples. Our results indicate that species with graphitic structure are a major component and may be the dominant component in both source-enriched and ambient samples. The implications of this observation could be quite important in terms of atmospheric chemistry, health effects, weather modifications, and the effects of aerosols on the earth's albedo.

In Figure 1 we show the Raman spectrum obtained from automobile exhaust. Similar spectra were observed for diesel exhaust, activated carbon, and polycrystalline graphite. The major features of the Raman spectrum are two intense lines at $\sim 1350 \text{ cm}^{-1}$ and $\sim 1600 \text{ cm}^{-1}$. In the ambient samples, where the signal to noise is severely limited by the large fluorescence background, the only lines that were clearly seen above the noise level were also in this spectral region. In Figure 2 we show the Raman spectrum for the various samples in the region between $1200-1700 \text{ cm}^{-1}$.

In perfectly ordered single crystal graphite specimens only the Raman mode near 1600 cm^{-1} is observed and from a group theoretical analysis has been assigned to the $k = 0, E_{2g}$ phonons of the graphite lattice.¹ The mode near 1350 cm^{-1} appears only in samples which are not perfectly ordered, and

its intensity relative to that of the one near 1600 cm^{-1} varies inversely with the crystallite size, L_a , as obtained from X-ray data.¹ It is evident from Figure 2 that the spectra of activated carbon, diesel exhaust, automobile exhaust, and ambient samples are very similar. The positions of the two Raman modes in these spectra are coincident to within $\pm 10\text{ cm}^{-1}$, which is the estimated error. Since the phonon frequencies are a sensitive probe of the lattice, we suggest that these spectra give strong evidence for the existence of physical structures similar to activated carbon in the samples studied.

Using the available results from the literature,¹ we can estimate the crystallite sizes in the various samples from the intensity ratios of the two observed Raman modes. The ambient, diesel exhaust, and automobile exhaust particles appear to have roughly the same peak intensity ratio, yielding crystallite sizes between 50 and 100 \AA .

Our results indicate that physical structures similar to activated carbon are present in exhaust and ambient samples. The fact that the two observed modes are the dominant features of the Raman spectrum may indicate that "graphitic" soot is the major component in these samples. However, the large intensity of these modes may be due just to their large Raman cross section. Quantitative interpretation of these results will have to await a more detailed analysis. Such analysis will have to include measurements of the Raman cross section, the optical absorption cross section, and also take into account the little-understood particle size effects.

References

1. F. Tuinstra and J. L. Koenig, *J. Chem. Phys.* 53, 1126 (1970).
2. F. S. Goulding, J. M. Jaklevic, and B. M. Loo, Report UCID-3767, Lawrence Berkeley Laboratory, University of California, Berkeley, CA 94720; Report EPA-650/2-75-048, U.S. Environmental Protection Agency, Washington, DC 20460 (April 1975).

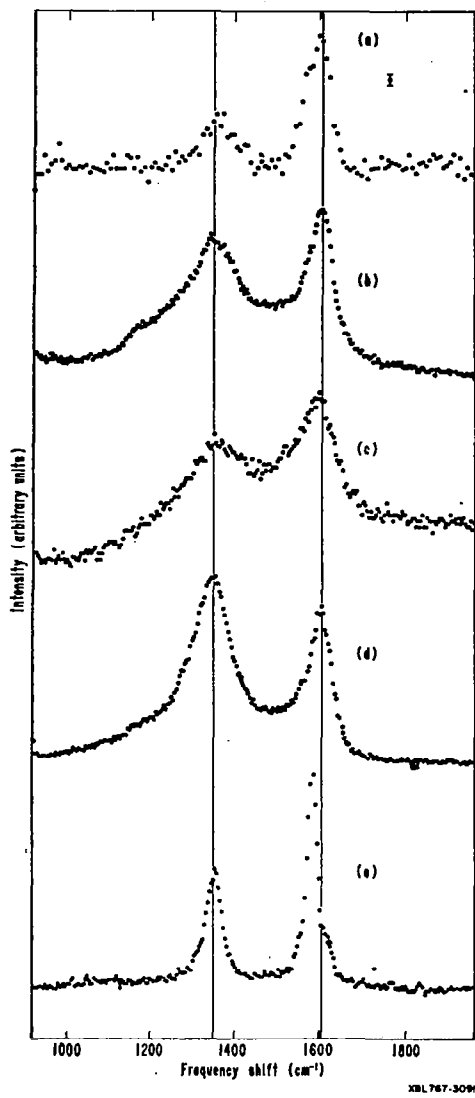
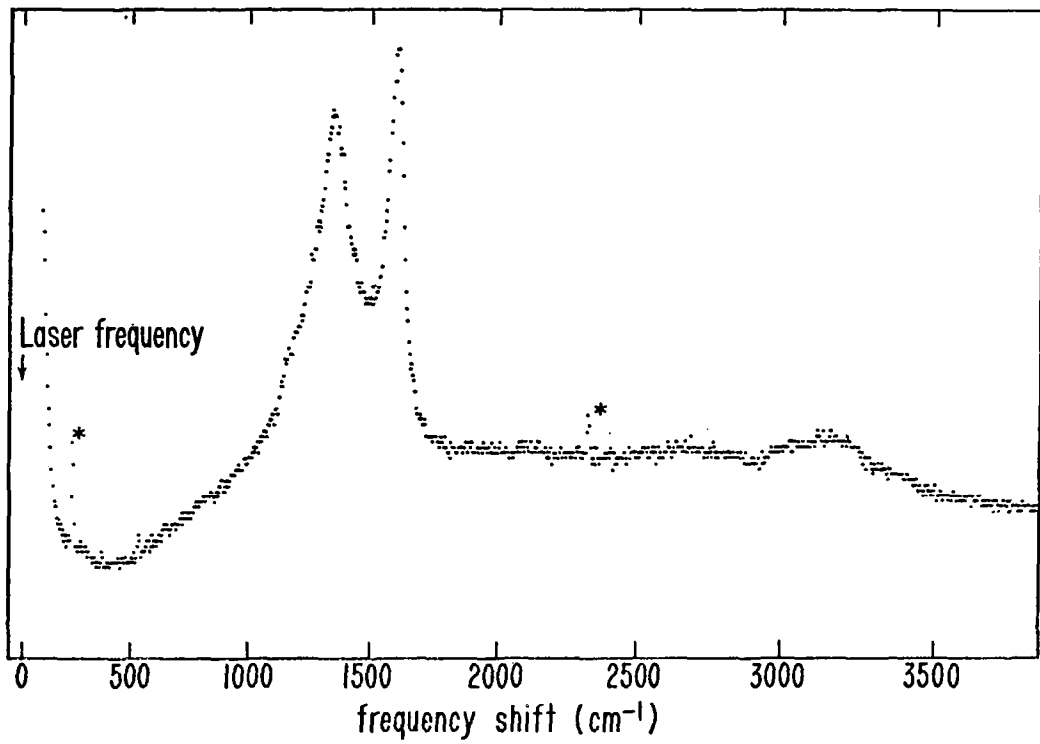


Figure 2. Raman spectra between 1200 and 1700 cm^{-1} of a) ambient sample collected in 1975 as part of the RAPS program (The sample was collected on a dichotomous sampler² and was in the small size range fraction.); b) automobile exhaust collected from 100 cold starts of a 1974 Pinto using lead-free gas and having no catalytic converter; c) diesel exhaust; d) activated carbon; and e) polycrystalline graphite. The slit width for samples b-e was 3 \AA ; while for sample a, 7- \AA slits were used to improve signal to noise.



XBL 767-3092

Figure 1. Raman spectrum of automobile exhaust in the spectral region between 90 and 3830 cm⁻¹. The sample was collected from 100 cold starts of a 1974 Pinto using lead-free gas and having no catalytic converter. The slit width for this scan was 3 Å. The lines identified with an asterisk are due to grating ghosts.

MEASUREMENTS OF THE INFRARED PROPERTIES OF AEROSOLS

John F. Ebersole, David M. Mann*, and Conrad M. Gozewski

Aerodyne Research, Inc.
Bedford, Massachusetts 01730

The experimental program described in this paper is designed to obtain data on the fundamental optical properties of atmospheric and dust-like aerosols at DF (deuterium fluoride) laser wavelengths in the 3 to 4 μm spectral region. Aerosol attenuation of DF laser radiation is not well defined at present. The 3 to 4 μm region is considered to be an atmospheric window because of relatively low molecular absorption. However, aerosol extinction has been estimated to be comparable to or greater than molecular absorption in this region. Unfortunately, the scarcity of data on the infrared optical properties of atmospheric and dust-like aerosols makes these estimates unreliable for systems evaluation, although both scattering and absorption contribute to laser attenuation. One important application is the effect of aerosol-induced absorption on the threshold of laser thermal blooming. Since this threshold is a function of the aerosol absorption coefficient at the particular wavelength of interest, there is particular interest in the degree of aerosol absorption at DF laser wavelengths.

Our experimental system is designed to measure the total extinction (scattering plus absorption) and the scattering of DF laser radiation by atmospheric aerosols. The data yield the corresponding extinction and scattering coefficients, the difference of which is the absorption coefficient. Such data permit a more accurate assessment of the role of aerosols in the attenuation and degradation of DF laser beam profiles.

An integral part of the program is an effort to characterize the aerosols used in the measurements according to chemical composition, particle number density, and mass loading. The primary emphasis on this present work phase is the development of a system capable of measuring the infrared properties of dust-like aerosols, such as silicates and aluminates, and smoke-like aerosols such as carbons and soots.

Figure 1 shows a schematic of the experimental apparatus. The output from the DF laser is split into two beams -- one beam is directed to a multiple-pass White Cell⁽¹⁾ with an effective path length of 0.24 km (for 40 passes), the other beam is directed into the Scattering Cell. By means of mirror M_1 and beam splitter BS_1 , the (visible) beam from He-Ne Laser No. 1 is made collinear with the infrared laser beam

*Now with the Air Force Rocket Propulsion Laboratory, Edwards AFB, California 93523

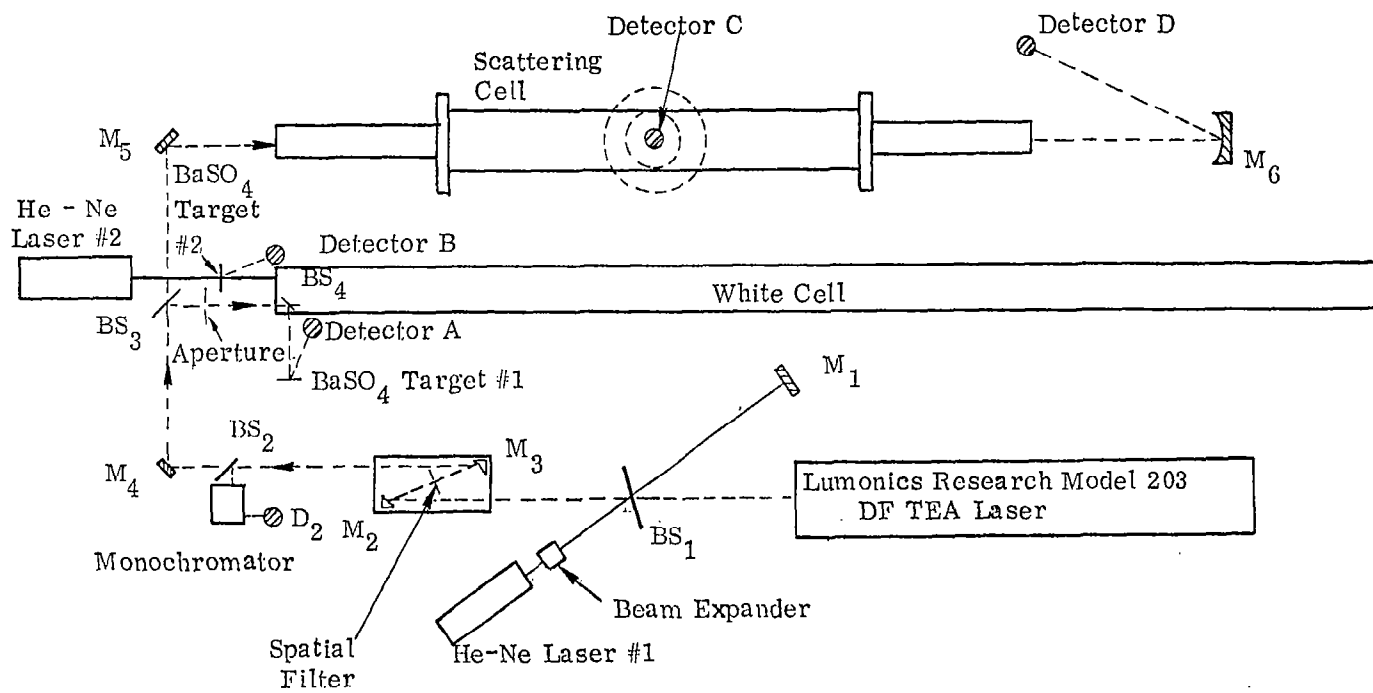


Figure 1. Schematic of experimental apparatus for measuring aerosol extinction and scattering at DF laser ($3-4 \mu\text{m}$) wavelengths. The (visible) He-Ne lasers are used for alignment.

from the DF laser to aid in alignment of the optics. Mirrors M_2 and M_3 are used for two purposes: (1) to focus the infrared beam to a small focal point, allowing use of a spatial filter (pinhole) to filter out the DF laser superradiant background (which has a larger divergence than the laser beam itself); and (2) to conveniently control the divergence/convergence of the infrared laser beam. Beamsplitter BS_2 is temporary, allowing the spectral output of the beam to be monitored by a monochromator. Beamsplitter BS_3 directs a portion--about 10% (5% from each surface)--of the laser light into the White Cell. The aperture (4 mm) after BS_3 is used to trim the beam size to match the entrance and exit ports of the White Cell. Beamsplitter BS_4 directs a portion of the laser beam onto Target #1, a diffuse surface of pressed $BaSO_4$ for Detector A (a PbSe detector). The output beam from the White Cell is directed onto a second target for Detector B. Target #2 is removable so that He-Ne Laser No. 2 can be used for alignment of the White Cell. The remaining 90% of the light from BS_3 is directed into the Scattering Cell. This cell has a liquid-nitrogen-cooled, 170° field-of-view InSb detector. Baffles in the Scattering Cell reduce background wall scattering to approximately 10^{-10} of the incident beam intensity. Most of the measurements to date have been with the White Cell, as discussed below.

One of the features of this White Cell is the use of aerodynamic windows (flowing dry nitrogen gas) and flowing aerosols in order to prevent contamination of the White Cell mirrors by aerosol deposition, a very important consideration when working with dust-like aerosols. The White Cell is 6 m in length, so 40 passes produce an effective path length of 0.24 km. When the aerodynamic windows are used, a single-pass path length of only 5 m is available for the input flowing air/aerosol mixture, since the dry nitrogen prevents the aerosols from reaching any closer than 0.5 m from the mirrors at each end of the cell. Thus, for 40 passes the effective length is 0.20 km when aerodynamic windows are used.

The calibration of the White Cell is achieved by first measuring the residual extinction (such as that due to reflection losses at the mirror surfaces in the White Cell) when filled with flowing air (with no aerosols). Then the extinction of the White Cell is measured when filled with flowing methane (500 to 1500 ppm mixture with nitrogen), while simultaneously flowing dry nitrogen for the aerodynamic windows. With an effective path length of 0.20 km, an extinction coefficient of $0.86 \text{ km}^{-1} \pm 0.15 \text{ km}^{-1}$ was measured at $\lambda = 3.80 \mu\text{m}$ from the DF laser. This compares very favorably with a value of the methane absorption coefficient of 0.83 km^{-1} (for a 1500 ppm mixture) as measured by D. J. Spencer et al.⁽²⁾ The methane extinction test was repeated in a

static (i.e., non-flowing) situation. Using the value of 6 m for the single-pass path length of the White Cell with no aerodynamic windows (0.24 km total path), a value of $0.86 \text{ km}^{-1} \pm 0.15 \text{ km}^{-1}$ for the extinction of methane was again obtained. These measurements show that the dry nitrogen aerodynamic windows are functioning properly.

Alumina (Al_2O_3) particles were next injected into the White Cell. The size and number distribution flowing through the White Cell was (according to a model 218 Royco particle counter) as follows: $1\text{--}3 \mu\text{m}$, 54000 per minute; $3\text{--}5 \mu\text{m}$, 45000 per minute; $5\text{--}10 \mu\text{m}$, 22000 per minute; $10 \mu\text{m}$ and greater, less than 100 per minute. Thus our distribution was primarily $1\text{--}5 \mu\text{m}$ size. We measured the extinction coefficient for this particle distribution (taking into account our calibration measurements) to be 0.4 km^{-1} . Based upon a geometrical scattering cross section calculation, a value of about 0.3 km^{-1} was expected, so our value of 0.4 km^{-1} seems reasonable and will be further compared with Mie theory as time allows.

We have also done work with ambient air Scattering Cell measurements. Although we have not yet injected dust-like aerosols into that cell, our preliminary measurements indicate that we can measure scattering coefficients on the order of 0.05 km^{-1} .

These measurements have proven the validity of the experimental technique. Further work is now being done to improve the accuracy of the measurements.

The authors thank Dr. Robert C. Sepucha for his important contributions in the early stages of this program.

This work was supported by the U.S. Army Missile Command, Redstone Arsenal, Alabama, Contract No. DAAH01-76-C-0647.

REFERENCES

1. J. U. White, J. Opt. Soc. Am. 32, 285 (1942).
2. D. J. Spencer, G. C. Denault, and H. H. Takimoto, Appl. Opt. 13, 2855 (1974).

APPLICATION OF SATELLITE IMAGE ANALYSIS TO TRANSPORT
AND DEPOSITION STUDIES OF DUST STORM AEROSOL:
SUMMARY*

William M. Porch and James E. Lovill

Lawrence Livermore Laboratory, University of California,
Livermore, CA 94550

* This is a summary paper based on original
Lawrence Livermore Laboratory Report UCRL-78685

1. INTRODUCTION

For the past four years our group at LLL has cooperated with the National Center for Atmospheric Research (NCAR) in studies of wind blown dust.¹⁻⁴ Our study has been focused on mechanisms of aerosol generation, suspension by wind, and subsequent transport and deposition. To better understand these mechanisms, experiments have been conducted in which fast response aerosol light scattering measurements were taken in conjunction with fast response measurements of vertical and horizontal wind profiles. To supplement these data, we have analyzed LANDSAT data taken during a Texas dust storm under cloud free conditions. We can tell much about the aerosol and its transport properties from analyses of the decrease in light scattering from suspended dust transported across a reservoir approximately 150 kilometres from our measurement site. The purpose of this paper is to compare the conclusions drawn from these two data sets. A good comparison is found between deposition velocities (estimated from the satellite sensed aerosol light scattering depletion ratios with distance across the reservoir) and measurements of aerosol surface deposition velocities.

2. DATA AND RESULTS

One of the early problems encountered when one studies wind blown dust from satellites is to distinguish between blown dust and water (or ice) cloud. This problem was solved in our case by comparing satellite images on two days. The first day was cloud free with blown dust near the surface. The second day was cloudy, but dust free. LANDSAT imagery was compared over northwest Texas on April 2 and 20, 1974, which represented these conditions. The LANDSAT system is in a sun synchronous orbit at an altitude of about 1100 km. The sensor scans cross-track swaths of 185 km width, imaging six scan lines across (three of which are used here) in each of the spectral bands simultaneously. The general area from which the satellite data came was between 31° and 32°N and 102° and 103°W. This area is approximately 150 kilometres south of Plains, Texas, where surface wind and aerosol filter measurements were being taken. This area also contains the Midland Weather Service Office which contributed helpful wind and weather information.

In order to study these properties of the dust, the original photographic data was digitized by a microdensitometer. The digitizations were done in 20 micrometre rows and columns, numbering 1024. Figures 1a) and 2a) show contour plots

constructed from this digitization for band 5 (wavelengths between .6 and .7 μm) and band 6 (wavelengths between .7 and .8 μm) respectively. The rectangular strip designates the rows and columns selected for digital averaging. Figures 1b) and 2b) display the decrease in film density on the specified columns from one end of the reservoir to the other in the direction of the wind and perpendicular to it with the column width averaged. If it is assumed that the decrease in absorbed light on the film is proportional to the light scattering aerosol (i.e., neglecting multiple scattering and aerosol absorption effects and water surface conditions over the reservoir) we can derive a useful measure of aerosol transport.

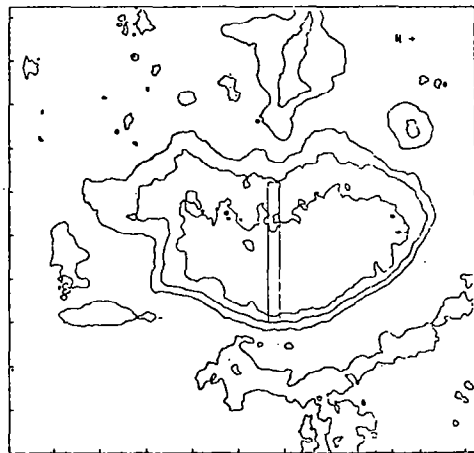


FIGURE 1a). Digital contour plot of band 5 (.6 to .7 μm wavelengths) filtered LANDSAT image of Orient Reservoir during a Texas dust storm with columns and rows specified for averaging to determine deposition of light scattering aerosols as they are transported across reservoir.

3. INTERPRETATION

It is possible to use some of the methodology of pollutant dispersion studies to derive a deposition velocity associated with the decrease in dust across the reservoir if the land surrounding the reservoir is considered as an area pollutant source from the surface. Because the total

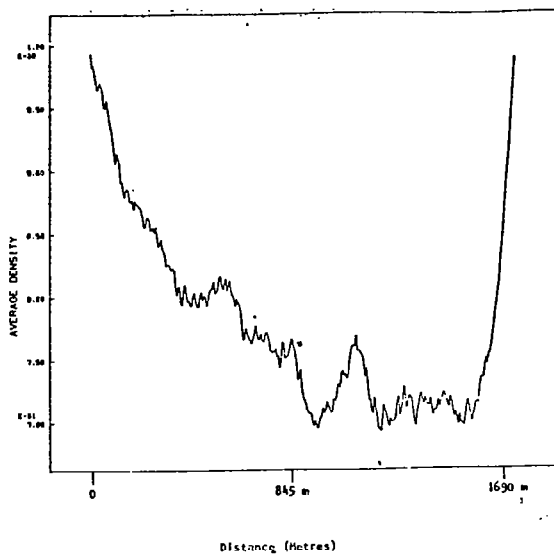


FIGURE 1b). Averaged photographic density as a measure of light scattering aerosol across rows specified in rectangle of Fig. 1a) from upwind to downwind side of 1690 m wide reservoir (band 5).

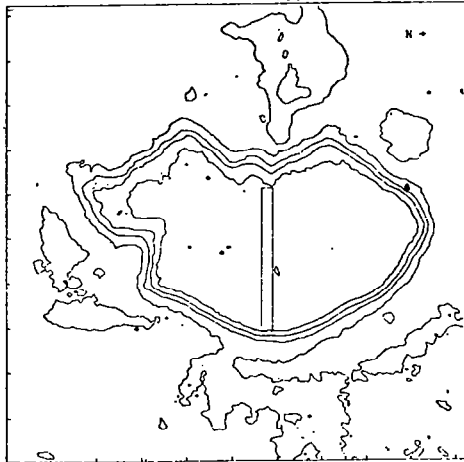


FIGURE 2a). Digital contour plot of band 6 (.7 to .8 μm wavelength) filtered LANDSAT image of Orient Reservoir during a Texas dust storm with columns and rows specified for averaging to determine deposition of light scattering aerosols as they are transported across reservoir.

vertical column of aerosol is being visually integrated, the aerosol concentration (x) is proportional to the source strength divided by the mean wind velocity (Q/\bar{u}) for a uniform area source. If there were no aerosol deposition, x would be uniform across the reservoir. We have assumed a widely distributed area source upwind of the reservoir so that horizontal diffusional

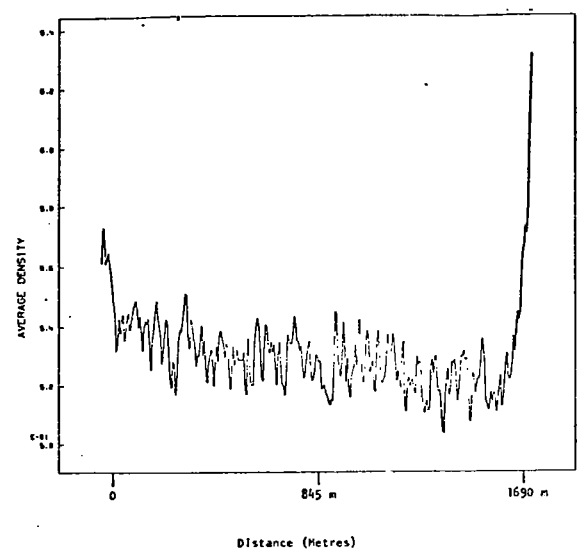


FIGURE 2b). Averaged photographic density as a measure of light scattering aerosol across rows specified in rectangle of Fig. 1a) from upwind to downwind side of 1690 m wide reservoir (band 6 filtered LANDSAT image).

effects are negligible. Since there is a decrease evident in Fig. 1b of between 35 and 50% (this percentage is a function of the location selected to study the dust effect), we can use the source depletion equations described by Van der Hoven.⁵ Assuming neutral stability (Pasquill category C) the depletion ratio (Q'_X/Q'_0) at deposition velocity (V_d) of .01 m/sec and mean wind speed (\bar{u}) of 1 m/sec is ~.6 from the charts in Ref. 5. Using the equation

$$\frac{\bar{u}_1 V_d 2}{\bar{u}_2 V_d 1} = .5 \text{ to } .35 = \left(\frac{Q'_X}{Q'_0} \right)_2 \left(\frac{Q'_X}{Q'_0} \right)_1 \quad (1)$$

where the subscript 2 refers to the conditions applicable to our data (i.e., $u_2 \sim 10 \text{ m/s}$) and 1 refers to the standard values listed above for which the charts were derived. Solving for $V_d 2$ (deposition velocity)

$$V_d 2 = .13 \text{ to } .2 \text{ m/sec} .$$

Because the particle size implied by the almost complete lack of scatter from band 6 would indicate very small particles, it is probable that turbulent deposition dominates gravitational settling in this case. If a more precise determination of deposition velocity range were required, a full blown particle-diffusion code with size discrimination such as that developed by Gudiksen et al.⁶ could be used. A deposition velocity of 13 to 20 sm/sec would be quite high under normal low wind speed conditions. However, the deposition velocity increases with wind speed and with high winds the water surface was undoubtedly rough and probably white capped increasing the surface friction. The

subsequent year measurements from a clay field (from which it is difficult to suspend particles due to their small size) of dust blown in from surrounding fields showed a turbulent deposition velocity of ~ 10 cm/sec.³ Deposition velocities measured in a wind tunnel by Sehmel⁷ are also on the order of 10 cm/sec for high friction velocities and particles smaller than 1 μm in radius.

Visibility studies have also been conducted in Texas dust storms.^{8,9} These studies emphasize the relatively large effect on visibility of particles greater than 1 μm diameter in dust storms, as compared to other visibility reducing situations such as smog or haze. If this were the case in our situation, it would be difficult to explain the major increase in contrast between band 5 and band 6. However, visibility measurements are taken near the ground and there is a dramatic difference between aerosol size distributions over just a few metres in height above the surface in a dust storm.⁴ These measurements also show that a sizable component of the light scattering aerosol even near the surface is from aerosol from .1 to 1 μm radius.³

4. CONCLUSIONS

Digital image analysis of LANDSAT data has proven to be a useful tool in understanding aerosol generated by wind in dust storms. The variation in contrast between band 5 (wavelengths between .6 and .7 μm) and band 6 (wavelengths between .7 and .8 μm) for dust blown across water indicate the aerosols transported any distance are mostly smaller than a micron in diameter. This effect was not observed when the reservoir was covered by a liquid water cloud twenty days later, indicating a larger particle bias in cloud droplet size distribution and/or higher concentrations of droplets. We were able to use the digitized image of the decreasing dust from the upwind boundary of the reservoir to estimate the aerosol deposition velocity to the water. The deposition velocity of approximately 15 cm/sec agrees well with measured deposition velocities for particles less than a micron in diameter on the surface, using an integrating nephelometer.

Further case studies of the type presented here should be conducted under varying terrain, soil conditions, and meteorological situations. Correlation of satellite observed aerosol transport, deposition and resuspension under a variety of conditions may permit meso-, synoptic- and/or global scale measurement of aerosol movement within the boundary layer. Additional radiometer channels on future earth resources satellites may accelerate our understanding of this phenomenon.

5. ACKNOWLEDGEMENTS

The author would like to thank Drs. M. H. Dickerson and J. B. Knox for their support with this project, R. Lange and K. R. Peterson for their help with the transport analysis.

This work was performed under the auspices of the U. S. Energy Research and Development Administration under contract W-7405-Eng-48.

6. BIBLIOGRAPHY

1. Porch, W. M., "Fast-Response Light Scattering Measurements of Aerosol Suspension in a Desert Area," *Atmos. Environ.*, 8, 877, 1974.
2. Porch, W. M. and J. H. Shinn, "Fast-Response Light Scattering Measurements of the Characteristics of Wind Suspended Aerosols," Lawrence Livermore Laboratory Report UCRL-76014, 1974.
3. Porch, W. M. and J. E. Lovill, "Aerosol Deposition and Suspension During a Texas Dust Storm," Lawrence Livermore Laboratory Report UCRL-78011, 1976.
4. Gillette, D. A., "Production of Fine Dust by Wind Erosion of Soil: Effect of Wind and Soil Texture," *Atmosphere-Surface Exchange of Particulate and Gaseous Pollutants*, ERDA Symposium Series 38, 1976.
5. Van der Hoven, I., "Deposition of Particles," *Meteorology and Atomic Energy*, D. H. Slade (Ed.), U. S. AEC, pp. 202-208, 1968.
6. Gudiksen, P. H., K. R. Peterson, R. Lange, and J. B. Knox, "Plume Depletion Following Postulated Plutonium Dioxide Releases from Mixed-Oxide Fuel-Fabrication Plants," Lawrence Livermore Laboratory Report UCRL-51781, 1975.
7. Sehmel, G. A. and W. H. Hodgson, "Predicted Dry Deposition Velocities," *Atmosphere-Surface Exchange of Particulate and Gaseous Pollutants*, ERDA Symposium Series 38, pp. 399-422, 1974.
8. Patterson, E. M., D. A. Gillette, and G. W. Grams, "The Relation Between Visibility and the Size-Number Distribution of Airborne Soil Particles," *J. Appl. Met.*, 15, pp. 470-478, 1976.
9. Hagen, L. J. and N. P. Woodruff, "Air Pollution from Dust Storms in the Great Plains," *Atmos. Environ.*, 7, pp. 323-332, 1973.

NOTICE

"This report was prepared as an account of work sponsored by the United States Government. Neither the United States nor the United States Energy Research & Development Administration, nor any of their employees, nor any of their contractors, subcontractors, or their employees, makes any warranty, expressed or implied, or assumes any legal liability or responsibility for the accuracy, completeness or usefulness of any information, apparatus, product or process disclosed, or represents that its use would not infringe privately-owned rights."

**Satellite Solar Occultation Measurements,
"SAM II and SAGE"**

M. P. McCormick, H. B. Edwards, L. E. Mauldin III, and L. R. McMaster
NASA Langley Research Center

The NASA Langley Research Center is developing satellite sensors for measuring stratospheric constituents via the measurement of atmospheric limb extinction of solar radiation (solar occultation). The radiance data from two of these sensors, the Stratospheric Aerosol Measurement II (SAM II), and the Stratospheric Aerosol and Gas Experiment (SAGE), will be inverted to determine aerosol extinction as a function of altitude in the following manner. As the satellite emerges from the earth's shadow during each orbit, the SAM II or SAGE sensor on board will acquire the sun and measure solar radiation in a number of wavelength bands. As the satellite continues in its orbit, the line of sight from the satellite to the sun will scan the earth's atmosphere from horizon up, resulting in a measurement of attenuated solar intensity at different atmospheric layers. The procedure is repeated in a reverse sense during satellite sunset. The sensors will have a field-of-view of approximately one-half arc minute which gives a vertical resolution of better than 1 kilometer. With proper correction of solar limb darkening and atmospheric refraction effects, data from each sunrise or sunset event is converted to an intensity versus atmospheric tangent-height profile. Inversion into an extinction coefficient versus altitude profile is then performed.

SAM II will be flown aboard the satellite Nimbus G, shown in figure 1 with it's payload complement. It will be launched October, 1978 into a highnoon sun-synchronous circular orbit at an altitude of 955 kilometers. Nimbus G is the seventh in a series of Nimbus spacecraft and is the first NASA satellite to have the primary objective of measuring environmental quality. The SAM II tangent profiles will be obtained for this orbit in a band of latitudes from 64° N to 80° N and 64° S to 80° S. SAM II is a one spectral channel photometer centered at 1.0 μ m with 400 μ m half-width. The extinction of solar radiation at this wavelength is dominated by aerosol scattering over the altitudes of prime interest, 10 to 30 kilometers. For example, for representative atmospheric models at 18 km, the aerosol extinction coefficient is more than an order of magnitude larger than the molecular extinction coefficient. The prime objective of SAM II is to monitor aerosols in the earth's polar region thus establishing a baseline in these inaccessible regions. From these data, hemispherical differences and transient phenomena will be investigated. The University of Wyoming, under the direction of Dr. T. J. Pepin, is the prime contractor for the SAM II hardware development. Ball Brothers Research Corporation, Boulder, Colorado is the major subcontractor. A science team has been assembled to direct the experiment development and archiving of the science data. They are: Dr. B. M. Herman, University of Arizona; Dr. P. B. Russell, Stanford Research Institute; Dr. G. W. Grams, National Center for Atmospheric Research;

and, Dr. T. J. Pepin, University of Wyoming. The SAM II hardware is shown in figures 2 and 3.

SAGE will fly aboard the Applications Explorer Mission-B satellite (AEM-B) scheduled for launch in March, 1979. AEM-B will have a circular orbit altitude of 600 km and 50 degree inclination. The high orbit precession relative to the sun will provide nearly global coverage from the equator to \pm 72 degrees latitude repeating this coverage approximately every 2 weeks. This is shown in figure 4 (from reference 1). SAGE has four spectral channels centered at $1.0\mu\text{m}$, $0.6\mu\text{m}$, $0.45\mu\text{m}$, and $0.385\mu\text{m}$. The $0.6\mu\text{m}$ channel is centered in the Chappius band for ozone profile determinations. Utilizing these data with ground truth information will allow the following studies to be performed: aerosol and ozone global concentrations to help establish baseline data; transient phenomena such as volcanic eruptions; hemispheric differences; transport phenomena; tropospheric/stratospheric exchange; and, radiation effects of stratospheric aerosol and ozone on the global climate and available solar energy. SAGE hardware, shown in figures 5 and 6, is being built by Ball Brothers Corporation and the AEM-B spacecraft by the Boeing Company, Seattle, Washington.

References

Mission Analysis for Satellite Measurements of Stratospheric Constituents by Solar Occultation,

E. F. Harrison, N. Green, D. R. Brooks, G. F. Lawrence, and M. P. McCormick.

AIAA 13th Aerospace Sciences Meeting
Pasadena, California, January 20-22, 1975

AIAA Paper 75-57.

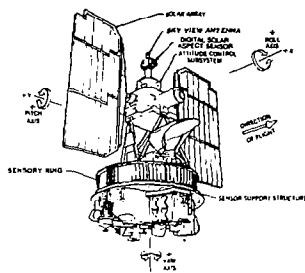


Figure 1. Nimbus G satellite with payload

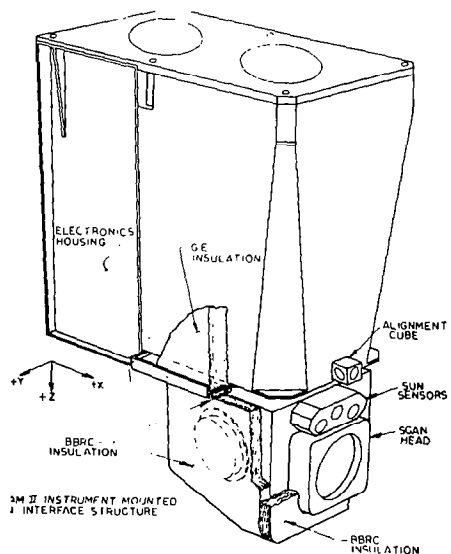


Figure 2. SAM II sensor

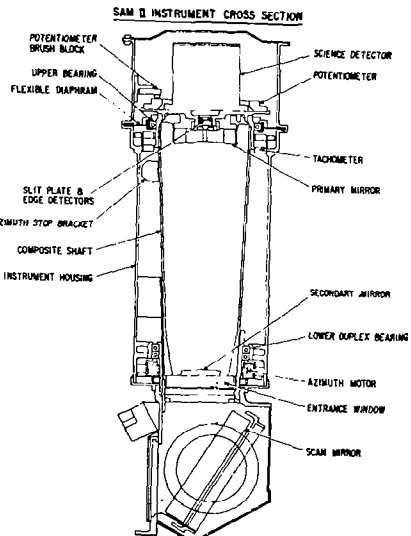


Figure 3. SAM II sensor cross section

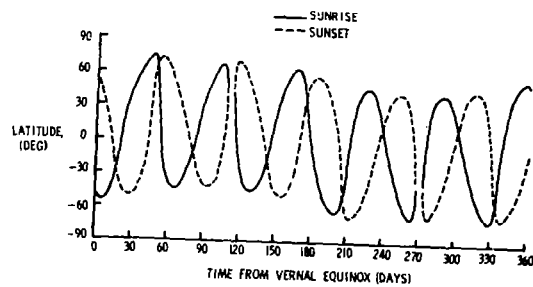


Figure 4. SAGE latitude coverage for 600 km 50° inclined orbit

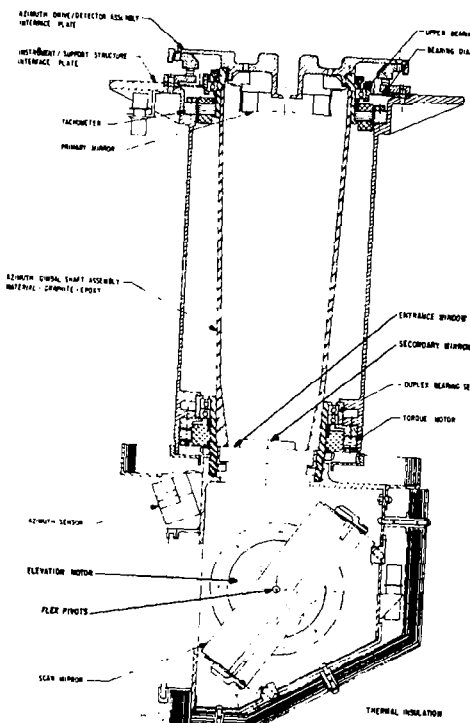


Figure 5. SAGE telescope and elevation mirror cross section

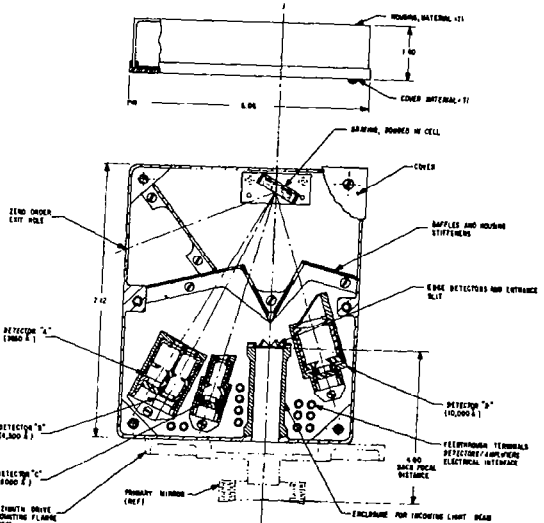


Figure 6. SAGE detector package

KOEPKE, P. and QUENZEL, H.
 Meteorologisches Institut der Universität
 Theresienstrasse 37, D - 8000 München 2, FRG

Remote Sensing of Atmospheric Turbidity from Geosynchronous Orbit

Introduction

The atmospheric turbidity plays an important role with respect to the radiation budget of the earth. Global mapping of the turbidity by satellite measurements would improve monitoring the optical depth caused by the aerosol particles. Here a method is presented to determine the atmospheric turbidity over water surfaces.

Dependency of the radiance on optical parameters

Solar radiation leaving a cloudless atmosphere after being scattered in the atmosphere or being reflected at the earth's surface does not only depend on the turbidity, but also e.g. on the amount of air molecules, the size distribution of the aerosol particles and their complex refractive index and the reflection properties of the earth's surface. All these values besides the turbidity must be understood as perturbing quantities because their actual values at time and location of measurement are unknown within certain limits and cause a certain variability of the outgoing radiances. This variability is numerically simulated.

Computational method and atmosphere-ocean model

Calculation of the radiance is done including multiple scattering with a computational accuracy better than 1%. Four aerosol models after Hänel (1976) are used: maritime aerosol particles and maritime aerosol particles plus Sahara dust, both with relative humidities of 70% and 90%. The reflection properties of the surface are those of an ocean with waves, determined by Raschke (1974) using a wavemodeI of Cox and Munk (1954).

Advantages of a geostationary satellite

A geostationary satellite can measure spectral radiances every half hour from the same points of the earth. The radiance from each point varies due to the course of the sun during the day. This variation over the day contains more information than a single measurement and can be used to get some information on the perturbing parameters. The wide field of view of a geostationary satellite is shown by fig.1 with SP the subsatellite point of the SMS-satellite during GATE as example. The geographical coordinates are relative to SP, because our results are valid relative to any SP.

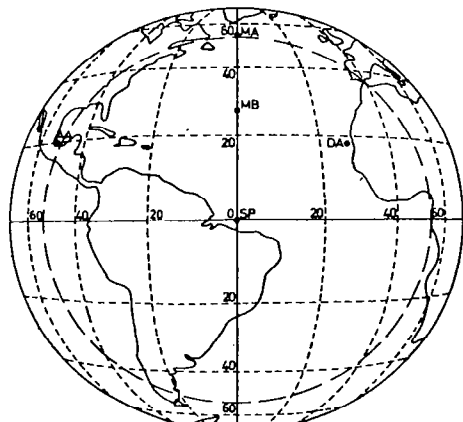


Fig.1

Variation of the radiance for different directions of observation
 In fig.2 calculated radiances at wavelength $0.7 \mu\text{m}$ are plotted versus the time of observation. The curves are valid for the points AA, MA and MB (see fig.1) with the same values of the atmosphere-ocean parameters including the same optical depth. The figure is to demonstrate the differences in the radiance which are only due to the geometry.

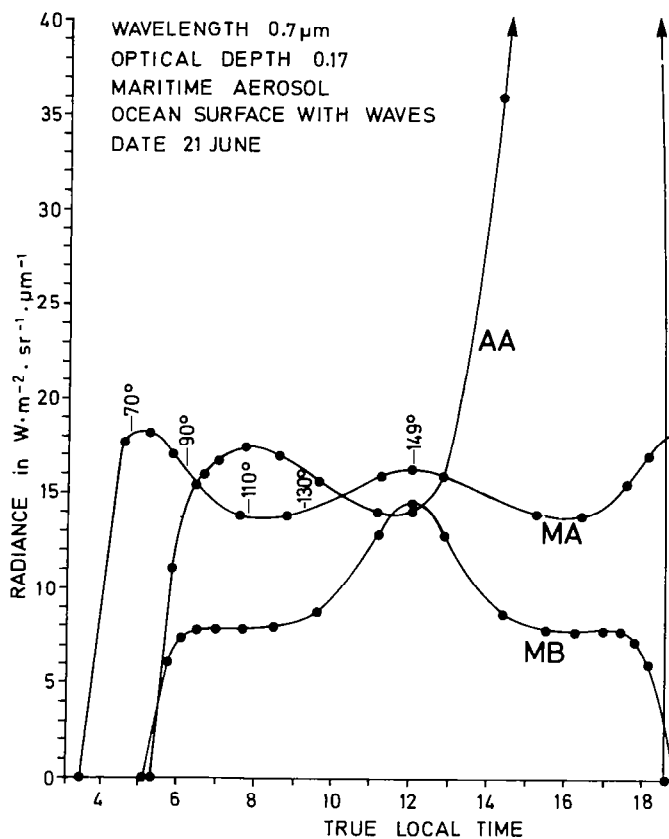


Fig.2

The strong increase of curve AA in the afternoon is caused by the sun glint. This high radiances are not suitable for the turbidity determination, because the variability of the sun glint is too strong due to differing wind speed and wave type and the contribution of the path radiance to the measuring signal is too small. In the vicinity of the sun glint the increase of the radiances caused by the increasing reflection values should not be misinterpreted as increasing turbidity. The high differences between curves MA and MB are because of different scattering features. In a satellite picture different parts therefore appear with differing brightness, which should not be misinterpreted as differing turbidity. The shape of the curves can be explained, e.g. the numbers 70° to 149°

at curve MA indicate the respective scattering angles.

Variation of the radiance due to variation of the optical parameters

Assuming a realistic bandwidth of atmospheric perturbing parameters, the perturbed signal over water surfaces can be interpreted with respect to the optical depth with an accuracy of $\pm 10\%$.

The advantage of water as an underlying surface is not only because of its small albedo, but more because of its highly anisotropic reflectance function with angular regions where its

values are zero. Due to the differing size of the area of the sunlitter, use of a realistic model for the reflection function of water including waves is necessary. Also the amount of white caps on the top of the waves must be considered including its apparent increase for low angles of incidence and observation.

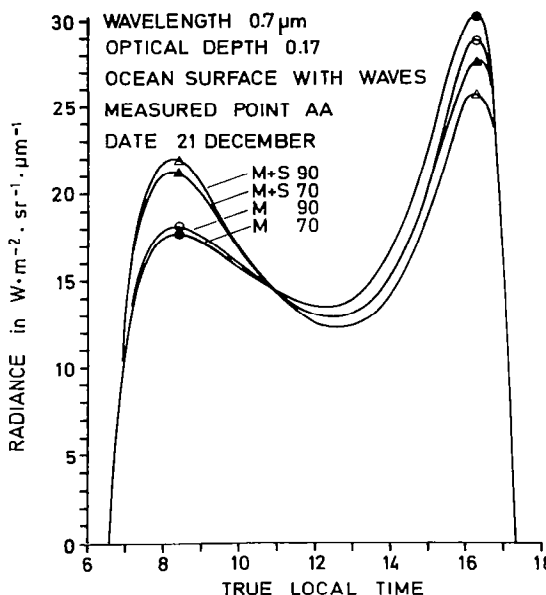


Fig.3

Radiances resulting from the four models of marine aerosols with and without Sahara dust are presented in fig.3 as an example for 21 December at point AA. In the morning and in the afternoon the radiances differ considerably. This demonstrates, that the variation of the radiances with the observational time contains information on the aerosol type. Between 10 and 11 a.m. the variation of the radiances due to the different aerosol models is negligibly small. Such a favorable time is mainly caused by a scattering angle with small differences between the scattering functions of the aerosol models, superimposed by the effect of multiple scattering. The favorable times allow a good turbidity determination because no information about the actual aerosol parameters are needed.

Favorable times exist within a large part of the field of view of a geostationary satellite. They change from point to point and from day to day due to the changing elevation and azimuth

of the incoming solar radiation. Because a geostationary satellite provides measurements every half hour, the measurement at the favorable time can be used for turbidity determination.

Comparison of calculated and measured radiances

The radiances calculated from marine aerosol with and without Sahara dust at 90 % relative humidity are presented in fig.4 as an example for the GATE area (17.9°N , 17.7°W) for 31 July. The high radiances in the morning are influenced by the sunlitter and therefore not suitable for the turbidity determination. The intersection points of the two curves are all influenced by the sunlitter and can therefore not be accepted as favorable times. Between noon and 4 p.m. the radiances related to the two aerosol models differ considerably. This demonstrates again, that the variation of the radiances with the observational time contains information on the aerosol type.

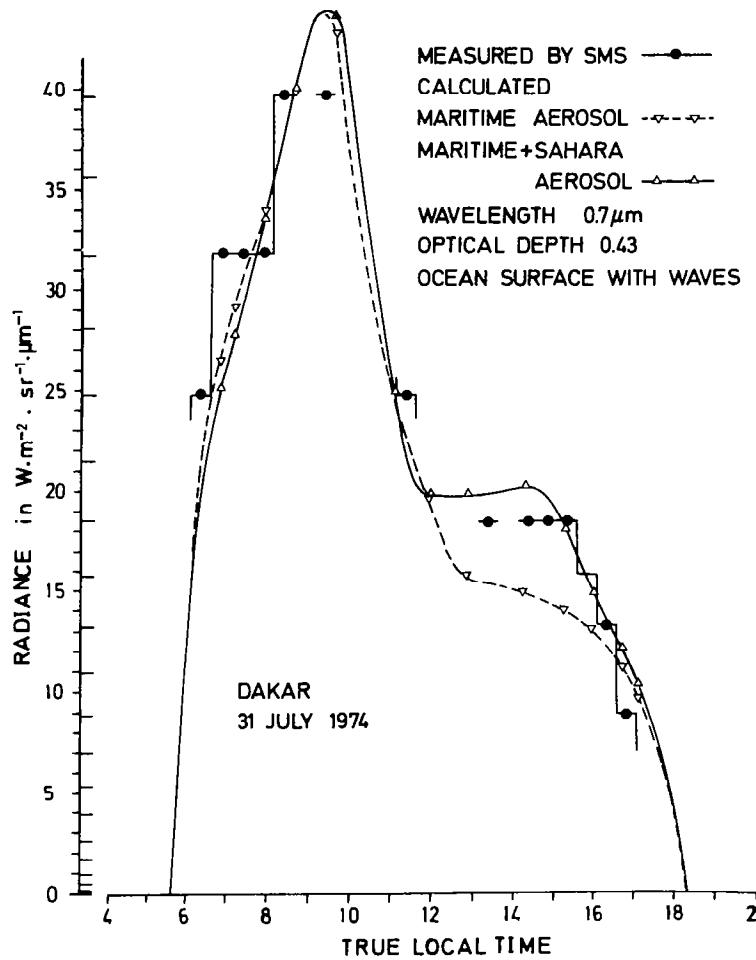


Fig. 4 contains in addition radiances measured by the SMS-satellite at 31 July 74. The line of measured values is interrupted because we had not available the SMS-data of every half hour. The digitalisation steps of the SMS-data are indicated on the right side of the ordinate. They are not small enough for a good turbidity determination. Nevertheless they allow the conclusion, that at the 31 July 1974 at point DA the aerosol was of Sahara dust type and the optical depth caused by aerosol particles was $\tau_d = 0.35$. From ground observations during GATE it is known, that indeed at this day an Sahara dust outbreak happened.

Fig. 4

Contour lines of optical depth

In case the acting aerosoltype and its scattering function is known, turbidity determination for all cloudless points outside the sunlitter is possible by use of only one satellite picture. This will be done for the GATE-area for 31 July 1974. The resulting contour lines will be presented at the meeting.

Literature

Cox, C. and Munk, W. (1954), J. Opt. Soc. Am., 44, 838-850
 Hänel, G. (1976), Adv. Geophys., 19, 74-183
 Raschke, E. (1974), private communication

SOME DATA FROM THE SKYLAB STRATOSPHERIC AEROSOL LIMB EXPERIMENT

David L. Tingey
Boeing Aerospace Company
Seattle, Washington

INTRODUCTION

The atmospheric aerosol content is related to natural causes such as volcanic eruptions, and to cultural services, such as industrial pollutants. For example, man-made and natural activity combine to initiate and grow an aerosol of mixed origin. Water vapor from stratospheric aircraft can nucleate on volcanic dust and normal evaporative water can condense on industrial particulates or sulfates. Atmospheric scientists have long been interested in the distribution of aerosols in the atmosphere and how the aerosol distribution might be related to these possible sources. This is reflected in the vast literature that has grown up on the subject and in the considerable efforts that have been made to determine aerosol distributions. These experiments include hundreds of aircraft, rocket, and balloon flights and many ground-based studies using searchlights and lasers. Some motivation was supplied by the purely scientific objective of understanding our atmosphere. However, other efforts were also motivated by a desire to make practical applications of this knowledge in astronomy, meteorology, defense, and other fields.

This paper describes one of the results obtained from a Skylab experiment designed to study the distribution of aerosols in the stratosphere. Data were from measurements made of the back-scatter brightness of the earth's limb from the earth's surface to an altitude of about 40 Km using a multispectral scanner.

APPROACH

The data presented in this paper were acquired with a multispectral conical scanner approximately every .01 seconds. Several hundred contiguous scans were recorded for each site over which data was acquired. Since horizontal homogeneity can be assumed over several kilometers, these scans served as redundant data which could be used to average gaussian noise. The scan averaging was limited only by the vehicle motion; that is, the instantaneous field-of-view of each detector element changes in altitude as the sensor pointing vector progresses across the limb. The sensor resolution was about

1/2 km (0.18 milliradians at 2400 km), and the nominal rate at which the sensor pointing vector scanned the limb was (2.2 ± 0.2) km/sec due to vehicle motion, therefore twenty-five scans covered about one resolution width (25 scans \times .01 sec/scan \times 2.2 km/sec). Each data point (pixel) was therefore derived by averaging the same data point for 25 adjacent scans thus reducing the gaussian noise by 80% $(1 - \frac{1}{\sqrt{\text{number points}}})$.

A method for determining the location of the field-of-view was also necessary. The location of the field-of-view was determined by ephemeris and ancillary data to about 12.5 milliradians. This accuracy was adequate for nadir viewing, for which the instrument was designed, but was inadequate for limb viewing. The apparent edge of the earth was also inadequate as a reference point since the true earth-atmosphere interface is detected only by the long wavelengths and is too often obscured by clouds. It was therefore necessary to compare the limb brightness curves above 25 km altitude with reference curves based on recent measurements (1), (2) to determine altitudes of the fields-of-view. It was found that, by allowing the sensor calibration constants to vary slightly from those provided with the data, the brightness curves agreed much better with the reference curves. The variations in calibration constants were always less than 10%. It should be noted that refraction effects were included in the comparison of the measured brightness and the simulated brightness, but, in fact, refraction effects were found to be very small in the 10-40 km region measured. Two refraction techniques were used (3), (4) to corroborate this conclusion.

RESULTS

The most distinctive observation was a peak in the limb brightness curve apparent in the lower altitudes. The peak was not present in the shorter wavelengths; it became evident at about 0.8 μm and grew relative to radiance values of adjacent altitudes. Figures 1 - 5 respectively represent the spectral dependence at $\lambda(\mu\text{m}) = .44, .65, .83, 1.14, 1.65$ (median value of the spectral band). These data were obtained from scans 600-624 of Pass 61 just south of the African continent ($\sim 45^\circ\text{S}, 34^\circ\text{E}$). A similar set of curves (not shown) obtained from scans 100-124 show the same peak demonstrating its extent over at least 10 n.m. Pass 47 (scans 300-324) over the United States ($\sim 43^\circ\text{N}, 104^\circ\text{W}$) also contained a similar peak. Figure 6 (Page 130) shows the fit of the limb brightness to the reference brightness curve. This is useful for assigning an

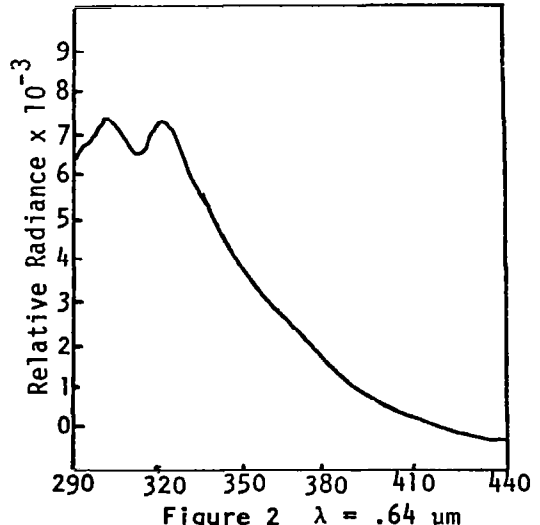
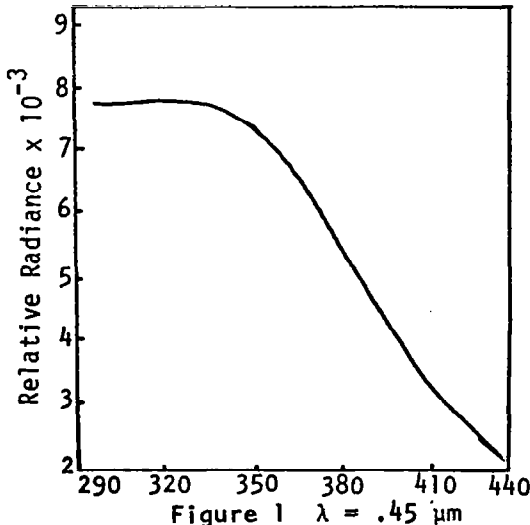
approximate altitude to the peak. With pixels 340 to 440 of Figure 1 corresponding to altitudes 17 km to 37 km of Figure 6 it is seen that there are approximately 5 Pixels/km (not accounting for the effects of the conical sensor in scanning the limb). To this approximation the peak is centered on pixel 320 or 4 km below the 17 km low point of Figure 6. Thus the peak appears to lie in the neighborhood of about 13 km.

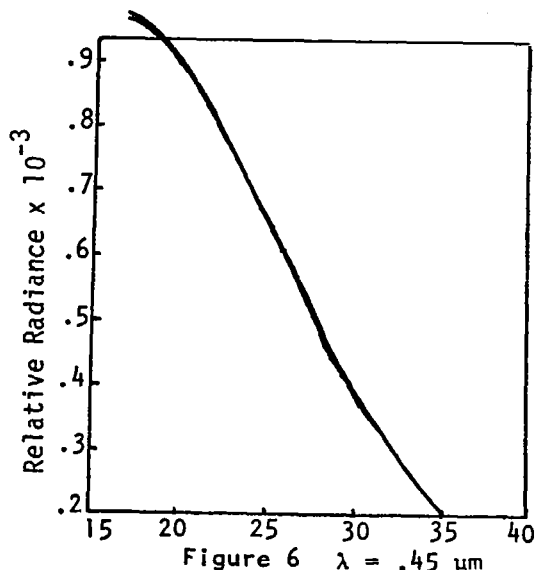
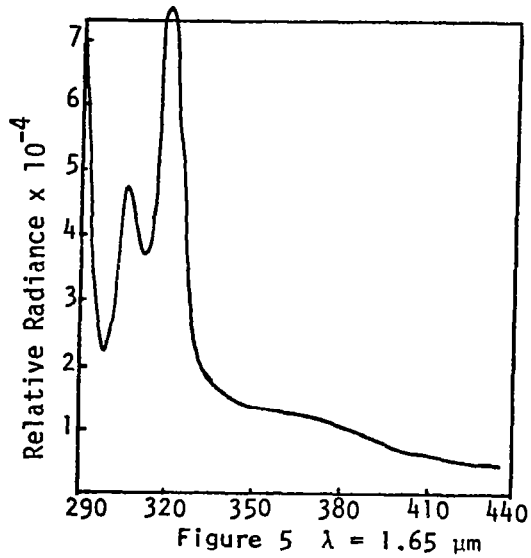
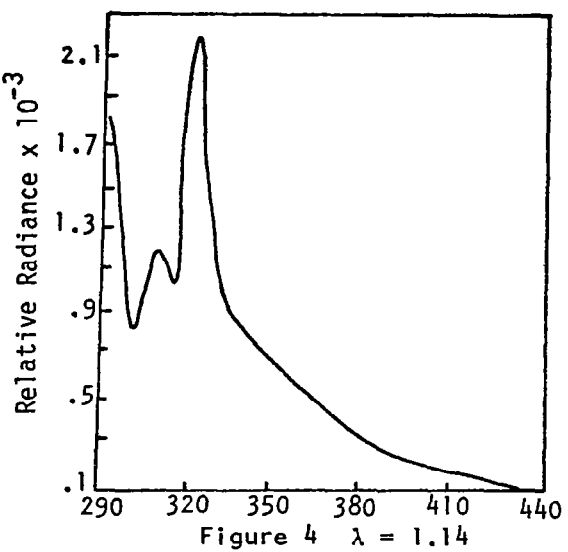
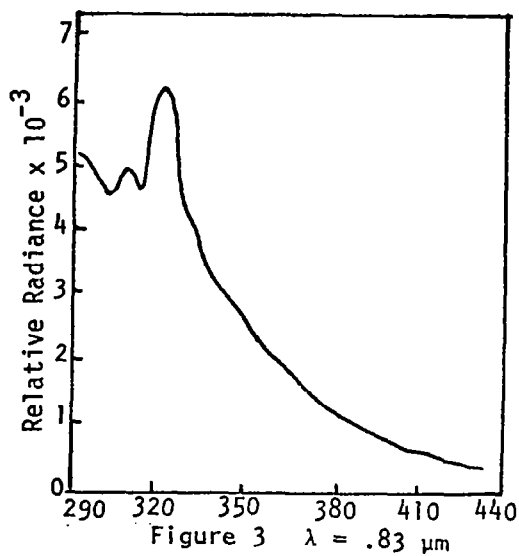
CONCLUSION

The main feature of the data is that a peak in the brightness curve of the limb was observed in the red and near infrared. The observed wavelength dependence is reinforced by the limb view: the blue portions of the incident light are scattered out of the incident and emergent paths through the atmosphere making the red component relatively stronger. It was noted that cirrus clouds were intermittent in the photographs of the observed areas. If this were the cause, the peaks would be the limb signature of high cirrus clouds (above 40,000 ft.).

REFERENCES

1. Elterman, L., "Atmospheric Attenuation Model, 1964, in the Ultraviolet, Visible, and Infrared Regions Altitude to 50 Km", Air Force Cambridge Research Laboratories, Environmental Research Paper, No. 46, 1964.
2. Elterman, L., "UV, Visible, and IR Attenuation for Altitudes to 50 Km", Air Force Cambridge Research Laboratories, Environmental Research Paper, No. 285, April 1968.
3. Pitts, David E. and Kyle, Kirby D., "A Model Atmosphere for Earth Resources Applications", Johnson Space Center, NASA TMX-58033, November 1969.
4. Baum, W. A., Code, A. D., "A Photometric Observation of the Occultation of σ Arietis by Jupiter", The Astronomical Journal, Vol. 58, No. 1208, May 1953.





IMPROVED ACCURACY OF SPECTRAL AEROSOL OPTICAL
DEPTH MEASUREMENTS: INFERRENCE OF TOTAL OZONE

Dale M. Byrne¹ and Michael D. King²

The University of Arizona
Tucson, AZ 85721

¹ Optical Sciences Center

² Institute of Atmospheric Physics

In recent years, much interest has developed in background levels of atmospheric aerosols, especially possible changes in these levels due to man's direct influence. One method to obtain size distribution information of the atmospheric aerosols is to measure the wavelength dependence of optical depth or the spectral extinction coefficient. Inferred optical depths at several wavelengths can be calculated using model size distributions and intercompared with measurements, or an "inversion" can be performed directly on the optical depth measurements to yield a size distribution.

A common method to obtain spectral transmission data representative of the entire atmosphere is to measure the direct solar irradiance at the surface of the earth within several wavelength bands. The directly transmitted solar irradiance will vary throughout the day due to the variation of air mass, and can be expressed as

$$F(\lambda) = F_0(\lambda) e^{-\tau_T(\lambda)m(\theta_0)}, \quad (1)$$

where $F(\lambda)$ is the solar irradiance reaching the earth's surface at wavelength λ ; $F_0(\lambda)$ is the irradiance incident on the top of the atmosphere ($\tau = 0$ level); $m(\theta_0)$ is the atmospheric air mass, a function of the solar zenith angle θ_0 ; and $\tau_T(\lambda)$ is the total optical depth. The total optical depths at the several wavelengths are obtained from Langley plots.

However, to arrive at the optical depth contribution due to atmospheric aerosols alone, proper correction must be made for molecular scattering and absorption. Considering wavelengths in the visible and near visible region of the spectrum, the aerosol optical depth can be written as

$$\tau_a(\lambda) = \tau_T(\lambda) - \tau_R(\lambda) - \tau_{O_3}(\lambda) - \tau_{ma}(\lambda), \quad (2)$$

where $\tau_R(\lambda)$ is the appropriate Rayleigh optical depth; $\tau_{O_3}(\lambda)$ is the optical depth due to ozone absorption (for measurements within the Chappuis band); and $\tau_{ma}(\lambda)$ is the optical depth caused by molecular absorption such as water vapor or oxygen. The ozone optical depth can be written as

$$\tau_{O_3}(\lambda) = \eta a(\lambda), \quad (3)$$

where $a(\lambda)$ is the absorption coefficient per cm of pure gas at STP, and η is the total ozone content in atm-cm. If measurements are made at wavelengths where $\tau_{ma}(\lambda)$ is negligible or zero, and proper pressure corrections are made for $\tau_R(\lambda)$, then only the ozone optical depth need still be accounted for.

Typically, seasonal values are assumed to account for the presence of ozone; or alternatively, the data reported by a remote measuring station is used. Either of these can introduce systematic errors in the estimate of the aerosol optical depth. Figure 1 illustrates the effect of varying the amount of

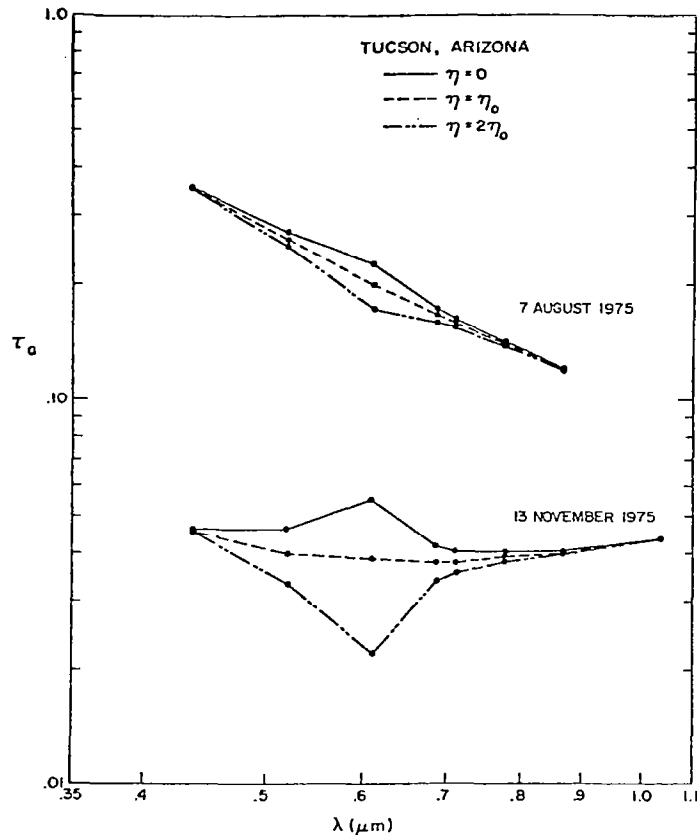


Figure 1

ozone correction when τ_a is plotted as a function of λ on a log-log scale for two days in 1975. It is readily seen that the inferred aerosol optical depths at wavelengths in the heart of the Chappuis band (centered near $0.6120 \mu\text{m}$) are characteristically high for little ozone correction ($\eta = 0$), while being noticeably low for large amounts of ozone correction ($\eta = 2\eta_0$).

To determine the optimum amount of ozone correction, it was assumed that the spectral aerosol optical depth values obeyed the quadratic functional form

$$\log \tau_a = a_0 + a_1 \log \lambda + a_2 (\log \lambda)^2. \quad (4)$$

This form was chosen since it permits some curvature on a $\log \tau_a$ vs. $\log \lambda$ plot. Curvature on a $\log \tau_a$ - $\log \lambda$ plot can result from Junge type size distributions which exist over finite radii limits as well as non-Junge type size distributions. Maximizing the probability that the $\log \tau_a$ observations have the functional form given by (4) is equivalent to minimizing the statistic χ^2 , which for this case assumes the form

$$\chi^2 = \sum_i \frac{1}{\sigma_i^2} [\log \tau_a(\lambda_i, \eta) - a_0 - a_1 (\log \lambda_i) - a_2 (\log \lambda_i)^2]^2. \quad (5)$$

Minimizing χ^2 as defined above is equivalent to making a weighted least-squares fit to the data.

The determination of the values of a_0 , a_1 , a_2 , and η which minimize (4) requires the solution of a non-linear least-squares problem. To simplify the procedure, the solutions for a_0 , a_1 , and a_2 are written as a function of η , the only variable which enters in a non-linear fashion. The value of η is incremented (while simultaneously determining a_0 , a_1 , and a_2) until the minimum value of χ^2 is attained. The amount of ozone, η_0 , which minimizes χ^2 , is then multiplied by the absorption coefficients at the several wavelengths to obtain the optimum spectral correction.

The method for inferring total ozone content described here has been employed at the University of Arizona since August 1975 in order to more accurately determine aerosol optical depths. Figure 2 illustrates the inferred ozone content for forty days between August 1975 and March 1976. The large daily variability which characterizes the measurements of total ozone is readily seen. Inspection of the data indicates an overall seasonal variation in which the total ozone content is highest in early spring and lowest in early autumn.

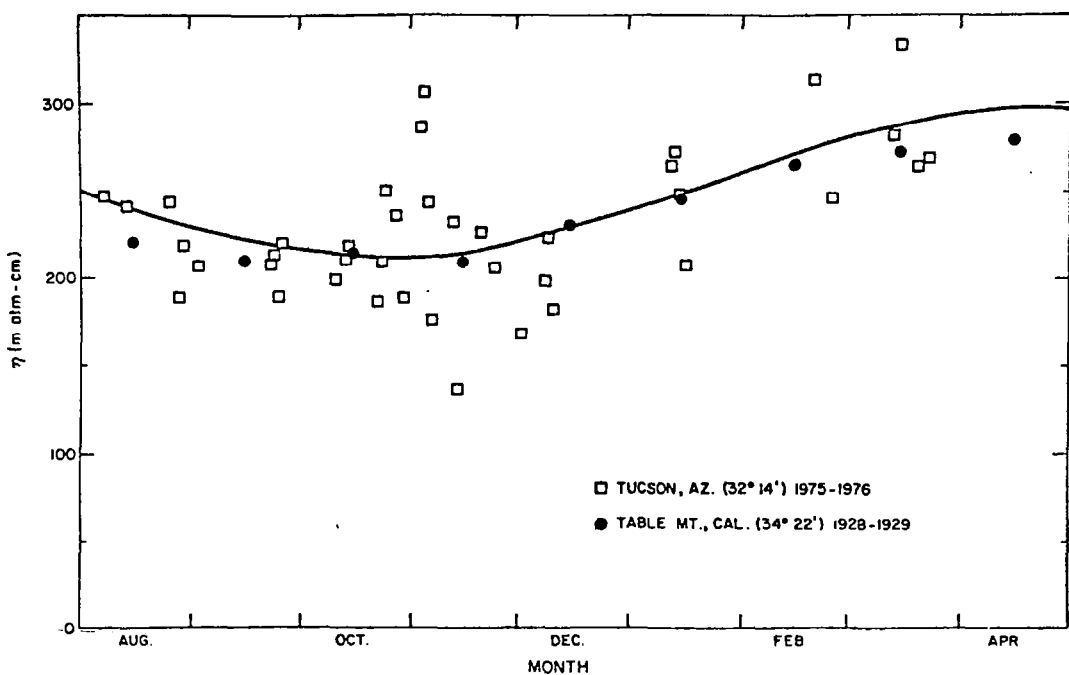


Figure 2

MONITORING OF TROPOSPHERIC AEROSOL
 OPTICAL PROPERTIES BY LIDAR

James Spinhirne

Institute of Atmospheric Physics
 University of Arizona
 Tucson, Arizona 85721

Past work in lidar measurement of tropospheric aerosol parameters has shown the feasibility of quantitative measurements (Barrett and Ben-Dov, 1967; Fernald, 1972), but also the need for improved measurement techniques and theoretical methods for processing measurements. Recent research efforts by part of the University of Arizona radiation group have been directed toward improving the technique for measuring the extinction and backscatter cross-section of aerosols with monostatic lidar, and, subsequently, to develop and apply a system capable of routine measurement of these parameters in the troposphere.

In order to obtain aerosol extinction and backscatter cross-section from lidar measurements, a solution technique of the lidar equation must be used. A form of the lidar equation is

$$P(z, \theta) = C[\beta_p(z, \theta) + \beta_r(z)] \exp[-2 \sec \theta \int_0^z \sigma_p(z') dz'] T_R^{z \sec \theta}$$

$$= z^2 \sec^2 \theta V(z, \theta)$$

where $V(z, \theta)$ = instantaneous measured return signal

z = height above receiver

θ = return zenith angle

β_p, β_r = particulate and molecular backscatter x-sections

σ_p = particulate extinction x-section

T_R = one way vertical Rayleigh transmission

C = system calibration constant

By defining a parameter relating backscatter to extinction cross-section, $S = \sigma_p/\beta_p$, an integral solution of the lidar equation is possible (Barrett and Ben-Dov, 1967). For the case given above where both angular dependence and separation of particulate and molecular scatter is included, a solution integrated over a horizontal layer from z_1 to z can be shown to be:

$$T_p^\gamma(z)T_R(z)^{x\gamma} = T_p^\gamma(z_1)T_R^{\gamma x}(z_1) - \gamma \int_{z_1}^z \frac{SP(z', \gamma)}{C} T_R(z')^{\gamma(x-1)} dz'$$

where

$$\gamma = 2 * \sec(\theta); \quad T_p(z) = \exp - \left(\int_0^z \sigma_p dz' \right); \quad x = \frac{3S}{8\pi}$$

For measurements at different zenith angles, the above equation represents a system of equations which can be solved for optimum values of the backscatter to extinction ratio and vertical distribution of particulate optical depth. By substitution back into the lidar equation, profiles of particulate backscatter and extinction cross-section are produced.

Data acquisition hardware and computer software were developed to enable routine measurement of the vertical distribution of aerosol cross-section by analysis of multiple angle lidar returns. A standard target technique was used for determining the lidar calibration constant. The accompanying table gives average profile results for 24 measurements taken during fall, winter and spring of 1975-76. The standard deviation values are primarily attributable to atmospheric variation. The average ratio for σ_p/β_p was 22.9 str. for particulates within the mixing layer.

It is well known that Mie theory indicates that the ratio of extinction to backscatter cross-section for particulates can be sensitive to complex index. Lidar measurements of the cross-section ratio were compared to cross-section ratios computed using particulate size distributions determined by inversion of solar radiometer wavelength dependent extinction data. Computations were made for different refraction indices, and the value of complex index giving best agreement was determined. Due to the effect of nonsphericity for real particulates, the value of complex index obtained would be an upper limit for the actual complex index. Results obtained show large variation of the characteristics of aerosol populations.

References

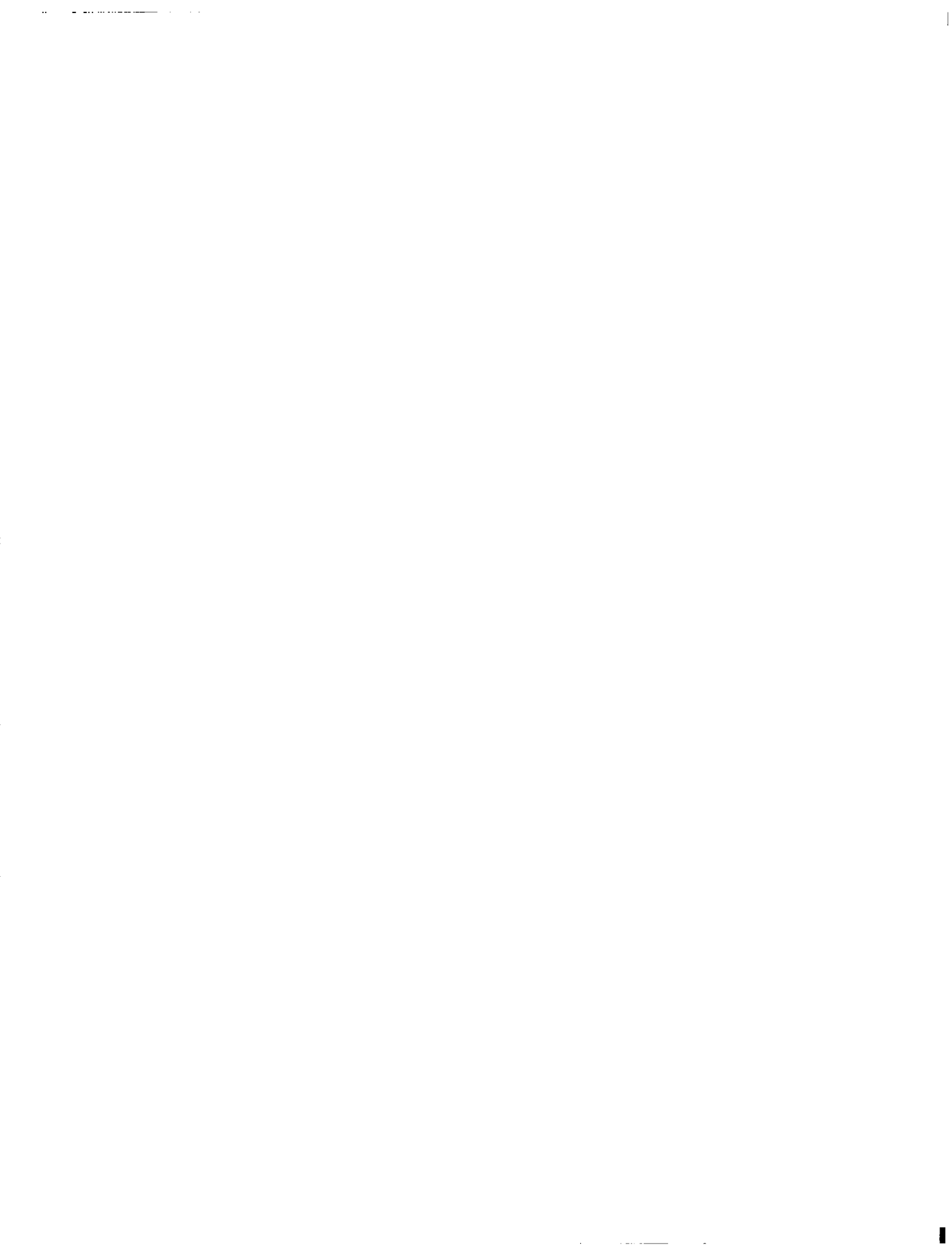
Fernald et al., 1972, J. Appl. Meteor., 11, 482-489.

Barrett and Ben-Dov, 1967, J. Appl. Meteor., 6, 500-515.

AVERAGE PARTICULATE VOLUME CROSS SECTIONS
OVER TUCSON, AZ. AT $\lambda = .6943\mu$

(Height is referenced from a ground level
750 m above sea level)

Height (km)	Particulate Optical Depth 0+h	Particulate Extinction X-Section (10^{-2}km^{-1})	% Standard Deviation of Extinction X-Section
.05	.002	5.10	31.2
.5	.021	2.63	23.1
1.0	.032	1.95	22.7
1.5	.041	1.54	24.5
2.0	.048	1.27	25.8
2.5	.053	.87	25.1
3.0	.057	.63	28.3
3.5	.060	.49	30.5
4.0	.062	.37	29.6
4.5	.063	.27	29.4
5.0	.064	.22	29.5
5.5	.066	.19	30.1
6.0	.066	.14	29.0
6.5	.067	.12	25.3
7.0	.068	.09	32.7
7.5	.068	.08	33.1
8.0	.069	.07	38.2
8.5	.069	.06	34.5
9.0	.069	.06	36.4
9.5	.069	.05	32.8
10.0	.070	.05	34.5
10.5	.070	.04	30.2
11.0	.070	.05	37.1
11.5	.071	.03	34.7
12.0	.071	.04	37.9
12.5	.071	.04	38.8
13.0	.071	.04	30.6
13.5	.071	.03	33.0
14.0	.071	.03	42.6
14.5	.072	.04	31.2
15.0	.072	.04	37.7



Comparative Analysis of Red-Blue Lidar and Rawinsonde Data

W. H. Fuller, Langley Research Center, NASA, Hampton, Va. 23665
 T. J. Swissler, Systems and Applied Sciences, Riverdale, Md. 20840
 M. P. McCormick, Langley Research Center, NASA, Hampton, Va. 23665

Lidar, an acronym for light detection and ranging, has proven to be a valuable tool for remote sensing of the atmosphere. A lidar system consists of a pulsed laser transmitter aligned parallel with an optical receiver whose operation can be described by the following general equation:

$$P(\lambda, Z) = \frac{E(\lambda) c A_r q^2(\lambda, Z) f(\lambda, Z)}{2 Z^2} \quad (1)$$

where $P(\lambda, Z)$ is the power incident on the optical receiver of area A_r due to the atmospheric backscattering of the laser pulse, of energy E and wavelength λ , from an altitude Z , c is the speed of light, $q^2(\lambda, Z)$ is the two-way transmissivity from the lidar to the scattering volume and return, and $f(\lambda, Z)$ is the backscattering function at the scattering volume. For the case of elastic scattering, the backscattering function can be written $f(\lambda, Z) = f_a(\lambda, Z) + f_m(\lambda, Z)$ where the subscripts a and m denote aerosol and molecular scattering, respectively.

Because of its long range capability and high sensitivity, lidar has been used very effectively to monitor the stratospheric aerosol layer. The capability of this technique to measure the vertical aerosol profile has been proven by comparison experiments with balloon borne particle samplers.¹ The results of these experiments have shown that in order to accurately extract the aerosol backscatter from the total backscatter, the real atmospheric molecular density must be known. It was found that significant errors can be introduced by using standard atmospheric densities, particularly when the aerosol burden is low.

During a typical lidar measurement, meteorological data are obtained from the nearest U.S. Weather Station rawinsonde launch. A more practical approach would be to provide real-time molecular density data in the same space as the lidar probe. This is especially important when operating from remote stations where rawinsonde data are not readily available.

The ruby laser operating at $0.6943 \mu\text{m}$ has been used extensively as the lidar transmitter for stratospheric observations. The fundamental frequency of this laser can be doubled, producing an output at $0.3472 \mu\text{m}$. Simultaneous lidar measurements of the tropospheric region, using the $0.6943 \mu\text{m}$ and $0.3472 \mu\text{m}$ wavelengths, were reported by M. P. McCormick² in 1971. In this paper, McCormick derived the backscattering functions $f_a(\lambda, Z)$ and $f_m(\lambda, Z)$ showing that the ratio f_m/f_a increases by a factor of eight in going from $0.6943 \mu\text{m}$ to $0.3472 \mu\text{m}$. This increase in molecular sensitivity and its comparison with the aerosol sensitivity is shown in the backscattering function model plotted in figure 1. The criterion used by lidar researchers

to compare the temporal stratospheric aerosol burden is to ratio the total backscatter to molecular backscatter at $0.6943 \mu\text{m}$. For the model used in figure 1, the peak backscatter ratio was 1.6, in April 1976 the backscatter ratio was 1.3 and presently, (October 1976) it is 1.15. The latter backscattering ratios represent lower stratospheric aerosol concentrations than used in the particular atmospheric model of figure 1. For these conditions the molecular backscattering at $0.3472 \mu\text{m}$ closely approximates the total backscattering for altitudes greater than 3 kilometers.

Near simultaneous red-blue stratospheric measurements were made at Langley Research Center in April 1976, using the Langley 48-Inch Lidar. An RDA crystal was operated external to the laser cavity and provided a second harmonic conversion efficiency of 10%, a marked improvement over earlier crystals. Although the laser emitted simultaneous outputs in the red and blue, the measurements were made serially because of the single channel limitation of the data acquisition system. Three, fifty-shot series with ten background data shots each were taken for the red and blue wavelengths with a time separation between series of 15 minutes. Each fifty-shot series was averaged and the background noise subtracted. The averaged return for each wavelength was corrected for Z^2 and plotted as a function of Z , these plots are shown in figure 2. Rawinsonde data were obtained from Wallops Flight Center and used to compute the molecular density profile and the molecular backscatter at $0.6943 \mu\text{m}$. The backscatter ratio, i.e., the total backscatter to molecular backscatter, was computed and plotted as a function of Z , shown as the Red/Mol plot in figure 3. The total backscatter at the blue wavelength, shown in figure 2, was assumed to be molecular backscatter and therefore used to compute the backscatter ratio for the red wavelength, shown as the Red/Blue plot in figure 3. The vertical structure of the two plots follow very closely up to 25 kilometers where the blue signal decreases to background noise level. The peak backscattering ratio occurs at the same altitude and is 1.29 for the Red/Mol plot and 1.24 for the Red/Blue plot. The agreement between these two backscatter ratios is very good considering the approximations involved.

Typically, the backscattering ratio is normalized to unity in the altitude region where the scattering is assumed to be solely molecular. This normalization is performed by choosing the minimum in the lidar ratio in the altitude range from 24 to 34 km. For the Red/Mol plot this altitude was 31 km. For the Red/Blue plot, the blue signal is weak at the higher altitudes and the ratio was normalized in the 8 to 12 km region. Thin cirrus clouds between 7 and 8 km are responsible for the peak in the backscatter ratio at these altitudes. These transient clouds can have an effect on the normalization of the lidar ratio in this altitude region. An effort is underway to improve the blue signal to noise ratio at the higher altitudes where aerosol scattering

is at a minimum and the backscattering ratio can be accurately normalized.

In conclusion, this preliminary analysis of the red-blue lidar measurements indicates that the assumption of total backscattering at $0.3472 \mu\text{m}$ being represented by the molecular backscattering is a valid one for low aerosol burdens. This red-blue technique is being further developed to provide real-time analysis of the lidar backscattering data.

References

1. Northam, G. B.; Rosen, J.M.; Melfi, S.H.; Pepin, T.J.; McCormick, M. P.; Hofmann, D. J.; and Fuller, W. H., Jr.: A Comparison of Dustsonde and LIDAR Measurements of Stratospheric Aerosols. *Applied Optics*, Vol. 13, No. 10, Oct. 1974, pp. 2416-2421.
2. McCormick, M.P., Simultaneous Multiple Wavelength Laser Radar Measurements of the Lower Atmosphere, *Proceedings of the Electro-Optics International Conference*, Brighton, England, 23-24 March 1971, pp. 495-512.

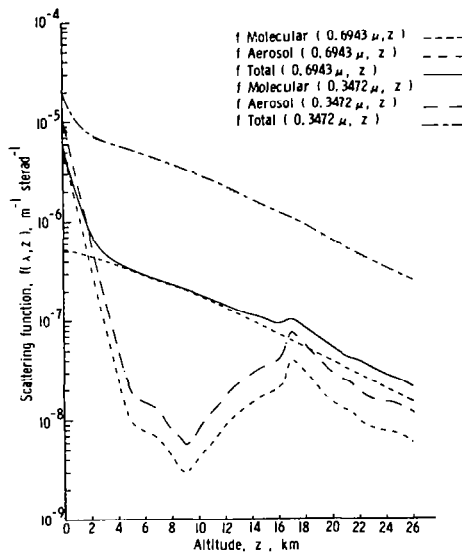


Fig. 1 Backscattering function model of the atmosphere for a wavelength of 0.6943μ and 0.3472μ . The molecular contribution, aerosol contribution, and their sum are shown.

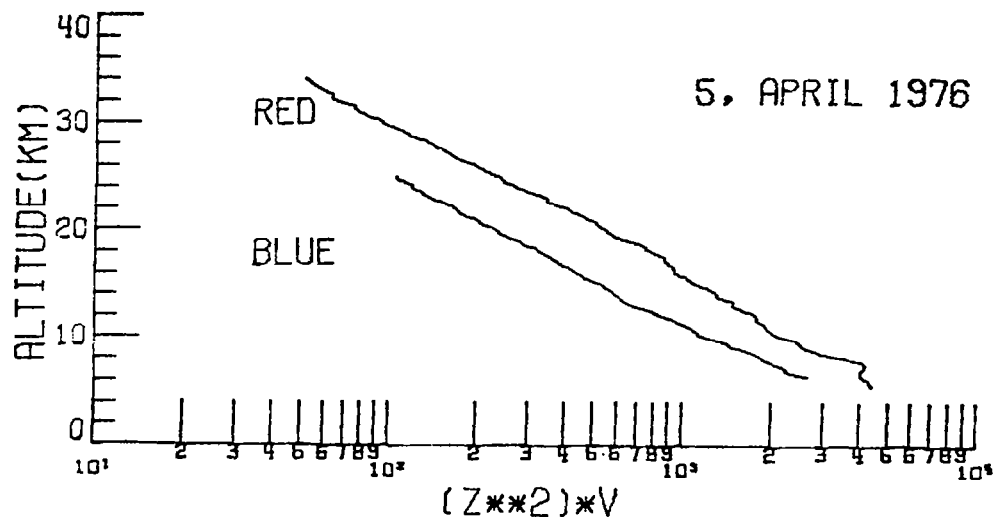


Figure 2. Range corrected backscattered returns for 0.6943 μm (Red) and 0.3472 μm (Blue)

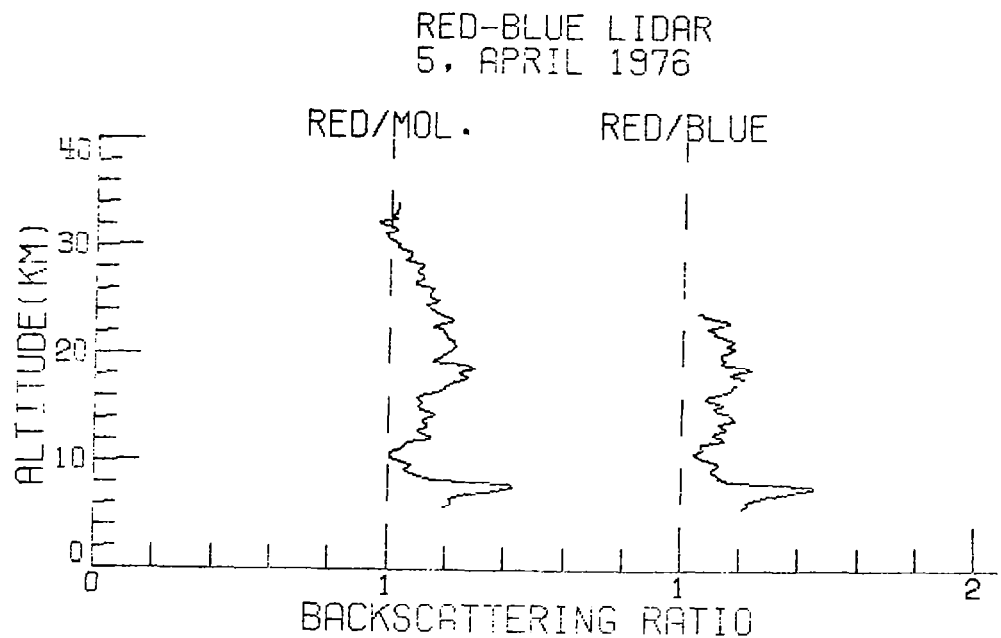


Figure 3. Scattering ratios for Red/Mol and Red/Blue from data in Figure 2

DETERMINATION OF THE COMPLEX REFRACTIVE INDEX OF AEROSOL PARTICLES
FROM BISTATIC LIDAR AND SOLAR RADIOMETER MEASUREMENTS

J. A. Reagan, D. M. Byrne, B. M. Herman and M. King

The University of Arizona, Tucson, Arizona 85721

Accurate specification of the refractive index of atmospheric aerosol particles is critically important in radiative transfer studies on the effects of aerosols because predictions of aerosol 'heating' rather than 'cooling', or vice-versa, can frequently be obtained by only slightly altering the assumed index value. This sensitivity coupled with the current lack of information about the refractive index of aerosols in realistic atmospheres makes it extremely difficult to definitively predict climatic variations that may occur due to aerosols. As such, considerable effort has been devoted in recent years to attempts to develop ways of accurately measuring the refractive index of aerosol particles. This paper outlines a remote sensing approach for making such measurements which utilizes combined bistatic lidar and multi-wavelength solar radiometer data.

Multi-wavelength solar radiometer measurements are employed to obtain accurate estimates of the aerosol or particulate optical depth component, $\tau_p(\lambda)$, at eight visible region wavelengths, λ , by processing Langley plots of radiometer data (including corrections to remove the molecular contributions) as

described by Shaw et al. (1973). The particulate optical depth versus wavelength data thus obtained are then processed to infer the columnar particulate size distribution by either extracting a simple Junge model fit from a straight-line fit to the $\log \tau_p(\lambda)$ versus $\log \lambda$ curve (Shaw et al., 1973) or by performing a mathematical size distribution inversion on the $\tau_p(\lambda)$ data (Herman et al. 1976). In either case, advantage is taken of the fact that the shape of the size distribution inferred from particulate optical depth (or particulate extinction coefficient) data is relatively insensitive to the particle refractive index value assumed in the analysis.

Next, bistatic lidar data is processed to extract a best fit estimate of the particle refractive index subject to the constraint that the particulate size distribution is assumed to follow the distribution obtained from the radiometer particulate optical depth data. Specifically, bistatic lidar measurements of the l and r scattered Stokes parameters (for several scattering angles, θ , between 90° to 180°) are processed to extract the particulate polarization ratio, R_{lr_p} , (ratio of the l th particulate scattered Stokes parameter divided by the r th particulate scattered Stokes parameter) as a function of scattering angle. The R_{lr_p} values obtained from the bistatic lidar measurements are then compared with theoretical R_{lr_p} curves computed for various refractive index values and the size distribution inferred from the particulate optical depth data. The particular refractive index value which yields the best agreement, in a least-squares sense, between the measured and theoretically computed R_{lr_p} values is selected as

the best fit refractive index. The refractive index values used in the fitting library include real components of 1.33, 1.40, 1.45, 1.50, and 1.54 and imaginary components of 0.000, 0.002, 0.005, 0.007, 0.10, 0.02, and 0.05.

Two cross checks are made on the refractive index determination. First, the bistatic lidar data is inverted, using the inferred refractive index value, to obtain a size distribution which is compared for similarity with the distribution initially obtained from the particulate optical depth data. Secondly, the extinction to backscatter ratio, defined as the S value, for the inverted bistatic lidar size distribution and inferred refractive index value is compared with the S value obtained from independent monostatic lidar slant path measurements. Depending on the closeness of the cross checks, the entire process can be iterated to attempt to obtain a better estimate of the particle refractive index.

Example results will be presented to demonstrate the utility of the above described method and to verify, at least under certain conditions, that refractive index determinations can be obtained which are consistent with combined solar radiometer, bistatic lidar, and monostatic lidar observations.

REFERENCES

Herman, B. M., M. King, J. Reagan, and D. M. Byrne, 1976: The Use of Inversion Techniques for Lidar and Radiometric Aerosol Studies. Paper presented at Symposium on Radiation in the Atmosphere, Garmisch-Partenkirchen, Federal Republic of Germany, 19-28 August.

Shaw, G. E., J. A. Reagan, and B. M. Herman, 1973: Investigations of Atmospheric Extinction Using Direct Solar Radiation Measurements Made with a Multiple Wavelength Radiometer. J. Appl. Meteor., 12, 374-380.

FEASIBILITY OF ATMOSPHERIC AEROSOL MEASUREMENTS
WITH LIDAR FROM SPACE SHUTTLE

Ellis E. Remsberg and G. Burton Northam
NASA-Langley Research Center
Hampton, Virginia 23665

An aerosol and cloud lidar experiment has been proposed to demonstrate the feasibility of conducting this and more complex lidar experiments from a Space Shuttle platform. This experiment will utilize a reliable fixed-frequency visible wavelength laser which will be operated in the nadir-viewing mode. The obvious targets for the lidar measurement are clouds, aerosols, and the molecular density profiles. Simulations using the lidar equation (see ref. 1) have been conducted to predict expected return signal levels. Table I lists the system parameters used in these simulations.

Table I
Parameters for Backscatter Simulations

Platform altitude	200 kilometers
Laser energy	0.5 joule per pulse at 0.53 micrometer
Beam divergence for transmitter	2 milliradians
Repetition rate	10 pulses per second
Telescope area	0.16 meter ²
Telescope FOV	2 milliradians
System receiving efficiency (Optical x Quantum)	6 percent
Filter-etalon bandwidth	0.2 nanometer
Cloud reflectance at 10 kilometers	10 percent

Due to the high reflectivity of clouds, a determination of the presence and altitude of clouds is one of the easiest lidar measurements from a signal level point of view. However, shot averaging to further improve signal statistics may not be possible, except in the case of extended layer clouds, because of the finite size of the cloud targets. Calculated return signals P_s (photoelectrons/ μ sec) for a single laser firing from an aerosol-free atmosphere and from a cloud of albedo 0.1 located at 10 km are shown in figure 1 for nighttime background lighting. These results indicate that the signal is

clearly large enough for detection with a single laser firing. Of course, in the case of cloud height measurements, only cloud detection is required, whereas cloud reflectivities represent the need to measure the return signal level accurately over a wide dynamic range. Since cloud measurements may be sought for day as well as night, the background return must be assessed also.

Background equivalent counts P_B are estimated by the following expression:

$$P_B = RTA \text{ (FOV)} B_w \epsilon$$

where R is the clear sky radiance adapted from a graph in Kildal and Byer (ref. 2) and is equal to 4×10^{14} photons m^{-2} micrometer^{-1} sr^{-1} microsecond^{-1} , T is the one microsecond gate time, A is the telescope area of 0.16 m^2 , the FOV is $\pi (2 \text{ mrad})^2/4$ in steradians and 2 mrad represents the full angle telescope divergence, B_w is the spectral bandwidth of 0.2 nm and ϵ is the system efficiency of 0.06. With these parameters, a P_B value of 2.4×10^3 photoelectrons/microsecond for daytime condition occurs when the effective Earth-atmosphere albedo (including the 10 percent reflecting clouds) is 10 percent. The signal P_s from the cirrus cloud in figure 1 is 10^3 photoelectrons per microsecond. Of course, if brighter clouds exist, the background will increase, but so will the return laser signal. An estimate of the error in a daytime measurement of 10 percent cloud reflectivities can be obtained from the expression:

$$E(\%) = \sqrt{\frac{P_s + P_B}{(P_s)^2}} \times 100$$

For measurements of cloud reflectivities, shot averaging will improve the signal statistics. At a 10 pps repetition rate, suitable averaging can be achieved with 10 shots, which represent an 8 kilometer distance of travel along the ground track. The 400-meter-wide field-of-view would probably preclude measuring reflectivities of small individual cumulus clouds; however, backscatter reflectivities of extended clouds can be obtained even during daylight. Reflectivities (backscatter albedo) of all clouds and the geometric thicknesses of thin clouds can be recorded at night. To measure the optical depth of clouds, the difference between the received signal from the leading edge of the cloud and the attenuated signal from just below the cloud must be measured accurately. For thin cirrus (fig. 1), the signal attenuation through the cloud is negligible and, thus, the optical depth cannot be determined. For thick clouds, the signal is completely attenuated before reaching the lower cloud boundary, and accurate optical thickness determinations are not possible.

The influence of aerosol profiles from the backscatter return was evaluated for the system parameters given in Table I. Figure 2 gives the Rayleigh (clean air) return and the return profiles for two haze models. The light haze represents a McClatchey aerosol model with a surface visibility of 23 km. The heavy haze model represents 10 times the particle density of the light haze below 3 km altitude. This effectively represents a 2-3 km visibility.

The random error in P_s for a single lidar return is better than 21 percent below 10 km. Lower tropospheric haze layers can be monitored with an accuracy of better than 3 percent from 0.5 km range cells and an average of 5 laser returns (4 km horizontal distance).

At the 20 km level, where stratospheric aerosols occur, the single shot signal error is approximately 30 percent. For a stratospheric aerosol scattering ratio (see ref. 1) of 1.2 percent at 0.53 micrometer, the aerosol portion of the return is 17 percent. By averaging 50 laser firings over a 1 km range cell at 10 pps, that total return can be measured with an accuracy of 2 percent. This integration time corresponds to an average measurement over a horizontal distance of 40 km, an averaging interval considerably better than that available with a limb-viewing solar occultation geometry.

From figure 1, the molecular signal returns from 40 km altitude can be estimated. For a 2 km range cell and 200 laser firings, a 2 percent density measurement is possible. At a rate of 10 pps, this represents molecular density data with a horizontal resolution of 160 km, comparable to that achievable with passive limb sounders.

Similar calculations have been performed for the 1.06 μm fundamental wavelength of a Nd:YAG laser and for detection quantum efficiencies typical in the near infrared. Performance at 1.06 μm is quite marginal for aerosols. Returns from clouds at night are still measurable, but the scientific value of simultaneous 0.53 and 1.06 μm wavelength backscatter data from clouds is questionable.

References

1. G. B. Northam, J. M. Rosen, S. H. Melfi, T. J. Pepin, M. P. McCormick, D. J. Hofmann, and W. H. Fuller, Jr., *Appl. Opt.*, 13, 2416 (1974).
2. H. Kildal and R. L. Byer, *Proc. IEEE*, 59, 1644 (1971).

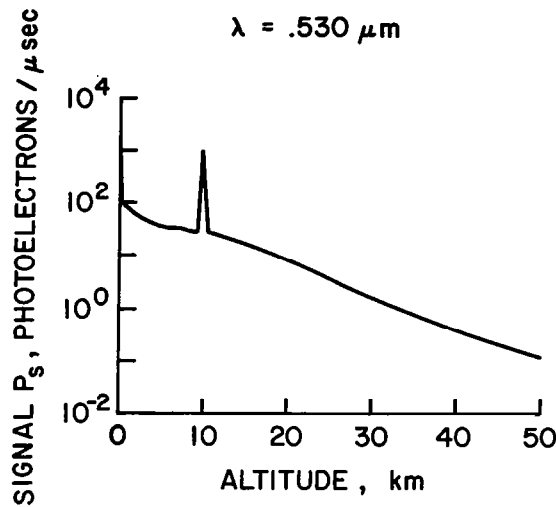


Figure 1.- Simulated return from a cirrus cloud and the molecular atmosphere.

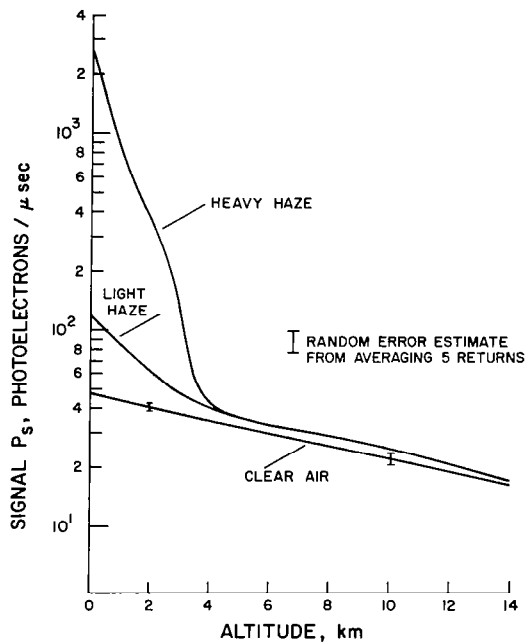


Figure 2.- Simulated returns for aerosols.

SCATTERING OF ULTRAVIOLET RADIATION BY
AEROSOLS IN THE LOWER ATMOSPHERE

M.E. Neer, G. Sandri, E.S. Fishburne

Aeronautical Research Associates of Princeton, Inc.
50 Washington Road, Princeton, New Jersey 08540

SCATTERING AND ATTENUATION MEASUREMENTS

Since 1974, A.R.A.P. has been conducting an experimental and theoretical investigation to determine the UV scattering characteristics of the lower atmosphere. The detection system used in this investigation is composed of filters to provide the wavelength selection and rejection of solar radiation, a rubidium telluride photomultiplier, and pulse counting electronics. The transmission characteristics of the basic filters necessary to obtain a high degree of solar blindness and wavelength discrimination in the spectral region between 2400 and 2700 \AA are described in Ref. 2. The overall system spectral response for the filter PMT combination used to obtain the data shown below was approximately 1.5×10^{-3} over the 2500-2700 \AA region.

The scattering and attenuation of UV radiation by the atmosphere were investigated employing the detection system described above and a high-intensity mercury xenon flashlamp. By pointing the detector directly at the radiation source from various distances using narrow field of view optics, the line-of-sight attenuation coefficient as measured in the field varied from 1.3/km to 3.2/km which is consistent with the values reported by Baum and Dunkelman (Ref. 1).

To measure scattering the detector was pointed away from the UV source so as to systematically determine the amount of scattered radiation coming from various portions of the sky. These systematic measurements which indicate the way in which UV radiation is scattered and absorbed by the atmosphere, are referred to as scattering "footprints." Typically, the source was located on the roof of a relatively low building at the Princeton University, and the detector was moved some distance away. The detector optical axis was first raised vertically to some angle of elevation and then rotated in the horizontal plane to some azimuthal position.

The first series of measurements showed that the atmospheric scattering footprints were symmetric with respect to positive and negative azimuthal angles. Samples of atmospheric scattering data obtained on two separate occasions at a

*This research was supported by the Defense Advanced Research Projects Agency of the Department of Defense and monitored by the U.S. Army Electronics Command, Fort Monmouth, New Jersey, under Contract No. DAAB07-75-C-0115.

distance 0.82 km are shown in Fig. 1. The difference in magnitude of the photon counts on the two days was due in part to a change in the setting of a pulse amplitude discriminator and in part due to different weather conditions.

If the data of Fig. 1 are plotted as a function of the absolute angle γ between the detector optical axis and the detector-to-source line of sight, we obtain the results shown in Fig. 2. The symmetry with respect to γ shown in Fig. 2 was somewhat surprising when first observed, since it had been expected that the intensity of scattered light would decrease at lower elevations due to absorption effects by the ground. It was later found that most of the photons reaching a given scattering volume were traveling very nearly in a radial direction from the source due to strong preferential scattering in the forward direction and due to the exponential decay with total path length.

Data were obtained at two different distances from source to detector on numerous occasions. Results of one such measurement are shown in Fig. 3, when the associated attenuation coefficient was found to be 1.30/km. On one occasion a light misty rain was observed to increase the scattered radiation signal by approximately a factor of 4 at a distance of 0.82 km.

SIMPLIFIED SCATTERING MODEL

An attempt has been made to construct a simplified phenomenological model which will accurately predict the observed atmospheric scattering footprints. One of the primary assumptions of the model is that most of the UV photons reaching a point in the atmosphere are traveling very nearly in a radial direction from the flashlamp as mentioned earlier.

The photon count obtained when the detector is pointed at an angle γ to a flashlamp located a distance x away is given by

$$PC(\gamma) = \iiint \frac{\sigma_{SCATT} P(\beta, g) I_o A_D FVF(\theta) e^{-(R+r)(\sigma_{ABS} + \eta' \sigma_{SCATT})}}{16\pi^2 R^2 r^2} dV \quad (1)$$

where the integrand is the contribution of a given volume element dV located at distances R and r from the source and detector, respectively, and the integral is evaluated over the entire field of view of the detector. The photon count can be seen to be directly proportional to the scattering coefficient σ_{SCATT} , the intensity of the flashlamp I_o , the area of the detector A_D , and the efficiency of the detector response or field of view factor $FVF(\theta)$. The exponential term in Eq. (1) represents the losses due to absorption and scattering, while the denominator of the integrand represents the inverse square losses from the source to the volume element and from the volume element to the detector. The η' factor in the exponential term represents the fraction of photons which are scattered into the backward

direction and therefore are assumed to result in a loss.

The term $P(\beta, g)$ represents the angular distribution of scattered radiation from the volume element where β is the scattering angle. $P(\beta, g)$ is represented by

$$P(\beta, g) = \frac{1}{4\pi} \frac{1 - g^2}{(1 + g^2 - 2 \cos \beta)^{3/2}} + \lambda'(3 \cos^2 \beta - 1) \quad (2)$$

where

$$g = g_0 e^{-c_1 \sigma_{\text{SCATT}}^R} \quad (3)$$

The term g_0 is the average value of $\cos \beta$ of the single scattering phase function. According to Eq. (3), the effective average value of g corresponds to single scattering in the near field (small R) and isotropic scattering in the far field. In the near field ($g = g_0$), the first term on the right-hand side of Eq. (2) reduces to the Henyey-Greenstein single scattering phase function. The second term is a correction factor designed to make the Henyey-Greenstein function resemble the highly complex but more realistic Diermendjian function (Ref. 3) as shown in Fig. 4.

The value of λ' in Eq. (1) is evaluated by integrating Eq. (2) over the rearward facing hemisphere. A computer program has been developed which numerically integrates Eq. (1). Results from the program were shown in Fig. 3.

ADDITIONAL RESEARCH

Further investigations are currently underway which include extending the measurements to longer distances, to other wavelength regions in the solar blind, and to various weather conditions. In addition, ozone concentration, aerosol size distribution, and the single scattering phase function are being measured simultaneously with the scattering footprints.

REFERENCES

1. W.A. Baum and L. Dunkelman, "Horizontal Attenuation of Ultraviolet Light by the Lower Atmosphere," J. Optical Society of America, Vol. 95, No. 3, 1955.
2. E.S. Fishburne, M.E. Neer, and G. Sandri, "Voice Communication Via Scattered Ultraviolet Radiation," Aeronautical Research Associates of Princeton, Inc., Report No. 274, Vol. I, 1976.
3. D. Diermendjian, Electromagnetic Scattering on Spherical Polydispersions, American Elsevier Publishing Co., New York, 1969.

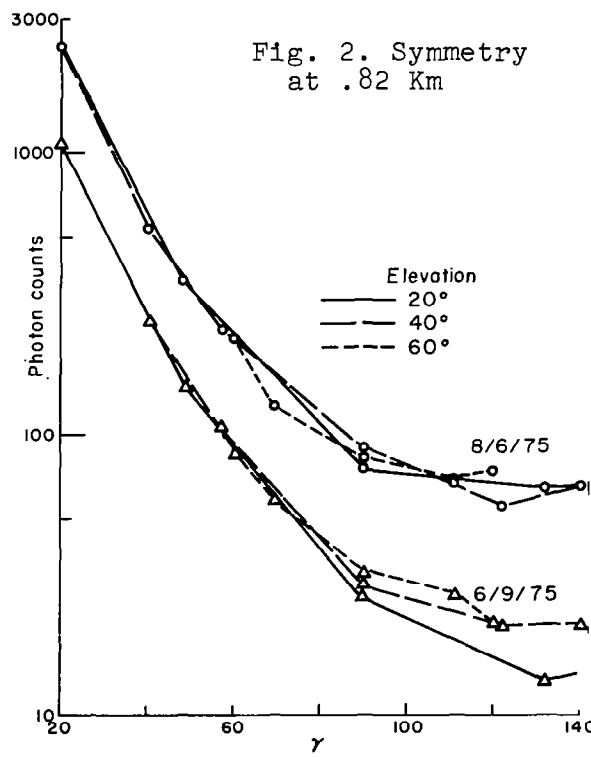
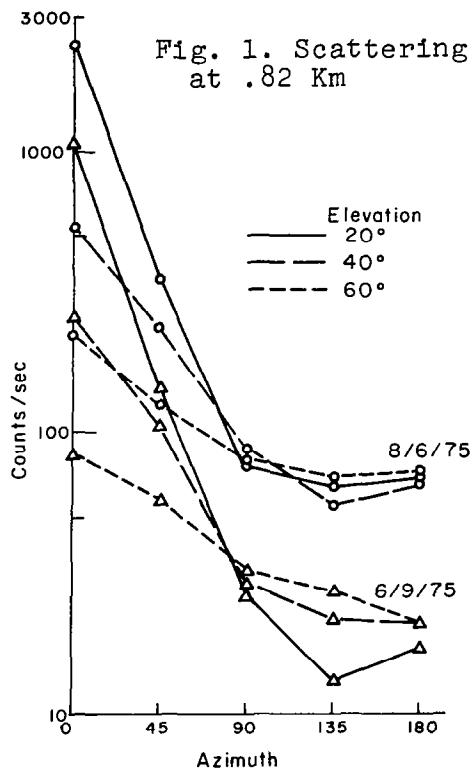


Fig. 3. Scattering at .82 and 2.08 Km

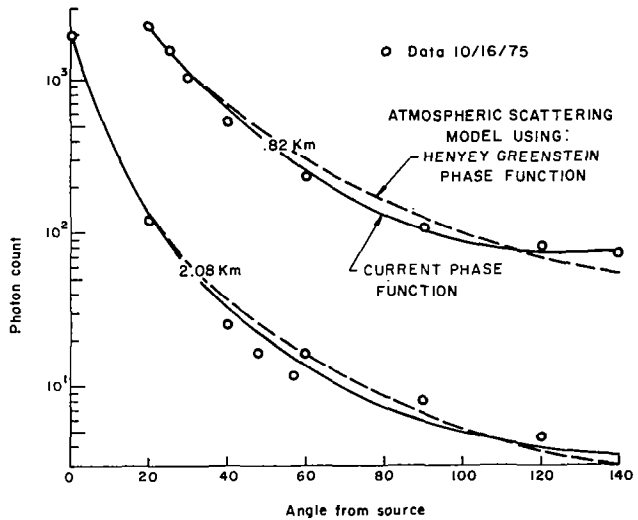
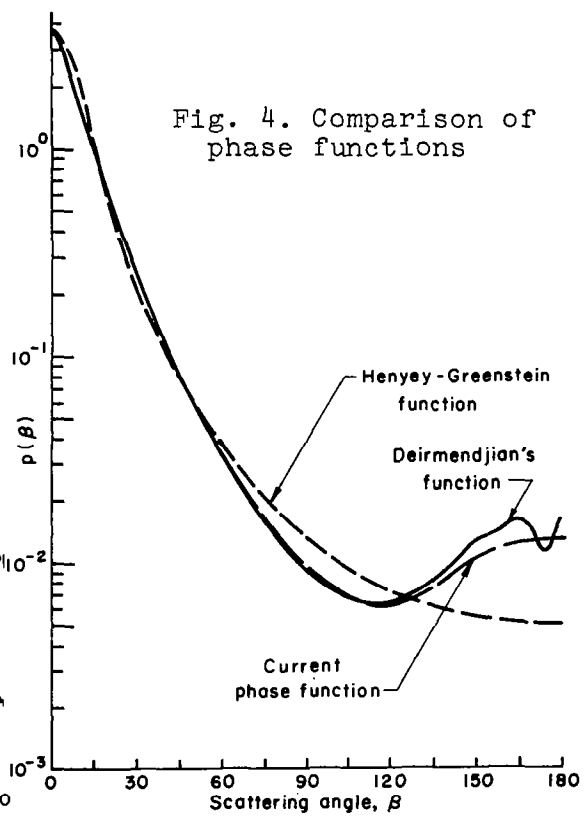


Fig. 4. Comparison of phase functions



Design Principles of a Slant Transmissometer for Airport Use

Harold Stewart, Willem Brouwer, Marion Shuler

HSS Inc., 2 Alfred Circle, Bedford, Mass 01730

This is a report on a single ended instrument for evaluating slant transmission to a specific range in fogs at airports. The optical and signal processing principles of this lidar transmissometer were developed and patented by HSS Inc. Raytheon Corp, using these new principles and with HSS Inc as subcontractor for the optical system, has been awarded an Air Force Geophysical Lab contract for construction of a system to measure transmission in fog to ranges from the instrument of $R_1 = 385$ m and $R_2 = 268$ m. These ranges are specific to required slant transmission measurements to altitudes of 200 ft and 100 ft. The transmissometer, which is mounted in a van, is complete and preliminary tests are underway.

The optical arrangement of the lidar receiver is modified so that the resultant lidar equation is independent of range throughout the region important to the slant transmissometer. The modification consists of a stop on the optical axis and in the focal plane of the collecting lens. This is shown in Figure 1 where the lens aperture area is A , its focal length is f , and the area of the stop is a . A source of intensity J (w ster^{-1}) on the axis and at range r within the near field forms a blur circle in the plane of the stop having area $S = A f^2 / r^2$. The power, p , from the source which passes through the stop is then

$$p = \frac{JA}{r^2} \frac{a}{S} = \frac{JA}{r^2} \frac{a}{A} \frac{r^2}{f^2} = \frac{Ja}{f^2} \quad (1)$$

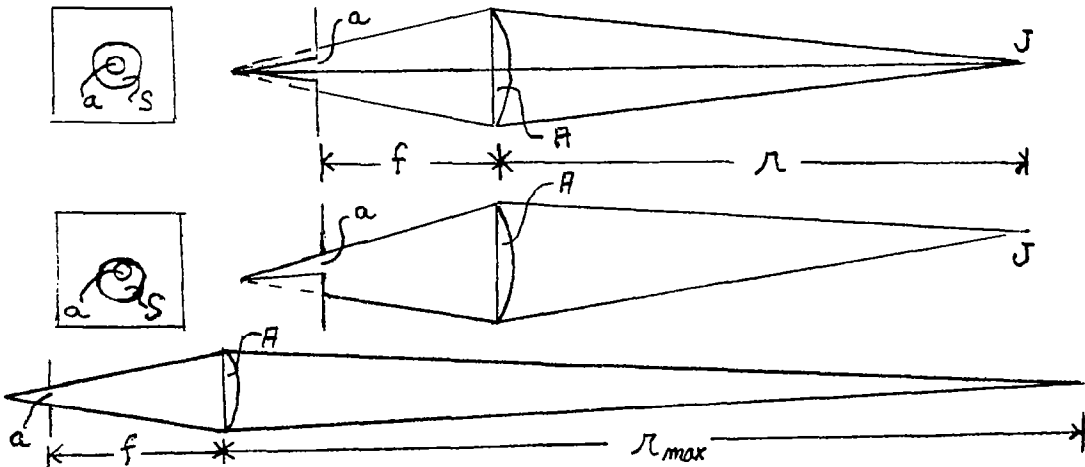


Figure 1

a result which is independent of range to the source. This holds within a conical volume having as base the aperture of the lens and as apex a point on the optical axis at range

$$r_{\max} = f (A/a)^{1/2} = fD/d$$

where D is the diameter of the lens aperture and d is the diameter of the stop. This conic volume is called the analog zone. The transmissometer built for AFGL has $f = 150$ cm, $D = 30$ cm, and $d = 0.045$ cm which results in a value for r_{\max} of one kilometer.

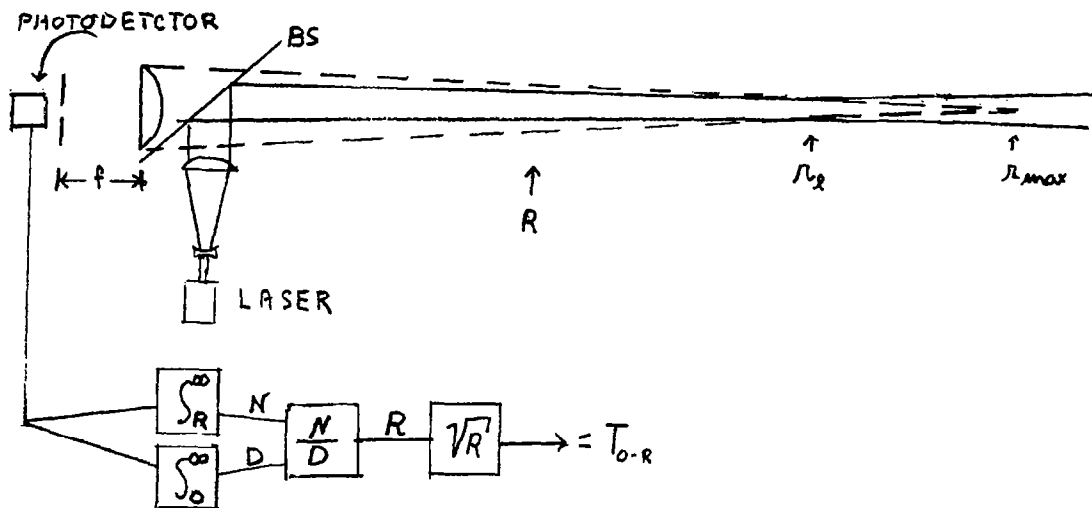


Figure 2

The principle of the transmissometer is illustrated in Figure 2. A beam splitter, BS, covers the full aperture of the collecting optical system and is used to project a laser pulse along the axis of the collector. The laser is focused at the maximum range, r_1 , for which the image lies completely within the analog zone. For the AFGL system $r_1 = 700$ m. A photodetector responds to the radiant power backscattered from the laser pulse to the aperture of the collecting system and through the hole in the stop. The photo current, $i(t)$, is divided equally and sent to two time-gated integrators one of which accepts current due to backscattered radiation from the range R and beyond (the numerator channel) and the other which accepts current due to back scattered radiation from the entire range starting within a few meters of the aperture (the denominator channel). The square root of the ratio of the numerator integral to the denominator integral is taken and this value presented in the read out as the transmission from the aperture of the transmissometer to range R , T_{0-R} . This may be expressed as

$$T_{0-R} = \left[\frac{\int_{0}^{\infty} i(t) dt}{\int_{0}^{\infty} \frac{2R/c}{i(t)} dt} \right]^{1/2} \quad (2)$$

The assumptions made in reaching equation 2 are that: (1) measurements are made at a wavelength free of molecular absorption, (2) the phase function for backscattering throughout the path of interest is constant and (3) the transmission of path R to r_1 is low. The error in measured transmission depends on the transmission of the path beyond the point R to which transmission is measured. If T_{R-r_1} is the per cent transmission from that point to the place where the laser beam spills over the analog zone, then

$$\% \text{ error in } T_{0-R} \leq \frac{1}{2} T_{R-r_1} (\%)$$

The symbol \leq is used to indicate that backscattering beyond r_1 contributes to the measured signal but less effectively than it would if the laser pulse were entirely within the analog zone.

Advantages of this design of single ended transmissometer are: (1) The optical compensation for the inverse square term reduces the dynamic range of signals to be processed dramatically; (2) The small analog hole reduces sky background signals and signals due to multiple scattering of the laser pulse to a minimum; (3) Since the analog zone is within the near field, there are no near field problems. Such problems are serious in systems designed to work in the far field; (4) The electronic information processing is simple. The square root of the ratio of two integrated photocurrents gives transmission; (5) No information regarding $\sigma(r)$ and $\Phi(\pi)$, the phase function for back scattering, is required and $\sigma(r)$ may vary along the path.

The system built for AFGL uses a frequency doubled ruby laser providing a 5 mJ pulse at 3471 Å and having a duration of 20 n sec. The Air Force School of Medicine at Brooks Field has reviewed the instrument design in terms of eye safety. They have approved it for Air Force use. To reduce the size of the optical system, the beam splitter is located between the lens of the collecting optics and its focal plane. In this way, the lens is also used as the objective of the laser projector. In addition, the optical trains are folded. The entire optical system was assembled in the laboratory in a complex plate glass frame. The frame and the optical components were locked in place with epoxy cement. The only moveable components are the photomultipliers, the laser and the focus of the beam expander. In recent tests, the diameter of the laser spot at 700 m was 3 cm.

LIGHT SCATTERING IN WATER DROPLET FOGS

A.I. Carswell, J.S. Ryan and S. R. Pal

Departments of Physics & CRESS

York University, Toronto, Canada

A number of recent investigations have shown the value of laser diagnostics for measurements of atmospheric aerosols. In particular, the complete polarization analysis of the scattered radiation has been shown to contain considerable information. Such measurements have been made at York with our field lidar system for several years.⁽¹⁾⁽²⁾ In this work it has been found that very substantial changes in the polarization of the incident wave can occur. The largest effects have been observed in very turbid situations (fog, cloud) where multiple scattering contributions are large.⁽³⁾ Interpretation of the field measurements is often hampered by the difficulty in obtaining adequate data on the scattering media with which to correlate the light scattering information.

In an effort to improve this situation a controlled laboratory experiment has been undertaken. The apparatus incorporates a one cubic meter chamber in which various aerosol and fog conditions can be generated. An argon laser with up to 2 watts output on a single line is used as the source along with polarizing and beam steering optics to direct a well-collimated and polarized beam into the chamber. Two photometers are arranged to detect the near forward and near backward regions of the scattered radiation. These photometers are equipped with rotatable polarizers and appropriate optics for adjusting the field of view and aperture dimensions.

In this paper we present results of measurements on a water droplet fog generated by ultrasonic nebulization. The optical depth of the fog was continuously varied over a range 0 to 5. The 514.5 nm argon laser beam was linearly polarized to better than one part in 10^4 . Measurements were made of the on-frequency scatter in both forward and backward directions. The forward scatter was

studied with a motor driven scanner equipped with a rotatable polarizer and several field stops and apertures. Scanning transversely over the beam cross-section revealed the dependence of beam width on fog density. In thick fogs, noticeable broadening occurred as evidenced by the considerable intensity in the wings of the beam profile. The measurements of the forward signal also revealed that the measured optical depth is dependent on receiver parameters.

Our measurements allow determination of true optical depth values in situations where multiple scatter is important. Although the beam was significantly broadened, no appreciable depolarization was observed in the forward scatter (the depolarization was typically less than 1%). Backscatter measurements, on the other hand, revealed considerable depolarization which increased with fog density and receiver field of view. When the primary backscatter was blocked, the multiple scatter depolarization reached 20% in the thickest fogs. This trend was also in evidence for total backscatter at a scattering angle of 179° . In these measurements, however, the depolarization was generally smaller due to the strong single scatter contribution which tends to preserve the polarization. Although the backscatter depolarization reached appreciable values, there were no observed changes in the dominant plane of polarization or in the ellipticity. In this paper we present a summary of these findings.

References

- (1) S.R. Pal and A.I. Carswell, Appl. Opt. 12, 1530 (1973).
- (2) W.R. McNeil and A.I. Carswell, Appl. Opt. 14, 2158 (1975).
- (3) S.R. Pal and A.I. Carswell, Appl. Opt. 15, 1990 (1976).

LIGHT SCATTERING AS A MEASURE OF AEROSOL CONCENTRATION

JIRI MOTYCKA

DEPARTMENT OF MECHANICAL ENGINEERING, UNIVERSITY OF TORONTO

Light scattering has the attraction of providing real-time measurements of concentration while leaving the aerosol's state undisturbed. However, the intensity of the light scattered into a specified solid angle is normally dependent not only on concentration but also on particle size and refractive index. It will be shown that a simple optical arrangement minimizes these unwanted dependencies.

The technique is shown in Fig. 1. A collimated light beam passes through a uniformly dispersed aerosol a distance L to a lens located at plane π . Coincident with the back focal plane of the lens is located a filter with density increasing with the radial distance from the centerline. The filter thus introduces a transmission function $p(\theta)$ dependent on the incident angle of light at plane π , or in

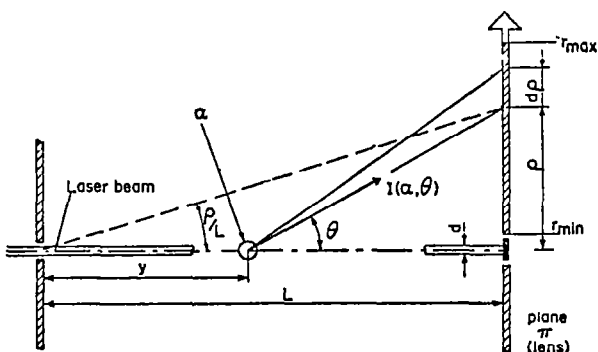


Figure 1.

The irradiance of the receiver plane π from a single particle has been expressed by Van de Hulst (1957) as

$$I = \frac{I_0 (i_1 + i_2)}{2k^2 r^2} \quad (1)$$

where

I = irradiance, I_0 = intensity of the incident light, i_1 and i_2 are the intensities of scattered light for two polarizations, $k = 2\pi/\lambda$, λ = wavelength and r is the distance shown in Fig. 1. For unpolarized

the present context, on the scattering angle, θ . Light transmitted through the lens and attenuated by the filter is detected photoelectrically. The direct light beam itself is absorbed by a non-reflecting opaque mask in front of the lens.

light $i(\alpha, m, \theta) = (i_1 + i_2)/2$. The function $i(\alpha, m, \theta)$ depends on the size parameter $\alpha = \pi D/\lambda$ (D = particle diameter), on the particle's refractive index m , and on the angle θ between the direction of incident light and the direction of scattering.

For a volume element of aerosol $A dy$ and for N particles in a unity volume, the flux reaching the area dS of plane π is, assuming simple scattering;

$$dF = I_0 \cos\theta dS = \frac{I_0 i(\alpha, m, \theta)}{k^2 r^2} A \cdot N \cdot \cos\theta \cdot dS \cdot dy \quad (2)$$

where A is the beam cross-section and I_0 its intensity. From the geometry, $dS = 2\pi\rho d\rho$. Also $L-y = \rho \cot(\theta)$, which gives $dy = \rho d\theta / \sin^2\theta$. Substituting into Eq. (2), we get

$$dF = \frac{I_0 \cdot i(\alpha, m, \theta)}{k^2 r^2} A \cdot N \cdot \cos\theta \frac{2\pi\rho^2 d\rho d\theta}{\sin^2\theta}$$

Since $\rho/r = \sin\theta$, we get

$$dF = C \cdot i(\alpha, m, \theta) \cdot \cos\theta \cdot d\rho \cdot d\theta$$

where $C = \text{constant}$. The total flux reaching the plane π for ($r_{\min} \leq \rho \leq r_{\max}$), from the entire pathlength corresponding to

$(\theta_0 \leq \theta \leq \frac{\pi}{2})$ is

$$F = C(r_{\max} - r_{\min}) \int_{\theta_0}^{\pi/2} i(\alpha, m, \theta) \cos\theta d\theta$$

For each radius ρ of the plane π , the scattered light is incident at a minimum angle $\theta = \tan^{-1}(\rho/L)$ and a maximum angle $\theta = \pi/2$. Since $\rho \ll L$, the lower integration limit $\theta_0 = (r_{\max} + r_{\min})/2L$.

The ratio $V(\alpha) = F/v$ is introduced in order to quantify the degree of the concentration measurement's dependency on size, α , and refractive index, m . (In this expression v is the volume of monodisperse aerosol in a unit volume of air). Hence, it is desired that the ratio

$$V(\alpha) = \frac{F}{v} = \frac{C_2}{\alpha^3} \int_{\theta_0}^{\pi/2} i(\alpha, m, \theta) \cos\theta p(\theta) d\theta \quad (3)$$

be constant for any α and refractive index m . The function $p(\theta)$ has been included to represent the angular transmission of the system.

To optimize $V(\alpha)$ the Mie scattering functions for spherical particles are used (Dave, 1968). Two variables are available for optimization of $V(\alpha)$; the integration limit θ_0 , and the angular transmission of the optical system $p(\theta)$. Several expressions for $p(\theta)$ have been tried. The best results were obtained from the function: $p(\theta) = \exp(-a\theta)$.

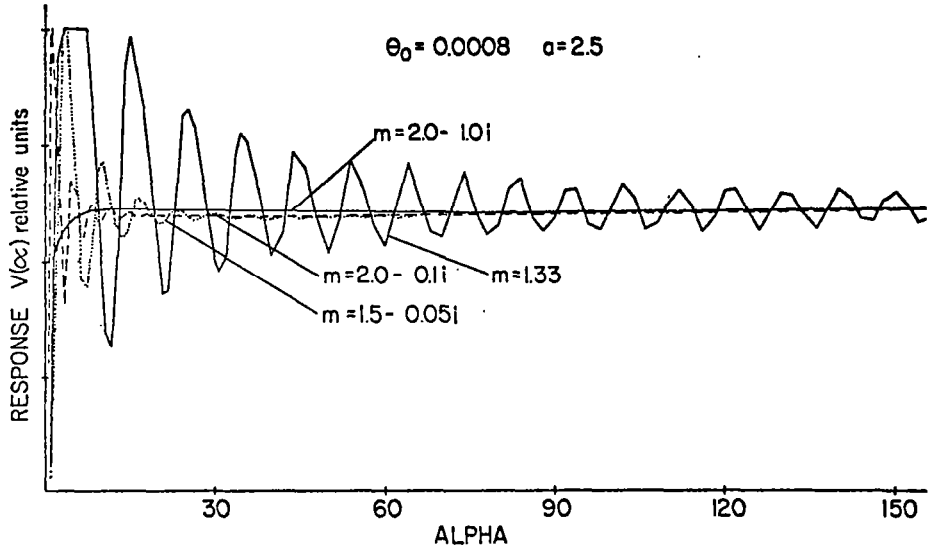


Figure 2.

Fig. 2 shows the responses $V(\alpha)$ for the exponential $p(\theta)$ for $\theta_0 = 0.8$ rad and $a = 2.5$, computed for a number of refractive indeces. The response for absorbing particles, such as carbon $m = 2.0 - 1.0 i$, is smooth and flat, but the curves for particles with a low value of the imaginary term of the refractive index oscillate. However, these oscillations will be averaged out for polydispersions, if their size distribution ranges over more than say, 20 units of α . It may be concluded that the forward scattered light from a laser beam, if detected by the described optical system, is a good measure of the volume concentration of polydispersed spherical particles regardless of their size and refractive index.

Mean size measurement

The oscillations of $V(\alpha)$ curves resemble those of the extinction cross-section Q_{ext} , a parameter expressing the flux removed from the beam, normalized by the geometric cross-section of the particle. This resemblance follows from the relation originally derived by Mie and presented by Kerker (1969):

$$I(\theta = 0) = \text{const. } \alpha^2 \cdot Q_{ext}$$

For a polydispersion of particles with a size distribution $N(\alpha)$ the ratio of the flux F collected for volume measurement to the flux E removed by extinction is:

$$\frac{F}{E} = C \frac{\int_{\alpha}^{\alpha} N(\alpha) V(\alpha) \alpha^3 d\alpha}{\int_{\alpha}^{\alpha} N(\alpha) Q_{ext} \alpha^2 d\alpha} = c \cdot \alpha_{32}$$

where α_{32} is the mean particle volume-to-area size.

Due to the similarity of functions $V(\alpha)$ and Q_{ext} the oscillations of both curves with size cancel out to a considerable extent which introduces the possibility of obtaining a mean size α_{32} only partly dependent of the refractive index of particles.

References

1. DAVE, J.V. (1968), Subroutines for computing the parameters of the electromagnetic radiation scattered by a sphere. Report No. 320-3237, IBM Scientific Center, Palo Alto, California, May 1968.
2. HODKINSON, J.R. (1966), Optical measurement of aerosols, in *Aerosol Science*, edited by C.N. Davies, Academic Press 1966.
3. VAN DE HULST, H.C. (1957), *Light scattering by small particles*, John Wiley.
4. KERKER, M. (1969), *The scattering of light and other electromagnetic radiation*, Academic Press.

TEMPORAL-AND SPATIAL-FREQUENCY SPECTRA FOR ATMOSPHERIC AEROSOLS

M. J. Post and R. L. Schwiesow

National Oceanic and Atmospheric Administration
Environmental Research Laboratories
Boulder, Colorado 80302

The literature abounds with spectra for the amplitude, phase, and phase-difference of optical signals propagated through an atmosphere with index fluctuations. Another fluctuating quantity, the backscatter coefficient, may be of equal or greater importance in propagation effects on a system such as lidar. The fluctuations in the volume backscatter coefficient β arise mainly from fluctuations in the total number of "clear air" aerosols, their size distribution, and their shape, chemical composition, and orientation. This work presents observations of the backscatter power spectra of these fluctuations for $\lambda = 10.6 \mu\text{m}$, but it does not attempt to explain their origins.

Observations

Measurements for this study were made in Boulder, Colorado, using the Wave Propagation Laboratory CO₂ Doppler lidar, a CW system. The experiment was designed to sense the instantaneous intensity of the total backscattered Doppler signal. By aligning the axis of the lidar parallel to the mean wind, the spatial distribution of the fluctuations, $I(x)$, could be derived from the temporal ones, $I(t)$, by associating an x with each observation time t as follows:

$$x_1 = t_1 = 0$$

$$x_{n+1} \approx x_n + \frac{[v(t_{n+1}) + v(t_n)]}{2} (t_{n+1} - t_n), \quad n = 1, 2, \dots, N-1 \quad (1)$$

where N is the total number of observations. Each observation consists of a complete Doppler spectrum, so the mean velocity and integrated intensity (as well as other spectral moments) are available at each observation time, typically occurring every 0.6 sec.

Strictly speaking, to make this transformation properly one must show that the advecting atmosphere is "frozen" or stationary for the entire observation period. This certainly is not true. However, having made many 1-2 hour observations, we observe that the shape of the spatial frequency spectrum is essentially maintained from day to day, indicating that the spatial structure of atmospheric aerosols is in some sort of steady-state motion.

Although the mode radius of an aerosol size distribution (such as Deirmendjian's¹ model Haze L) peaks near $0.1 \mu\text{m}$ in radius, as depicted in Figure 1, a surprisingly heavy backscatter contribution at $10.6 \mu\text{m}$ is due to relatively rare, larger particles. For $10.6 \mu\text{m}$ wavelength the small particles fall in the Rayleigh regime and the larger in the Mie regime, where stronger

scattering occurs. For this experiment, assuming a size distribution similar to Deirmendjian's Haze L, the system is most sensitive to particles whose radius lies in the 0.3 - 2.3 μm range.

Analysis

Reduction of raw spectral data for $I(t)$ and $v(t)$ was done on a small digital computer. The temporal power spectrum $I(w)$ was found for each data run of time T (typically 30 minutes) using the Fourier transform

$$I(w) \approx (2\pi)^{-\frac{1}{2}} \int_0^T e^{-iwt} I(t) H(t, T) dt. \quad (2)$$

The function $I(w)$ should not be confused with Tatarski's $W(w)$, the spectral density². $H(t, T)$ is a filter used to smooth the beginning and end of the observed intensity function $I(t)$, so as not to artificially introduce high frequency components due to discontinuities at $t = 0$ and $t = T$. In practice this is accomplished more efficiently in the frequency domain by the use of a Hanning filter.

The spatial power spectrum $I(k)$ may also be found from the constructed spatial intensity function $I(x)$ by

$$I(k) = (2\pi)^{-\frac{1}{2}} \int_0^D e^{-ikx} I(x) H(x, D) dx, \quad (3)$$

where D is the total spatial length of the data run (typically 10 km).

It is not claimed that these power spectra arise from three dimensional eddies of the corresponding size. In the spatial domain, the height of the observations clearly rules out a concept encompassing eddies of sizes larger than 30 m. Similarly the length of the probing volume eliminates detection of eddies less than 20 m in size.

Results

Examples of the Fourier transform pairs $I(w)$ and $I(t)$, and $I(k)$ and $I(x)$ are displayed in Figure 2 for single data runs. Single spectra are very noisy, and several may be averaged and smoothed to produce composite spectra of each type. Interesting features of these more representative composite spectra will be discussed at the conference, giving insight to the spatial structure, or inhomogeneity, of aerosols in the atmosphere.

References

1. D. Deirmendjian, Electromagnetic Scattering on Spherical Polydispersions. (Elsevier, New York, 1969)
2. V. I. Tatarski, The Effects of the Turbulent Atmosphere on Wave Propagation. (Springfield, Va.: U.S. Dept. Commerce, 1971)

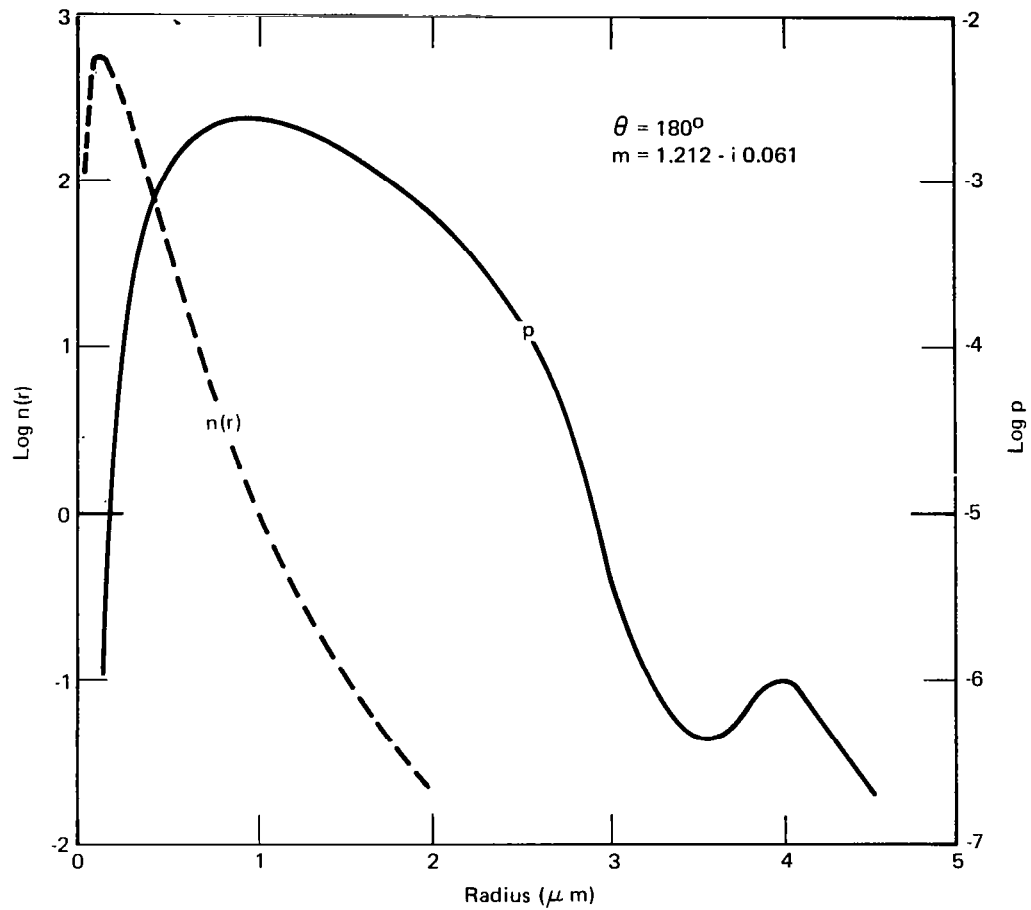


Figure 1. Aerosol size distribution (Haze L) and contributions to signal (p) vs. radius for $\lambda = 10.6 \mu m$.

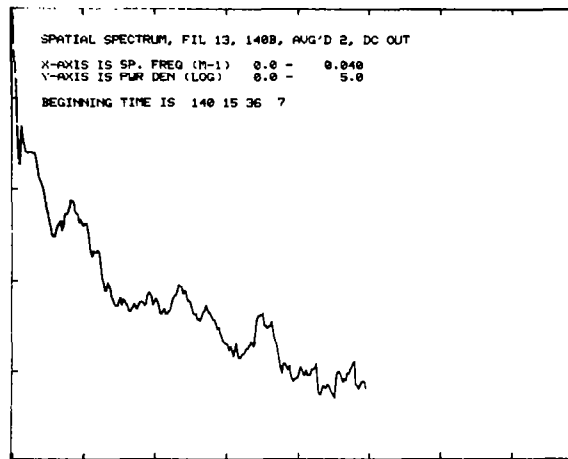
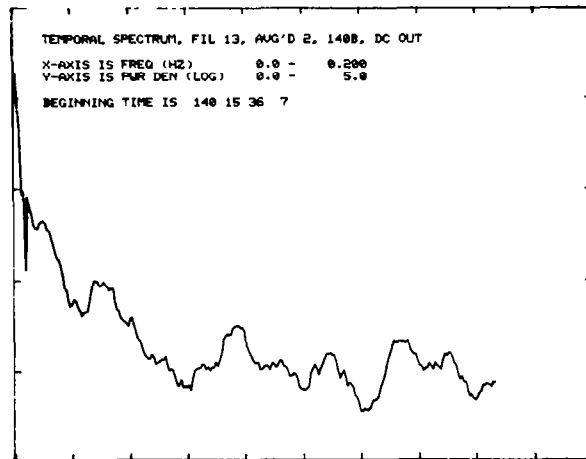
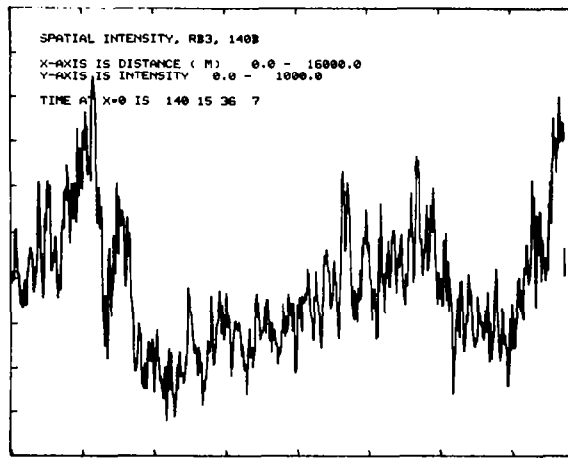
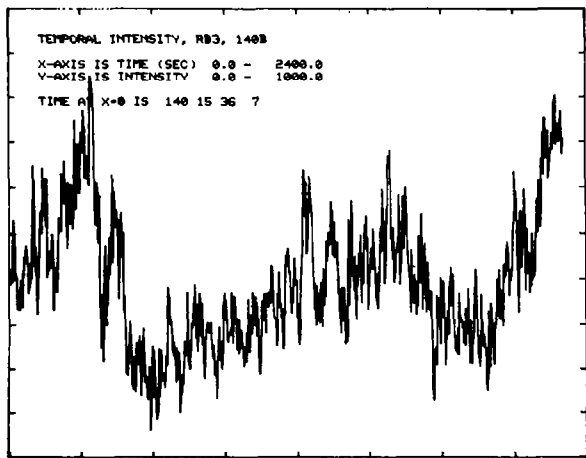


Figure 2. Typical raw aerosol intensity data (above) and associated spectra (below).

FIELD COMPARISON OF OPTICAL PARTICLE COUNTERS*

by

Edward E. Hindman II
Research Department
Naval Weapons Center
China Lake, CA 93555

1. INTRODUCTION

Optical particle counters (OPC) are devices for determining the sizes and concentrations of aerosol particles which scatter visible light (typically particles $\geq 0.2 \mu\text{m}$)¹. The amount of light which an individual particle scatters is a function of its size, shape, and index of refraction. The responses of a variety of commercial OPC to spherical particles of known sizes and indices of refraction were determined by Liu *et al.* (1974a) in the laboratory. The responses of a variety of commercial OPC to particles in the free air were measured at Trinidad, California between 9 and 16 July 1976. This paper presents the measurements obtained with the OPC at Trinidad, the systematic differences between the measurements, the size resolution of the instruments, and the influence of the ambient relative humidity on the measurements.

2. INSTRUMENTS

Seven different types of OPC were located at a field site on top of Trinidad Head² between 9 and 16 July 1976. The types of instruments and their characteristics are listed in Table 1. Each OPC was calibrated by its manufacturer. There were three ROYCO 225 counters present at Trinidad and one each of the remaining counters.

The inlet and sensor portions of the counters were located within 12 m of each other at the field site. The sensor of the ROYCO 202 counter was located within a trailer³. The sensors of the remaining counters were located essentially *in situ* (the distances between the inlets and sensors were negligible). The inlets to the sensors of the ROYCO 225 counters and the Climet 208 were directed perpendicular to the flow while the inlets to the PMS counters were directed parallel to the flow. It was found, however, that the perpendicular orientation of the inlets did not affect the measurements.

* The measurements reported in this paper represent the combined efforts of E. E. Hindman of the Naval Weapons Center (NWC), G. L. Trusty and J. W. Fitzgerald of the Naval Research Laboratory (NRL), and J. G. Hudson and C. F. Rogers of the Desert Research Institute (DRI).

¹All sizes refer to equivalent diameters.

²Trinidad Head is a 107 m high, 600 m diameter rock located adjacent to the northern California coast at Trinidad. A detailed description of the field site and additional studies which took place at the site have been reported by Hindman (1976).

³The air sample reached the sensor through a 180 cm long, 5 cm diameter tube; the sample losses were negligible for particles $< 1.0 \mu\text{m}$, the losses were 27% for particles $1.0 \mu\text{m}$ and 42% for particles $10 \mu\text{m}$; the ambient relative humidity was reduced 30% at the sensor [i.e., Ambient RH(%) - 30% = Sensor RH(%)].

TABLE 1
CHARACTERISTICS OF THE OPTICAL PARTICLE
COUNTERS ASSEMBLED AT TRINIDAD

Model	Size Range (μm)	Size Intervals	Light Source	Scattering Angle	Description
ROYCO* 202	0.3 - 10	14	Incandescent	Right angle	Zinky (1962)
ROYCO 225	0.5 - 20	4	Incandescent	Near-Forward	-
ROYCO 245	0.5 - 5	4	Incandescent	Near-Forward	Liu <i>et al.</i> (1974a)
Climet** 208	0.5 - 5	4	Incandescent	Forward	Lepper (1976)
PMS*** Active Scattering Aerosol Spec- trometer (ASAS)	0.2 - 1.5	15	Laser	Forward	Knollenberg (1976)
PMS Classical Scattering Aerosol Spec- trometer (CSAS)	2.0 - 30	15	Laser	Forward	Knollenberg (1976)
PMS 2-D Probe	30 - 90	-	Laser	N/A****	Knollenberg (1976)

* ROYCO Instruments, Inc., 141 Jefferson Dr., Menlo Park, CA 94025.
** Climet Instruments Co., 1320 W. Colton Ave., Redlands, CA 92373.
*** Particle Measuring Systems Inc., 1855 S. 57th Court, Boulder, CO 80301.
**** Particles interrupt the laser beam and their shadows are cast onto a photodiode array for sizing.

TABLE 2
OPERATION OF THE INSTRUMENTS AT TRINIDAD

Date	Time (PDT)	Relative Humidity (%)	NRL			DRI			NWC		
			PMS Probes	ROYCO 225	ROYCO 208	CLIMET 208	ROYCO 202	ROYCO 245	TSI EAA		
7-9-76	0838	86	yes	yes	yes	no	no	no	no	no	no
"	0905	87	yes	yes	yes	yes	yes	yes	yes	yes	yes
"	1055	83	yes	yes	yes	yes	yes	yes	yes	yes	yes
"	1409	80	yes	yes	yes	yes	yes	yes	yes	yes	yes
7-10-76	0815	87	yes	yes	yes	no	no	no	no	no	no
"	1020	88	yes	yes	yes	yes	yes	yes	yes	yes	yes
"	1330	80	yes	yes	yes	yes	yes	yes	yes	yes	yes
7-12-76	1420	80	no	yes	yes	no	yes	yes	yes	yes	yes
7-13-76	0855	91	yes	yes	no	no	yes	yes	yes	yes	yes
"	1430	83	yes	yes	no	no	yes	yes	yes	yes	yes
7-14-76	0815	97	yes	yes	yes	no	no	no	no	no	no
7-15-76	0750	100(fog)	yes	yes	yes	no	no	no	no	no	no
"	0820	100(fog)	yes	no	yes	no	yes	yes	no	yes	yes
7-16-76	0946	100(fog)	yes	no	yes	no	yes	no	yes	no	yes

TABLE 3
QUOTIENTS OF CUMULATIVE CONCENTRATIONS [$N_1(>D)/N_2(>D)$]
AS A FUNCTION OF PARTICLE DIAMETER

N_1 from	N_2 from	Particle Diameter (μm)				
		0.5	1.0	2.0	4.0	6.0
NRL-ROYCO 225	DRI-ROYCO 225	0.95 \pm 0.03	1.34 \pm 0.10	2.51 \pm 0.15	2.81 \pm 0.38	No Data
NRL-ROYCO 225	NRL-PMS Probes	0.52 \pm 0.05	0.72 \pm 0.07	0.87 \pm 0.09	0.82 \pm 0.12	1.04 \pm 0.25
DRI-ROYCO 225	DRI-Climet 208	1.49 \pm 0.11	1.91 \pm 0.19	1.67 \pm 0.27	2.58 \pm 0.48	No Data
NRL-ROYCO 225	NWC-ROYCO 245	1.50 \pm 0.14	1.25 \pm 0.22	1.21 \pm 0.16	0.94 \pm 0.20	No Data

size resolution of the OPC is illustrated by the size distribution; the finest resolution is achieved by the PMS probes (~0.2 to 2 μm) and the coarsest resolution is achieved by the ROYCO 225 counters (~0.5 to 5 μm).

The systematic differences between the measurements obtained from the OPC were determined in the following manner. The concentrations of particles with diameters $>D$ (cumulative concentrations, N) from one counter [$N_1(>D)$] were divided by the concentrations of particles with diameters $>D$ from another counter [$N_2(>D)$]; both measurements were from the same sampling period. The procedure was repeated for values of D of

⁴Model 3030, manufactured by Thermo-Systems Inc., 2500 Cleveland Ave North, St. Paul, MN 55113.

⁵A complete tabulation of the measurements obtained during the operations of the instruments listed in Table 2 are given by Hindman *et al.* (1976).

Measurements of particle size distributions between 0.01 and 0.56 μm were obtained with an electrical aerosol analyzer⁴ (EAA). The EAA has been described by Liu *et al.* (1974b). The EAA was mounted immediately down stream of the ROYCO 202 counter in the trailer. The calibration of Whitby and Cantrell (1976) was used to reduce the data from the EAA.

3. PROCEDURES

During the period 9 to 16 July 1976, fourteen sampling periods occurred in which various combinations of the OPC were operated. Table 2 summarizes which instruments were operated during the fourteen periods. Each sampling period lasted from 5 to 10 min.

4. RESULTS

Particle size distributions were constructed from the measurements collected during each of the fourteen sampling periods⁵. The particle size distribution from the sampling period at 1330 PDT on 10 July 1976 is shown in Fig. 6 of the article in these proceedings by G.L. Trusty and T.H. Cosden. Referring to this figure, the size distribution is representative of the good agreement achieved between the measurements from the OPC, and the good agreement between the measurements from the OPC and the EAA in the region of overlapping particle sizes. Furthermore, the particle

0.5, 1.0, 2.0, 4.0, and 6.0 μm and for each sampling period in which the two counters were operated. The N_1/N_2 values were averaged, the uncertainties of the averages calculated, and the results are listed in Table 3.

It can be seen from Table 3 that systematic differences occurred between the four pairs of counters investigated. In fact, systematic differences occurred between two identical counters, the NRL- and DRI-ROYCO 225 counters (the differences are negligible for concentrations of particles $>0.5 \mu\text{m}$ but the NRL counter measured 2.8 times as many particles $>4 \mu\text{m}$ as did the DRI counter). The differences among the four pairs of counters range from a low of 0.52 (the NRL-ROYCO 225 measured a factor of 1.9 fewer particles $>0.5 \mu\text{m}$ than did the NRL-PMS ASAS probe) to a high of 2.8 (the NRL-ROYCO 225 measured a factor of 2.8 more particles $>4 \mu\text{m}$ as did the DRI-ROYCO 225 counter). The results in Table 3 indicate that commercial OPC will measure particle concentrations with a precision of about a factor of ± 2.0 , assuming the particle size measurements are precise.

An estimation of the accuracy of the OPC measurements is obtained by comparing the seven simultaneous measurements from the TSI-EAA and the PMS-ASAS probe made at relative humidities $<97\%$; these instruments can measure the concentrations of particles $>0.2 \mu\text{m}$ but the EAA employs the principle of electrical mobility of charged particles to determine the concentrations of particles. The EAA measured a concentration of particles $>0.2 \mu\text{m}$ which was 1.62 (± 0.19) times greater than the concentration of particles $>0.2 \mu\text{m}$ measured with the ASAS probe. This small difference between the measurements indicates that the OPC measurements are accurate.

The effect of relative humidity on the measurements became pronounced for free-air humidities $>97\%$. The three simultaneous measurements with the EAA and ASAS probe showed that the concentrations of particles $>0.2 \mu\text{m}$ are, on average, 17 times greater in the free air (ASAS measurements, taken at $>97\%$ RH) than in the air drawn into the trailer (EAA measurements, taken at $\sim 70\%$ RH). Furthermore, the concentrations of particles $>3 \mu\text{m}$ in fog (ASAS measurements) were two to three orders larger than in the air sampled at 70% RH in the trailer (ROYCO 202 measurements).

5. CONCLUSIONS

Particle size distribution measurements obtained at the same time in the field with seven different commercial optical particle counters showed that particle concentrations were measured with a precision of a factor of ± 2 . Systematic differences between the measurements from the various counters occurred and the magnitudes of the differences were calculated. The particle size resolution of the counters ranged from $0.2 \mu\text{m}$ to $0.5 \mu\text{m}$. The particle measurements became extremely sensitive to the free air relative humidity at values $>97\%$.

REFERENCES

Hindman, E. E., II, 1976: Aerosol particles in a coastal environment. Proc. Workshop on Remote Sensing of Marine Boundary Layer, NRL TP (in preparation).

Hindman, E. E., II, G. L. Trusty, W. A. Hoppel, J. W. Fitzgerald, and J. G. Hudson, 1976: Aerosol particle measurements at Trinidad, California. NWC TP (in preparation).

Knollenberg, R. G., 1976: Three new instruments for cloud physics measurements: The 2-D spectrometer, the forward scattering spectrometer probe, and the active scattering aerosol spectrometer. Preprints - Int. Conf. Cld. Phys., American Meteorological Society, Boston, Mass., 554-561.

Lepper, J. M., 1976: Synoptic analysis of aerosol particles. Proc. Workshop on Aerosol Measurement, 24-26 March 1976, Dept. Mechanical Engineering, University of Florida, Gainesville, Fla.

Liu, B. Y. H., R. N. Berglund and J. K. Agarwal, 1974a: Experimental studies of optical particle counters. Atmos. Env., 8, 717-732.

Liu, B. Y. H., K. T. Whitby and D. Y. H. Pui, 1974b: Aerosol analyzer for size distribution measurement of submicron aerosol. J. Air. Poll. Cont. Assn., 24, 1067-1072.

Whitby, K. T., and B. K. Cantrell, 1976: Electrical aerosol analyzer constants. Proc. Workshop on Aerosol Measurement, 24-26 March 1976, Dept. Mechanical Engineering, University of Florida, Gainseville, Fla.

Zinky, W. R., 1962: A new tool for air pollution control, the aerosol particle counter, J. Air Poll. Cont. Assn., 12, 578-583.

ATMOSPHERIC AEROSOL DATA FROM CIRCUMSOLAR TELESCOPE MEASUREMENTS*D. F. Grether, A. J. Hunt⁺, M. WahligEnergy & Environment Division, Lawrence Berkeley Laboratory
University of California, Berkeley, California 94720ABSTRACT

Four automatic scanning telescopes currently provide small-angle forward-scattering data from the sun by measuring the wavelength dependence of the circumsolar and solar profiles.

Intensity profiles of the sun and the solar aureole provide a means of characterizing the atmospheric aerosols.^{1,2,3} Under some circumstances these aerosols can cause a significant fraction of the solar flux to be deviated to angles of several degrees or more. Solar energy conversion techniques utilizing high concentration ratios, such as the Central Receiver concept, essentially collect only the direct sunlight. Pyrheliometers, the instruments normally used to estimate the direct solar radiation, typically have a field of view of 5-6°. The Pyrheliometer measurement includes a large portion of the circumsolar radiation and thus overestimates the amount of direct sunlight that would be collected by a concentrating system. The detailed angular distribution of the circumsolar radiation is important, as it affects the radiant energy distribution on the surface of the receiver in solar thermal power plants. We have developed and built four similar instruments to measure the circumsolar radiation as well as other properties of sunlight, as part of the ERDA Solar Thermal Conversion program. The measurement will be used in performance calculations of solar power plants, and to determine under what conditions pyrheliometer data are adequate for estimating this performance. Modeling of the aerosol scattering will be undertaken in an effort to understand and predict circumsolar levels.

The basic instrument that was designed and fabricated at LBL is illustrated in Fig. 1. It consists of a "scanning telescope" that is mounted on a precision solar tracker and a digital electronics control system. The design has been described in more detail elsewhere.⁴ The telescope is illustrated in Fig. 2. The basic optical element is an off-axis mirror of 7.5 cm diameter and one meter focal length. A fused silica window protects the mirror from the environment. The mirror forms an image of the sun and adjacent sky on a plate off to the side of the incoming light. A small hole in this plate, the detector aperture, defines the angular resolution (1/20 the solar diameter), and the amount of light passing through the aperture into the detector assembly constitutes the fundamental measurement. In the detector assembly, the light is mechanically chopped, optically filtered, and focused onto a pyroelectric detector, a type of thermal detector. This detector was chosen for its uniform wavelength response in the .3 to 2.5 micrometer region and its wide dynamic range.

The telescope scans through a 6° arc with the sun at the center, and measures the brightness of the solar and circumsolar radiation as a function of angle. The instrument scans in declination, so that at sunrise and sunset it travels nearly parallel to the horizon, and at noon it moves in a vertical

plane. A number of precautions are taken to reduce the scattered light levels to less than 10^{-6} at 3° . This, in conjunction with a total dynamic range of 10^7 , effectively solves the problem of measuring the very large intensity differences between the sun and aureole region.

Each scan takes one minute of time, with a digitization of the brightness every $1.5'$ of arc. Within $.5^\circ$ on either side of the sun, an aperture of size $1.5'$ of arc is used and outside this region the aperture is increased to $5'$ of arc. A set of measurements consists of one scan at each of ten "filter positions". There are eight optical filters that divide the solar spectrum into eight bands of roughly equal energy content, one open (or "clear") position, and one opaque position. The latter is used to monitor the detector noise. The absolute determination of the normally incident flux (within 2.5° of the sun center) is provided by an active cavity radiometer.⁵ This device is self-calibrating and has an accuracy of 0.5 percent. This pyrheliometer is provided with a set of filters that rotate synchronously with those on the scanning telescope. Thus an absolute calibration of the normally incident flux in combination with the detailed solar profile in eight wavelength bands provides enough information to determine both the atmospheric turbidity and the scattering phase function.

A portable, prototype instrument has been making measurements at Berkeley for some time and is scheduled to do so at a variety of geographical locations. Three additional "fixed-site" telescopes have been constructed; one is near the 5 megawatt (thermal) solar test facility, Albuquerque, N.M., a second is at the site of a total energy system pilot plant, Ft. Hood, Texas. The third, currently located at China Lake, Ca., will be located at the site of a 10 megawatt (electric) Central Receiver pilot plant. These latter telescopes are capable of unattended operation for up to a week, although they typically receive a daily inspection during the work week. During the night the solar trackers run backwards and automatically initiate operation at the beginning of each day. The data is recorded on magnetic tape and processed at the laboratory's computer center.

Figure 3 is a computer-plotted graphical display for a scan using the clear filter from measurements made at China Lake, Ca. at 10:38 hours on July 30, 1976. The dots are the individual scan digitizations. The small, vertical arrows indicate the angles where the aperture was switched from $5'$ of arc to $1.5'$ of arc, and then back again. The computer code proceeds as follows. A search is made for the peak brightness point of the sun. The two "edges" of the sun are then empirically defined as the angles at which the brightness is down by a factor of 30 from the peak. These edges are indicated by the two vertical, dotted lines. The center of the sun is then taken as the angle midway between the two edges, and is indicated by the solid vertical line. An effective radius is then defined as the true radius of the sun plus the radius of the detector aperture ($0.8'$ of arc). The effective radii are indicated by the solid vertical lines at the top and bottom of the graph, and are nearly coincident with the edges of the sun. The brightness is then integrated from the center of the sun to the effective radius to give the intensity of the direct solar radiation, and integrated from the effective radius to the end of the scan to give the intensity of the circumsolar radiation. The ratio of circumsolar to solar radiation is given at the top of the graph (C/S=). Also indicated is the normal incidence measurement provided by the pyrheliometer (NI=). This particular scan has a circumsolar to solar ratio of only .67%, and a normal incidence value of 795 watts/meter squared.

Figures 4, 5 and 6 illustrate measurements taken at China Lake during a time of unusually high turbidity. The diagrams are similar to Fig. 3 but taken through band pass filters in three consecutive minutes later the same day. The pass bands of the filters are indicated above the graph. The data contains several interesting features. Note the rather severe limb darkening in the visible and violet scans in contrast to the nearly flat solar profile in the infrared scan. The circumsolar to solar ratios are approximately equal for all scans but the aureole profiles differ. Note in particular the symmetrical shoulders that occur about 1 degree from sun center in both of the shorter wavelength scans. The shoulder appears less obvious in the long wavelength data. The clear filter data taken at 12:05 yielded a total solar flux of only 600 watts/square meter, indicating a very high turbidity. The feature at 1 degree would indicate the presence of large particles with a narrow size distribution. A scattering inversion program is being developed but is not yet available for aerosol modeling. These data represent an episode of high circumsolar levels of concern to solar energy conversion as well as an interesting study of aerosol scattering.

The instruments produce a very large data base, (over 800 scans each day per telescope). Thus, the first priority in data management is to develop suitable cataloging techniques. Then statistics can be developed to identify various classes of days and aerosol modeling performed to identify seasonal or episodic variations of the circumsolar levels. The data will be augmented in late 1976 by the addition of automated weather instruments associated with each telescope.

The excellent engineering and technical support of the Special Projects group at LBL has been vital to the success of this project. The able assistance of Stephen Kanzler in coping with the day-to-day problems of the project is gratefully acknowledged. We also thank the people at Albuquerque, Ft. Hood and China Lake, too many to mention, who have cooperated in setting up and running the telescopes at their respective locations.

1. Deirmendjian, D., Use of Scattering Techniques in Cloud Microphysics Research 1. The Aureole Method. Rand Report. R-590-PR (1970).
2. Shaw, G. E. and C. S. Deehr, On the Relation Between Circumsolar Sky Brightness and the Atmospheric Aerosols. Final Report EPA Grant R801113-01-2, Geophysical Institute, Fairbanks, Alaska (1974).
3. Green, A. A., Deepak and B. Lipofsky, 1971, J. Appl. Opt. 10, 1263.
4. D. F. Grether, J. Nelson, and M. Wahlig, Proc. of the Soc. Photo-optical Instr. Eng., 68, 41, Aug. 1975.
5. R. C. Willson, Appl. Opt. 12, 810 (1973).

* This work was done with support from the U.S. Energy Research and Development Administration.

⁺presented paper

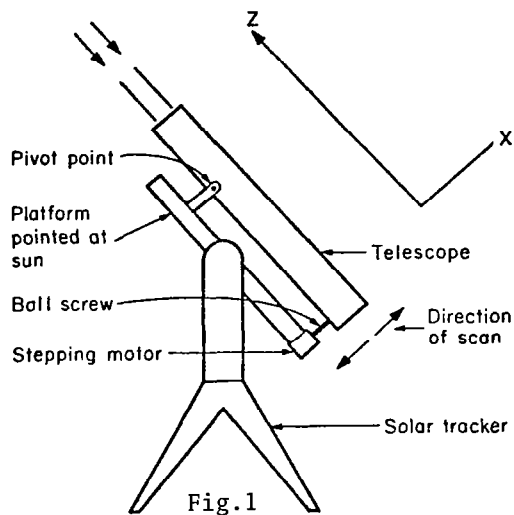


Fig. 1

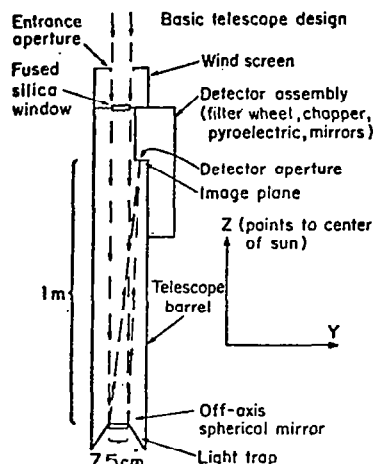


Fig. 2

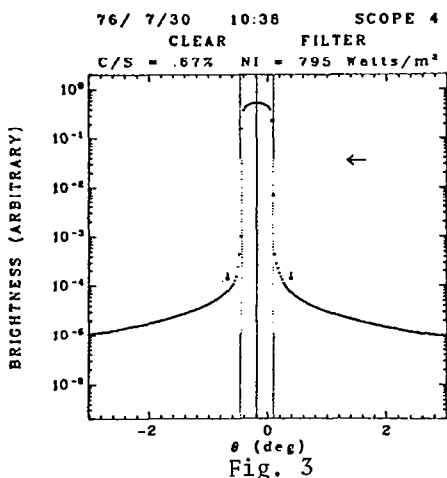


Fig. 3

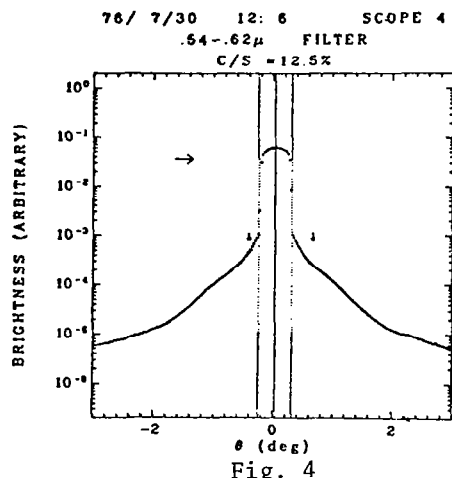


Fig. 4

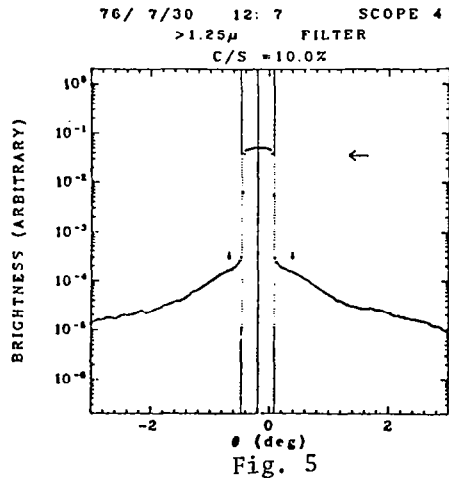


Fig. 5

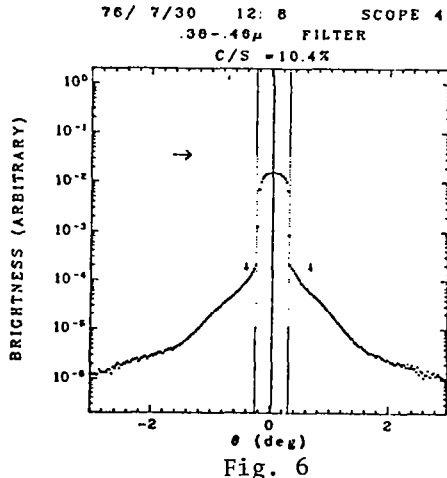


Fig. 6

A COMPREHENSIVE AEROSOL GROWTH MODEL

by

Ronald L. Drake

Atmospheric Sciences Department
Battelle, Pacific Northwest Laboratories
Richland, Washington

SUMMARY

This paper describes the aerosol component of a user-oriented code for the solution of the continuity equations for trace atmospheric constituents. The code, named PROTEUS, is written with the intent that any experimentalist can employ the algorithms rapidly to test hypothetical mechanisms of observed atmospheric behavior. The important features and limitations of the code are as follows:

- Provides for a general wind field in all directions;
- Assumes that all turbulent mixing processes are treated in terms of eddy diffusivities;
- Assumes that the longitudinal diffusion is unimportant, otherwise assumes a general diffusivity field;
- Assumes a steady state system in a fixed eulerian frame of reference, or a quasi-steady state system in a moving eulerian frame;
- Provides for generalized chemical reaction kinetics for all reactant species;
- Provides for generalized aerosol coagulation, breakup condensation and settling;
- Provides for a generalized treatment of precipitation scavenging; and
- Provides for generalized dry - deposition - resuspension behavior.

The starting point of the aerosol component of the PROTEUS code is a general equation for the i^{th} aerosol specie. This system considers the time and space evolution of the particle number density under the processes of

(a) advection by the mean, ambient wind field, $v_m = v_m(x_m, t)$,

- (b) gravitational settling, $v_{si} = v_{si}(x_m, v, t)$,
- (c) condensational growth, $I_i = I_i(x_m, v, t)$,
- (d) turbulent diffusion, $K_{jm} = K_{jm}(x_m, v, t)$,
- (e) coagulation, $\beta_{ij} = \beta_{ij}(x_m, u, v, t)$,
- (f) breakup, $\alpha_i = \alpha_i(x_m, u, v, t)$, $\gamma_{ij} = \gamma_{ij}(x_m, u, v, t)$,
- (g) source and sink distributions, $s_i = s_i(x_m, v, t)$,

where v is the particle volume, x_m the space coordinates, and t the time. The physical coagulation parameters β_{ij} describe the coagulation and scavenging processes, and the breakup processes are described by the parameters α_i and γ_{ij} .

The problems with this formulation for the evolution of aerosols are two-fold: (a) the existence of five independent variables exceed the memory and time constraints placed on many computational facilities, and (b) the system is not in the form of the PROTEUS Code. To alleviate these problems, we invoke the following assumptions.

ASSUMPTION ONE

Let $n = n(x_m, v, t)$ represent the number density of an aerosol in and around an urban or industrial area and assume that n is a composite of three-interacting spectra:

$$n(x_m, v, t) = \sum_{i=1}^3 n_i(x_m, v, t) , \quad (1)$$

where n_1 is dominate over the smallest sizes, n_3 over the largest sizes, and n_2 over the intermediate sizes.

The coagulation terms and the breakup terms in the general equation represent the interaction mechanisms between the three spectra, including the scavenging of smaller particles by the larger particles or by raindrops.

ASSUMPTION TWO

Each of the three spectra is assumed to vary with v in a log-normal fashion; that is,

$$n_i(v) = \frac{M_i(0)}{\sqrt{2\pi} v \alpha_i} \exp \left[-\frac{1}{2\alpha_i^2} \left\{ \ln \frac{v}{\beta_i} \right\}^2 \right] \quad (2)$$

where (x_m, t) has been suppressed for simplicity. The parameters β_i are the geometric mean volumes and the α_i are the logarithms of the standard deviations. The quantity $M_i(0)$ is the zeroth integral power moment of n_i ; the ℓ th integral power moment is defined by

$$M_i(\ell) = M_i(x_m, t; \ell) = \int_0^\infty v^\ell n_i(x_m, v, t) dv. \quad (3)$$

The parameters α_i^2 and β_i , and the moments $M_i(N)$, for any real N , can be expressed in terms of $M_i(I)$, $I = 1, 2, 3$:

$$\alpha_i^2 = \ell \ln \left[\frac{M_i(0) M_i(2)}{M_i^2(1)} \right], \quad \beta_i = \frac{M_i^2(1)}{M_i^{3/2}(0) M_i^{1/2}(2)}, \quad (4)$$

$$M_i(N) = \left[M_i(0) \right]^{1 + \frac{1}{2}N^2} - \frac{3}{2}N \left[M_i(1) \right]^{2N} - N^2 \left[M_i(2) \right]^{\frac{1}{2}N^2 - \frac{1}{2}N}$$

ASSUMPTION THREE

The v -dependency in V_{si} , I_i , K_{ij} , β_{ij} , α_i and γ_{ij} can be isolated in the following manner:

$$p(x_m, v, t) = \sum_{\ell} p(x_m, t; \ell) v^{\alpha(\ell)}, \quad (5)$$

where p represents any of the above parameters.

ASSUMPTION FOUR

The quantities $V_m(x_m, t)$ and $S_i(x_m, v, t)$ are specified.

ASSUMPTION FIVE

Assume the system is in a steady state.

ASSUMPTION SIX

Assume that the flow field is incompressible.

Applying these six assumptions, we find that the steady state number density $n(x_m, v)$ can be represented by the nine moments

$$M_i(N) \equiv M_i(x_m; N); \quad i=1, 2, 3; \quad N=0, 1, 2. \quad (6)$$

The defining equations for these moments are derived from the general aerosol equation for the i^{th} species. Specifying proper boundary conditions allows us to solve this system of nine equations for the moments and, in turn, allows us to reconstruct the number density $n(x_m, v)$ from (1) and (2).

The system of equations for the moments is consistent with the equations in the PROTEUS Code.

H_2SO_4 Gas Phase Concentration in the Stratosphere

Patrick Hamill, Ames Research Center (NASA), Moffett Field, CA 94035

The gas phase concentration of sulfuric acid in the stratosphere is an important parameter in evaluating nucleation and growth rates for the stratospheric aerosol particles. Unfortunately, this parameter is not amenable to direct measurement due to the very low volatility of sulfuric acid; nevertheless, chemical models have been constructed (Harrison and Larsen, 1974; Harker, 1975; Hamill et. al., 1976) which give estimates of H_2SO_4 concentrations due to the photooxidation of SO_2 in the stratosphere. Here we report on a model-independent method of estimating the sulfuric acid vapor pressure in the stratosphere.

The vapor pressures of sulfuric acid - water solutions is a sensitive function of the temperature. As the temperature rises, the vapor pressures increase rapidly. For a standard atmosphere temperature profile the H_2SO_4 vapor pressure variation with altitude will be as shown by the solid curves in Figure 1. The H_2SO_4 vapor pressures were calculated for water vapor mixing ratios as measured by Mastenbrook (1968) and by Sissenwine et. al. (1968). Note that there is an increase in sulfuric acid vapor pressure of some five orders of magnitude as the altitude varies from 12 to 36 km. Evidently, when the vapor pressure becomes greater than the partial pressure, the sulfuric acid - water solution droplets will evaporate. As pointed out by Hamill, Toon and Kiang (1976), this limits the vertical extent of the aerosol layer.

Somewhere near the top of the layer the vapor pressure must be equal to the partial pressure. It should be pointed out that the evaporation of droplets at high altitudes is quite rapid. Hamill, Toon and Kiang (1976) estimate that at 30 km a one micron radius droplet will evaporate in less than one day. Furthermore, mixing velocities are small, of the order of 1 mm/sec. Therefore, the top of the layer as observed can be expected to be fairly close to the level at which evaporation is occurring, i.e., the altitude at which the partial pressure of sulfuric acid is equal to the vapor pressure of sulfuric acid. Therefore, if we can evaluate the vapor pressure of sulfuric acid at the top of the layer, we have a value for the partial pressure, which is directly related to the sulfuric acid concentration at that altitude.

The top of the aerosol layer can be determined by lidar observations, and by balloon borne instruments. It might be mentioned that evidence of the evaporation of particles at the top of the layer is found in the data of balloon borne optical scanners as recently reported by Hofmann, Rosen and Pinnick(1976). They found that the ratio of 0.15 micron radius particles to those with radii greater than 0.25 micron radius drops off slowly as one goes up through the layer, but at the top of the layer and above, this ratio suddenly increases. That is, above the layer there are relatively more small particles than in the layer. This observation can be explained by the fact that water and sulfuric acid are evaporating from the particles, probably leaving only an ammonium sulfate core.

In Figure 2 we present lidar measurements of the stratospheric aerosol layer taken on 12 November 1975 at Menlo Park, California by Dr. P. B. Russell of Stanford Research Institute. We also present a radiosonde temperature profile taken at Oakland, California on the same day.

In Figure 3 we give H_2SO_4 vapor pressure as a function of altitude for various values of H_2O mixing ratio and the temperature points of Figure 2. The smooth curve was obtained by fitting the temperature profile with a third order polynomial and assuming water vapor mixing ratio of 3.5 ppmv. Note that at an altitude of 35 km the H_2SO_4 vapor pressure for a solution droplet is about 10^{-8} to 10^{-9} mm Hg. Since this altitude corresponds to the top of the aerosol layer (Fig 2), we conclude that sulfuric acid partial pressure at that altitude must also be in the range of 10^{-8} to 10^{-9} mm Hg.

This indirect measurement gives an estimate of sulfuric acid concentration at 35 km of about 4×10^8 molecules/cm³. This value is in good agreement with the values estimated at 35 km by the models of Harrison and Larsen and Harker.

Hamill, Patrick, R. P. Turco, O. B. Toon, R. C. Whitten and C. S. Kiang: A one-dimensional model of the stratospheric aerosol layer. Submitted to Geophys. Res. Lett. (1976).

Hamill, Patrick, O. B. Toon and C. S. Kiang: A physical model of the stratospheric aerosol particles. Submitted to J. Atmos. Sci. (1976).

Harker, A. B., J. Geophys. Res., 80, 3399 (1975).

Harrison, H. and T. Larson. J. Geophys. Res., 79, 3095 (1974).

Hofmann, D. J., J. M. Rosen and R. G. Pinnick: Measurements of stratospheric aerosol size distributions and optical model calculations. Paper presented at IAMAP Symposium on Radiation in the Atmosphere. Garmish, Aug. 1976.

Mastenbrook, J. J., J. Atmos. Sci., 25, 299 (1968).

Sissenwine, N., D. D. Grantham and H. A. Salmela, J. Atmos. Sci., 25, 1129, (1968).

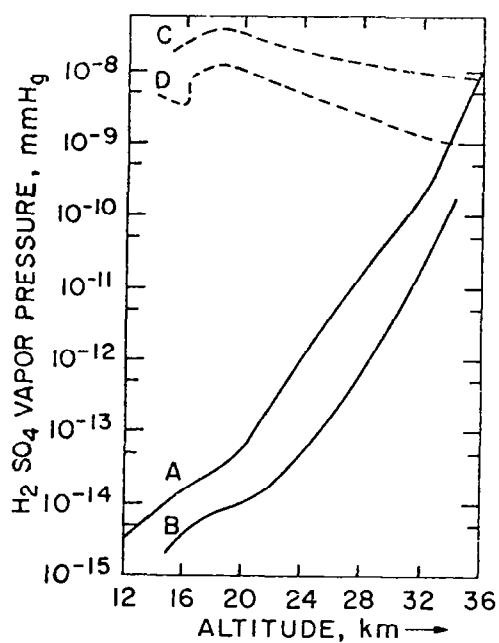


FIGURE 1. CURVE (A): H_2SO_4 VAPOR PRESSURE USING MASTENBROOK (1968) WATER VAPOR PROFILE. CURVE (B): H_2SO_4 VAPOR PRESSURE USING SISSENWINE ET. AL. (1968) WATER VAPOR PROFILE. CURVE (C): HARRISON AND LARSON (1974) SULFATE PROFILE. CURVE (D): HARKER (1975) SULFATE PROFILE.

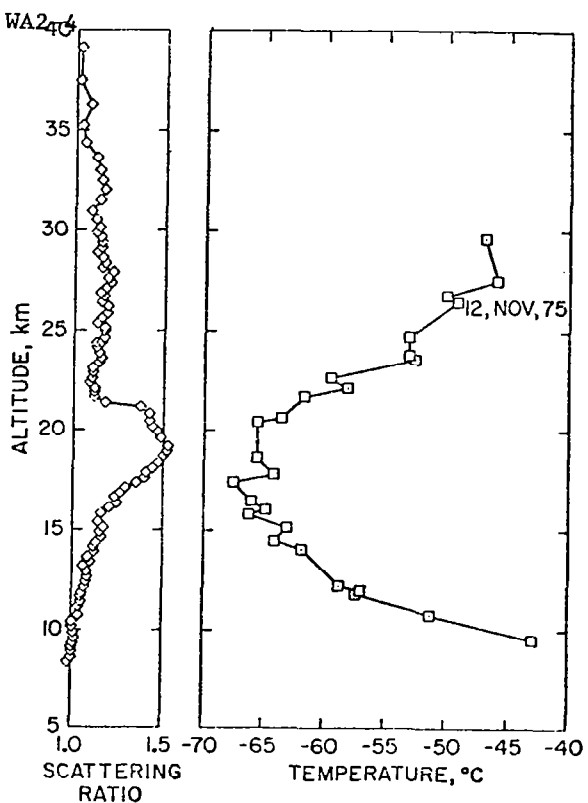


FIGURE 2. LIDAR BACKSCATTER RATIO AND TEMPERATURE PROFILE FOR 12 NOVEMBER 1975.

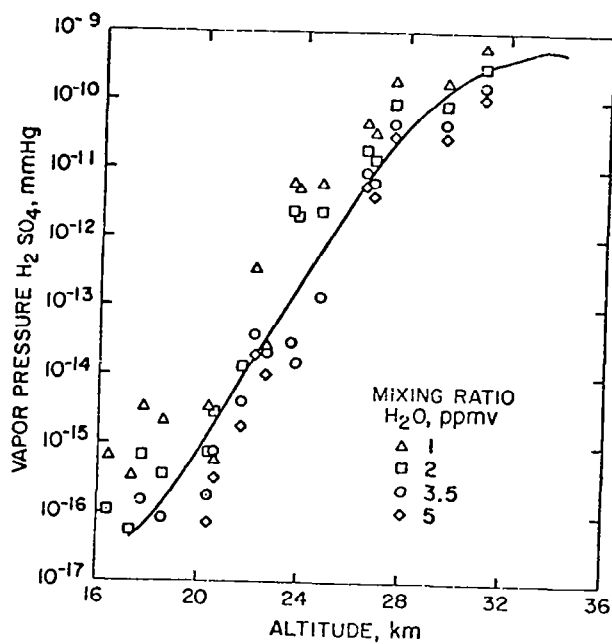


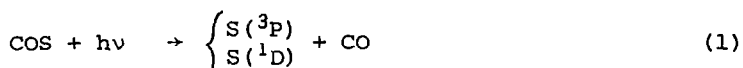
FIGURE 3. H_2SO_4 VAPOR PRESSURE FOR TEMPERATURE PROFILE OF FIGURE 2.

Gas Phase Chemistry in the Ames Stratospheric Aerosol Model

R.C. Whitten, NASA-Ames Research Center, Moffett Field, CA 94035
 R.P. Turco, R and D Associates, Marina del Rey, CA 90201

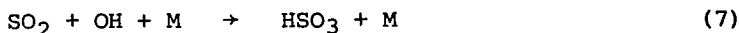
The formation of the stratospheric sulphate layer is governed in part by gas phase chemistry which leads to the production of sulphuric acid. The presence of sulphur gases in the stratosphere is evidently due to direct injection of SO_2 by volcanic eruptions and to the upward transport of COS (and perhaps CS_2) from non-volcanic surface sources (Crutzen, 1976). Unlike SO_2 , COS has a very long tropospheric lifetime, which permits it to be effectively transported to stratospheric altitudes.

Our model currently employs the COS dissociation chemistry suggested by Crutzen (1976), which can be summarized by the reactions which lead to the formation of SO_2



Since CS_2 has a molecular structure similar to COS, its decomposition scheme can be expected to be similar to the above.

The important reaction sequence which leads to the oxidation of SO_2 and subsequent conversion to sulphuric acid is





There are other possible reactions which oxidize SO_2 , but their rates are too small for them to be competitive with (7) - (9). The rate coefficient for the three-body reaction (7), which is pressure-dependent, has been measured by several investigators; we use the one reported by Castleman *et al.* (1975), who obtained a three-body coefficient of

$$k_7^* = 1.6 \times 10^{-31} \text{ cm}^6 \text{ sec}^{-1}$$

at 300 K with N_2 as the third body, and an effective two-body coefficient at 760 torr of

$$k_7^+ = 6 \times 10^{-13} \text{ cm}^3 \text{ sec}^{-1}$$

One can take account of the pressure saturation effect on (7) by writing k_7 as

$$k_7 = \frac{1.6 \times 10^{-31}}{1 + 2.2 \times 10^{-19} [\text{N}_2]} \text{ cm}^6 \text{ sec}^{-1}$$

The rate constant of reaction (8) has not been measured, but we estimate it to be fast, $\sim 10^{-11} \text{ cm}^3 \text{ sec}^{-1}$; the rate coefficient for reaction (9) is $9.1 \times 10^{-13} \text{ cm}^3 \text{ sec}^{-1}$ (Castleman, *et al.*, 1975). Hence, at stratospheric pressures, reaction (7) is probably the rate-controlling step.

The sulphuric acid vapor found through the scheme outlined above can condense to form droplets (as discussed in detail in other papers presented at this conference). It can be transported downward into the stratosphere where it is "rained-out" or it can rise to the upper stratosphere where it is photolyzed.

The chemistry outlined above has been employed in the Ames Research Center one-dimensional model of the stratospheric sulphate layer to compute the altitude distribution of sulphuric acid vapor. The essential features

of the model are described elsewhere (e.g. Turco and Whitten, 1975); in the computations reported here we employed a modification of the eddy diffusivity profile suggested by Wofsy and McElroy (1973). Some typical stratospheric concentrations of SO_2 , OH and H_2SO_4 vapor computed in our model (with H_2SO_4 condensation included) are given below in Table I. Preliminary aerosol layer results have been recently submitted for publication (Hamill, et al., 1976) and some additional ones will be reported in other papers at this conference.

Table I
Typical Altitude Distributions of OH, SO_2 , and H_2SO_4
Concentrations Are in cm^{-3}

Altitude km	[OH]	[SO_2]	[H_2SO_4]
16	8.8(5)	6.9(7)	1.0(5)
18	1.1(6)	6.4(7)	1.3(5)
20	1.3(6)	4.6(7)	1.3(5)
22	1.6(6)	2.0(7)	9.1(4)
24	2.0(6)	1.0(7)	9.2(4)
26	2.6(6)	5.6(6)	1.9(5)
30	5.1(6)	2.5(6)	2.3(6)

References:

Castleman, A.W., R.E. Davis, H.R. Hunkelwitz, I.N. Tang, and W.P. Wood,
Kinetics of association reactions pertaining to H_2SO_4 aerosol
formation, Int. J. Chem. Kin. Symposium I, 629-640 (1975).

Crutzen, P.J., The possible importance of CSO for the sulphate layer of
the stratosphere, Geophys. Res. Lett. 3, 73-76, (1976).

Hamill, P., R.P. Turco, O.B. Toon, R.C. Whitten, and C.S. Kiang, A one-
dimensional model of the stratospheric aerosol layer, J. Geophys.
Res. Lett. (submitted, 1976).

Turco, R.P. and R.C. Whitten, Chlorofluorométhanes in the stratosphere and some possible consequences for ozone, Atmos. Env., 9, 1045-1061 (1976).

Wofsy, S.C., and M.B. McElroy, On vertical mixing in the upper stratosphere and lower mesosphere, J. Geophys. Res., 78, 2619-2624 (1973).

A Model of the Stratospheric Sulfate Aerosol

R. P. Turco

R & D Associates, Marina del Rey, Ca. 90291

P. Hamill

O. B. Toon

R. C. Whitten

Space Sciences Division, NASA Ames Research Center
Moffett Field, Ca. 94035Introduction

The origin and characteristics of the stratospheric aerosol layer are not yet well understood. The layer is apparently important to the global radiation balance of the earth (Pollack et al, 1976); it may also have a role in catalyzing chemical reactions between air constituents (Cadle et al, 1975). The possibility of contamination of the aerosol layer by sulfur emissions from aircraft and industry, and by condensation nuclei from aerospace engines needs to be studied. What is required is a comprehensive model linking gas phase sulfur chemistry to aerosol formation mechanisms. We have developed such a model for terrestrial aerosol (Hamill et al, 1976 a). Here we will briefly outline the structure of our model and describe some of the preliminary numerical calculations we have performed to test its viability.

The Photochemical Model

In our model we calculate concentrations of S, SO, SO₂, SO₃, HSO₃, H₂SO₄ and OCS between the earth's surface and 60 km altitude. The detailed chemistry is discussed in another summary by R.C. Whitten. The abundances of the atmospheric gases which interact with the sulfur compounds are taken from a detailed photochemical-dynamical model of the ambient atmosphere (e.g. Turco & Whitten, 1975); nominal air temperatures and densities are taken from the U.S. Standard Midlatitude Spring/Fall Atmosphere (1966); an eddy diffusion profile with a tropopause height near 13 km has been selected from some earlier work on stratospheric composition (e.g. Turco & Whitten, 1975). After extensive analysis with a completely interactive model, we have found that sulfur reactions have a negligible aeronomical influence on oxygen-nitrogen-hydrogen constituents; this conclusion does not consider possibly significant aerosol radiation and surface reaction feedback mechanisms.

Our model accounts for sulfur dioxide injection directly into the stratosphere by volcanoes (Cadle, 1975), and in situ production by ultraviolet photolysis of OCS (Crutzen, 1976). Sulfur dioxide is subsequently oxidized into sulfuric acid vapor, the rate limiting process being the reaction of OH with SO_2 to form HSO_3 . The aeryonomy of sulfur compounds is only partially known, but it is presently believed that gas phase chemistry alone can account for the sulfuric acid molecules found dissolved in aerosol droplets. Accordingly, we have assumed that HSO_3 radicals are rapidly converted into H_2SO_4 under stratospheric conditions.

The Aerosol Model

Hamill et al. (1976 b,c) have developed the theory of the nucleation of solution droplets in a sulfuric acid-water vapor environment. Condensation nuclei, which are necessary for aerosol formation in this theory, diffuse upwards from their source in the troposphere. Subsequent particle growth by heteromolecular condensation of acid and water vapors is limited by the rate of H_2SO_4 molecular diffusion to the particle surface (Fuchs & Stugin, 1971). Droplet coalescence rates are calculated using aerosol coagulation kernels from the work of Fuchs (1964). Gravitational sedimentation velocities are determined using the Stokes-Cunningham equation for spherical droplets. Particles are also assumed to be transported by turbulence in the same way as gases. P. Hamill discusses some of these aerosol processes more completely in another summary.

For numerical calculations, aerosol sizes are divided into 25 categories, or bins, ranging from $0.01 \mu\text{m}$ to $2.56 \mu\text{m}$, with particle volume doubling between bins. Both aerosol droplet and condensation nuclei size distributions are calculated simultaneously at 2 km intervals from 0 to 60 km. The aerosol computer simulation is time dependent, and is coupled to the sulfur chemistry scheme by sulfuric acid vapor condensation and evaporation. We treat droplet coagulation by considering the rates at which particles of one size coagulate with all other particles, incrementing the appropriate size bin populations according to the rates of mass transfer. Tests with the model have demonstrated that our coagulation scheme is an excellent approximation suitable for atmospheric studies.

Preliminary model simulations of the earth's aerosol layer are in excellent agreement with observations. Total particle number and mass mixing ratios are within a factor of about 2 of most of the data everywhere in the stratosphere. The predicted aerosol layer has a peak mass mixing ratio near 20 km, as expected. The ratios of the number of particles with radii greater than $0.15 \mu\text{m}$ to those with radii greater

than 0.25 μm are in good agreement with measurements. The predicted aerosol droplet weight percentage of sulfuric acid is also very close to a single experimental determination of this quantity.

Summary

The encouraging agreement of our first model calculations of terrestrial aerosol characteristics with existing stratospheric data leads us to believe that we have developed an excellent diagnostic model for investigating both naturally occurring and anthropogenically disturbed aerosol layers in planetary atmospheres.

References

Cadle, R.D., J. Geophys. Res. 80, 1650, 1975.

Cadle, R.D., P.J. Crutzen & D. Ehhalt, J. Geophys. Res. 80, 3381, 1975.

Crutzen, P.J., Geophys. Res. Lett. 3, 73, 1976.

Fuchs, N.A., The Mechanics of Aerosols, MacMillan Co., 1964.

Fuchs, N.A. & A.G. Stugin, Topics in Current Aerosol Research, Vol 2, G.M. Hidy & J.R. Brock, eds. Pergamon Press, 1, 1971.

Hamill, P., R.P. Turco, O.B. Toon, R.C. Whitten & C.S. Kiang, manuscript submitted to Geophys. Res. Lett., 1976 a.

Hamill, P., O.B. Toon & C.S. Kiang, manuscript submitted to J. Atmos. Sci., 1976 b.

Hamill, P., O.B. Toon & C.S. Kiang, manuscript submitted to J. Atmos. Sci., 1976 c.

Pollack, J.B., O.B. Toon, C. Sagan, W. Van Camp, A. Summers & B. Baldwin, J. Geophys. Res. 81, 1071, 1976.

Turco, R.P. & R.C. Whitten, Atmos. Env. 9, 1045, 1975.

U.S. Standard Atmosphere Supplements, 1966.

A Steady State One Dimensional Model of the Stratospheric Aerosol

J. M. Rosen, D. J. Hofmann, and P. Singh
Department of Physics & Astronomy, University of Wyoming 82071

It is well known that a relative maximum exists on a global scale in the aerosol mixing ratio approximately 10 km above the tropopause. The particles are composed of H_2SO_4 (for the last decade at least) with many of them containing smaller solid inclusions. Following a large volcanic eruption the aerosol layer may experience a large increase in concentration; but during quiet periods of volcanic activity the layer seems to approach quasi steady state. It is the purpose of this paper to present a particular model describing this quasi steady state situation and to examine its plausibility. At the heart of the model is the assumption that a supersaturated layer of H_2SO_4 exists about 10 km above the tropopause. Although the model itself is not concerned with the chemistry of this layer's source, it could be formed from sulfur bearing gases such as SO_2 or CSO (Crutzen 1976) diffusing up through the tropopause and after a series of chemical reactions eventually forming H_2SO_4 ; or the source could be continual small volcanic eruptions with the required effective injection altitude. Since H_2SO_4 has a very low vapor pressure at stratospheric temperatures and water vapor concentrations (Gmitro & Vermeulen 1963) even a very modest production rate of H_2SO_4 could produce a large supersaturation.

The model further assumes that this saturated vapor condenses on any particles that are present at a rate governed by the thermal flux of H_2SO_4 molecules onto the particles' surface. Replenishment of the particles comes from diffusion of tropospheric aerosol upward and as an option a meteoric source can also be added. The effect of coagulation is also taken into account by the model.

The basic equation describing the time rate of change of the differential

size distribution $n(r,z)$ at altitude z is

$$\frac{\partial n}{\partial t} = - \frac{\partial F}{\partial z} - \frac{\partial}{\partial r} \{Gn\} + C$$

where F is the particle flux due to sedimentation and eddy diffusion, G is the growth rate and C is the coagulation term.

Under certain simplifications the above equation can be solved without resorting to a computer. This will be referred to as the quasi analytic solution.

A modified finite difference method has been used to obtain a computer solution to the basic equation. Errors arise in this type of solution due to a finite grid and the fact that the upper boundary cannot be taken at $z = \infty$. By making the upper boundary well above the growth layer and by using the fact that sedimentation-diffusion is the only important process at high altitude, a boundary condition can be chosen (flux = 0) that will produce an accurate solution. Errors due to the finite grid were investigated by comparing solutions with two different grids. Where applicable the computer solution was compared with the quasi analytic solution. Finally, the overall solution was checked for conservation of mass flux and also (in the case of no coagulation) conservation of particle flux.

In this work two basic types of atmospheres were considered: polar and equatorial. Since the general character of the computer solution in both cases is essentially the same, only the results of the polar model will be discussed here.

Typical computer generated profiles are shown in figures 1, 2, and 3 along with the range of actual measured values -- taken from Hofmann et al (1975), Rosen et al (1975), Pinnick et al (1976), and Rosen and Hofmann (1975). In this particular example the eddy diffusion profile of Chang has been used for altitudes below 22 km (Johnston et al, 1976) and the profile of Hunten has

been used above 22 km (Johnston et al, 1976). The gravitational settling velocities have been adopted from Kasten (1968) by fitting his tabulated data to a curve that is proportional to the particle radius and density and inversely proportional to the ambient air density. A particle density has been used that is consistent with a composition of 75% H_2SO_4 and 25% H_2O . The vapor pressure profile of H_2SO_4 was taken to be a gaussian function centered at 20 km and several km wide. A peak concentration of 2.76×10^{-11} mm Hg was chosen, a value in considerable excess of 100% saturation. A constant coagulation coefficient was chosen, the value of which is consistent with the work of Walter (1973).

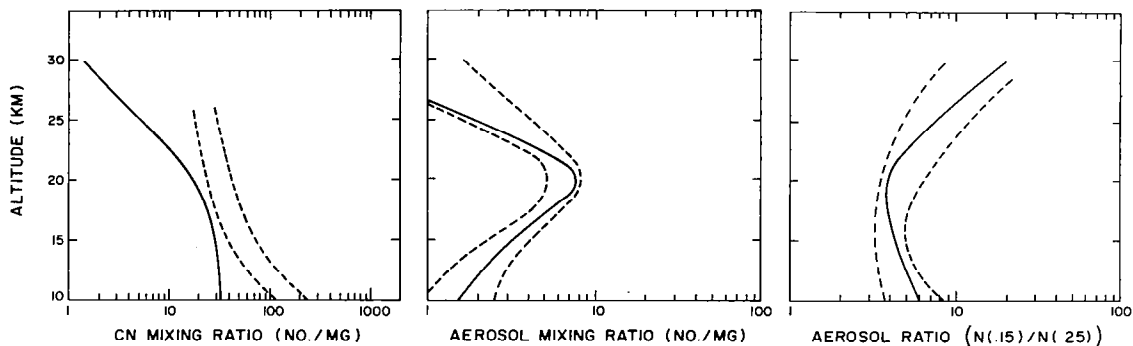


Figure 1. The profile of particles with $r \geq 0.01\mu$.

Figure 2. The profile of particles with $r \geq 0.15\mu$.

Figure 3. The ratio profile where $N(r)$ is the concentration of particles with radii $\geq r$.

Our experience with this model has led us to several conclusions. The integral size distribution predicted from the model at 20 km agrees almost exactly with the measured size distribution reported by Pinnick et al (1976) and by Toon and Pollack (1976). The best fits of the computer solution to the actual measurements were obtained by using an eddy diffusion profile that has a minimum near the observed aerosol maximum. The overall CN profile from the computer solution cannot be made to fit the measurements very well. This

suggests that not all CN diffusing up from the tropopause may be capable of acting as centers of condensation for the H_2SO_4 vapor and that there may be a small additional meteoric source of CN. The mass flux of sulfur required to sustain the H_2SO_4 vapor layer (1.6×10^5 equivalent tons SO_2 per year) is in the plausible range discussed by Crutzen (1976).

In conclusion, we feel that this model accounts for many of the physical aspects of the stratospheric aerosol data, but continued measurements are necessary to determine whether or not a steady state condition ever actually exists.

References

Crutzen, P. J., Geophys. Res. Lett. 3, 73-76, 1976.

Gmitro, J. I. and T. Vermeulen, AI ChE J. 10, 740-746, 1964.

Hofmann, D. J., J. M. Rosen, T. J. Pepin and R. G. Pinnick, J. Atmos. Sci. 32, 1446-1456, 1975.

Johnston, H. S., D. Kattenhorn and G. Witten, J. Geophys. Research 81, 368-380, 1976.

Kasten, F., J. Appl. Meteor. 7, 944-947, 1968.

Pinnick, R. G., J. M. Rosen and D. J. Hofmann, J. Atmos. Sci. 33, 304-313, 1976.

Rosen, J. M. and D. J. Hofmann, Balloon-Borne Measurements of Condensation Nuclei Report #CN-3 of the Atmos. Physics Group, Univ. of Wyoming 1975 (submitted for publication).

Rosen, J. M., D. J. Hofmann and J. Laby, J. Atmos. Sci. 32, 1457-1462, 1975.

Toon, O. B. and J. B. Pollack, J. Appl. Meteor. 15, 223-246, 1976.

Walter, H., Aerosol Sci. 4, 1-15, 1973.

Data Inversion for Spacecraft Solar Occultation Experiments in the Near IR, UV, and Visible Region

Chu, W. P.

Dept. of Physics, Old Dominion University, Norfolk, VA

Swissler, T. J.

System and Applied Sciences, Riverdale, MD

McCormick, M. P.

NASA Langley Research Center, Hampton, VA

An analysis of satellite measurements of stratospheric aerosol and ozone vertical profiles using the solar occultation technique is discussed in this paper. The wavelength region of interest covers the UV, where Rayleigh scattering predominates; the visible near $0.6 \mu\text{m}$ which is at the peak of the ozone Chappuis absorption band; and the near IR at $1.0 \mu\text{m}$ where aerosol scattering is significant.

The experimental geometry for spacecraft solar occultation is illustrated in Figure 1. During each measurement event, the radiometer on board the spacecraft will point to selected positions on the solar disk and measure solar irradiance in different spectral channels. As the spacecraft continues in its orbit, the line of sight from the spacecraft to the sun will scan the earth's atmosphere at different tangent altitudes, resulting in a measurement of attenuated solar radiation at different atmospheric heights. Assuming the atmosphere is spherically symmetric, the equation describing the measurement is simply the Lambert-Beer law relating the horizontal atmospheric transmission profiles to the vertical extinction properties of the atmosphere. The optical pathlength within the atmosphere can be determined by simple geometry. However, in the lower stratosphere, atmospheric refraction effects are significant. Optical ray trace techniques have been developed to calculate these pathlengths within different atmospheric layers. It is found that a refracted ray path could be differed from a straight ray path by as much as 10% in total length. The optical ray trace technique has also been used to compute the change in solar radiance profile caused by atmospheric refraction. Figure 2 illustrates the computed solar images as observed on the spacecraft at an orbital altitude of 925 km.

The inversions of the multiwavelength irradiance data have been analyzed based on the inversion of computer simulated spacecraft data using various atmospheric models with differing amounts of aerosol and ozone loading in the stratosphere. A radiometer with a field of view of 0.5 arc-minute has been assumed in order to produce vertical resolution of approximately one kilometer. Uncertainties in measurement such as instrument noise, the pointing error of the radiometer, and the bias error in determining the atmospheric tangent height have been included in the simulated data in order to determine the sensitivity of the inversion results.

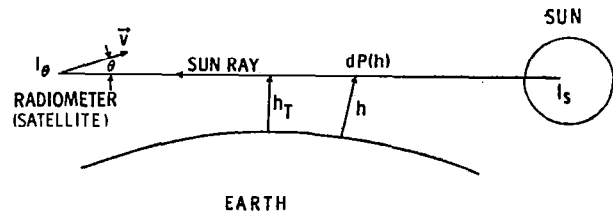
The equation for inversion is

$$\ln \left(\frac{1}{T_\lambda} \right) = \int \beta_\lambda(h) dP(h)$$

where T_λ is the measured transmission at wavelength λ , $\beta_\lambda(h)$ is the total extinction at wavelength λ as a function of altitude h , and $P(h)$ is the optical pathlength. Subdividing the atmosphere into n homogeneous spherical layers, the above equation can be approximated by a matrix equation of similar form. The inversion procedure starts by inverting the multiwavelength transmission profiles separately into total extinction vertical profiles. At each altitude layer, the multiwavelength extinction coefficients are then separated into Rayleigh, ozone, and aerosol components with a separate inversion. A two or three parameters fit to the aerosol extinction coefficient versus wavelength characteristic has been used to invert the aerosol profiles. Twomey's second derivative smoothing scheme (1) has been used in performing the above inversions.

Figures 3 and 4 illustrate the inversion results based on a typical instrumental noise figure. A pointing uncertainty of 3 arc-second and a noise term of 0.1% of full-scale radiance were assumed. The results indicated that aerosol and ozone vertical profiles can be retrieved to approximately 10% over most of the stratosphere. The bias error in determining the absolute tangent altitude was found to produce a shift in the overall retrieved profiles.

(1) S. Twomey, J. Assn. Computing Machinery, 10, 99 (1963)



SOLAR OCCULTATION GEOMETRY

$$I_\theta = \tau(h_T(\theta)) I_s$$

LAMBERT-BEER LAW

$$\tau(h_T) = \exp \left\{ -2 \int_{h_T}^{\infty} \beta(h) dP(h) \right\}$$

 $\beta(h)$ - EXTINCTION PROFILE $P(h)$ - REFRACTED OPTICAL PATH

Figure 1

SUN SHAPE
1962 STD. ATM.
SAT. ALT. = 925 KM

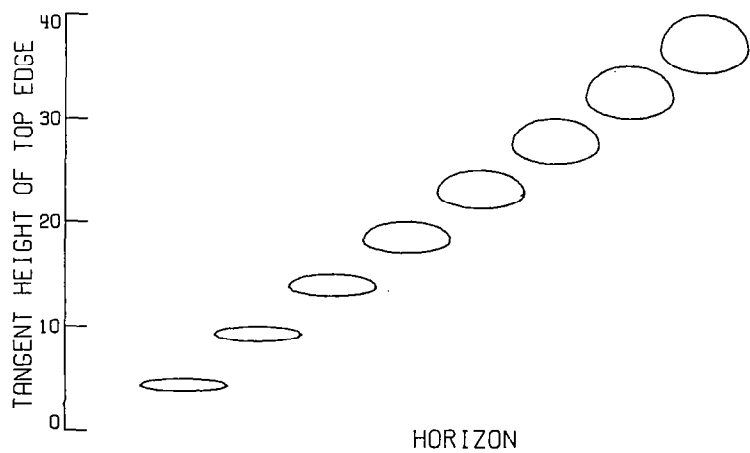


Figure 2

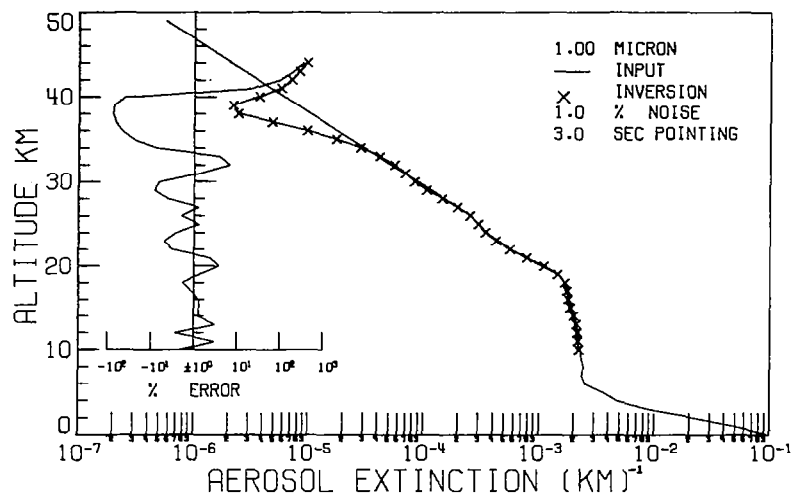


Figure 3

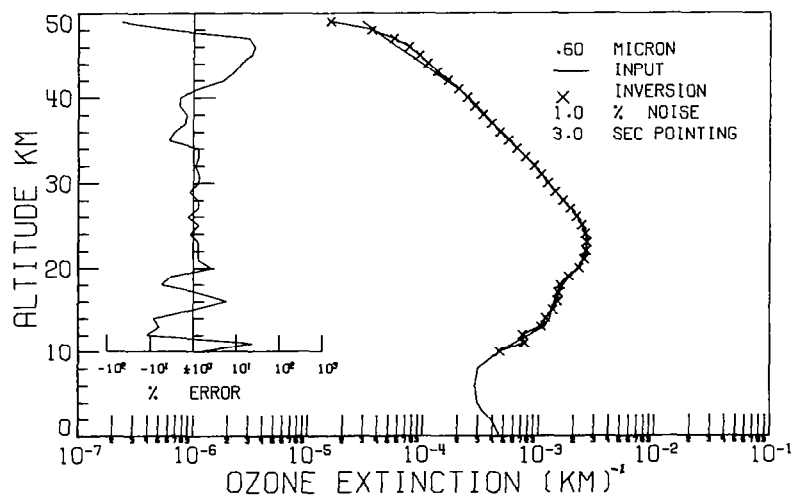


Figure 4

The Effect of Horizontal Rayleigh Air Mass Models Upon
 Evaluation of Stratospheric Aerosol Optical Depth Remote Sensing
 Measurements from Earth Orbit.

GREGORY L. MATLOFF

Research Scientist, Department of Applied Science
 New York University, 26-36 Stuyvesant Street, New York,
 N.Y. 10003

There are 4 basic contributors to extinction that must be accounted for if orbital occultation measurements of bright stars (Fig. 1) similar to those attempted by Hays and his associates (1-3) are to be used to remotely monitor stratospheric aerosol. These are aerosol (Mie) scattering, ozone absorption, molecular (Rayleigh) scattering, and refraction. Refraction has been considered by Link (4). In order to monitor aerosol or ozone or aerosol optical thickness in the stratosphere, the horizontal air mass must be calculated, for a Rayleigh atmosphere.

The treatment of Zenith Rayleigh scattering is simple, at least conceptually. (5). Following Condron (6),

$$k_m(h) = k_m(0) e^{-h/H_m} \quad (\text{cm}^{-1}), \quad (1)$$

where $k_m(h)$ is the molecular scattering at height h , $k_m(0)$ is the molecular scattering coefficient at sealevel, and H_m is the scale height for a Rayleigh atmosphere ($H_m \approx 8 \text{ km}$). The coefficient $k_m(0)$ has been tabulated by Penndorf (7). Now, from Bouguer's law (8), the transmission of a Rayleigh scattering atmosphere can be written:

$$T_{x\lambda} = \exp \left\{ -[k_m(h)]_\lambda (x) \right\}, \quad (2)$$

where x is the distance travelled by the light beam, of wavelength λ , through the Rayleigh atmosphere.

The magnitude extinction of the observed star, due to Rayleigh extinction, can be written:

$$\Delta M_\lambda = 2.5 \log_{10} \frac{1}{T_{x\lambda}} = 1.04 [k_m(h)]_\lambda (\bar{x}). \quad (3)$$

Assuming a 100 km top to the Rayleigh atmosphere and integrating the differential form of Bouguer's law using the above results, we obtain for a zenith star observed at h_0 :

$$\Delta M_{\text{zenith}} = 1.09 [k_m(0)]_\lambda e^{-0.125 h_0} \quad \left\{ \begin{array}{l} h_0 \text{ in km} \\ [k_m(0)]_\lambda \text{ in } \frac{\Delta \text{magnitude}}{\text{Air Mass}} \end{array} \right\}. \quad (4)$$

For a star observed at zenith angled through a relative air mass \bar{x} (8),

$$\Delta M_{\lambda, \delta} = (\Delta M_{\text{zenith}, \lambda}) \bar{x}, \quad (5)$$

For the occultation situation illustrated in Fig. 1,

$$\Delta M_{\lambda \text{ occultation}} = 2 (\Delta M_{\text{zenith}, \lambda}) \bar{x}_{\text{horizontal}}, \quad (6)$$

where $\bar{x}_{\text{horizontal}}$ is the ratio of horizontal/zenith atmospheric optical thickness.

For 5000Å observations [km(a)]=0.15 magnitude/sea-level air mass and for $h_0 = 15 \text{ km}$. Using Eq. 4, $\Delta M_{\text{zenith}, \lambda} = 0.025$ magnitude. Hays and Roble have applied the Abel integral technique to the calculation of Rayleigh scattering coefficients at various tangent ray heights and wavelengths (1). For an occultation observation at $h_0 = 15 \text{ km}$, $\lambda = 5000\text{\AA}$, they obtained $T \approx 0.30$. Substituting into Eq. 3, we find $\Delta M_{\lambda \text{ occultation}} \approx 26$.

Other methods of estimating $\bar{x}_{\text{horizontal}}$ are reported in the literature. From Link's 1963 tabulation (4), we learn that the horizontal optical thickness of the atmosphere above 15 km is equivalent to 9.75 km of normal density air. Since the zenith optical thickness above 15 km is about 1.2 km, this corresponds to $\bar{x}_{\text{horizontal}} \approx 8.1$.

A more recent tabulation of Link and Neuzil (9) considers light trajectories within the atmosphere under a variety of conditions. From an approximation to Bemporad's tables (10),

$\bar{x} = 10$ for zenith angle 84°, to an accuracy of 1%. Consider from Ref. 9 the light trajectory between two points, one at 20 km above the earth's surface and the other at 50 km. Observing the higher point from the lower point for summer conditions (Link and Neuzil, Situation 3), with a zenith angle of 85°, the relative air mass is 64. For the same conditions but a zenith angle of 90°, the relative air mass is 250. This indicates that if $\bar{x} = 10.0$ at $\delta = 84^\circ$, $\bar{x} = 39$ for $\delta = 90^\circ$.

Clearly, then, there is considerable spread in horizontal air mass estimates among various models. Only some of this spread can be accounted for by seasonal variation in the density of stratospheric layers, since these are not much greater than 10% (11). Diurnal variations are insignificant in the atmospheric layers of interest.

Because of the difficulty inherent in photometric observations near the horizon, experimental validation of the various values for $\bar{x}_{\text{horizontal}}$ is hard to come by. A literature search revealed that the most reliable and accurate attempt to directly observe this property is the 1951 Mount Lemon observations reported by Dunkleman and Scolnik (12). The highest value of $\bar{x}_{\text{horizontal}}$ obtained during these observations

of the sun during the sunrise-sunset interval is 12.0.

In designing an operational stratospheric aerosol or ozone remote-sensing monitor operating from a station above the stratosphere, it would be unwise to depend too heavily upon values of $\chi_{\text{horizontal}}$ obtained theoretically or from terrestrial observations. Happily, it might be possible to directly calibrate $\chi_{\text{horizontal}}$ in situ for $h_0 \geq 40$ km, since, as shown in Fig. 2, molecular scattering is the dominant extinction agency in this altitude region.

REFERENCES

1. Hays & Roble, J. Atm. Sci., 25, 1141 (1968).
2. Hays, Roble & Shah, Science, 176, 793 (1972).
3. Roble & Hays, Plan. Space Sci., 20, 1727 (1972).
4. Link, Adv. Astron. Astrophys., 2, 87 (1963).
5. Matloff, Monitoring Stratospheric Aerosols and Ozone from Earth Orbit, Ph.D. thesis, New York Univ., June, 1976.
7. Penndorf, J. Opt. Sci. Am., 47, 176 (1957).
6. Condron, in USAF Handbook of Geophysics, Macmillan, New York, 1960, p.14--1.
8. Dufay, Introduction to Astrophysics: The Stars, Dover, New York, 1964.
9. Link & Neuzil, Tables of Light Trajectories in the Terrestrial Atmosphere, Hermann, Paris, 1969.
10. Hardie, in Astronomical Techniques (ed. Hiltner), Univ. of Chicago Press, 1962, p. 178.
11. CIAP Monograph No. 1, DOT-TST-75-51, Nat'l. Tech. Inf. Service, Springfield, Va., Sept. 1975.
12. Dunkleman and Scolnik, J. Opt. Sci. Am., 49, 356 (1959).

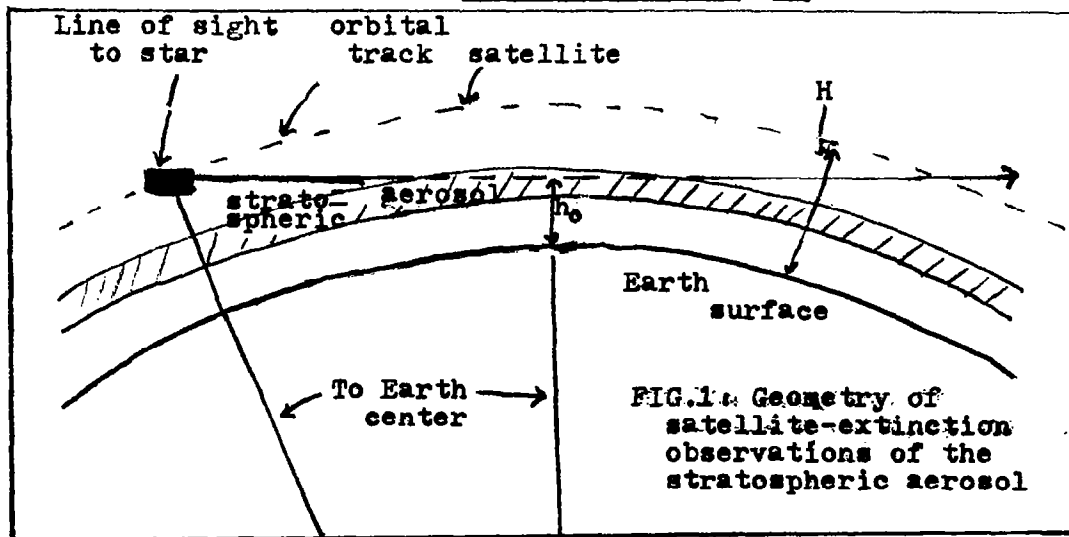
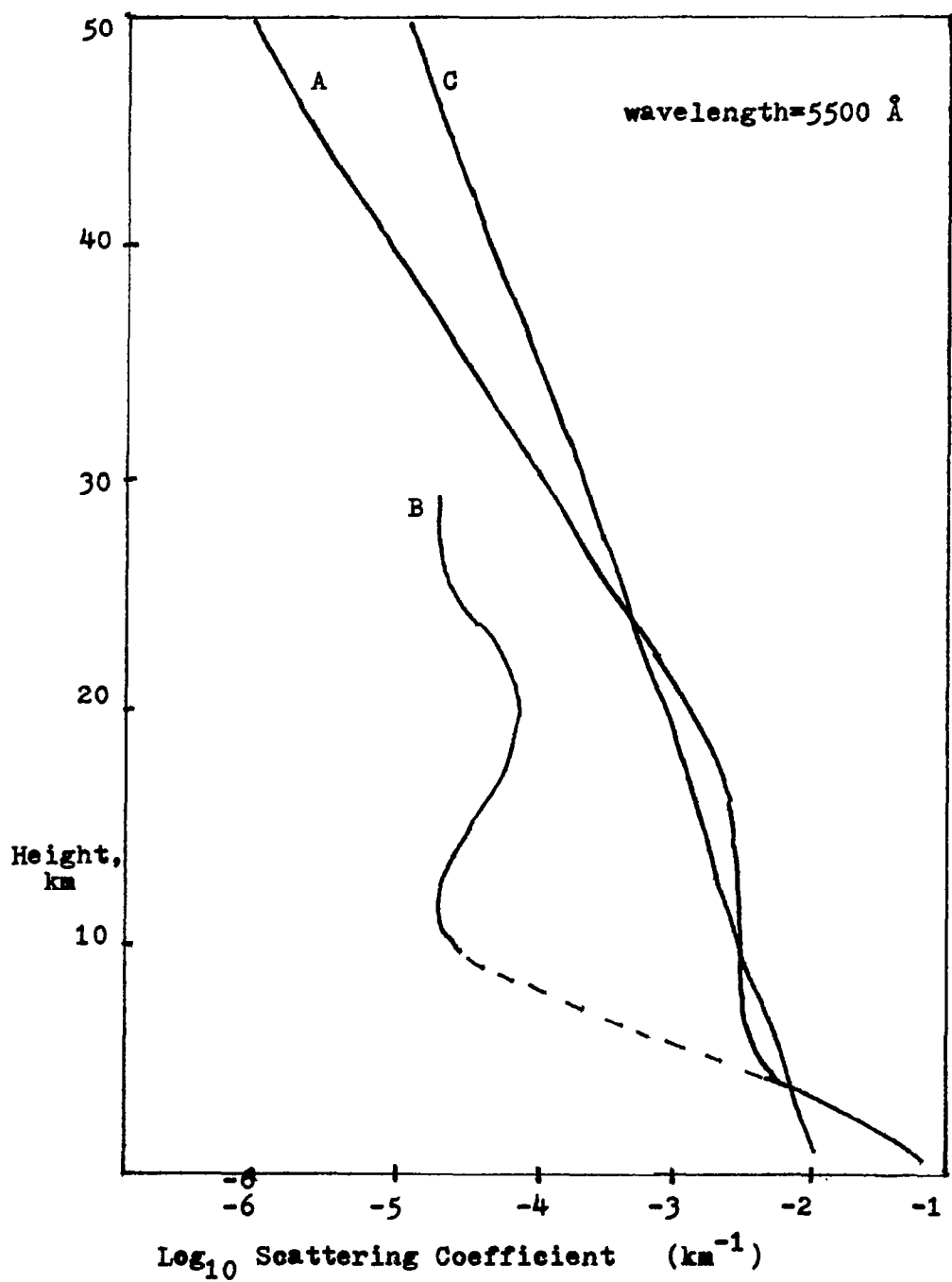


FIG. 2: Variation of scattering coefficients with height:
Curve A-Elterman's 1968 Aerosol Model; Curve B-Elterman's
1964 Aerosol Model; Curve C-Pure Molecular (Adopted
from Elterman, AFCRL-68-0153, April 1968, Fig. 10)



Analytical Modeling of Aerosol Size Distributions, Adarsh Deepak, Old Dominion University, Norfolk, VA

Various analytic models of atmospheric aerosols will be discussed.

APPROXIMATE DETERMINATION OF AEROSOL SIZE DISTRIBUTIONS

Michael A. Box and Shui-yin Lo

School of Physics,
University of Melbourne,
Parkville, Victoria 3052, Australia.

Although it is possible to invert multispectral extinction data directly, using either analytical or numerical integration procedures, such approaches make severe demands on the experimenter. Because the attenuation of solar radiation in the visible region is reasonably small, intensity measurements have to be made with considerable precision in order to extract sufficiently accurate extinction data. As the inversion process is quite sensitive to the accuracy of this data, poor data leads to instability in the final size distribution of the polydispersion.

This points up the need for a method (or methods) of approximate inversion, which would be suitable for use with rough field data, such as may be obtained from daily monitoring. Before considering any such method, it is necessary to ask: how much information can be extracted from a typical set of multispectral extinction data?

The answer to this question is clearly connected to the quality and accuracy of the data. If the data is exceedingly rough, then probably only the average turbidity has any real meaning. Since this is only one piece of information, we can only expect to extract one parameter concerning the polydispersion. If, however, the data is a little better, one may obtain the line of best fit when the data is plotted on suitable graph paper. Since a straight line gives us two parameters, we can expect to extract two pieces of information about the haze. With more accurate data, we may fit a higher order curve to the data, and so extract more parameters.

Since we expect to obtain only limited information about the aerosol, we fit the data with aerosol models, with as many adjustable parameters as there are pieces of information available. Commonly used models are Junge's power law:

$$n(r) = Ar^{-v} \quad r_1 < r < r_2 \quad (1)$$

and Deirmendjian's modified gamma distributions:

$$n(r) = ar^\alpha e^{-br^\gamma} \quad (2)$$

which all contain two adjustable parameters (r_1 , r_2 , α and γ are usually preset). The real and imaginary parts of the refractive index are also unknowns, though their extraction is somewhat more difficult, and we will assume suitable values.

With a model in hand one can proceed to determining the adjustable parameters by fitting it to the data. This seems to be a simple task with Junge's distribution, because in this case we see that the turbidity is given by

$$\tau(k) = \int_0^\infty Q_{ext}(x, m) \pi r^2 n(r) dr \quad (3)$$

$$= A \pi k^{v-3} \int x^{2-v} Q(x, m) dx \quad (4)$$

$$\text{where } x = kr = 2\pi r/\lambda$$

As the wavelength dependence factors out of the integral, we see that the parameter v can be extracted from a power law fit to the data, which can be done by plotting the data on a log-log plot or using a programmable calculator. (The parameter A can be obtained from this fit, though this is rarely done.)

However, the Junge distribution must clearly be cut off at some minimum radius r_1 (and possibly some maximum radius r_2) to avoid unphysical infinities. Thus the integral in (4) is bounded by wavelength-dependent cut-offs, and the final result may in fact be quite sensitive to the lower cut-off. This means that the extraction of v is not as straight-forward as is often assumed, and the extraction of A is seriously affected by the cut-offs.

For these (and other) reasons, we have developed a similar procedure for the extraction of the parameters a and b of Deirmendjian's Haze H (which corresponds to setting $\alpha = 2$, $\gamma = 1$ in (2)). As the turbidity integral no longer separates, there is no simple method of extraction as there was in the Junge case. We have, therefore, produced a set of tables as a basis for data analysis.

Firstly, we rewrite the size distribution in the form

$$n(r) = \frac{1}{2}ab^3r^2e^{-br} \quad (2')$$

so that a is now the total number of particles in a column of unit area. (Since r is usually in microns, b has units μ^{-1} , and this column has area $1 \mu^2$.) Setting $a = 1$ for the moment, and choosing values for b and m , we then numerically integrate (3) for a series of wavelengths between 0.3μ and 0.8μ , using the exact Mie form for Q .

Having obtained such a set of $\tau(\lambda)$ values, we then fit a power law

$$\tau(\lambda) = \beta(\lambda/\lambda_0)^{-\alpha}, \quad \lambda_0 = 1 \mu \quad (5a)$$

or an exponential law

$$\tau(\lambda) = \beta e^{-\alpha\lambda} \quad (5b)$$

to the calculated values.

For each value of b (and m), there will be a corresponding value of α and β . (Note also that β is directly proportional to a , which is used later to obtain a .) These values are tabulated.

The data analysis is then almost as straightforward as it was for the Junge distribution. The data are fitted by a power law or exponential law, and experimental values of α and β extracted. Then, having chosen a suitable value of m , the appropriate table gives b from this value of α . Finally, the value of a may be obtained from the experimental β , and the value of b .

Unlike the naïve analysis of Junge's distribution our analysis of Haze

H is dependent on both the wavelength range, and the refractive index. (Note, however, that as Q is a function of k and r only through the product kr - i.e. Q scales in kr - different wavelength ranges can be allowed for.)

However, we would emphasise that the correct analysis of the Junge distribution which takes into account the finite λ dependent limits on the integral in (4) will also depend on the wavelength range and the refractive index. The inadequacy of the naïve approach is emphasised by considering the limit $\lambda \rightarrow 0$ in eqn (4). It would seem that $\tau(\lambda) \propto \lambda^{3-\nu}$ and so either approaches 0 or ∞ . But it is easy to show that $\tau(\lambda=0)$ is just twice the geometrical cross-section of the polydispersion, a result which is obtained from (4) only when the limits of the integral are considered.

Our method also gives an alternative parameterisation for the size distribution. The main parameter of the Junge distribution is ν , the "decay rate" of the distribution. It is difficult to obtain A , and hence the mass loading. The main parameter extracted in our analysis is b , from which the mode radius may be found. Our method also yields the total number of particles in a very simple way.

Finally, we note that, although different values of m will yield different values of b for a given α , these different values are of course related. This relation can be understood in terms of the Anomalous Diffraction approximation, where the natural variable is not b but rather $b/|m-1|$. A given value of α approximately fixes $b/|m-1|$, and the values of b and m which are eventually selected must be determined from other considerations.

INVERSION OF MULTISPECTRAL EXTINCTION DATA
- THE ANOMALOUS DIFFRACTION APPROXIMATION

Michael A. Box and Bruce H.J. McKellar

School of Physics,
University of Melbourne,
Parkville, Victoria 3052, Australia.

The problem of inverting multispectral extinction measurements on a polydispersion to obtain the size distribution has received considerable attention [1]. About 10 years ago it was noted by Shifrin and Perelman [2] that the anomalous diffraction approximation to the extinction coefficient of a single sphere [3] permitted an analytic discussion of the inversion problem in terms of Mellin transforms. However quite elaborate techniques were necessary to avoid the divergence of various integrals entering the analysis. In particular it was found to be necessary to consider the region of large wave numbers separately.

In this paper we present a technique for inverting the multispectral extinction coefficient which avoids some of the difficulties encountered in ref. 2. The key to our method is the recognition that the extinction coefficient of a sphere in the A.D. approximation can be written in terms of the Struve function $H_{3/2}(x)$ [4], which is defined by

$$H_v(z) = \frac{2}{\sqrt{\pi}} \frac{(\frac{1}{2}z)^v}{\Gamma(v+\frac{3}{2})} \int_0^{\pi/2} \sin(z \cos t) \sin^{2v} t dt.$$

From the A.D. approximation for the extinction coefficient $Q(m, kr)$ for scattering light of wave number k from a sphere of radius r and real refractive index m given by Van de Hulst

$$Q(n, kr) = 4 \int_0^{\pi/2} (1 - \cos(\rho \sin t)) \sin t \cos t dt$$

where $\rho = 2kr(m-1)$, a change of variable from τ to $t = \pi/2 - \tau$ and an integration by parts shows that

$$Q(n, kr) = 2\sqrt{2\pi} \rho^{-\frac{1}{2}} H_{\frac{3}{2}}(\rho).$$

The multispectral extinction is then given by

$$\tau(k) = \pi \int_0^\infty r^2 Q(n, kr) n(r) dr$$

where the radius distribution function of the polydispersion is $n(r)$.

This leads us to consider $\tau(k')$ where $k' = 2(m-1)k$ as a "Struve Transform" of $r^2 n(r)$.

$$\tau(k') = (2\pi)^{\frac{3}{2}} \int_0^\infty (k'r)^{-\frac{1}{2}} H_{\frac{3}{2}}(k'r) r^2 n(r) dr$$

This type of Struve Transform with as a kernel the Struve Function $H_v(k'r)$ was considered by Titchmarsh [5], who found the inversion formula for $-\frac{3}{2} < v < \frac{1}{2}$. The extension to the larger positive values of v of interest here runs into difficulties because various integrals which formally appear, diverge - essentially the same difficulties encountered in ref. [2]. By taking account of the asymptotic behaviour of $\tau(k)$ [6] we can obtain an inversion formula,

$$n(r) = \frac{1}{(2\pi)^{\frac{3}{2}}} \int_0^\infty (k'r)^{-\frac{1}{2}} H_{\frac{3}{2}}(k'r) k'^2 [\tau(k') - A - \frac{4\pi N}{k'^2}] dk'$$

if $\int_0^\infty r^2 n(r) dr$ exists, which it must, on physical grounds, and $n(r) = 0(r)$ as $r \rightarrow 0$. A and N are derived from the asymptotic expansion of $\tau(k')$ for large k' ,

$$\tau(k') \sim A + \frac{4\pi N}{k'^2} + O(\frac{1}{k'^6}) .$$

They are also related to the moments of the size distribution function,

$$A = \pi \int_0^\infty r^2 n(r) dr$$

and
$$N = \int_0^\infty n(r)dr,$$

as discussed in ref. [7].

Subtracting the asymptotic behaviour makes the integral for $n(r)$ convergent. The integrand behaves like k'^{-4} for large k' , and like k'^2 for small k' , the dominant contribution to determining the size distribution function for the value r coming from $k' \sim \pi/r$, as expected on physical grounds.

Our inversion formula has been tested in a number of analytic cases, such as Deirmendjian's Haze H distribution, and it remains to use it in the analysis of data.

Without evaluating the inversion integral, we may determine the mass loading directly, exploiting some of the properties of Struve Functions [7]. If we weight the expression for $\tau(k')$ by k'^{-2} , and integrate with respect to k' , we may reverse the order of integration on the right hand side to obtain

$$\int_0^\infty k'^{-2}\tau(k')dk' = \frac{4\pi}{3} \int_0^\infty r^3 n(r)dr \int_0^\infty 3\left(\frac{\pi}{2}\right)^{1/2} H_{3/2}(\rho) \rho^{-5/2} d\rho$$

i.e.
$$\int_0^\infty k^{-2}\tau(k)dk = 2(n-1)V^{1/2}\pi$$

where V is the total volume of aerosol, from which the mass loading, Γ , may be obtained, once the density is known or assumed. We are further able to show that, under certain reasonable assumptions about the aerosol density and refractive index, that we may use the exact Mie theory in a similar manner to obtain the approximate formula

$$\Gamma \doteq \int_0^\infty k^{-2}\tau(k)dk$$

References

- [1] See for example G. Yamamoto and M. Tanaka, *Appl. Opt.* 8, 447
- [2] K.S. Shifrin and A.Y. Perelman, *Opt. Spectroscopy*, 15, 434 (1963);
16, 61 (1964); 20, 75 (1966); *Tellus* 18, 566 (1966).
- [3] H.C. Van de Hulst, Light Scattering by Small Particles, Wiley N.Y.
1957.
- [4] M. Abramowitz and I.A. Stegun, "Handbook of Mathematical Functions",
Dover N.Y. 1965.
- [5] E.C. Titchmarsh, *Proc. Lond. Math. Soc.* (2) 23 (1925) xxii.
- [6] M.A. Box and B.H.J. McKellar, University of Melbourne report UM-P-76/30.
- [7] M.A. Box and B.H.J. McKellar, University of Melbourne report UM-P-76/39.

APPROXIMATIONS TO THE AEROSOL EXTINCTION

Michael A. Box, Shui-yin Lo, Bruce H. J. McKellar and Michael Reich

School of Physics, University of Melbourne,
Parkville, Victoria, Australia 3052.

The exact Mie theory of the scattering of electromagnetic radiation from a spherical particle is now well known. As the theory involves the solution of Maxwell's equations inside and outside the sphere, with a matching at the boundary, the resultant expressions are quite complicated. For example, the extinction coefficient (scattering cross-section divided by geometrical cross-section) is given by

$$Q^{(\text{MIE})}(x, m) = 2x^{-2} \sum_{n=1}^{\infty} (2n+1) \operatorname{Re} (a_n + b_n)$$

where a_n and b_n are complex rational functions of the Riccati-Bessel functions (and their derivatives) of order n , and

$$x = kr = 2\pi r/\lambda.$$

The expressions for the scattering phase functions are even more complicated.

Although the wide availability of high-speed computers has made the evaluation of these expressions a straight-forward task, the large numbers of such evaluations which may be required in some analyses has led to the employment of a number of approximate expressions. Such approximations are also useful in providing insight into the problem. In this paper we consider the two best known approximations: the Rayleigh-Gans approximation, valid for particles with $r \ll \lambda/|m-1|$, and Anomalous Diffraction, valid for particles with r somewhat larger than λ . Both approximations require $|m-1| \ll 1$, which, of course, is not satisfied by aerosol refractive indices, which usually lie between 1.33 and 1.7.

The Rayleigh-Gans approximation is based physically on a model in which the electromagnetic wave is considered to scatter only once from individual point scatterers within the particle. This leads to the following expression for the extinction coefficient:

$$Q^{(\text{RG})}(x, m) = (m-1)^2 \left\{ \frac{5}{2} + 2x^2 - \frac{\sin 4x}{4x} - \frac{7(1-\cos 4x)}{16x^2} \right. \\ \left. + \left(\frac{1}{2}x^{-2} - 2 \right) (\gamma + \log 4x - \operatorname{Ci}(4x)) \right\}$$

where γ is Euler's constant and $\operatorname{Ci}(z)$ is the cosine integral.

Anomalous Diffraction, on the other hand, takes into account the phase difference experienced by a ray as it passes through the particle

(which hence needs to be large enough to allow the wave to propagate freely). For a real refractive index, the resulting extinction coefficient is

$$Q^{(AD)}(x, m) = 2 - 4\sin\phi/\rho + 4(1-\cos\phi)/\rho^2 = 4(\pi/2\rho)^{1/2} H_{3/2}(\rho)$$

where $\rho = 2x(m-1)$ and $H_{3/2}$ is Struve's function of order 3/2.

One of the most obvious differences between $Q^{(MIE)}$ and the two approximations is the ripple structure in the exact case. This ripple, which is well-pronounced for aerosol refractive indices, makes direct comparison between $Q^{(MIE)}$ and the approximations difficult. A graph of the errors involved will also display this pronounced ripple structure.

Real aerosols never consist of one radius only, but are, in fact, polydispersions. When $Q^{(MIE)}$ is integrated over the appropriate size distribution, $n(r)$, of the aerosol, the ripple structure will be smoothed out. Thus we expect the approximation to scattering by a polydispersion to be better than that to scattering by a single drop. For this reason, in making our comparisons between the three expressions for Q , we have first integrated each over Deirmendjian's Haze H ,

$$n(r) = \frac{1}{2}ab^3r^2e^{-br},$$

to yield the resulting turbidity, τ :

$$\tau(k) = \int_0^{\infty} \pi r^2 Q(x, m) n(r) dr.$$

In the case of $Q^{(MIE)}$, this integral must clearly be done numerically, but in the other two cases we may obtain an analytical result:

$$\begin{aligned} \tau^{(RG)}(k) &= \frac{1}{2}ab^{-2}\pi(m-1)^2 \{ (8/z-24)\log(1+z) \\ &\quad + (90z^5 + 320z^4 + 414z^3 + 236z^2 - 4z - 8)(1+z)^{-4} \} \end{aligned}$$

where $z = (4k/b)^2$

$$\text{and } \tau^{(AD)}(k) = 4ab^{-2}\pi(45y^6 + 40y^4 + 25y^2 + 6)(1+y^2)^{-4}$$

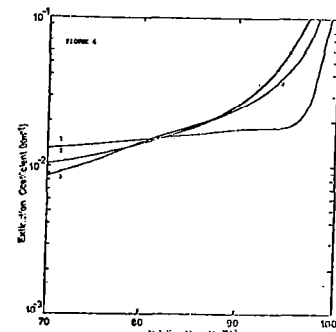
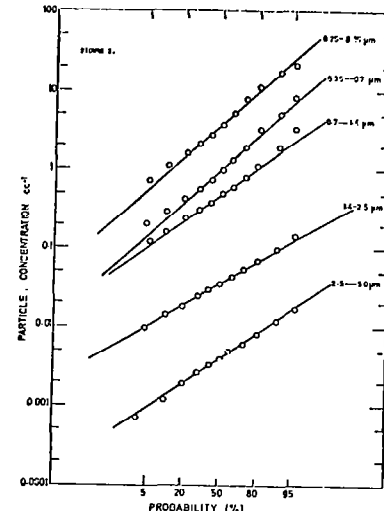
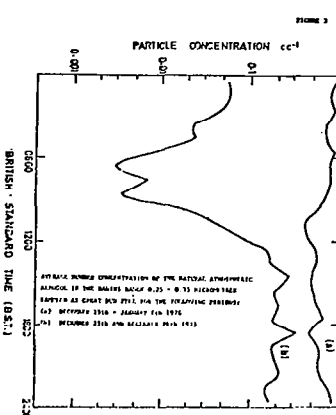
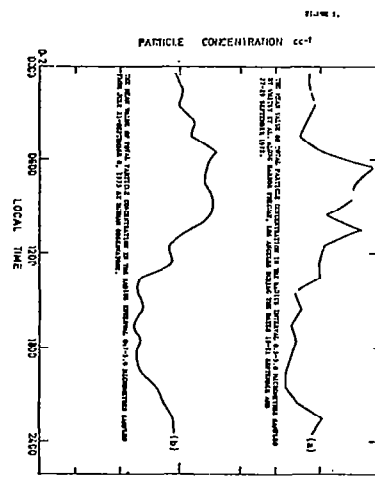
where $y = b/2k(m-1)$.

In the accompanying figure we have plotted $\bar{Q}^{(AD)} = \tau^{(AD)} \cdot b^2/12\pi a$ against y , for y from 0 to 5. The Rayleigh-Gans results for $m = 1.5$ is also plotted, and finally the Mie results, for $m = 1.33, 1.5$ and 1.7 are presented as a series of dots. Neither approximation gives a particularly good account

of the Mie results, especially for $y \lesssim 2$, though it is clearly apparent that Anomalous Diffraction gives a much better account of the general shape of the Mie results than does Rayleigh-Gans.

As mentioned before, aerosol refractive indices lie outside the region of validity of both of these approximations. Because of its ability to reproduce the general shape of the Mie results, we believe that Anomalous Diffraction is a good starting point for the development of approximations valid for larger m .

We have also considered other Hazes and the case of a complex refractive index, and again conclude that Anomalous Diffraction is the superior approximation.



The extinction coefficient due to a concentration of 1 microgram of carbon dioxide aerosol with the following size distributions:

1. A uniform size aerosol of particle radius $0.1 \mu\text{m}$ (spherical).
2. A spherical ice spray distribution.
3. A James-type distribution.

TABLE 2(a)

W.F. Particle Radius (μm)	Relative Humidity (%)	Particle concentration (cc^{-3})	Extinction coefficient (cm^{-1})	TABLE 2(b)	
				Relative Humidity (%)	Extinction coefficient (cm^{-1})
0.0230	10^{-15}	10,000	1.6×10^{-4}	70	10^{-3}
0.0233	10^{-15}	1,070	1.6×10^{-4}	70	10^{-3}
0.1111	10^{-14}	100	1.0×10^{-3}	70	10^{-2}
0.238	10^{-13}	10	3.1×10^{-2}	70	10^{-1}
0.513	10^{-12}	3	3.5×10^{-1}	70	10^{-1}
1.11	10^{-11}	0.3	1.4×10^{-1}	70	10^{-1}
0.0273	10^{-16}	10,000	4.4×10^{-4}	95	10^{-3}
0.0246	10^{-15}	1,000	4.0×10^{-4}	95	10^{-3}
0.101	10^{-14}	100	1.6×10^{-3}	95	10^{-2}
0.221	10^{-13}	10	2.3×10^{-2}	95	10^{-1}
0.410	10^{-12}	1	5.4×10^{-1}	95	10^{-1}
1.03	10^{-11}	0.1	3.0×10^{-1}	95	10^{-1}

SELECTED VALUES OF THE EXTINCTION COEFFICIENT AS A FUNCTION OF PARTICLE SIZE AND HUMIDITY.

TABLE 3(a)

W.F. Particle Radius (μm)	Relative Humidity (%)	Particle Concentration				
		10^{-14}	10^{-13}	10^{-12}	10^{-11}	10^{-10}
0.0230	70	1.6×10^{-4}	1.6×10^{-3}	1.6×10^{-2}	1.6×10^{-1}	1.6×10^{-1}
0.0233	70	1.6×10^{-4}	1.6×10^{-3}	1.6×10^{-2}	1.6×10^{-1}	1.6×10^{-1}
0.1111	70	1.0×10^{-3}	1.0×10^{-2}	1.0×10^{-1}	1.0×10^{-1}	1.0×10^{-1}
0.238	70	3.1×10^{-2}	3.1×10^{-1}	3.1×10^{-1}	3.1×10^{-1}	3.1×10^{-1}
0.513	70	3.5×10^{-1}	3.5×10^{-1}	3.5×10^{-1}	3.5×10^{-1}	3.5×10^{-1}
1.11	70	1.4×10^{-1}	1.4×10^{-1}	1.4×10^{-1}	1.4×10^{-1}	1.4×10^{-1}

TABLE 3(b)

W.F. Particle Radius (μm)	Relative Humidity (%)	Particle Concentration				
		10^{-14}	10^{-13}	10^{-12}	10^{-11}	10^{-10}
0.0230	95	1.6×10^{-4}	1.6×10^{-3}	1.6×10^{-2}	1.6×10^{-1}	1.6×10^{-1}
0.0233	95	1.6×10^{-4}	1.6×10^{-3}	1.6×10^{-2}	1.6×10^{-1}	1.6×10^{-1}
0.1111	95	1.0×10^{-3}	1.0×10^{-2}	1.0×10^{-1}	1.0×10^{-1}	1.0×10^{-1}
0.238	95	3.1×10^{-2}	3.1×10^{-1}	3.1×10^{-1}	3.1×10^{-1}	3.1×10^{-1}
0.513	95	3.5×10^{-1}	3.5×10^{-1}	3.5×10^{-1}	3.5×10^{-1}	3.5×10^{-1}
1.11	95	1.4×10^{-1}	1.4×10^{-1}	1.4×10^{-1}	1.4×10^{-1}	1.4×10^{-1}

TABLE 3(c)

W.F. Particle Radius (μm)	Relative Humidity (%)	Particle Concentration				
		10^{-14}	10^{-13}	10^{-12}	10^{-11}	10^{-10}
0.0230	70	1.6×10^{-4}	1.6×10^{-3}	1.6×10^{-2}	1.6×10^{-1}	1.6×10^{-1}
0.0233	70	1.6×10^{-4}	1.6×10^{-3}	1.6×10^{-2}	1.6×10^{-1}	1.6×10^{-1}
0.1111	70	1.0×10^{-3}	1.0×10^{-2}	1.0×10^{-1}	1.0×10^{-1}	1.0×10^{-1}
0.238	70	3.1×10^{-2}	3.1×10^{-1}	3.1×10^{-1}	3.1×10^{-1}	3.1×10^{-1}
0.513	70	3.5×10^{-1}	3.5×10^{-1}	3.5×10^{-1}	3.5×10^{-1}	3.5×10^{-1}
1.11	70	1.4×10^{-1}	1.4×10^{-1}	1.4×10^{-1}	1.4×10^{-1}	1.4×10^{-1}

Particle Concentration Range Size Radius (μm)	Relative Humidity Range Size Radius (μm)	TABLE 2.1				
		Relative Humidity Range Size Radius (μm)	Relative Humidity Range Size Radius (μm)	Relative Humidity Range Size Radius (μm)	Relative Humidity Range Size Radius (μm)	Relative Humidity Range Size Radius (μm)
0.0230	70	0.0230	0.0233	0.1111	0.238	0.513
0.0233	70	0.0230	0.0233	0.1111	0.238	0.513
0.1111	70	0.0230	0.0233	0.1111	0.238	0.513
0.238	70	0.0230	0.0233	0.1111	0.238	0.513
0.513	70	0.0230	0.0233	0.1111	0.238	0.513
1.11	70	0.0230	0.0233	0.1111	0.238	0.513
2.33	70	0.0230	0.0233	0.1111	0.238	0.513
5.13	70	0.0230	0.0233	0.1111	0.238	0.513
11.11	70	0.0230	0.0233	0.1111	0.238	0.513
23.33	70	0.0230	0.0233	0.1111	0.238	0.513
51.33	70	0.0230	0.0233	0.1111	0.238	0.513
111.11	70	0.0230	0.0233	0.1111	0.238	0.513
233.33	70	0.0230	0.0233	0.1111	0.238	0.513
511.11	70	0.0230	0.0233	0.1111	0.238	0.513
1111.11	70	0.0230	0.0233	0.1111	0.238	0.513
2333.33	70	0.0230	0.0233	0.1111	0.238	0.513
5111.11	70	0.0230	0.0233	0.1111	0.238	0.513
11111.11	70	0.0230	0.0233	0.1111	0.238	0.513
23333.33	70	0.0230	0.0233	0.1111	0.238	0.513
51111.11	70	0.0230	0.0233	0.1111	0.238	0.513
111111.11	70	0.0230	0.0233	0.1111	0.238	0.513
233333.33	70	0.0230	0.0233	0.1111	0.238	0.513
511111.11	70	0.0230	0.0233	0.1111	0.238	0.513
1111111.11	70	0.0230	0.0233	0.1111	0.238	0.513
2333333.33	70	0.0230	0.0233	0.1111	0.238	0.513
5111111.11	70	0.0230	0.0233	0.1111	0.238	0.513
11111111.11	70	0.0230	0.0233	0.1111	0.238	0.513
23333333.33	70	0.0230	0.0233	0.1111	0.238	0.513
51111111.11	70	0.0230	0.0233	0.1111	0.238	0.513
111111111.11	70	0.0230	0.0233	0.1111	0.238	0.513
233333333.33	70	0.0230	0.0233	0.1111	0.238	0.513
511111111.11	70	0.0230	0.0233	0.1111	0.238	0.513
1111111111.11	70	0.0230	0.0233	0.1111	0.238	0.513
2333333333.33	70	0.0230	0.0233	0.1111	0.238	0.513
5111111111.11	70	0.0230	0.0233	0.1111	0.238	0.513
11111111111.11	70	0.0230	0.0233	0.1111	0.238	0.513
23333333333.33	70	0.0230	0.0233	0.1111	0.238	0.513
51111111111.11	70	0.0230	0.0233	0.1111	0.238	0.513
111111111111.11	70	0.0230	0.0233	0.1111	0.238	0.513
233333333333.33	70	0.0230	0.0233	0.1111	0.238	0.513
511111111111.11	70	0.0230	0.0233	0.1111	0.238	0.513
1111111111111.11	70	0.0230	0.0233	0.1111	0.238	0.513
2333333333333.33	70	0.0230	0.0233	0.1111	0.238	0.513
5111111111111.11	70	0.0230	0.0233	0.1111	0.238	0.513
11111111111111.11	70	0.0230	0.0233	0.1111	0.238	0.513
23333333333333.33	70	0.0230	0.0233	0.1111	0.238	0.513
51111111111111.11	70	0.0230	0.0233	0.1111	0.238	0.513
111111111111111.11	70	0.0230	0.0233	0.1111	0.238	0.513
233333333333333.33	70	0.0230	0.0233	0.1111	0.238	0.513
511111111111111.11	70	0.0230	0.0233	0.1111	0.238	0.513
1111111111111111.11	70	0.0230	0.0233	0.1111	0.238	0.513
2333333333333333.33	70	0.0230	0.0233	0.1111	0.238	0.513
5111111111111111.11	70	0.0230	0.0233	0.1111	0.238	0.513
11111111111111111.11	70	0.0230	0.0233	0.1111	0.238	0.513
23333333333333333.33	70	0.0230	0.0233	0.1111	0.238	0.513
51111111111111111.11	70	0.0230	0.0233	0.1111	0.238	0.513
111111111111111111.11	70	0.0230	0.0233	0.1111	0.238	0.513
233333333333333333.33	70	0.0230	0.0233	0.1111	0.238	0.513
511111111111111111.11	70	0.0230	0.0233	0.1111	0.238	0.513
1111111111111111111.11	70					

Concerning the Retrievability of Aerosol Size Distribution
Parameters from Remote Sensing Experiments

W.A. Pearce and R.W.L. Thomas
Wolf Research and Development Group
EG&G/Washington Analytical Services Center, Inc.
6801 Kenilworth Avenue
Riverdale, Maryland 20840

The maximum retrievable information characterizing atmospheric aerosol properties is limited to that which may be inferred from the most complete possible experiment. From the remote sensing point of view, this means an experiment which measures all the scattering phase matrix elements.

Suppose that the experimental measurements are a set of intensities, $\underline{I} = (I_1, I_2, \dots, I_n)$ and that the parameters to be measured are $\underline{n} = (n_1, n_2, \dots, n_m)$. These are related (non-linearly) through $\underline{I} = f(\underline{n}) + \underline{\epsilon}$, where $\underline{\epsilon}$ represents a vector of measurement noise. Linearizing this expression, one obtains

$$\underline{I} = \underline{I}_0 + B \underline{\delta n} + \underline{\epsilon}$$

where $[B]_{ji} = \frac{\partial I_j}{\partial n_i}$, $\underline{I}_0 = f(\underline{n}_0)$, and \underline{n}_0 is an initial estimate of the parameter set. If Σ is the $n \times n$ variance-covariance matrix of the measurements, then the variance-covariance matrix of the n_i is

$$V = (B^T \Sigma^{-1} B)^{-1}$$

and the weighted least squares estimate of the adjustments to be made in the model parameters, \underline{n}_0 , is given by

$$\underline{\delta n} = V B^T \Sigma^{-1} (\underline{I} - \underline{I}_0) . \quad (1)$$

Let v_i and λ_i be the eigenvectors and eigenvalues, respectively, of the variance-covariance matrix: $V v_i = \lambda_i v_i$ and $B^T \Sigma^{-1} (\underline{I} - \underline{I}_0) = \sum_i a_i v_i$. Thus, we can write $\underline{\delta n} = \sum_i a_i \lambda_i v_i$. The a 's contain the impact of the measurement residuals with respect to the model while the λ 's chiefly reflect the sensitivity of the model. Convergence, then, presumes or

relies upon a suitable connection and interplay between the parameter behavior dictated by the structure of the model and that dictated by the measurement residuals.

The analysis has been applied to a model aerosol of spherical particles whose size distribution is given by the log normal form:

$$f(d) = \frac{\delta}{(D-a)\sqrt{\pi}} \exp \left\{ - \left[\delta \ln \left(\frac{D-a}{D_o-a} \right) \right]^2 \right\} \quad (2)$$

with

$$\begin{array}{ll} \text{minimum diameter,} & a = .05 \mu\text{m} \\ \text{median diameter,} & D = .45 \mu\text{m} \\ \text{variance parameter,} & \delta^o = 0.896 \end{array}$$

The aerosol mass density was taken to be $\rho = 2.65 \text{ gm/c.c.}$ The index of refraction was $m = (1.55, 0)$ and the size parameter, $x = \frac{\pi D}{\lambda}$ was in the range .2 to 40. for a wavelength $\lambda = .546 \mu\text{m}$.

These values were chosen so as to model the (non-spherical) aerosol of the nephelometric study by Holland and Gagne (1) as though it were spherical. The observables I were taken to be the ten measurements $UU, HH, VV, DD, dR, dd, RD, Rd, DR, \text{ and } RR$ of reference (1) at 18 different scattering angles from 20° through 166.6° . The measurements variance-covariance matrix, Σ , was taken to be that of reference (1)

With the parameter values initiated at

$$\rho = 3.0 \text{ gm./cc.}, \delta = 0.85, D_o = 0.4 \mu\text{m}, a = 0.1 \mu\text{m}$$

the third iteration of equation (1) provided convergence. At the final iteration, the eigenvectors, and eigenvalues were

i	λ_i	EIGENVECTOR COMPONENTS ALONG			
		ρ	δ	D_o	a
1	$.4323 \times 10^{-1}$	-.4351	-.1503	.6097	.6453
2	$.1547 \times 10^{-2}$.8303	.2516	.4632	.1808
3	$.3466 \times 10^{-4}$.3414	-.6649	-.4437	.4945
4	$.2638 \times 10^{-6}$.06894	.6871	-.4657	.5535

The large dynamic range of the eigenvalues acts to restrict the amount of information retrievable from the data.

The variance-covariance matrix for the parameters was

	ρ	δ	D_o	a
ρ	.00925	.00314	-.01088	-.01190
δ	.00314	.00109	-.00377	-.00413
D_o	-.01088	-.00377	.01641	.01713
a	-.01190	-.00413	.01713	.01806

from which the parameter correlation matrix was derived:

	ρ	δ	D_o	a
ρ	1.000	.989	-.883	-.920
δ	.989	1.000	-.892	-.932
D_o	-.883	-.892	1.000	.995
a	-.920	-.932	.995	1.000

Thus, all parameters appear as highly correlated and their individual impacts are difficult to resolve.

Turning to the impact of the data-model residuals and their effect upon convergence, the a_i 's were found to be:

<u>Iteration</u>	<u>a_1</u>	<u>a_2</u>	<u>a_3</u>	<u>a_4</u>
1	.1542E+02	-.3028E+03	.6177E+04	.1944E+05
2	-.9115	.6894E+02	-.6347E+02	-.2313E+05
3	.1886	.3452E+01	-.1393E+02	-.6734E+03

The $a_i \lambda_i$ products (which determine the actual steps through parameter space and control the dynamic behavior of the convergence) were:

<u>Iteration</u>	<u>$a_1 \lambda_1$</u>	<u>$a_2 \lambda_2$</u>	<u>$a_3 \lambda_3$</u>	<u>$a_4 \lambda_4$</u>
1	.2251	-.3598	.1641	.3476E-02
2	-.3524E-01	.1038	-.1826E-02	-.4749E-02
3	.8154E-02	.5340E-02	-.4829E-03	-.1776E-03

Only at this level is it finally clear that two eigenvectors are dominant containing, at the third iteration, about 95% of the strength.

Similar analyses will be presented for two cases: 1) data sets containing broader angular coverage (more extreme forward and backward angles; 2) data sets limited to particular experiments; e.g., UU, HH and VV only.

REFERENCES

1. Holland, A.C. and Gagne, G., *Appl. Optics*, 9, 1113 (1969).

On the Extraction of Extinction Coefficients
Profiles from Sun Photometer Measurements

by

Alistair B. Fraser
Associate Professor
The Pennsylvania State University
Department of Meteorology
503 Deike Building
University Park, Pennsylvania 16802

Abstract

The odd portion of the $\ln I$ versus elevation angle function is independent of the integral properties of extinction and is thus easily transformed to give $b = b(z)$.

The sun photometer is used extensively to measure the path-integrated extinction coefficient between the instrument and the top of the atmosphere. This measurement can be made at various different solar elevation angles and thus give a plot of measured intensity versus elevation angle. At large elevation angles (large β_e), $\ln I_e$ merely varies as $\csc \beta_e$ reflecting the nearly plane parallel nature of the atmosphere (subscript e indicates the value at the eye or earth). At small elevation angles (small β_e), the spherical nature of the atmosphere will result in the measured values of $\ln I_e$ being dependent on the details of the vertical profile of extinction coefficient. It should therefore be possible to deduce an extinction coefficient profile from measurements of $\ln I_e$ versus β_e for small β_e . This paper addresses one way this can be done.

The change of intensity, I , as the light passes down through the atmosphere is given by

$$d \ln I = b \csc \beta dr \quad (1)$$

where b is the volumetric extinction coefficient, β is the elevation angle

of the ray from the surfaces of constant b , and r is the distance from the center of symmetry (earth).

Integrating this expression from the sun to the eye and assuming spherical homogeneity of b , one obtains

$$\xi_e = -2 \int_{\phi_e}^{\infty} \zeta' d\phi \quad (2)$$

where $\zeta = \ln I/I_t$, (I_t = I at the target or sun), $\phi = \tan \beta \cos \beta_e$, $\zeta' \equiv d\zeta/d\tau$ and $\zeta = - \int_{r_e}^r b(nr/n_e r_e) dr$, $\tau = 1 - (nr/n_e r_e)^2$.

Atmospheric refraction is included in this analysis through the equation $nr \cos \beta = n_e r_e \cos \beta_e$, or in the transformed system $\tau = \phi_e^2 - \phi^2$. (The odd choice of the form of the ζ variable is to maintain consistency with previous work on refraction).

Equation (2) expresses the integrated intensity variable ξ_e as a function of the angular elevation variable ϕ_e and the extinction profile variable ζ' . By successively differentiating ξ_e with respect to ϕ_e and evaluating each derivative at $\phi_e = 0$ ($\beta_e = 0$, the astronomical horizon), one obtains a relation between the $\xi_e = \xi_e(\phi_e)$ function and the $\zeta = \zeta(\tau)$ or $b = b(z)$ function as follows:

$$\xi_o^{(2m-1)} = 2^{2m-1} (m-1)! \zeta_o^{(m)} \quad (3a)$$

$$\xi_o^{(2m-2)} = -2 \frac{(2m-2)!}{(m-1)!} \int_0^{\infty} \zeta^{(m)} d\phi \quad (3b)$$

$$\text{where } \zeta_o^{(m)} \equiv \left(\frac{d^m \zeta}{d\phi_e^m} \right)_{\phi_e=0}, \quad \zeta^{(m)} \equiv \frac{d^m \zeta}{d\tau^m}, \quad \text{and} \quad \zeta_o^{(m)} \equiv \left(\frac{d^m \zeta}{d\tau^m} \right)_{\tau=0}$$

It is seen that the odd portion of the $\xi_e = \xi_e(\phi_e)$ function is curiously independent of the integral properties of the extinction coefficient profile.

Furthermore, this says that the actual value of ξ_e is irrelevant so that only relative values of I need be measured. If intensity versus angular elevation measurements are fitted with a Maclaurin series, then the odd coefficients (derivatives) can be used to give

$$\frac{dI}{d\tau} = \sum_{m=1}^{\infty} \frac{\xi_o^{(2m-1)} \tau^{m-1}}{2^{2m-1} [(2m-1)!]^2} \quad (4)$$

where some knowledge (guess) as to the refractive index profile would be needed to recover $b = b(z)$. If we assume that refraction can be neglected and that $\tau \approx -2z/r_e$, then Eq.(4) can be written

$$b = \frac{1}{r_e} \sum_{m=1}^{\infty} \frac{\xi_o^{(2m-1)}}{[(m-1)!]^2} \left(\frac{-z}{2r_e}\right)^{m-1} \quad (5)$$

One remarkable aspect of this relation is the result that the volumetric extinction coefficient at eye level is given by

$$b_e = \frac{1}{r_e} \left(\frac{d \ln I_e}{d \beta_e} \right)_{\beta_e=0} \cdot$$

THE SENSITIVITY OF ZENITH TWILIGHT POLARIZATION
TO STRATOSPHERIC AEROSOL PARTICLE CONCENTRATION

D. Q. Wark and L. L. Stowe

NOAA, National Environmental Satellite Service
Washington, D. C. 20233

1. INTRODUCTION

A "mock-interferometer" spectrometer (Mertz, et al., 1963) with a resolution of 300 has recently been modified optically and electrically by W. A. Morgan to improve its performance and to extend its spectral range to .25-.6 μm . S. A. Twomey, among others, hoped to use the instrument during twilight to study the ozone and aerosol composition of the stratosphere. Recently he hypothesized that the polarization of the twilight sky in the wings of the Huggins-Hartley band of ozone would yield even more information about stratospheric aerosols, particularly their vertical distribution.

Some preliminary radiative transfer computations for single scattering have been made to test Twomey's hypothesis and also to estimate whether polarization measurements are feasible with the "mock-interferometer."

2. ATMOSPHERIC MODELS

Two contrasting aerosol atmospheric models derived from Stowe (1974) have been used. They differ from Stowe's low latitude models in that: Deirmendjian's (1969) water haze model H was used to represent stratospheric aerosol size distribution; the 1962 standard atmosphere was used for the temperature profile; ozone was added, using the volume absorption coefficients tabulated by Elterman (1968); and all data were extrapolated to 0.1 mb (~65 km).

Figure 1 illustrates the properties of the two models. Rosen's (1967) measured aerosol profile represents high stratospheric aerosol concentrations, while Elterman's average aerosol profile typifies a low concentration condition in the stratosphere.

The optical thickness of each model constituent in the vertical is listed in Table 1 at four wavelengths.

TABLE 1. Model Constituent Optical Thicknesses

λ (μm)	Rayleigh	Ozone	Aerosol	
			Elterman	Rosen
.32	.927	.303	.50	.36
.38	.450	.000	.40	.29
.45	.223	.001	.31	.23
.60	.069	.045	.20	.15

Rayleigh scattering optical thicknesses were found in Elterman (1968), and the model H aerosol optical properties were taken from Deirmendjian (1969) after extrapolation.

3. RADIATIVE TRANSFER CONSIDERATION

The spherical atmosphere is divided into 49 equally thick layers. For primary scattering in the principal plane of the sun, the parallel and

perpendicular components, I_2 and I_1 , respectively of the intensity in the zenith are given by the expressions

$$I_1(\theta) = \int_{z_t}^0 (P_1^M(\theta) \frac{d\tau_M}{dz} + P_1^A(\theta) \frac{d\tau_A}{dz}) F(\theta, z) \exp\{-(\tau(0) - \tau(z))\} dz$$

$$I_2(\theta) = \int_{z_t}^0 (P_2^M(\theta) \frac{d\tau_M}{dz} + P_2^A(\theta) \frac{d\tau_A}{dz}) F(\theta, z) \exp\{-(\tau(0) - \tau(z))\} dz$$

where, P_1^A , P_2^A = normalized aerosol phase function components.

P_1^M , P_2^M = normalized Rayleigh phase function components.

z_t = altitude of top of atmosphere.

τ_A = aerosol optical thickness.

τ_M = Rayleigh optical thickness.

τ_0 = ozone optical thickness.

$\tau = \tau_A + \tau_M + \tau_0$ = total optical thickness.

$$F(\theta, z) = F_o \exp\{-\int_{z_t}^0 M(\theta, z) \frac{d\tau}{dz} dz\}$$

F_o = solar spectral extraterrestrial irradiance (Thekaekara, 1971).

$M(\theta, z)$ = air mass factor for spherical atmosphere.

θ = solar zenith angle.

The air mass factor was computed from geometrical relationships. For the special cases when the sun's rays do not intercept the vertical column in the lowest layers, ($\theta > 90^\circ$), the slant path optical thickness was computed for the properties at the point of mean density along the path. Otherwise, the properties at the mean density of the layers were used.

Effects of refraction, which are negligible for the case of twilight illumination of the stratosphere, have not been included. Multiple scattering has not been considered at this time, but ways of incorporating it into the computations are being examined.

4. RESULTS

The sensitivity of twilight polarization to stratospheric aerosol particle concentration will be expressed through the quantity S , defined by the expression (E = Elterman, R = Rosen):

$$S = \frac{r^E}{r^R} - 1 = \frac{I_1^E / I_2^E}{I_1^R / I_2^R} - 1 = \frac{I_2^R}{I_2^E} - 1,$$

since, $I_1^E \approx I_1^R$.

Large values of S are indicative of greater sensitivity of polarization to stratospheric aerosol particles. This quantity thus enables one to determine which spectral regions and solar zenith angles provide optimum polarization sensitivity to changes in stratospheric aerosol concentration.

Figure 2 is a plot of S vs θ computed for the four wavelengths in Table 1. Also shown for $90^\circ \leq \theta < 96^\circ$ are results derived from the polarization measurement of Steinhorst (1974). These measurements were taken in 1968 (comparable with Rosen's model) and in 1973 (comparable with Elterman's model). Values of S were computed from the ratio $r(73)/r(68)$ where, $r = (1 + P)/(1 - P)$, and the degree of polarization, P , was read from figures.

Figure 2 shows poor agreement between measurement and computation. This is largely due to the absence of multiple scattering in the computations, which reduces the polarization sensitivity. The effects of multiple scattering diminish as the optical thickness decreases (wavelength increases).

Dependence of S on solar zenith angle is fairly well represented by the single scattering computation. The peak sensitivity moves to larger solar zenith angles as the wavelength increases. (Steinhorst's measurements indicate that, for $\theta > 95^\circ$, the sensitivity decreases.)

At $\lambda = 0.6 \mu\text{m}$, aerosol scattering is the dominant optical effect. As the sun sets, ($\theta > 90^\circ$), the illuminated region of the atmosphere moves to higher altitudes increasing the sensitivity to the aerosols in the stratosphere. At $\lambda = .45$, $.38$, and $.32 \mu\text{m}$, Rayleigh scattering is comparable to or dominates aerosol scattering. Peak sensitivity occurs at $\theta = 90^\circ$ due to the nature of the Rayleigh scattering phase function for the I_2 component. At $\lambda = 0.32 \mu\text{m}$, absorption by ozone reduces the irradiance of the stratospheric aerosols, lowering S . Also, multiple scattering further reduces the polarization sensitivity.

These results do not lend much support to Twomey's hypothesis. However, the hypothesis cannot truly be tested until the effects of multiple scattering are included in the computations.

Twilight polarization components I_1 and I_2 decrease by approximately 4 orders of magnitude as the solar zenith angle changes from $60^\circ - 95^\circ$. The "mock-interferometer" system, adapted with a Glan-Taylor polarizing prism, should be capable of making polarization measurements over this dynamic range in the $0.3-0.6 \mu\text{m}$ spectral region.

REFERENCES

Deirmendjian, D., 1969: Electromagnetic Scattering on Spherical Polydispersions, New York, Elsevier, 290 pp.

Elterman, L., 1968: UV, Visible and IR Attenuation for Altitudes to 50 km, Environ. Res. Paper, No. 285, AFCRL-68-0153.

Mertz, L., N. O. Young, and J. Armitage, 1963: Mock Interferometry, Optical Instruments and Techniques, Chapman and Hall, Great Britain, pp. 51-56.

Rosen, James M., 1967: Simultaneous Dust and Ozone Soundings Over North and Central America, Report N68-11414, Atmos. Phys. 25, University of Minnesota.

Steinhorst, G., 1974: Recent Measurements of Twilight Polarization, Applied Optics, 13, p. 219-220.

Stowe, L. L. 1974: Effects of Particulate Matter on the Radiance of Terrestrial Infrared Radiation; RESULTS, J. Atmos. Sci., 31, 755-767.

Thekaekara, M. P., 1971: Solar Electromagnetic Radiation, NASA Report SP-8005, (second printing, May 1973).

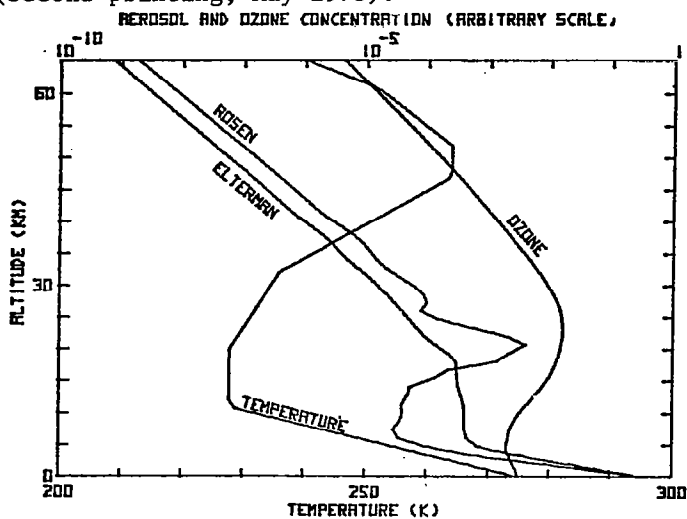


Figure 1 - Atmospheric model properties

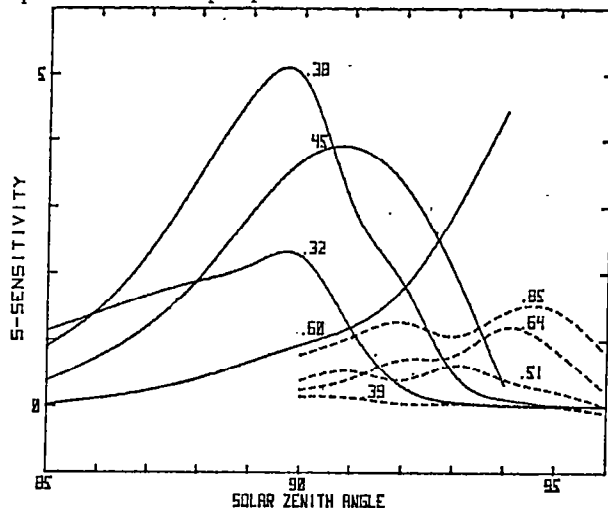


Figure 2 - Polarization sensitivity versus solar zenith angle at the wavelengths indicated (micro-meters). (solid-computed; dashed-measured)

ON AEROSOL PROPERTY DISCRIMINATION THROUGH
SKY POLARIZATION MEASUREMENTS

By

Robert W.L. Thomas
William A. Pearce
EG&G/Wolf Research and Development Group
6801 Kenilworth Avenue
Riverdale, Maryland 20840
U.S.A.

And

A.C. Holland
NASA/Wallops Flight Center
Wallops Island, Virginia 23337
U.S.A.

This paper describes the results of a study of the properties of the sky polarization observed at the ground in directions which were at right angles to the solar direction. The maximum polarization of the sky occurs in or near to this direction. Using a Monte Carlo radiative transfer code, we have succeeded in demonstrating a sensitivity of the maximum polarization to the total aerosol loading, the aerosol size distribution and refractive index and the albedo of the surface. In the work described here, however, we discuss the possible implications of the maximum sky polarization variation with solar zenith angle as an indicator of the vertical aerosol distribution.

In our simulations we used the Mueller calculus to describe the polarizations. Our sampled polarization was defined as

$$P = \frac{Q}{I} = \frac{I_l - I_r}{I_l + I_r} \quad (1)$$

where I_l and I_r were the intensity components parallel and perpendicular to the vertical plane containing the receiver pointing direction.

In our simulations we computed results for the two vertical aerosol distributions illustrated in Figure 1. The solid line is an Elterman type distribution whereas the dashed line represents thin cirrus clouds. We adjusted the densities so that the total column count was the same for both models. We assumed that the particles had a lognormal size distribution with a medium diameter of 0.45μ , a minimum diameter of 0.05μ and a variance parameter of 0.896. The refractive index was taken to be 1.55, and we computed the scattering matrix elements by Mie theory.

We obtained solutions for both model aerosols at wavelengths of 3500 \AA , 5500 \AA , and 7000 \AA using a spherical shell backtracking code. The solar zenith angles were varied in the range 0° to 88.85° .

The maximum discrimination between the two aerosol models occurred at 5500 \AA . The results for the absolute value of Q/I as a function of solar zenith angle cosine is shown in Figure 2 for the two models and surface Lambertian reflection albedos of 0 and 0.4. In this case the observations were in the solar zenith plane. The results for single scattering alone are also presented on this graph. All values of Q/I obtained were actually negative.

The character of these graphs is best described in terms of the single scattering polarization for 90° scattering. For Rayleigh scattering we neglected molecular anisotropy so that the single scattering polarization was -1. The corresponding value for aerosol scattering in our model was 0.18. Thus Rayleigh scattering resulted in large polarization with small opposite polarization for aerosol scattering.

When the sun was close to the zenith ($\mu_o \sim 1$) the receiver was pointing towards the horizon, and in this case the most likely scatter channel involved scattering in the lowest

atmospheric layer. This was manifested by lower polarization for the Elterman model which had many more aerosol particles in this layer. On the other hand, when the sun was close to the horizon ($\mu_0 \sim 0$) and the receiver pointing towards the zenith, the most likely scatterings occurred above the aerosol layer so that both models displayed much higher polarization. In this case the modified model with aerosol at a greater altitude gave the lower polarizations.

For large solar zenith angles (greater than about 70°) the effect of surface albedo was quite small and the aerosol property discrimination was much larger than effects due to surface reflection characteristics. Recent simulations have shown that, in these cases, discrimination of the models could be enhanced by observing the polarization at several different azimuths in the plane perpendicular to the solar direction. This had the effect of varying the altitude of the region where the most important scatterings occurred thus providing an indication of aerosol concentration at different levels. It appears, therefore, that the measurement of sky polarization at right angles to the solar direction as the sun sets offers promising information regarding the vertical distribution of aerosols.

FIGURE 2
POLARIZATION AS FUNCTION OF SOLAR ZenITH ANGLE COSINE

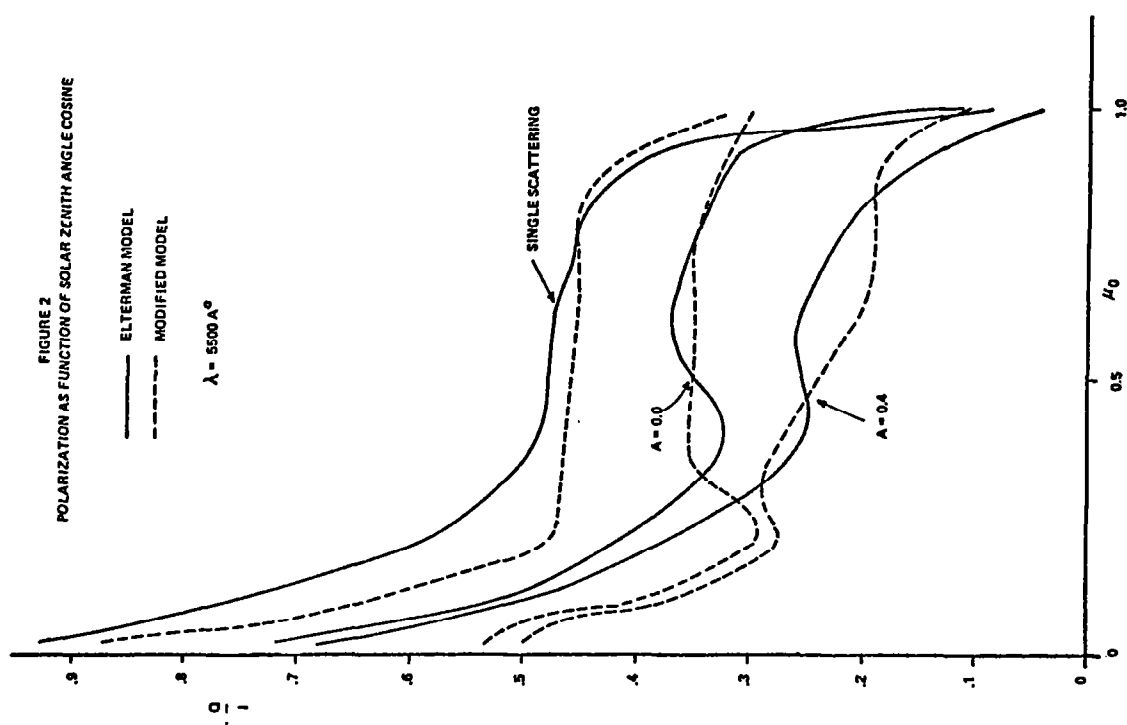
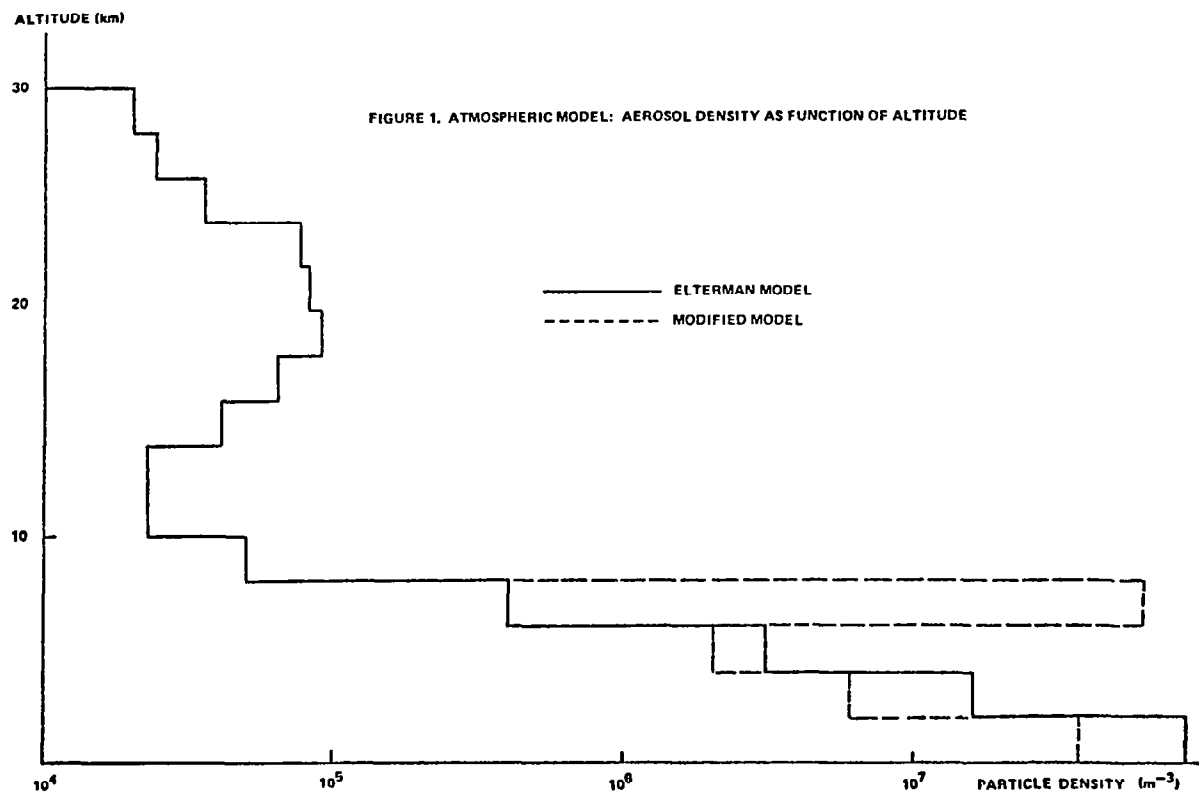


FIGURE 1. ATMOSPHERIC MODEL: AEROSOL DENSITY AS FUNCTION OF ALTITUDE



RADIATIVE TRANSFER IN RURAL, URBAN, AND
MARITIME MODEL ATMOSPHERES

Eric P. Shettle

Atmospheric Optics Branch, AFGL, L. G. Hanscom AFB, MA 01731

INTRODUCTION: The solar radiation scattered back out of the earth's atmosphere strongly depends on the nature and the amount of aerosols present in the atmosphere. This dependence of the upward radiation on aerosol content of the atmosphere has been the basis of several studies on remote satellite measurements of the properties of the atmospheric aerosols particularly their total optical thickness or mass (e.g. Fraser, 1974; and Ludwig et al, 1974). While it is possible to develop a functional relationship between the upwelling radiances and the total aerosol content of the atmosphere, the details of such a relationship will vary depending on the aerosol properties. In this paper we will briefly examine how the nature of the aerosols affects the solar radiances emerging from the earth atmosphere. The results presented below are primarily for a wavelength of 0.55 microns, although the radiances for other wavelengths will also be discussed.

ATMOSPHERE MODEL: The Light scattering calculations were made using a modified form of FLASH, which is a Monte Carlo type program developed by Radiation Research Associates (Collins et al, 1972) for AFGL. The program allows one to include the effects of the spherical nature of the earth and its atmosphere, absorption by ozone water and carbon dioxide, bending of the photon path by variations of the refractive index of air, and the polarized nature of the scattering of light.

The properties of the aerosols were based on the models developed by Shettle and Fenn (1976). Different sets of calculations were made using their rural, urban or maritime aerosol models within the boundary layer (below 2 km), with a 10 km "meteorological range" at the surface. For all of the calculations their tropospheric aerosol model was used above the boundary layer, with extinction coefficients appropriate for moderate volcanic conditions used in the stratosphere to represent the prevailing conditions due to the residual effects of the Fuego Volcanic eruption of November 74.

The extinction coefficients, for a wavelength of 0.55 microns, (and therefore the transmissions) were the same for each of the model atmospheres since the visibilities were the same (Note, for simplicity, we have neglected the fact that Koschmeider's relationship is strictly valid only if there is no absorption). The only differences between the various models at 0.55 microns are the relative amounts of scattering and absorption, and minor differences in the phase functions. For other wavelengths the models also differ in their extinction coefficients, although the differences between the urban and rural extinction coefficients is relatively small for most wavelengths.

RADIANCES: The upward radiances for a wavelength of 0.55 microns were calculated as a function of the viewing direction and sun angle for each of the different atmospheric models, as seen looking downward from an altitude of 20 km. The radiances seen from satellite altitudes would be essentially the same after making appropriate transformations of the viewing directions, because the optical thickness of the atmosphere remaining above 20 km is only 0.03 and that is mostly absorption by ozone. The radiances using the rural aerosol model are shown for azimuth angles of 0° and 90° in figures 1 and 2. As might be expected the greatest radiances are observed when viewing near the horizon with the sun low in the sky. The decrease in radiances as the sun goes from 75° toward 90° (and the scattering angle approaches 0°) is due to the longer optical path through the atmosphere and the increased attenuation along the path. It should be noted that for a polar view angle of 180° or a solar zenith angle of 0° the radiances are independent of azimuth. The small differences between Figures 1 and 2 for these angles are due to the statistical fluctuations inherent in a Monte Carlo type calculation.

The general features of the dependence of the radiance on viewing and sun geometries are similar for the different atmospheric models. Therefore the radiances for different atmospheric conditions are best compared by examining their ratios, as in Figure 3 for the urban and rural models. The upward radiances from the urban model are less than from the rural atmosphere, as would be expected because of the greater absorption for the urban conditions. The ratio approaches 1 when the sun is low in the sky or when looking towards the horizon, because of the increased optical path of the solar radiation before penetrating to the boundary layer where the models differ. So proportionately more of scattering occurs in the upper troposphere or stratosphere where the atmospheric conditions are less sensitive to the surface conditions. A comparison of the upward radiances from the maritime versus rural condition indicates the differences are only about 5 to 10% which is comparable to the accuracy of the present radiance calculations.

DISCUSSIONS: A major conclusion that can be drawn from this work is the importance to consider the effects of variations in the optical properties of the aerosols in assessing potential methods for making remote satellite measurements of the atmospheric aerosols. The most important of these is the aerosol albedo for single scattering and to a lesser extent the angular distribution of the aerosol scattering. The vertical variation of the aerosol properties can be significant, when looking near the horizon or when there is an appreciable amount of absorption.

For other wavelengths the variation of the upward radiances with the viewing/sun geometry is similar to Figures 1 and 2, with the radiances increasing for shorter wavelengths because of the increased scattering. The difference between the maritime and rural conditions become more pronounced, especially in the new infrared.

REFERENCES

Collins, D. G., W. L. Blattner, M. B. Wells, and H. G. Horak (1972), "Backward Monte Carlo Calculations of the Polarization Characteristics of the Radiation from Spherical-Shell Atmospheres", Appl. Opt., 11, 2684-2696.

Fraser, R. S. (1974), "Measurement of Atmospheric Particles from Satellites", in WMO Special Environmental Report No. 3, Observation and Measurement of Atmospheric Pollution.

Ludwig, C. B., M. Griggs, W. Malkmus, and E. R. Bartle (1974), "Measurement of Air Pollutants from Satellites", Appl. Opt., 13, 1494-1509.

Shettle, E. P. and R. W. Fenn (1976), "Models of the Atmospheric Aerosols and their Optical Properties" in AGARD Conference Proceedings No. 183, Optical Propagation in the Atmosphere, presented at the Electromagnetic Wave Propagation Panel Symposium, Lyngby, Denmark, 27-31 October 1975.

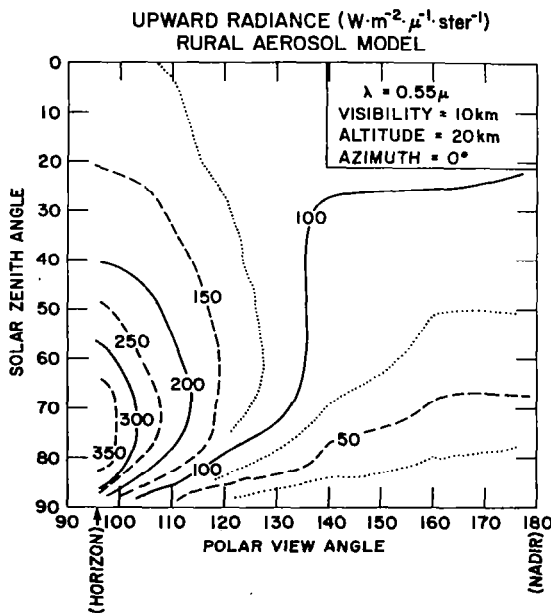


FIGURE 1

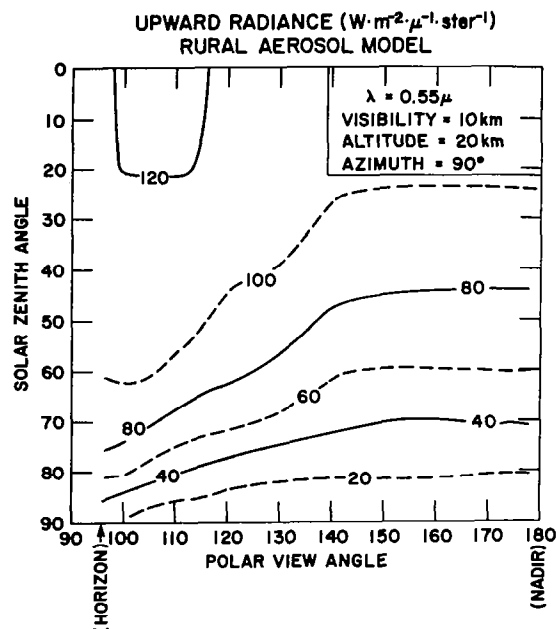


FIGURE 2

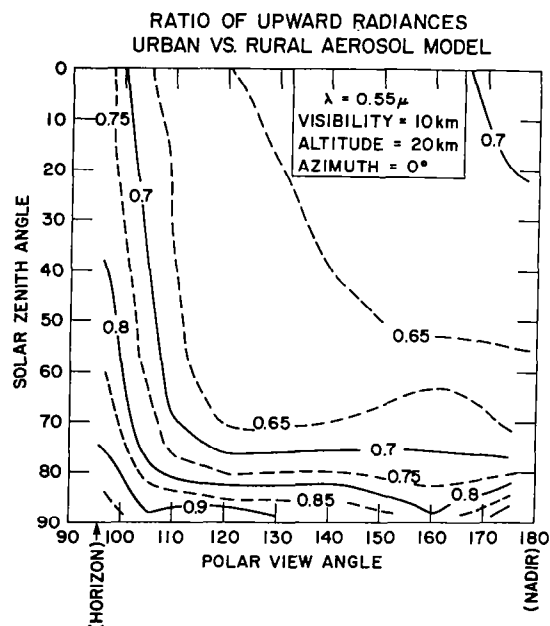


FIGURE 3

INFLUENCE OF AEROSOL PARTICLES ON THERMAL PROPERTIES OF THE UPPER ATMOSPHERE

G. W. Grams

National Center for Atmospheric Research*, Boulder, Colorado 80303

G. Fiocco and A. Mugnai

Università, Istituto di Fisica, Roma, Italy

1. Introduction.

The energetic equilibrium of small particles in the earth's atmosphere has been treated in a model that has been described in a number of recent publications.¹⁻⁴ We extended this model to demonstrate the effect of impure sulfuric-acid droplets and fine-ash particles on the thermal structure of the stratosphere. We also applied the model to ice particles in the mesosphere; the latter results have implications for noctilucent cloud formation.

Our analysis is based on establishing a balance among the energy absorbed from solar and planetary radiation fields, the energy radiated by the particles, and the sensible heat exchanged through collisions with the ambient gas. The planetary radiation field is calculated as a function of altitude and includes radiation from the surface as well as emission and absorption by the infrared bands of carbon dioxide, ozone, and water vapor.

In our previous papers, we studied the dependence of particle temperatures and atmospheric heating rates on particle size and altitude for different aerosol materials, different latitudes and seasons, different times of day, and different values of the planetary albedo. We also integrated the hour-by-hour values of the heating rate to obtain daily-average heating rates; and we integrated those daily-average heating rates over various particle size distributions to study the effects of the aerosol layer on the energy budget of the atmosphere.

2. Stratospheric particles.

We present here the results of our most recent work, in which we consider the well-documented effects of the volcanic dust emitted into the earth's atmosphere from the Mt. Agung eruption of 1963. Following the eruption, Newell⁵ attributed anomalous increases in the stratospheric temperature to the presence of the volcanic dust. One figure from his paper is reproduced here as Figure 1. It shows the difference in stratospheric temperature between January 1964 and January 1963, as a function of geographical location at an altitude of about 19 km. A large temperature increase is evident in the latitude strip between 0° and 20°S, with maxima over Africa, New Guinea, and South America. This unusual effect can be explained by taking into account geographical variations in the earth's albedo. Our previous results showed that, as the albedo of the underlying earth-atmosphere system increases, the ambient gas heating rates induced by the aerosol particles can be significantly enhanced. From satellite data, Vonder Haar

*The National Center for Atmospheric Research is sponsored by the National Science Foundation.

and Ellis⁶ calculated seasonal-average planetary albedo values as a function of latitude and longitude. The general characteristics of the albedo patterns--relatively high values over land and lower values over the oceans--fit the longitudinal patterns observed in the temperature differences of Figure 1.

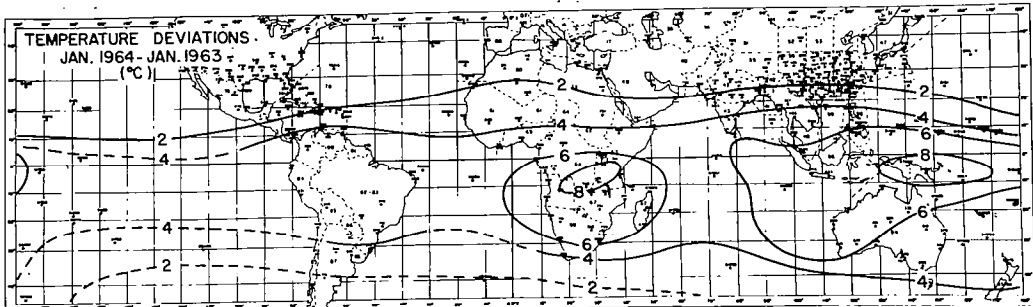


Figure 1. Increase of temperature [K] at 19 km from January 1963 to January 1964 (from Newell⁵).

We calculated heating rates as a function of latitude and longitude by using data on the geographical variation of aerosol concentration at the 19-km level obtained by Cadle, Kiang, and Louis.⁷ They used a two-dimensional dynamic model to study the global-scale dispersion of the eruption cloud of the Agung volcano; they adjusted the strength and the chemical composition of the source functions used in their model so that the calculated concentrations of fine-ash particles and sulfuric-acid droplets agreed well with actual measurements at various times and places after the eruption. In our aerosol-heating model, we used the aerosol concentrations published by Cadle and his collaborators for 300 days after the Agung eruption to establish the amount of fine-ash particles and impure sulfuric-acid droplets at the 19-km level in mid-January 1964. On the basis of our previous studies, we assumed that the particle size distribution could be represented by the Junge⁸ power-law size distribution function in the radius interval $0.03 \leq r \leq 3 \mu\text{m}$. We specified the complex refractive index spectrum of the fine-ash particles by using the "synthetic aerosol" data published by Ivlev and Popova⁹ and that of the impure sulfuric-acid droplets by using the data published by Palmer and Williams¹⁰ for a 75% solution of sulfuric acid in water, modified by setting the imaginary refractive index equal to 0.001 in the visible spectrum. We used Vonder Haar and Ellis' seasonal-average data for the winter (Dec.-Jan.-Feb) to specify the geographical variation in the planetary albedo. The sum of the fine-ash and sulfuric acid heating rates is shown in Fig. 2. A very high correlation between

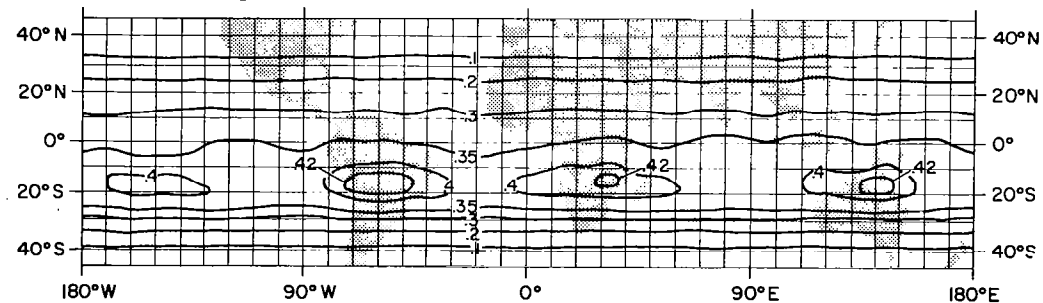


Figure 2. Daily average heating rates [K day^{-1}] at 19 km for the distribution of fine-ash particles and impure sulfuric-acid droplets obtained by Cadle, Kiang, and Louis.⁷ See text for more details.

the temperature differences in Figure 1 and the heating rates in Figure 2 is evident. Maximum heating rates of about 0.4 K day^{-1} are associated with temperature differences of about 8 K. From this, we infer radiative relaxation time constants of the order of 20 days at the 19-km level.

3. Mesospheric particles.

McDonald¹¹ and Schilling¹² pointed out that there are regions of the earth's atmosphere in which it is not thermodynamically possible for clouds of ice particles to exist. In these regions, the ambient temperature is sufficiently warm that the saturation vapor pressure over the surface of an ice particle maintained at the air temperature would actually exceed the total ambient pressure, and the particle would quickly disappear by sublimation. By applying this basic thermodynamic principle to the pressure-temperature relations established in a model atmosphere, both were able to show that ice in the mesosphere would exist only in the approximate altitude interval of 68-95 km. However, neither of these studies considered the possibility that the temperature of the particle could differ significantly from that of the ambient gas.

We calculated equilibrium temperatures of ice particles in the upper atmosphere, and we found temperature differences as high as about 50 K--depending on altitude and particle size. Figure 3 shows some results obtained with our model for spherical ice particles at twilight with refractive indices specified by the spectral data presented by Bertie, Labbe, and Whalley.¹³ The lines are loci on the $z-r$ diagram for the condition that the saturation vapor pressure equals the ambient atmospheric pressure. Ice particles can exist within these boundaries for the atmospheric models for different latitudes and seasons indicated on the figure. The summertime results show successively smaller

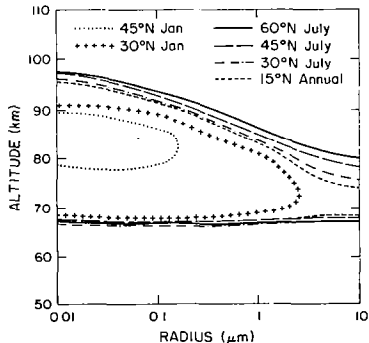


Figure 3. Regions in which spherical ice particles exist at twilight as a function of latitude and season.

height intervals for the existence regions of all particle sizes as one progresses equatorward. The wintertime results are less favorable at any given latitude; most significantly, the present calculations show that mesospheric ice particles would not exist at all in the model atmosphere for 60°N in January. This is consistent with the observed seasonal variations in noctilucent cloud activity at high latitudes.

References

1. Fiocco, G., G. Grams, and G. Visconti, Equilibrium temperatures of small particles in the earth's upper atmosphere (50-110 km), J. Atmos. Terr. Phys., 37, 1327-1337, 1975.
2. Fiocco, G., G. Grams, and A. Mugnai, Energy exchange and temperature of aerosols in the earth's atmosphere (0-60km), J. Atmos. Sci., 1976 (in press).
3. Grams, G., and G. Fiocco, Equilibrium temperatures of spherical ice particles in the upper atmosphere and implications for noctilucent cloud formation, J. Geophys. Res., 1976 (in press).
4. Mugnai, A., G. Fiocco, and G. Grams, Effect of aerosol optical properties and size distributions on heating rates induced by stratospheric aerosols, Quart. J. R. Meteor. Soc., 1976 (to be submitted).
5. Newell, R. E., The global circulation of atmospheric pollutants, Sci. Am., 224, 32-42, 1971.
6. Vonder Harr, T. H., and J. S. Ellis, Atlas of Radiation Budget Measurements from Satellites (1962-1970), Atmospheric Science Paper No. 231, Department of Atmospheric Science, Colorado State University, Fort Collins, Colorado, 1974.
7. Cadle, R. D., C. S. Kiang, and J.-F. Louis, The global scale dispersion of the eruption clouds from major volcanic eruptions, J. Geophys. Res., 81, 3125-3132, 1976.
8. Junge, C. E., Air Chemistry and Radioactivity. New York, Academic Press, Inc., 1963.
9. Ivlev, L. S., and S. I. Popova, The complex refractive indices of substances in the atmospheric-aerosol dispersed phase, Izv. Atmos. and Oceanic Phys., 9, 1034-1043, 1973.
10. Palmer, K. F., and D. Williams, Optical constants of sulfuric acid: application to the clouds of Venus, Appl. Optics, 14, 208-219, 1975.
11. McDonald, J. E., Atmospheric exclusion limits for clouds of water and other substances, J. Geophys. Res., 69, 3669-3672, 1964.
12. Schilling, G. F., Forbidden regions for the formation of clouds in a planetary atmosphere, J. Geophys. Res., 69, 3663-3667, 1964.
13. Bertie, J. E., H. J. Labbe, and E. Whalley, Absorptivity of Ice I in the range 4000-30 cm⁻¹, J. Chem. Phys., 50, 4501-4520, 1969.

Influence of Airborne Particles (Aerosols)
on the Earth's Radiation Balance

RUTH A. RECK

Research Laboratories, General Motors Corporation, Warren, MI 48090

The overall objective of our atmospheric research has been to determine how the global radiative energy balance is influenced by trace gases and airborne particles so that the changes caused by man may be delineated from those caused by natural phenomena. The present discussion summarizes some of my more important findings of several years of theoretical research to parameterize the thermal and radiative effects of aerosols in terms of their physical and optical properties.

Mie-scattering aerosols¹ have been introduced by us into a one-dimensional radiative-convective atmospheric model originally developed by Manabe and Wetherald (M-W)² at the Geophysical Fluid Dynamics Laboratory of Princeton University. The M-W model uses an initial value approach and by recalculation of the energy flux divergence at each time step (at a series of nine-vertically-aligned points), integrates forward in time to reach the final steady-state temperature profile (at discrete altitudes) throughout the troposphere and stratosphere. The radiative effects of CO₂, O₃, relative humidity and several (usually three) layers of water clouds are included.³

To modify the M-W model to include aerosols we have chosen an aerosol parameterization developed by Sagan and Pollack (S-P)⁴ for two-stream anisotropic scattering. Aerosols appear in the model in the same manner as clouds. However whereas the cloud properties are empirical, the aerosol properties are computed.

In the S-P parameterization a mean complex aerosol refractive index is assumed in the visible (1.5-0.1i), and the infrared as well as a specific size distribution. (Only slight thermal effects are obtained as the imaginary component is varied from 0.01 to 0.1.) Multiple scattering results are used to determine two aerosol parameters, 1) the single-scattering albedo and 2) the anisotropic scattering factor. These two optical parameters then define the radiative contribution of the aerosol at a given altitude for a specific visible extinction, σ_{vis} , the optical thickness, τ .

Our results illustrate the physically complex manner in which aerosols alter the atmospheric radiative balance. Aerosols backscatter and absorb downward solar radiation and backscatter and absorb the portion of solar radiation already reflected from the earth's surface. To a lesser degree they also absorb terrestrial radiation (all interactions

except the first produce heating). At the earth's surface the resultant heating or cooling is determined by the earth's shortwave surface albedo, ω_s (Fig. 1). As ω_s increases, more reflected solar radiation is back-scattered earthward with a trend toward more heating at the surface and less radiative cooling in the atmosphere.

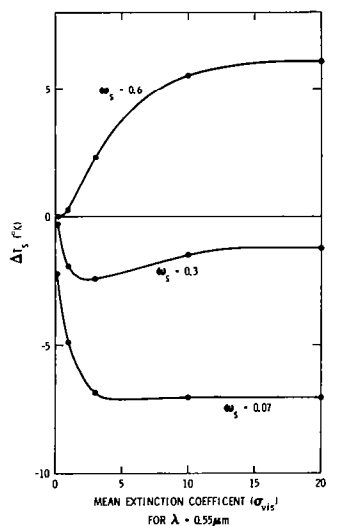


Fig. 1. Changes in the earth's surface temperature ($^{\circ}$ K) (T with aerosols - T without aerosols) as a function of mean visible ($\lambda = 0.55 \mu m$) extinction coefficient for the earth's shortwave surface albedo, $\omega_s = 0.07, 0.3$, and 0.6

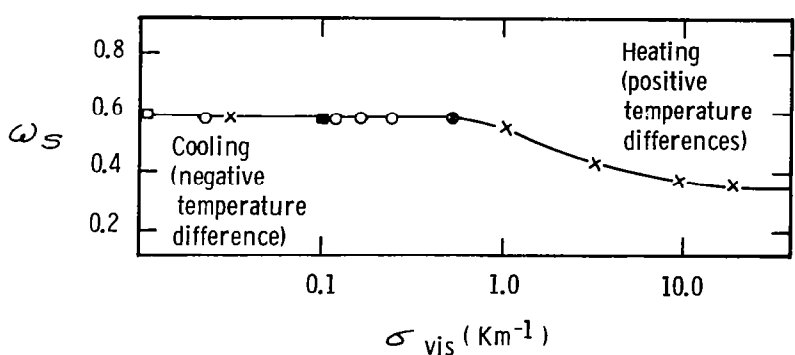


Fig. 2. Values of ω_s and σ_{vis} for which no surface heating or cooling occurs due to a low-lying aerosol.

Since the thermal impact diminishes as the height above the surface increases,⁶ aerosols have their greatest impact when they are low-lying over a dark surface. Only over highly reflecting surfaces (such as snow) do they lead to heating⁷ (except for visible extinction coefficients greater than 0.9 (see Fig. 2)).⁸ At the southern polar region the additional thinness of the atmosphere (due to the high elevation, 2000 m) makes the calculated surface temperature an order of magnitude more sensitive to aerosol-produced heating.

It is possible to summarize the thermal behavior of aerosols for global average conditions by finding the curve of ω_s versus extinction coefficient for which heating and cooling balance. For this purpose we assume

an aerosol with average optical properties¹ ubiquitously distributed in a low-lying layer. The resultant curve is shown in Fig. 2. It has been found that the curve is independent of the presence of water clouds. In the limit of high optical density the critical ω approaches 0.35 while for most naturally occurring optical densities⁸ the critical $\omega_s \rightarrow 0.6$.

Latitudinal variations in the thermal contribution are expected due to nonuniformity in solar heating from differing zenith angles and to geographic variations in the atmospheric constituents and in the earth's albedo and absorptivity. We have explored these differences by performing calculations with increasing optical density for model parameters describing 10° latitudinal zones between 5° and 85° N latitude (April parameters).

Between 5° and 35° we find the surface temperature change is monotonic with increasing ω_s (Fig. 3a), and latitudinal differences are minor. At 55°N and poleward the latitudinal differences are greater but more importantly the surface temperature change is double-valued with a minimum (extremum) value for an albedo near 0.3 (Fig. 3b). This implies that an increase in aerosol abundance produces accelerated cooling as the seasonal variation in ω_s (Table I) approached this critical albedo value from either a higher or lower value. This, in turn, changes the rate of seasonal changeover between winter and summer. Melting is delayed in spring and freezing accelerated in fall to result in an extended winter season with more ice coverage. Some empirical evidence supports this phenomena as one possible explanation for the 12% northern hemisphere ice abundance increase in 1971 that was reported by Kukla and Kukla.¹¹

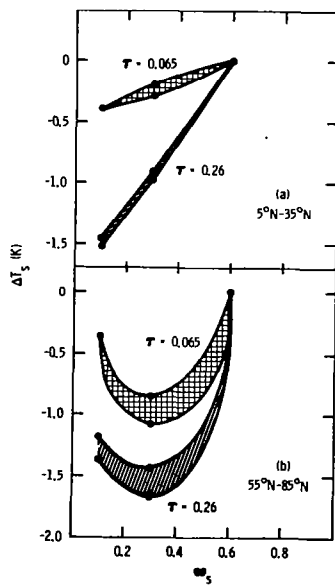


Fig. 3a. Range of calculated surface temperatures as a function of surface albedo for latitudes 5-35°N, for a particular aerosol layer having $\tau = 0.065$ and $\tau = 0.26$;
 3b. Same as a) except for 55-85°N latitude.

TABLE I. Values of shortwave surface albedo, ω_s .¹⁰

Latitude (°N)	Month			
	April	July	October	January
55	0.24	0.13	0.18	0.31
65	0.54	0.19	0.38	0.50
75	0.72	0.31	0.61	0.70

What can be concluded from these studies?

- 1) Mie-scattering aerosols can lead to either heating or cooling, depending on the balance between backscatter and absorption.
- 2) The role of aerosols can be shown to be complicated by non-linear effects when other global parameters vary simultaneously.
- 3) The thermal and radiative effect of aerosols can be predicted accurately only when more measurements of optical properties become available.

REFERENCES

1. R. A. Reck, Influence of surface albedo on the change in the atmospheric radiation balance due to aerosols, *Atmospheric Environment* 8, 823-833 (1974).
2. S. Manabe and R. T. Wetherald, Thermal equilibrium of the atmosphere with a given distribution of relative humidity, *J. Atmos. Sci.* 24, 241-259 (1967).
3. A special thanks to R. T. Wetherald for the latitudinal data.
4. C. Sagan and J. B. Pollack, Anisotropic nonconservative scattering and the clouds of Venus, *J. Geophys. Res.* 72, 469-477 (1967).
5. J. A. Coakley and P. Chylek, The two-stream approximation in radiative transfer: including the angle of incident radiation, *J. Atmos. Sci.* 32, 409-418 (1975).
6. R. A. Reck, Influence of aerosol cloud height on the change in the atmospheric radiation balance due to aerosols, *Atmospheric Environment* 9, 89-99 (1975).
7. R. A. Reck, Aerosols and polar temperature change, *SCIENCE* 188 728-730 (1975).
8. R. A. Reck, Aerosols in the atmosphere: calculation of the critical absorption/backscatter ratio, *SCIENCE* 186, 1034-1036 (1974).
9. R. A. Reck, Thermal and radiative effects of atmospheric aerosols in the northern hemisphere calculated using a radiative-convective model, *Atmospheric Environment* 10, 611-617 (1976).
10. C. Schutz and W. L. Gates, Global climatic data for surface, 800 mb, 400 mb: January (R-915-ARPA (Nov. 1971)), July (R-1029 ARPA (Nov. 1972)), April (R-1317-ARPA (Dec. 1973)), October (R-1425-ARPA (Mar. 1974)), Defense Advanced Research Projects Agency, Rand, Santa Monica, CA.
11. G. J. Kukla and M. J. Kukla, Increased surface albedo in the northern hemisphere, *SCIENCE* 183, 709-714 (1974).

Stratospheric Aerosols and Climatic Change

Owen B. Toon
James B. Pollack
Theoretical and Planetary Studies Branch
NASA-Ames Research Center
Moffett Field, CA 94035

Stratospheric sulfuric acid aerosols scatter sunlight and scatter, absorb, and emit terrestrial thermal radiation. These interactions play a role in the earth's radiation balance and therefore affect climate. Earlier work (Pollack et al. 1976a, b) showed that stratospheric aerosols from volcanic explosions can produce serious climatic changes, but the aerosols produced by Space Shuttles, will be too few in number to produce significant climatic changes. Our work also showed, that the size distribution of volcanic aerosols evolved after an eruption and that the aerosols first warmed and then cooled the earth's surface. Unfortunately, aerosol size distributions after volcanic eruptions are poorly known (Toon and Pollack, 1976). Therefore we use a photochemical-aerosol model to estimate size distributions after a volcanic eruption (Hamill et al. 1976a, b). We then perform radiative transfer calculations to estimate changes in surface temperature.

Our earlier calculations of the climatic impact of Space Shuttle exhaust showed that the injected aluminum oxide particles will not, by themselves, cause significant climatic changes. However, the Al_2O_3 particles could serve as nucleation centers for stratospheric sulfuric acid and thereby enhance the stratospheric sulfate layer (Hofmann, 1975). We use the photochemical-aerosol model to estimate the size distribution and optical depth changes

caused by the Al_2O_3 particles and then perform radiative transfer calculations to assess the climatic significance of these changes.

Hamill, P., O. B. Toon, and C. S. Kiang, A Physical Model of the Stratospheric Aerosol Particles, Submitted to J. Atmos. Sci., 1976.

Hamill, P., R. Turco, O. B. Toon, R. Whitten and C. S. Kiang, A One Dimensional Model of the Stratospheric Aerosol Layer, submitted to Geophys. Res. Lett. 1976.

Hofmann, D. J., D. E. Carroll and J. M. Rosen, Estimate of the Contribution of the Space Shuttle Effluent to the Natural Stratospheric Aerosol, J. Geophys. Res. Lett., 2, 113, 1975.

Pollack, J. B., O. B. Toon, C. Sagan, A. Summers, B. Baldwin and W. Van Camp, Volcanic Explosions and Climatic Change: A Theoretical Assessment, J. Geophys. Res., 81, 1976.

Pollack, J. B., O. B. Toon, A. Summers, W. Van Camp and B. Baldwin, Estimates of the Climatic Impact of Aerosols Produced by Space Shuttles, SST's and other High Flying Aircraft, J. Appl. Meteor., 15, 247, 1976.

Toon, O. B., and J. B. Pollack, A Global Average Model of Atmospheric Aerosols for Radiative Transfer Calculations, J. Appl. Meteor., 15, 225, 1976.

Effects of Aerosol Particles on Visibility, Atmospheric Pollution, Radiation Budget and Climate

by K. Bullrich and R. Eiden

Institut für Meteorologie, Johannes Gutenberg-Universität, Mainz, FR Germany

Abstract:

Particles produced by natural and anthropogenic effects may pollute the atmosphere severely at distinct places and time intervals. This pollution reduces visibility and influences significantly radiation budget and climate.

Summary:

Atmospheric aerosol particles influence significantly scattering and absorption processes in the solar spectral range. In the longwave range of the electromagnetic spectrum especially the window region is affected by absorption and emission of the particles.

Aerosol particles are generated by gas to particle conversion, sea water droplets, forest fires, soil dust and human activities. The transport and the life time of the particles depend on the atmospheric surface conditions and on the properties of the particles. The visibility is influenced by light scattering and absorption of the particles; it depends on the relative humidity of the air. The absorption is important for heating and cooling the atmosphere, it almost doesn't depend on the relative humidity.

The following discussion of the influence of the aerosol particles on the radiant energy balance refer to the measurements of average data which characterize scattering and absorption under consideration of the surface albedo and cloud properties.

The influence of the aerosol particles on the short wave spectrum has two aspects:

- a) The aerosol particles absorb radiation thus effecting radiant flux divergences which can be expressed as heating rates per day. This heating increases with the increase of aerosol content and with increasing particle absorption.
- b) The aerosol particles scatter radiation in all directions, also back to space. The latter portion increases with increasing turbidity; this would result in a cooling effect of the whole system earth-atmosphere, however, this is counteracted by the aero-

sol absorption thus diminishing the portion of radiant energy scattered back to space through the upper boundary of the atmosphere. This counteraction increases with increasing turbidity and increasing surface albedo both of which augment the number of multiple scattering processes thus increasing the absorption: The final result is a decrease of the albedo of the planet earth.

In any case, the existence of aerosol particles causes a cooling of the earth surface and a heating of the lower troposphere.

The Influence of the Aerosol Particles on the Infrared Radiation

The absorption of short wave radiation by the aerosol particles mentioned above results in a decrease of the planetary albedo on the one hand and a heating of the atmosphere on the other hand. Recent investigations have revealed that there is also radiant emittance by the aerosol particles due to their strong absorption bands in the window near 9 μm . Thus, the above discussed heating effect is counteracted by radiation losses causing cooling of the atmosphere.

The Net Radiation Effected by the Aerosol Particles

The counteraction of heating and cooling due to absorption as well as emission of radiation described above results in a net effect as follows: Computations which are valid for average aerosol conditions and for dry aerosol in the geographical latitude of 50° , yield a net effect of 0.2°K per day. This is a small amount, and in humid tropical regions it is negligible in comparison with the absorption effect by the water vapour dimers. In middle and northern latitudes, however, it can be estimated that a possible increase of turbidity and aerosol absorption would enhance the net heating to become approximately 1°K per day.

Summing up, the statement can be made that the influence exerted by the aerosol particles - integrated over all latitudes - increases with increasing turbidity and aerosol absorption being especially enhanced when the mean surface albedo surpasses the value of 20 %. Aerosol particles cause a heating of the atmosphere and a simultaneous slight cooling of the surface. It is therefore deemed important to control both the increase of the aerosol content and absorption and the change of the surface albedo with special emphasis to human activities.

The influence of the Aerosol Particles on the Radiant Energy Balance of Clouds

Aerosol particles suspended within clouds influence directly and indirectly the energy balance of clouds. An increase in the number of aerosol particles in clean air increases the number of small droplets; over the continents this is evident from the increase in the reflectivity of the clouds. On the other hand an increase in the number of aerosol particles increases the multiple scattering within the clouds, i.e. the path-length of radiation is prolonged considerably resulting in a significant increase of radiation absorbed by the aerosol particles. Therefore, the influence of both the cloud droplets as well as the aerosol particles results in a temperature increase. The absorption within the clouds sets an upper limit to the albedo of clouds of about 85 %.

Literature:

B. Bolin et al., 1974, Tellus, 26, 185
R. Eiden, G. Eschelbach, 1973, Zeitschr. f. Geophysik, 39, 189
K. Fischer, H. Grassl, 1975, Tellus, 27, 522
H. Grassl, 1975, Contrib. Atm. Phys., 48, 199

WEISS, R.; CHARLSON, R.J.; WAGGONER, A.P.; BAKER, M.B.; COVERT, D.; THORSELL, D. and YUEN, S.
Civil Engineering Department, University of Washington, Seattle, WA 98195, USA

Application of Directly Measured Aerosol Radiative Properties to Climate Models

Chemical and optical data on atmospheric aerosols has been collected in a variety of sites across the U.S. in order to obtain information on the nature of the aerosols, the variability of their characteristics, and a crude estimation of the climatic impact of the particles at the present time. The information thus gathered has been put through a simple calculation of aerosol interaction with visible radiation, which is an important part of any climate model.

Light scattering measurements

The measurements were made at 530 nm using adapted versions of an integrating nephelometer (Beuttel and Brewer, 1949). Table 1 shows the averages by site of the measurements of b_{sp} and R, the light scattering coefficient and hemispheric backscatter-total scatter ratio [$R \equiv \int_{\pi/2}^{\pi} \beta_{sp}(\theta) \sin \theta d\theta / \int_{0}^{\pi} \beta_{sp}(\theta) \sin \theta d\theta$].

Absorption coefficient

The absorption coefficient is measured using the opal glass integration method (Lin, *et al.*, 1973) and involved collecting the particles on a nuclepore filter then comparing transmission through the filter plus sample to that through a clean filter. The method is expected to yield values of b_{ap} accurate to a factor of 2. Two kinds of measurements were done. Earlier, all filterable mass was collected on the filters, and later the samples were divided so that particles of radius less than about 2 μm were collected on one filter and larger particles on the other.

Table 2 shows the results of the size-segregation. Absorption by small particles is greater than that by larger ones by a factor of 4 to 32 (average about 16), while the mass of the small fraction is larger than that of the other by a factor of 2 to 4. Thus for typical atmospheric size distributions absorption by small particles is likely to be much more important than that by large ones.

Table 3 shows the absorption data for the total filter samples. Since the absorption measurements were not carried out at all sites it is difficult to characterise the variation in b_{ap} but it appears to fall in the range $(.07-.7) \times 10^{-4} \text{ m}^{-1}$.

Chemical composition

The chemical composition of the aerosol determines not only its complex refractive index and thus interaction with radiation but also its response to changing environmental conditions; e.g., relative humidity, and thus is an important subject of inquiry for climatic related studies. An integrated analysis of much data on the elemental composition and molecular form of atmospheric aerosols (Dzubay and Stevens, 1975; Bolin and Charlson, 1976; Brossel, *et al.*, 1975) shows that for two large geographic regions of the globe, eastern U.S. and northern Europe, the accumulation mode mass is dominated by sulfate compounds. At the Tyson, Mo., Milford, Mi., and Hall Mtn., Ak. sites information on the composition and molecular form of the light scattering aerosol was available from humidity controlled nephelometer data (Charlson, *et al.*, 1974). Sulfates $\text{H}_2\text{SO}_4/(\text{NH}_4)\text{HSO}_4$ or $(\text{NH}_4)_2\text{SO}_4$ were seen to dominate light scattering 80% to 90%

of the time.

Analysis of the absorbing fraction proceeded on the supposition that the most likely atmospheric compounds which are both efficient absorbers of visible radiation and exist in sufficient concentrations are metal oxides, especially hematite or magnetite, elemental carbon, and possibly some high molecular weight organic compounds. Elution techniques applied to the filter samples to remove metal oxides and most organic compounds did not decrease the measured absorption coefficients so that carbon, either in its elemental form or in large organic molecules, is probably of major importance in absorption of solar radiation by particles. This hypothesis is supported by the fact that the samples look gray and measured values of b_{ap} at $\lambda = 438, 525$ and 628 nm from St. Louis show that b_{ap} has an approximate $1/\lambda$ dependence, which is consistent with a wavelength independent refractive index in this range, such as that of graphitic carbon. Thus atmospheric aerosols in the sites mentioned appear to consist largely of sulfate solutions and carbon.

Implications of measured aerosol properties

The climatologically significant aerosol parameters can be divided into two classes; those which depend on total concentration and those which do not. In the simplest models the significant intensive parameters are the ratio of hemispheric backscattering to the total scattering coefficient R and the single scattering albedo, $\omega_0 \equiv b_{sp}/b_{ext}$. These are shown in Table 4. Because of the variability in b_{ap} and b_{ext} the figures shown in Table 4 are derived from considerations of pairs of data points and not from the averages in Tables 1 and 2. It can be seen that ω_0 ranges between .53 and .87 and there appears to be a correlation between low values of ω_0 and high values of R , which indicates a decrease in the sizes of the optically important particles. In the third column of Table 4 we have listed the parameter $(1-\omega_0)/\omega_0 R$, which according to Chylek and Coakley (1974) indicates whether the aerosol will have a net heating or cooling effect. For a surface albedo of 0.2, typical of farm and urban areas, the critical value of this parameter is about 2, so that according to the measurements, the aerosols in the St. Louis and Denver areas heat and the Arkansas aerosol cools.

In order to estimate the role played by the aerosol in interacting with solar radiation we have adapted the simple 2-stream heating-cooling calculation of Chylek and Coakley (1974) to include cloud cover in a crude way.

We assume that the depth of aerosol layer is 2.5 km, and that the fraction, f , covered by cloud is a stratus layer with an optical depth of 32 in the upper km. The earth-atmosphere system albedo for an unpolluted case is

$$A = (1-f)A_s + f A_{cl}$$

and for the polluted case, neglecting any change in f due to particles

$$A' = (1-f)A'_s + f A'_{cl}$$

where A_s is the surface albedo, A'_s is the albedo of the aerosol layer; and A'_{cl} and A_{cl} are the albedo of the cloud cover fraction with and without particles, respectively.

Therefore, the fractional change of albedo due to the inclusion of particles is

$$\frac{A'-A}{A} = \frac{(1-f)(A'_s - A_s) + f(A'_{cl} - A_{cl})}{(1-f)A_s + f A_{cl}}$$

Insertion of measured values of the parameters from Table 4 shows that the aerosols in the populated areas has a net heating effect for all cloud cover and the sign of the effect of the "clean site" aerosol depends on the amount of cloud cover.

TABLE 1. LIGHT SCATTERING

$\lambda = 530 \text{ nm. UNITS OF } 10^{-4} \text{ m}^{-1}$. 63% OF ALL DATA POINTS FALL BETWEEN $b_{sp}(\text{LOW})$ and $b_{sp}(\text{HIGH})$

LOCATION	$b_{sp}(\text{AVERAGE})$	$b_{sp}(\text{LOW})$	$b_{sp}(\text{HIGH})$	R	SAMPLE AIR HEATED 5°-20°C ABOVE AMBIENT TEMPERATURE
RICHMOND	0.4	0.2	1.4	-	
PT. REYES	0.12	0.04	0.4	-	
FRESNO	1.0	0.3	1.9	$18 \pm 5\%$	
HUNTER LIGGETT	0.4	0.2	0.8	-	
CAL TECH	1.5	0.8	3.0	$20 \pm 8\%$	
POMONA	1.8	0.6	6.0	$16 \pm 8\%$	
WASHINGTON					
UNIVERSITY	1.58	1.12	2.24	$12 \pm 1\%$	
TYSON	0.63	0.28	1.41	$14 \pm 4\%$	
ST. LOUIS					
UNIVERSITY	0.71	0.40	1.25	$14 \pm 2\%$	
HENDERSON	0.31	0.08	1.25	$17 \pm 8\%$	
TROUT FARM	0.56	0.22	1.58	$18 \pm 6\%$	
TYSON	0.76	0.3	0.89	$15 \pm 5\%$	
MILFORD	0.44	0.16	0.56	$18 \pm 5\%$	
HALL MT.	0.4	0.22	0.56	$18 \pm 5\%$	

TABLE 2. LIGHT ABSORPTION: SIZE SEGREGATED SAMPLES

$\lambda = 530 \text{ nm. 50% OF ALL DATA POINTS FALL BETWEEN LOW AND HIGH VALUES.}$

LOCATION	$b_{ap}(\text{x10}^{-4} \text{m}^{-1})(\text{AVE})$	$b_{ap}(\text{LOW})$	$b_{ap}(\text{HIGH})$	$\rho(\mu\text{g/m}^3)(\text{AVE})$
TYSON (13 POINTS)	$r < 2\mu\text{m}$ 0.11 $r > 2\mu\text{m}$ 8.3×10^{-3}	$.079$ 3.8×10^{-3}	$.125$ 8.7×10^{-3}	16.2 5.04
MILFORD (10 POINTS)	$r < 2\mu\text{m}$ 0.17 $r > 2\mu\text{m}$ $.04$	$.09$ 5.6×10^{-3}	$.16$ $.02$	16.9 9.5
HALL MT. (18 POINTS)	$r < 2\mu\text{m}$ $.07$ $r > 2\mu\text{m}$ 5.0×10^{-3}	$.04$ 3.2×10^{-3}	$.09$ 6.8×10^{-3}	11.3 2.92

TABLE 3. LIGHT ABSORPTION: TOTAL FILTER SAMPLES

$\lambda = 521 \text{ nm. 50% OF ALL DATA POINTS FALL BETWEEN LOW AND HIGH VALUES.}$

LOCATION	$b_{ap}(\text{x10}^{-4} \text{m}^{-1})(\text{AVE})$	$b_{ap}(\text{LOW})$	$b_{ap}(\text{HIGH})$
TYSON (1975) (52 POINTS)	0.12	.064	0.14
MILFORD (1975) (13 POINTS)	0.17	0.065	0.18
HALL MT. (43 POINTS)	0.067	.031	.092
TYSON (1973) (97 POINTS)	0.19	.12	.32
ST. LOUIS U. (50 POINTS)	0.49	.3	1.0
WASHINGTON U. (51 POINTS)	0.36	.25	.54
HENDERSON (13 POINTS)	0.46	.11	.75
TROUT FARM (23 POINTS)	0.64	.34	.91

TABLE 4. AEROSOL PARAMETERS

LOCATION	ω_0	R	$\frac{1-\omega_0}{\omega_0} R$
TYSON (52 POINTS)(1975) (97 POINTS)(1973)	.81 .78	.148 .14	1.58 2.01
MILFORD (13 POINTS)	.74	.18	1.95
HALL MT. (62 POINTS)	.87	.18	.83
ST. LOUIS U. (50 POINTS)	.6	.14	4.76
WASHINGTON U. (51 POINTS)	.76	.12	2.63
HENDERSON (13 POINTS)	.53	.17	5.20
TROUT FARM (23 POINTS)	.55	.18	4.54

References

Beuttel, R. G. and Brewer, A. W., *J. Sci. Instrum.* **26**, 357-359 (1949).
 Bolin, B. and Charlson, R. J., *Ambio* **5**, #2, 47-54 (1976).
 Brosset, C., Andreasson, K. and Fern, M., *Atm. Environ.* **9**, 631 (1975).
 Charlson, R. J., et al., *Atm. Environ.* **8**, 1257-67 (1974).
 Chylek, P. and Coakley, J. A., *Science*, **183**, 75-77 (1974).
 Dzubay, T. G. and Stevens, R. K., *Env. Sci. & Tech.* **9**, 663-668 (1975).
 Lin, C. I., Baker, M. B. and Charlson, R. J., *Applied Optics*, **12**, #6, 1356-1362 (1973).

Laser Beam Broadening in Aerosol Media

Adarsh Deepak, Old Dominion University, NASA-LRC 475, Hampton, VA 23665

The paper describes a theoretical treatment for the propagation of a laser beam, with an arbitrary beam amplitude profile, through an aerosol medium, in which particles scatter according to Mie theory. It is shown that the effects of aerosol scattering on the width (defined by e^{-1} amplitude points) of converging/diverging laser beams can be treated [1] by (i) assuming that the medium as a whole has a complex refractive index,

$$\bar{m} = n + jn' \quad (1)$$

(ii) considering that if $\bar{m} \approx 1$ and if single scattering conditions exist, then according to van de Hulst [2], the total extinction coefficient

$$\beta_e = 2 k n' \quad (2)$$

and, (iii) using the Rayleigh-Sommerfeld diffraction formula [3] in a medium with a complex refractive index \bar{m}_{12} , namely,

$$\psi_2 = \iint_{\substack{\text{Aperture} \\ \text{Area}}} \psi_1 \frac{e^{jk|\vec{R}_{12}|} \bar{m}_{12}}{j\lambda |\vec{R}_{12}|} dx_1 dy_1 \quad (3)$$

where $k = 2\pi/\lambda$, ψ_1 and ψ_2 are amplitudes at positions 1 and 2, \vec{R}_{12} is the radial distance between 1 and 2, and \bar{m}_{12} represents the complex refractive index of the medium.

The scattering and extinction effects due to aerosol particles then directly enter into the factors containing the beam width in expressions for the amplitude and intensity of beam at a distant position 2. A numerical parametric study has been carried out to depict the effects of particle scattering on the broadening of laser beams. Results of the study will be shown.

References

- [1] A. Deepak, "Computer Modeling of Laser Doppler Velocimeter (LDV) Systems and the Performance of CO₂-LDV in Fogs and Comparison with Experimental Results," published in the Proc. of the "2nd International Workshop on Laser Velocimetry," Purdue University, March 27-29, 1974.
- [2] H. C. van de Hulst, Light Scattering by Small Particles, John Wiley & Sons, Inc., New York, 1962.
- [3] J. W. Goodman, Introduction to Fourier Optics, McGraw Hill Book Co., New York (1968).

Multiwavelength visible and IR transmission investigations of atmospheric aerosols

A Hågård, B Nilsson, H Ottersten and O Steinwall
National Defence Research Institute, S-104 50 Stockholm, Sweden

Introduction

With the introduction of optical and IR systems for such applications as communication, guidance, surveillance, ranging and remote sensing, the need developed to account for the atmospheric influence on such systems, and to improve, in particular, knowledge of the atmospheric extinction due to gas absorption and to scattering and absorption by aerosol particles. Gas absorption has been studied thoroughly and can now be calculated from meteorological variables with satisfying accuracy (1). Models of the aerosol extinction need considerable improvement, however, particularly for IR radiation.

The potential of obtaining statistical descriptions of optical extinction from available weather statistics has motivated us to seek a relationship between the aerosol extinction and ordinary meteorological variables such as visibility, humidity, and air mass type. We attempt to model the dependence of aerosol extinction on these variables by accounting for their influence on size distribution and refractive index of aerosol particles, calculating the extinction from Mie theory. The model will be fitted to results obtained through measurements with a multiwavelength transmissometer OLA (Optical Link in the Atmosphere) and simultaneous monitoring of meteorological variables.

Theoretical models

The aerosol extinction of optical waves can be calculated from the Mie theory assuming spherical particles of given size distribution and refractive index. A proper choice of size distribution is generally more critical and difficult than the choice of refractive index.

Recent measurements by Whitby (2) and others have revealed a structure in the size spectra which generally may be divided into three modes, each of which can be fitted by a log-normal distribution. Only the two larger modes, the accumulation and the coarse particle mode, seem to be relevant for optical calculations.

The bimodal model offers several advantages over the more simple power law distribution for calculating atmospheric scattering and extinction. Most important is that it seems to fit measured particle spectra closer than other models and allows a distinction between the optical properties of particles of different origin and thus belonging to different modes. Moreover the use of a log-normal size distribution eliminates the choice of a proper integration interval and permits analytical relationships between distribution parameters and aerosol extinction. Therefore it becomes possible to determine these parameters by mathematical inversion (3). If the particle growth due to increasing relative humidity is independent of radius, its effect on the extinction can easily be estimated for log-normal distributions since this simply corresponds to a translation along the r_m/λ -axis.

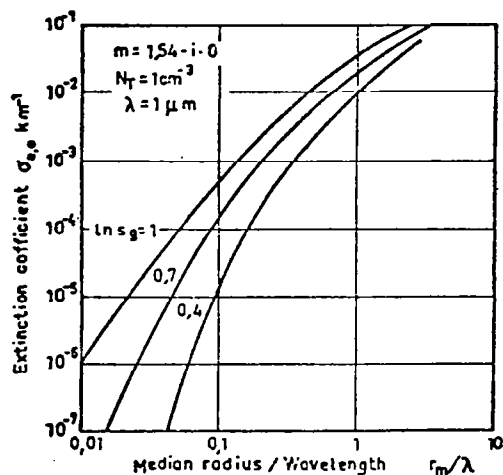


Fig 1. The normalized extinction coefficient $\sigma_{e,0}$ for log-normal particle distributions.

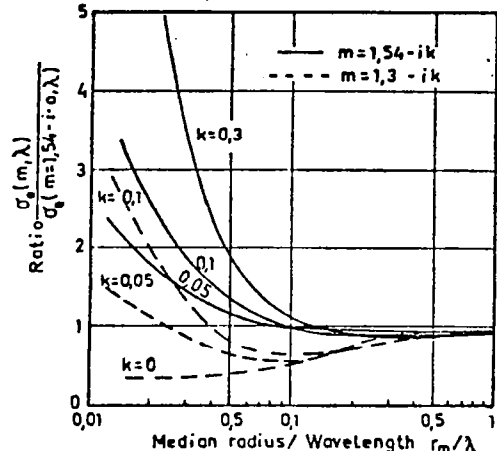


Fig 2. The extinction coefficient for a log-normal distribution with $\ln sg = 0.7$ and a refractive index different from $m = 1.54 - i \cdot 0$.

Fig 1 shows the dependence of the extinction coefficient $\sigma_{e,0}$ on the ratio r_m/λ for different values of $\ln sg$, the standard deviation of $\ln r$. The $\sigma_{e,0}$ value is normalized to a total number $N_T = 1 \text{ cm}^{-3}$ and $\lambda = 1 \mu\text{m}$. Scaling to other values is given by $\sigma_e = \sigma_{e,0} \cdot N_T \cdot \lambda^2$, and this expression may be used together with the curves of fig 1 to obtain the wavelength dependence.

The effect of changing the refractive index to other values than $m = 1.54 - i \cdot 0$ is greatest for small particles according to fig 2.

Taking typical values from measured particle distributions (2) it turns out from fig 1 and 2 that the transmission for visible wavelengths is mainly determined by the accumulation mode and the IR transmission by the coarse mode with the exception for maritime aerosols where only the coarse mode seems relevant.

Transmissometer OLA

The transmissometer is a folded path system with a blackbody radiation source and the detecting system at one terminal and a reflector at 500 m distance. A reference beam is used to compensate for source and receiver instability. The system is designed for the wavelength region 0.5 - 15 μm and measures the extinction at 15 filter wavelengths within this band. The filter bandwidths are approximately 3 % of the transmission wavelengths. The principle is shown in figure 3.

A measurement beam and a reference beam are generated from the 1600 K Globar radiation source, and modulated at $f_M = 16$ and $f_R = 20 \text{ Hz}$, respectively, by a chopper with two slit circles. The measurement beam is collimated and directed at the reflector, which consists of a spherical mirror with a secondary plane mirror in its focal plane.

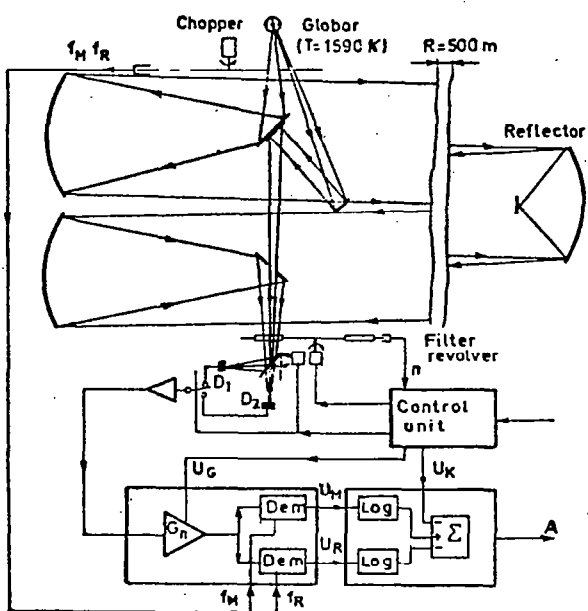


Fig 3. Principle of OLA transmissometer.

The detector generates two signals with frequencies f_M and f_R and amplitudes proportional to the beam powers P_M and P_R . Both amplitudes are proportional to the same source radiance, filter bandwidth, filter transmission and detector sensitivity, but the measurement beam is attenuated by the atmosphere.

The signals are amplified in a gain controlled amplifier and detected separately in synchronous demodulators. The amplitudes U_M and U_R are low-pass filtered and fed to logarithmic amplifiers, whose outputs are fed to a summation amplifier together with a calibration voltage $U_{K\lambda}$, which is generated in the control unit for each filter position. The output voltage is proportional to the attenuation of the measurement beam:

$$A_\lambda = -10 \log^{10} \left(\frac{P_{M\lambda}}{P_{R\lambda}} K_\lambda \right) \quad (\text{dB})$$

where K_λ is a calibration factor corresponding to the voltage $U_{K\lambda}$.

Calibration and estimation of accuracy

Calibration is performed in weather with low extinction and corrections are made for the atmospheric attenuation. The aerosol extinction at 0.5 μm is measured with a nephelometer and estimated at other wavelengths. Normally these extinctions are very low. Absorption by water vapor is calculated from the Lowtran 3 model (1). Absorption due to other gases is regarded as a system constant. Finally, the calibration potentiometer for each filter is adjusted so that the correct attenuation output is obtained.

Measured data are corrected for gas absorption as above and thus the aerosol attenuation $A_{a\lambda}$ is obtained. The aerosol extinction coefficient is obtained from

After passing through the atmosphere a part of the beam reaches the receiver and is focused on one of two detectors through one of 15 filters in a filter revolver. The reference beam passes via an aperture through the same filter on to the same detector. Its intensity is adjusted to be approximately the same as for the measurement beam without attenuation. During a measurement sequence the filter revolver is turned stepwise and stopped at the filter positions for signal integration. For wavelengths below 1 μm a silicon detector (D_1) is used. For longer wavelengths the beams are shifted to a pyroelectric detector (D_2).

$$\sigma_\lambda = (\ln 10 / 20R) A_{a\lambda} \quad (\text{m}^{-1})$$

where R is the path length.

The accuracy of the measured σ -values is limited by essentially two factors: deviations Δt in the system transmission, and noise in the detected signal. The standard deviation of the measured power P_M can be written $\Delta P_M = \Delta t P_M + N$ and the relative error in σ

$$\left| \frac{\Delta \sigma}{\sigma} \right| = \frac{1}{2R\sigma} \left[\Delta t + \frac{N}{P_0} \exp(2R\sigma) \right]$$

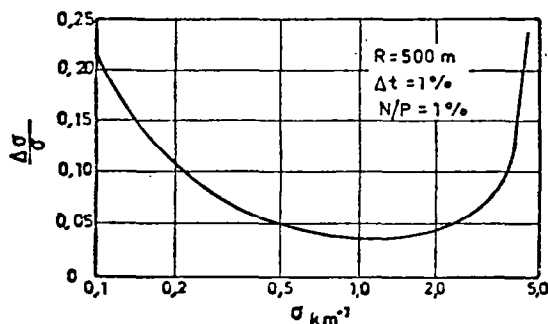


Fig 4. Calculated relative error for OLA.

Preliminary results

When this was written only a few measurements in turbid air had been obtained.

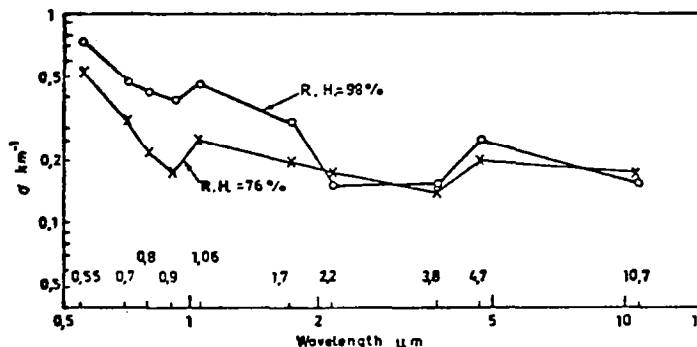


Fig 5. Examples of measured σ -values.

References

- (1) Selby J E A and Mc Clatchey R A; Atmospheric transmittance from 0.25 to 28.5 microns. Computer code Lowtran 3. AD/A 017 734, 1975.
- (2) Whitby K T; Modeling of atmospheric aerosol particle size distributions, Particle Technology Laboratory, Univ. of Minnesota, April 1975.
- (3) Heintzenberg J and Baker M; Appl. Optics, 5, 1178, 1976.

where N is noise equivalent power and P_0 is the received power with no atmospheric attenuation. In fig 3 $(\Delta\sigma/\sigma)$ is shown as a function of σ for $R=500$ m with errors Δt and $N/P_0=10^{-2}$, which approximately apply to the OLA transmissometer. The figure shows that σ -values within the interval $0.2-3 \text{ km}^{-1}$ are obtained with errors less than 10 %.

ATMOSPHERIC ALBEDO CHANGES MEASURED IN THE MT. SUTRO TOWER
AEROSOL AND RADIATION STUDY*

Philip B. Russell and Edward E. Uthe

Stanford Research Institute
Menlo Park, California 94025, U.S.A.

The purpose of the Mt. Sutro Tower Aerosol and Radiation Study is to document changes in atmospheric albedo and in radiative heating profiles caused by changes in atmospheric aerosol content. Albedo and radiative heating measurements are emphasized because numerous modeling studies have shown that these are two primary links between aerosol particles and climate.

Albedos and heating profiles are derived from continuous measurements of upward and downward solar irradiance made by three pairs of pyranometers mounted on the Mt. Sutro Tower as shown in Figure 1. Simultaneously,

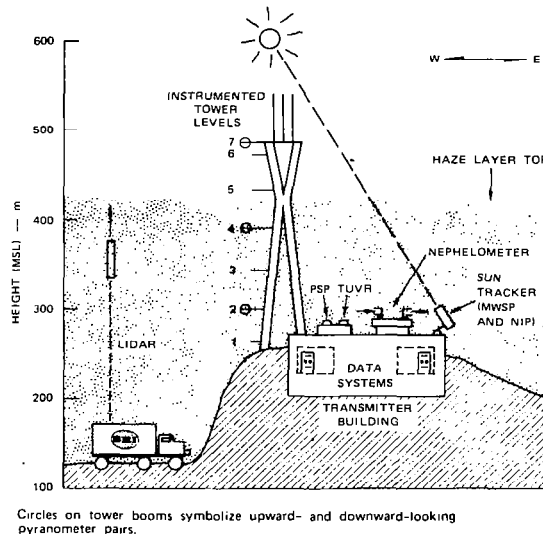


Figure 1 Arrangement of Instruments in the 1975 Field Program, Mt. Sutro Tower Aerosol and Radiation Study.

*Research supported by the Atmospheric Sciences Section, National Science Foundation, and by the Office of Research Operations, Stanford Research Institute.

measurements at the tower base document aerosol layer properties and near-surface radiation. The instruments and their measurements are:

<u>Instrument</u>	<u>Measurement</u>
Integrating nephelometer	Local aerosol scattering coefficient
Total ultraviolet radiometer	Downward ultraviolet irradiance
Pyranometer	Downward solar irradiance
Pyrheliometer	Direct solar radiance
12-channel sunphotometer	Multiwavelength aerosol and water vapor optical thickness

The SRI Mark IX Mobile Lidar System¹, parked downhill from the tower, continuously documents the aerosol layer top and vertical structure with respect to the tower-mounted pyranometers. (Because of the prevalent subsidence inversion at the tower, the urban-marine aerosol layer is usually confined below the tower top--see below.) Extensive meteorological and ozone measurements are made on the tower by San Jose State University.²

An example of an atmospheric albedo change associated with increased aerosol content was observed on 16 October 1975. As shown in Figure 2(a), a peak in local scattering coefficient and in the diffuse-to-direct ratio of solar radiation occurred at the tower base at 1200 PDT. A simultaneous peak in atmospheric aerosol optical thickness was observed by the sunphotometer (Figure 2(b)). The lidar data (Figure 3) show that essentially all of the optical thickness increase was confined below tower Level 7, and that most of it was confined below tower Level 4.

Figure 2(c) shows the "sector albedos"^{*}, α_2 and α_4 , measured on Levels 2 and 4, respectively (Level 7 was not functioning properly). The major features in the diurnal variation of α_2 and α_4 are determined by surface characteristics (viewed area, hill slope, trees, etc.), and are the same on all days, independent of aerosol concentrations. However, the two small peaks in α_2 and α_4 at 1200 PDT are unique to 16 October and are attributable to the coincident peaks in aerosol content documented in Figures 2(a), 2(b), and 3.

^{*}The sector albedos--ratios of measured upward-to-downward irradiance--differ from hemispheric albedos A because a 70° sector of each pyranometer was covered to prevent measurement of reflections from the tower. Because of this $\alpha \approx 0.8 A$ after about 1100 PDT.

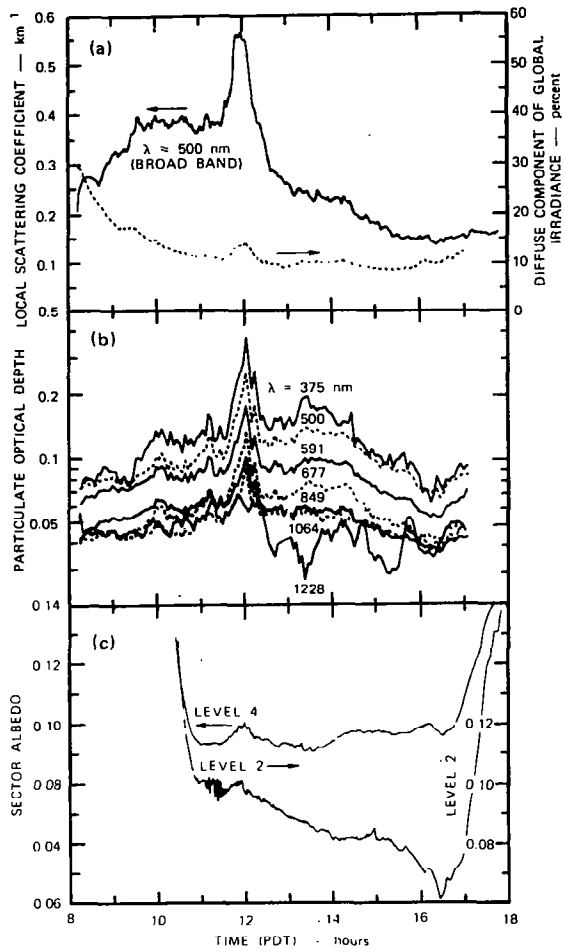


Figure 2(a) Local Scattering Coefficient and Diffuse-to-Direct Ratio, (b) Particulate Optical Depths, and (c) Sector Albedos Measured at Mt. Sutro, 16 October 1975.

The data in Figures 2(a), 2(b), and 3 indicate that the mid-visible particulate optical thickness increase $\Delta\tau_p$, between Level 4 and the tower base, occurring between 1130 and 1200 PDT, was about 0.07. As shown in Figure 4, the measured albedo change on Level 4 ($\Delta\alpha_4 \approx 0.008$, $\Delta A_4 \approx 0.010$) is consistent with theoretical predictions based on the scattering computations of Cadle and Grams³ and the simple albedo-change expression discussed by Russell and Grams.⁴

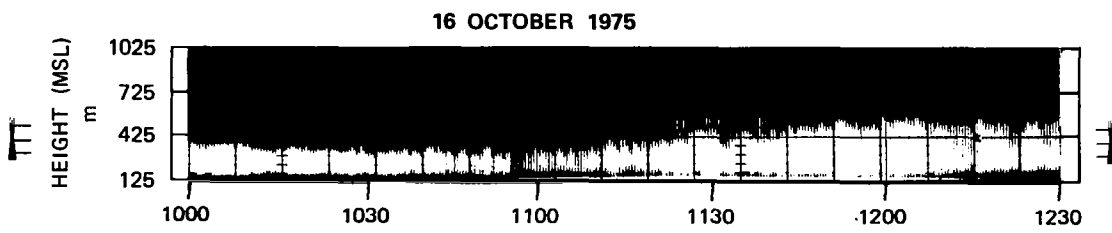


Figure 3 Intensity-Modulated Display of Haze Structure Observed by Lidar at Mt. Sutro, 16 October 1975. (Horizontal tick marks on tower symbols indicate heights of booms 2, 4, and 7.)

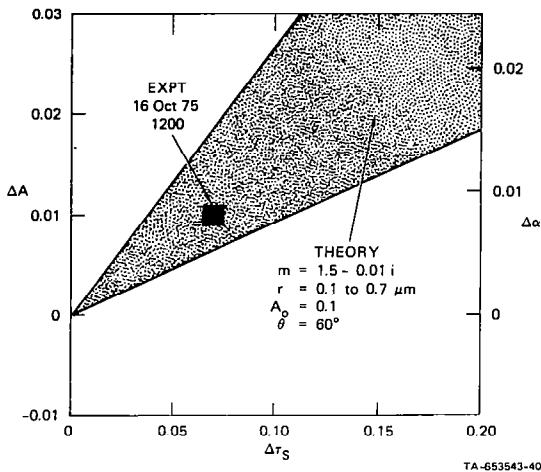


Figure 4 Comparison of the Albedo Change Measured on Level 4 at 1200 PDT, 16 October 1975, with Theoretical Predictions Based on References 2 and 3.

If the aerosol layer observed on 16 October 1975 persisted worldwide, the results could be climatically significant. Simple, globally averaged computations⁴ predict that such a layer would decrease solar energy input to the earth-atmosphere system by 0.0 to 0.7%, and would decrease input to the surface³ by 0.5 to 2.3%. Several models⁵ predict major changes in global ice and snow cover for energy changes of this size.

Of course, the aerosol concentrations of 16 October 1975, though not extreme for urban locations, are not typical of global conditions. The continuing Sutro Tower Aerosol and Radiation Study will document typical aerosol concentrations at the tower and their actual effects on albedo and radiative heating, so that conclusions of climatic significance can be drawn.

REFERENCES

1. Utthe, E.E., Allen R.J., Opt. Quantum Electronics, 7, 121-129 (1975).
2. Miller, A., Bull. Amer. Meteor. Soc., 56, 52-55 (1975); Report, February 1976, Dept. of Meteor., San Jose State University, San Jose, California 95192.
3. Cadle, R.D., Grams, G.W., Rev. Geophys. Space Phys., 13, 475-501 (1975).
4. Russell, P.B., Grams, G.W., J. Appl. Meteor., 14, 1037-1043 (1975).
5. Sellers, W.O., J. Appl. Meteor., 8, 392-400 (1969), and Op Cit., 12, 241-254 (1973); Chylek, P., Coakley, J.A., Jr., Atmos. Sci., 32, 675-679 (1975).

Multiple Scattering in Thick Layers, H. C. van de Hulst, Rijksuniversiteit
Leiden, Leiden, Nederland

(Abstract and Summary not available.)

Meeting on Atmospheric Aerosols, Their Optical Properties and Effects.
 Williamsburg, Virginia - December 13-15, 1976

Review of Radiative Transfer Methods in Scattering Atmospheres

Jacqueline LENOBLE

Laboratoire d'Optique Atmosphérique - Université de Lille I
 B.P. 36 - 59650 Villeneuve d'Ascq - France

-.-.-.-

The transfer of radiation in the real atmosphere is mainly controlled by the scattering properties of air molecules, aerosols and cloud droplets. Using the usual notations for the optical parameters of the atmosphere and for the radiation field, the general equation of transfer for the monochromatic radiance I can be written

$$\hat{\Delta}I(\vec{r}, \vec{\Omega}) = K(\vec{r}) \left\{ I(\vec{r}, \vec{\Omega}) - \frac{\bar{\omega}(\vec{r})}{4\pi} \int \int p(\vec{r}; \vec{\Omega}; \vec{\Omega}') I(\vec{r}, \vec{\Omega}') d\omega' \right\} ; \quad (1)$$

here we have neglected the polarization and the thermal emission.

1 - Plane parallel homogeneous atmosphere

The simplest problem consists of an atmosphere limited by two parallel and infinite planes, uniformly illuminated on its upper boundary by the solar beam and above an homogeneous ground ; the atmosphere is called homogeneous if only the extinction coefficient K is function of the altitude z .

A great deal of work has been devoted to this case and the various methods can be roughly classified into three groups.

Exact analytical methods

We understand by exact analytical methods the methods leading to a solution in terms of mathematical functions, which have finally to be tabulated ; therefore the accuracy of these methods may be not better than the accuracy of more direct numerical methods. Their main interest is in the understanding of the mathematical structure and of the general behaviour of the solutions. Their basic drawback is the difficulty to use these methods in the case of a real atmosphere. Among these methods we will classify the singular eigenfunctions (or Case) method, the Wiener - Hopf method and the reduction to H , or X - and Y - functions.

Computational methods

We understand here methods specifically designed for computers, but they may include some analytical treatment before the numerical procedure. The more directly numerical methods are the Monte Carlo and the Dart Method but their main interest is not in the plane parallel case, but in the more complex ones. The spherical harmonics and the discrete ordinates methods use discretizations

of the transfer equation, whereas the successive orders of scattering and the Gauss-Seidel methods use iteration procedures. The matrix operator, the adding (or doubling) and the invariant imbedding use interaction principles to express the reflection and transmission functions of a layer. Finally the asymptotic method is an analytical solution valid in the case of very thick layers.

Approximate methods

These methods include a very rough approximation of the atmospheric properties and (or) of the transfer problem. They are generally used only for the fluxes and their main interest is to give simple analytical expressions. In this group we find the Eddington, two-stream, similarity and exponential Kernel methods.

2 - Realistic atmospheres

In many cases, the inhomogeneity of the actual atmosphere has to be taken into account. Most of the methods reviewed for the homogeneous case can be applied to the vertically inhomogeneous atmosphere ; but the advantage in computation time of the fastest methods often disappears.

The horizontal inhomogeneity may be due either to the inhomogeneity of the ground, or to the inhomogeneity of the atmosphere itself (finite clouds). Then the equation of transfer takes a much more complex form and until now only the Monte Carlo method has been successfully applied to this case.

In some cases sphericity of the planetary atmosphere cannot be neglected and this is specially important in remote sensing problems (inverse problems) which use twilight measurements or limb scanning from satellites. The Monte Carlo method applies without further difficulties and the Dart method has been specially developed for this problem. Some promising analytical methods have been tried but they are at their very beginning.

Finally all the methods we have described concern monochromatic radiation. If we have to deal with scattering and gaseous absorption, we will have to treat the monochromatic problem for a great number of wave lengths even in a spectral interval containing a single line. Therefore global methods have been sought, in order to save computation time ; they generally use the path length distribution of the scattered photons.

Extending Radiative Transfer Models By Use of Bayes' Rule

by

Cynthia Whitney
C. S. Draper Laboratory, Inc.
Cambridge, MA 02142

I. Introduction

Computer modeling of radiative transfer is a vital tool in the analysis of experimental data concerning aerosols. But there is currently a certain degree of mismatch between the techniques available and the problems presented. The majority of techniques are appropriate for a flat atmosphere. Examples include successive orders of scattering, matrix operator, doubling Gauss-Sidel iteration, discrete ordinates, and spherical harmonics⁽¹⁾. But the problems of interest often require more than a simple flat atmosphere. Examples include twilight and limb scan simulations. These problems are difficult because atmospheric curvature and layering cannot be excluded from the computation. Furthermore the output twilight and limb scan radiances often cover several orders of magnitude within a few degrees of illumination or scan direction variation, and small details appear in correspondence with layers in the atmosphere. At present, the only techniques available for dealing with such problems are Monte Carlo simulation and the DART technique⁽¹⁾.

This paper presents a procedure for extending the more restricted radiative transfer techniques to more general problems such as those involving curvature. The procedure is borrowed from the DART model, which was the first to use it. The procedure exploits a mathematical similarity between some quantities that appear in radiative transfer modeling and some quantities that appear in probability theory.

2. The Radiative Transfer Problem

The general problem is to determine the radiance (or more generally the Stokes' vector) S , expressed as a function of propagation direction \hat{k} and position ξ . The function S is governed by the intego-differential equation of radiative transfer. At best, the computer simulation of this equation provides only an approximation to S . This is the case because \hat{k} and ξ are continuous variables, so the function S comprises an uncountable infinity of numbers. Since the computer can only manipulate finite sets of numbers, the radiance has to be approximated by a finite set of numbers.

The numbers in the finite set representing the radiance have different physical meaning in different radiative transfer models. There are essentially four types of numbers used by the existing radiative transfer modeling techniques. They are all obtained by integrating the radiance over solid angles, but with different weighting functions in the integrals.

In the first case, the unit sphere of \hat{k} 's is simply partitioned into small solid angle regions and the weighting function is 1 within a particular region. This simple connecting rule is commonly used in the Monte Carlo, successive orders of scattering, matrix operator, doubling, and Gauss-Sidel iteration methods.

For the second case, a spherical coordinate system with z axis normal to the plane of the flat atmosphere is defined. The discrete numbers used are the Fourier coefficients for expansion in azimuth of the radiance integrated over a band of zeniths. This formulation is used in the discrete ordinates method, and often in conjunction with the matrix operator technique.

For the third case, the radiance is Fourier expanded in azimuth and Legendre polynomial expanded in zenith. This constitutes the spherical harmonics approach.

For the fourth case, the weighting function is highly peaked around a particular propagation direction, and falls away continuously to zero as a power of the cosine of the angle between \hat{k} and the particular propagation direction. This weighting function is used in the DART approach.

To discuss the four cases listed above, we need a common notation for describing them. Although they differ in detail, the discrete numbers in all cases come out in units of irradiance and can be called "streams" in all cases. For identifying the streams, the first case suggests a particularly simple notation. We can let a vector \hat{p} identify a particular propagation direction associated with a solid angle region, and use \hat{p} as a subscript to identify the stream associated with that solid angle. The stream is represented by $S_{\hat{p}}$. To use this notation in general, we have to modify the interpretation of \hat{p} in the other cases. In the discrete ordinates case, we let the θ coordinate of \hat{p} identify the band in zenith which is integrated over. Then we let the ϕ coordinate of \hat{p} identify the Fourier index. In the spherical harmonics case we let the \hat{p}_{ϕ} identify the Fourier index and \hat{p}_{θ} identify the Legendre index. In the DART case we let \hat{p} be the vector location of the peak in the weighting factor.

The essential fact of computer simulation is that it produces only a finite array of streams ($S_{\hat{p}}$'s) where a complete function $S(\hat{k})$ is desired. Thus it presents the following general problem: given an array of streams, estimate the radiance function.

The solution to the general problem stated will be based on analogies. The important point to note about $S(\hat{k})$ is that, apart from an overall scale factor of dimension Watt/(cm² - steradian - wavelength), it is like a probability density function. That is, it expresses the density of probability that \hat{k} is the propagation direction of a random photon traveling through point \hat{x} . The domain of this probability density function is 4π steradians. Similarly, the important point to note about $S_{\hat{p}}$ is that it is proportional to a probability. It expresses the probability that a photon traveling through location \hat{x} is counted in the stream identified by \hat{p} . The domain of this probability function is the countable number N of streams.

3. The Probabilistic Solution

Bayes' Rule is the tool used to solve the hypothetical problem from probability theory: given two random variables which are theoretically correlated, and given a probability density function for one of them, estimate the probability density function for the other one.

Bayes' Rule is a relationship between conditioned probabilities and unconditioned (prior) probabilities. Let a and b represent values of two random variables α and β . The various probabilities concerning α and β are all designated by a "p" for "probability", so it is helpful to distinguish them by subscripts involving α and β . Using a slash to denote conditioned probability and a subscript zero' to denote prior estimate of probability, we write Bayes' Rule

$$p_{\alpha/\beta}(a/b) = p_{0\alpha}(a) p_{\beta/\alpha}(b/a) / p_{0\beta}(b)$$

Application of Bayes' Rule allows one to improve the accuracy of an arbitrary prior estimate for a distribution for α by incorporating information obtained by sampling β . Let $p_{0\alpha}(a)$ be the prior estimate of the desired function. Then $p_{\alpha/\beta}(a/b)$ is the posterior estimate of it, obtained by incorporating the fact that $\beta = b$. The incorporation requires that the conditioned probability $p_{\beta/\alpha}(b/a)$ be formulated from a theoretical model. The $p_{0\beta}(b)$ is then formulated in turn as

$$p_{0\beta}(b) = \int p_{\beta/\alpha}(b/a) p_{0\alpha}(a) da$$

Bayes' rule for updating $p_{0\alpha}(a)$ is thus

$$p_{\alpha/\beta}(a/b) = \frac{p_{0\alpha}(a) p_{\beta/\alpha}(b/a)}{\int p_{\beta/\alpha}(b/a) p_{0\alpha}(a) da}$$

Suppose now that the information to be incorporated is not just a single value $\beta = b$, but rather a probability distribution for β , $p_\beta(b)$. Then the best posterior estimate for the distribution for β is the average over b values of the individual $p_{\alpha/\beta}(a/b)$ functions:

$$p_\alpha(a) = \int p_{\alpha/\beta}(a/b) p_\beta(b) db$$

Substituting in the definition of $p_{\alpha/\beta}(a/b)$ we obtain

$$p_\alpha(a) = p_{0\alpha}(a) \int \left[\frac{p_{\beta/\alpha}(b/a) p_\beta(b)}{\int p_{\beta/\alpha}(b/a) p_{0\alpha}(a) db} \right] db$$

This is the equation which is adapted to solve the radiative transfer problem.

4. The Radiative Transfer Solution

Adapting the probabilistic solution to the radiative transfer problem requires that the proper analogs be identified. They are as follows:

- (1) The variable a becomes the continuous propagation direction \hat{k} .
- (2) The variable b becomes the discrete stream label \hat{p} .
- (3) the estimated function $p_\alpha(a)$ becomes the desired radiance function $S(\hat{k})$.
- (4) The prior estimate function $p_{0\alpha}(a)$ becomes a prior estimate of the radiance $S_0(\hat{k})$.
- (5) Integration over continuous variable b becomes summation over the discrete \hat{p} .
- (6) The measured function $p_\beta(b)$ becomes the array of streams $S_{\hat{p}}$ generated by a discrete radiative transfer simulation.
- (7) The theoretical connecting function $p_{\beta/\alpha}(b/a)$ becomes the weighting function connecting \hat{k} and \hat{p} . It is different for each radiative transfer model, but can be represented in general as $w(\hat{p}/\hat{k})$.

The radiative transfer solution is obtained by substituting the above analogs in the probabilistic solution. Taking account of the fact that $w(\hat{p}/\hat{k})$ is not necessarily normalized as $p_{\beta/\alpha}(b/a)$ is, we put

$$S(\hat{k}) = \frac{S_0(\hat{k})}{\sum_{\hat{p}} w(\hat{p}/\hat{k})} \sum_{\hat{p}} \left[\frac{w(\hat{p}/\hat{k}) S_{\hat{p}}}{\int_{4\pi} w(\hat{p}/\hat{k}) S_0(\hat{k}) d^2 \hat{k}} \right]$$

To evaluate $S(\hat{k})$ for particular cases, we must specify the function $w(\hat{p}/\hat{k})$ that corresponds to each stream definition that is used. For the simple case common to most of the radiative transfer models $w(\hat{p}/\hat{k})$ is simply 1 for \hat{k} inside the solid angle region specified by \hat{p} . For the discrete ordinates case,

$$w(\hat{p}/\hat{k}) = \frac{1}{2\pi} \cos[m(\phi - \phi_0)]$$

for θ inside the band specified by \hat{p}_θ . For the spherical harmonics case,

$$w(\hat{p}/\hat{k}) = \frac{1}{4\pi} \cos[m(\phi - \phi_0)] P_M^m(\mu)$$

where μ is $\cos(\theta)$. For the DART case

$$w(\hat{p}/\hat{k}) = (\hat{p} \cdot \hat{k})^n$$

5. Application to Non Flat Atmospheres

The simulation of radiative transfer in a curved atmosphere is a natural application for Bayesian estimation. Use of the method allows incorporation of the curvature through the prior estimate $S_0(k)$, so that the discrete computer simulation can be done solely for a flat atmosphere. This means that existing techniques for handling the discrete equation can be used directly without the necessity for any generalization.

The incorporation of curvature in the overall transfer simulation is mainly a matter of producing results with realistic features: variation of the radiance over several orders of magnitude within a few degrees of variation in illumination or scan direction, and appearance of significant details due to atmospheric layers over even smaller angular ranges. The dynamic range and angular resolution required in the final solution is conveyed in the prior estimation function $S_0(k)$. The discrete streams are used to carry information about absolute amount of flux and angular shaping due to phase functions.

To apply the method, one must formulate a prior estimate function $S_0(k)$. A simple procedure for doing this is to make use of information obtained by simulating just single scattering in the curved atmosphere. The single scattering solution has all the features of dynamic range and angular resolution required in the final total solution. Furthermore, it is generally easy to calculate with both accuracy and speed, regardless of realistic features that make multiple scattering so difficult to compute.

As a first cut, it would be very reasonable to set $S_0(k)$ simply equal to the single scattering result, except with phase function factors deleted. Experience with the DART model has shown that this is fairly good as judged by comparison to Monte Carlo simulations. Some simple modifications make it even better. In calculating the prior estimate, it is advantageous to delete a fraction of optical depths that can be attributed to extreme forward scattering. It is also advantageous to neglect extinction prior to scattering into the scan direction. Using these techniques, it is possible to use the DART method with only twelve streams and produce results which are indistinguishable from benchmark Monte Carlo results.

On the basis of such evidence, it is believed that eventually excellent results in a curved atmosphere can be expected from any of the currently available flat radiative transfer models when fully adapted to the problem.

Reference:

Standard Procedures to Compute Atmospheric Radiative Transfer In A Scattering Atmosphere, Vol. I, ed. J. Lenoble (IAMPA Radiation Commission, 1975).

AN IMPROVED DIFFUSION APPROXIMATION TO RADIATIVE TRANSFER
IN ATMOSPHERES AND CLOUDS

W. E. Meador and W. R. Weaver
NASA, Langley Research Center, Hampton, VA 23665

A new diffusion model has been developed for determining radiative transfer in particulate media, including atmospheres with clouds and aerosol layers. The principal merits of diffusion approximations to the multiple scattering of light are the following: they provide adequate solutions of a number of problems involving complex geometries and boundary conditions for which solutions of the more detailed radiative transfer equation are intractable; and, at least for simple geometries, they provide closed-form analytic results that are especially desirable as parts of large programs for atmospheric sensing and heat-balance studies. A deficiency that severely limits the general applicability of standard diffusion methods to photon transport is their inability to describe the effects of phase functions (i.e., scattering laws) more complex than linear anisotropic, whereas cloud and aerosol phase functions correspond to Mie scattering with sharp forward peaks. Another deficiency is that standard models are invariably formulated such that the contribution to the net flux of diffuse photons by the anisotropic part of the scattering of the incident beam is neglected. The required addition to Fick's law, which credits the net flux entirely to density gradients and ignores scattering of the incident beam into preferred directions, has never been discussed.

An objective of the present research was to extend the applicability of diffusion methods to the complex phase functions associated with clouds and aerosol layers, while simultaneously including the proper effects of these complexities on the generation (and subsequent flux) of diffuse photons from incident beams. This was accomplished by a judicious definition and mathematical

analysis of diffuse photons, as distinguished from those of the attenuated beam, and by the assumption of a simple all-encompassing phase function that reasonably approximates actual scattering all the way from isotropic to needle shaped. A modified diffusion equation was then obtained by combining these assumptions with the radiative transfer equation, which procedure also gave the corresponding modified Fick's law relating the flux and number-density gradient of diffuse photons and including the contribution to flux from asymmetric scattering of the incident beam. The results make diffusion models applicable for the first time to the important transition region in which an incident beam is diffused.

Figures 1 and 2 illustrate the accuracy of the new model (solid curves) compared with exact results (dots) and with standard diffusion methods (dashed curves) for the reflectance (plane albedo) R of a normally illuminated plane-parallel scattering material of optical thickness τ' . Two values of the single-particle albedo ω_0 appear in each plot, the first plot corresponding to isotropic scattering (asymmetry factor $g = 0$) and the second to sharp forward scattering as represented by a Henyey-Greenstein phase function with $g = 0.75$. Similar accuracy is expected for more complex geometries (e.g., finite clouds) and for transport of particles other than photons (e.g., neutrons and electrons).

Reference:

Meador, W. E.; and Weaver, W. R.: An Improved Diffusion Approximation to Radiative Transfer in Atmospheres and Clouds. To be submitted to J. Atmos. Sci. (1976).

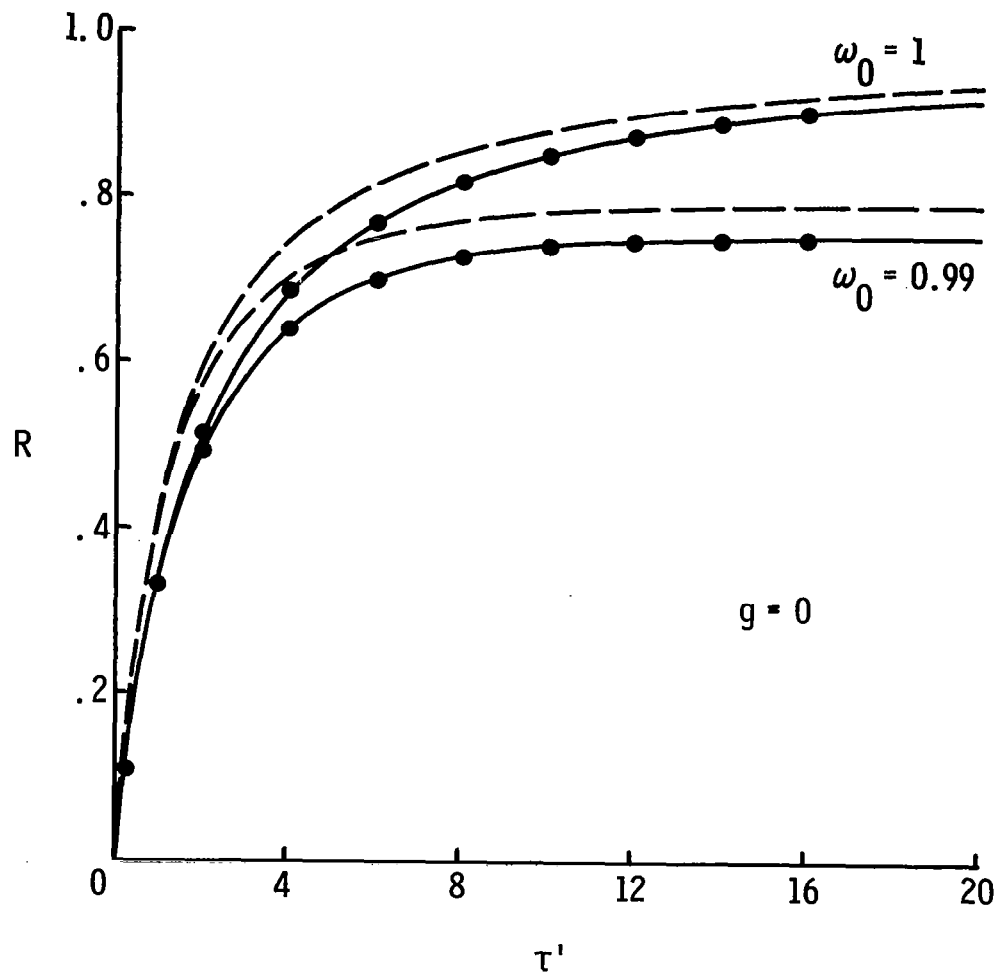


Figure 1.- Reflectance for normal incidence on a plane-parallel layer of optical thickness τ' for isotropic scattering ($g = 0$) and two values of single-particle albedo ω_0 . Solid curves: new diffusion model; dashed curves: standard diffusion model; dots: exact results.

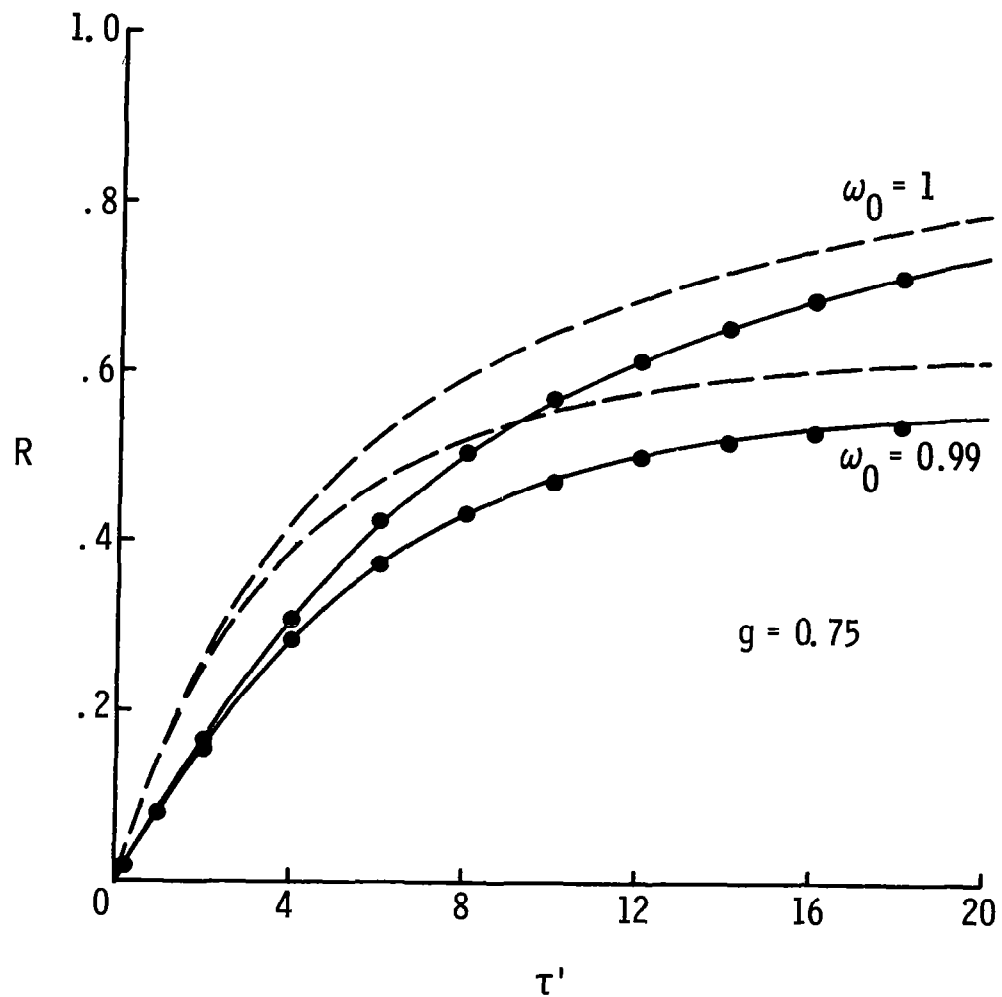


Figure 2.- Same as Fig. 1 except Henyey-Greenstein scattering with $g = 0.75$ (sharply peaked in forward direction).

A SOLUTION TO THE RADIATIVE TRANSFER EQUATION EMPLOYING
A SEMI-ANALYTIC INTEGRATION OVER OPTICAL DEPTH

Benjamin M. Herman

Institute of Atmospheric Physics
University of Arizona
Tucson, Ariz. 85721

In the past 10 years, several techniques have been developed for solving the equation of radiative transfer in its complete form, that is, including all orders of scattering. In its most general form, this equation involves integration of a source term over three variables, two angular coordinates and optical depth. Various schemes have been employed to perform these integrations, most of which have been numerical in nature. Recently (Dave et al., 1970; Breslau et al., 1973; Herman et al., 1975) expansions in terms of Legendre Polynomials have been employed which enable the integration over the azimuthal angle to be performed analytically. Even more recently Dave et al. (1974) have demonstrated a technique employing expansions in both the azimuthal and polar angles which allows analytic integrations to be performed over both angular coordinates. To date, only numerical schemes have been employed for the integration over optical depth.

In this work, a technique will be demonstrated which allows for what is called a semi-analytic integration over optical depth, τ . The technique employs functional curve fitting to the intensity field as a function of τ in a given direction. This procedure is made feasible because of the smooth character of the distribution of intensity with τ for optically thick atmospheres, except near the atmospheric boundaries. This smoothness makes it possible to describe the intensity with integrable functions over relatively large increments of optical depth. Analytic integrations may then be performed over these large increments of τ .

The above procedure enables rapid calculations to be performed for optically thick atmospheres which previously consumed large amounts of computer time with the Gauss-Seidel technique, and also by most other methods. Complete flexibility in so far as form of phase matrix and vertical inhomogeneities is still maintained, while the accuracy over straight numerical integrations is improved.

Results employing this new technique will be presented, and comparisons with the original Gauss-Seidel solution scheme employing numerical integration over optical depth will be presented.

References

Breslau, N., and J. V. Dave, 1973: Effect of aerosols on the transfer of solar energy through realistic model atmospheres. Part I: Non-absorbing aerosols. J. Appl. Meteor., 12, 601-615.

Dave, J. V., and J. Gazdag, 1970: A modified Fourier transform method for multiple scattering calculations in a plane parallel atmosphere. Appl. Opt., 9, 1457-1466.

Dave, J. V., and J. Canosa, 1974: A direct solution of the radiative transfer equation: Application to atmospheric models with arbitrary vertical nonhomogeneities. J. Atmos. Sci., 31, 1089-1101.

Herman, B. M., and S. R. Browning, 1975: The effect of aerosols on the earth-atmosphere albedo. J. Atmos. Sci., 32, 1430-1445.

RADIATIVE TRANSFER FOR IMAGING PURPOSES

BRUCE W. FOWLER

Advanced Systems Concepts Office, US Army Missile Research, Development, and Engineering Laboratory, US Army Missile Command, Redstone Arsenal, AL 35809
and

Smoke/Aerosol Working Group, Joint Technical Coordinating Group/Munitions Effectiveness

The theory of Radiative Transfer (RT) has been well developed by Chandrasekhar and others.¹ These developments have been largely limited to problems involving stellar or planetary atmospheres where inhomogeneities in the extinction medium are limited to one dimension. Specifically, the medium is limited to be either plane- or spherical-parallel so that the variations in the intensity function are limited to being normal to the parallel surfaces. In the former case, the general equation of RT,

$$\mathbf{k} \cdot \nabla I(\mathbf{r}, \mathbf{k}) = -\alpha(\mathbf{r}) I(\mathbf{r}, \mathbf{k}) + \frac{\omega(\mathbf{r}) \omega(\mathbf{r})}{4\pi} \int p(\mathbf{k}, \mathbf{k}') I(\mathbf{r}, \mathbf{k}') d^2 \mathbf{k}' , \quad (1)$$

where \mathbf{k}, \mathbf{k}' are unit propagation vectors,

\mathbf{r} is the position vector,

$I(\mathbf{r}, \mathbf{k})$ is the intensity at \mathbf{r} along the direction \mathbf{k} ,

$\alpha(\mathbf{r})$ is the extinction coefficient at \mathbf{r} ,

$\omega(\mathbf{r})$ is the single scattering albedo at \mathbf{r} , and

$p(\mathbf{k}, \mathbf{k}')$ is the single scattering phase function, not necessarily position independent, may be cast into the form,

$$\frac{\partial I}{\partial \tau}(\tau, \mu) = -I(\tau, \mu) + \frac{\omega}{2} \int p(\mu, \mu') I(\tau, \mu') d\mu' , \quad (2)$$

where $\mu = z$ component of \mathbf{k} ,

$\tau = \int_0^z \alpha(z') dz'$, the optical depth, and

$\omega(\mathbf{r}) = \omega$, a constant, with the additional assumptions of uniform

boundary illumination and isotropic phase function and albedo. Equation (2) is not applicable to situations involving non-uniform boundary illumination that are of increasing importance in determining the performance of contrast dependent imaging sensors (including the eyeball) in aerosol environments.

While Equation (1) may be solved in principle for those cases of non-uniform boundary illumination, it is possible to develop a formalism for the description of those cases. In developing this formalism, it is first useful to note that the $\mathbf{k} \cdot \nabla \mathbf{I}$ term of Equation (1) is a directional derivative of \mathbf{I} along \mathbf{k} . This allows the replacement of the directional derivative by a functional derivative with respect to the functional \mathbf{I} which is specified at this time only to the extent that it is defined to lie along \mathbf{k} .

Second, it may be noted that $\omega(r)$ is bounded everywhere on $[0,1]$, and for $\tilde{\omega}(r) = \omega$, a series of the form, $\mathbf{I}(\mathbf{r}, \mathbf{k}) = \sum_{n=0}^{\infty} \omega^n \mathbf{I}_n(\mathbf{r}, \mathbf{k})$ represents a series in orders of scattering² that is convergent for $\mathbf{I}_n < \mathbf{I}_0 / \omega^n$. If these two conditions are used, and the constancy of the phase function is retained, a set of N equations, corresponding to N^{th} order extinction, may be derived from Equation (1),

$$\frac{d\mathbf{I}_0}{d\mathbf{I}} = -\alpha(\mathbf{r}) \mathbf{I}_0, \text{ and} \quad (3)$$

$$\frac{d\mathbf{I}_n}{d\mathbf{I}} = -\alpha(\mathbf{r}) \mathbf{I}_n + \frac{\alpha(\mathbf{r})}{4\pi} \int p(\mathbf{k}, \mathbf{k}') \mathbf{I}_{n-1} d^2\mathbf{k}', \quad n > 0. \quad (4)$$

Equations (3) and (4) have solutions of the form,

$$I_0(\underline{r}, \underline{k}) = I_0(\underline{r}_0, \underline{k}) \exp\{-\int_0^1 \alpha(\underline{r}') d\underline{l}'\} \quad (5)$$

$$I_n(\underline{r}, \underline{k}) = I_n(\underline{r}_0, \underline{k}) \exp\{-\int_0^1 \alpha(\underline{r}') d\underline{l}'\} + \int_0^1 \frac{\alpha(\underline{r}')}{4} \int p(\underline{k}, \underline{k}') I_{n-1}(\underline{r}', \underline{k}') d^2 \underline{k}' \exp\{-\int_0^1 \alpha(\underline{r}'') [1' - 1''] d\underline{l}''\} \quad (6)$$

where the \underline{r} dependence of \underline{l} has been suppressed. It may be noted that Equation (5) is Beer's Law; a result that would be expected from an order-of-scattering expansion of Equation (1).

While Equations (5) and (6) constitute general solutions for RT in situations of non-uniform illumination, it is necessary to establish their relationship with the boundary conditions. This is done by defining an extinction volume V surrounded by a surface S . Within V , we shall require that the extinction coefficient $\alpha(\underline{r})$, the albedo ω , and the phase function $p(\underline{k}, \underline{k}')$ be known. In this particular case, both the sensor and all sources will be exterior to V since this is the simplest case possible to the situations of interest, but does not critically alter the formalism. Further, at all points \underline{r}_0 on S , the intensity along all directions \underline{k} (\underline{k} lying above S in the sense of an interior normal at \underline{r}_0) must be defined.

These conditions are adequate to allow Equations (5) and (6) to be solved. Additionally, they allow \underline{l} to be defined for the specific situation and geometry involved, and by the very nature of the definition of intensity on S , reduce the $I_n(\underline{r}_0, \underline{k})$ to be zero for $n > 0$. Equations (6) may then be iterated and reduced, allowing a simple numerical algorithm for any given geometry of exterior sources.

The extension of this formalism to interior sources or sensors is straightforward and will be described, with relevant examples in later papers.

REFERENCES:

1. *for example, S. Chandrasekhar, RADIATIVE TRANSFER, Dover Publications, Inc., New York, 1960.*
2. *Nayfeh, A. H., PERTURBATION METHODS, John Wiley and Sons, New York, 1973.*

EARTH-ATMOSPHERE ALBEDO RELATIONSHIPS FOR REALISTIC ATMOSPHERES

ROBERT E. TURNER
 ENVIRONMENTAL RESEARCH INSTITUTE OF MICHIGAN
 P.O. BOX 618
 ANN ARBOR, MICHIGAN 48104

Abstract

Simplified relationships are formed from radiative transfer analysis which connect the albedo of the Earth-Atmosphere system with radiometric quantities measured by satellites and ground-based devices.

1.0 Introduction

The mean temperature and the climate of Earth depend upon the reflectance of the Earth's surface and the scattering and absorption properties of the atmosphere. In general, if the surface reflectance is high and the atmosphere scatters a large part of the incoming solar radiation then the temperature of Earth will be lower than if the surface and atmosphere absorb radiation.

Ideally one should measure the spectral radiance and integrate over a hemisphere to determine the albedo of a planetary body. In the case of the Earth one measures the radiance in a band or series of bands in a satellite for one direction only. Thus, assumptions must be made concerning the direction of the upwelling radiation. In this paper we shall consider the relationships between measurable radiometric quantities and the spectral albedo of the Earth-Atmosphere system.

2.0 Albedo of the Earth-Atmosphere System

2.1 Definition of Terms

In general, albedo means the ratio of output power to input power and must therefore range in value from zero to one. For the Earth-Atmosphere system we consider unidirectional solar radiation incident on the top of the atmosphere and then we analyze the radiant exitance at the top of the atmosphere. For an atmosphere there is a term called the single-scattering albedo, ω_o , which is the ratio of the volume scattering coefficient to the volume extinction coefficient. For the case of no absorption $\omega_o = 1$. The albedo or reflectance of the Earth's surface will be designated by ρ and the albedo of the entire system of atmosphere with surface is A . Expressed in mathematical terms we have

$$\mu_o E_o = E_+(0) + (1 - \rho) \tilde{E}_-(\tau_o) + (1 - \omega_o) E_\ell \quad (1)$$

where μ_o is the cosine of the solar zenith angle, E_o is the extraterrestrial solar irradiance, $E_+(0)$ is the exitance at the top of the atmosphere, $E_-(\tau_o)$ is the total irradiance at the bottom of the atmosphere and E_ℓ is the loss of energy by absorption in the atmosphere. The albedo of the Earth-Atmosphere system is then defined as

$$A = E_+(0)/\mu_o E_o \quad (2)$$

2.2 Radiative-Transfer Model

A specific atmospheric-radiative-transfer model must be used to calculate the quantities in Eqs. (1) and (2). The model used is a modified two-stream model especially developed for hazy atmospheres [1], [2], [3]. Using the model the albedo is expressed as

$$A = \frac{\mu_o \rho + (1 - \eta) \tau_o [1 + 2(1 - \eta) (1 - \rho) \tau_o]}{[\mu_o + (1 - \eta) \tau_o] [1 + 2(1 - \eta) (1 - \rho) \tau_o]} \quad (3)$$

where η is an anisotropy parameter and τ_o is the total optical thickness of the atmosphere. Special cases of interest are when the atmosphere becomes thin, i.e. when $\tau_o \rightarrow 0$. From Eq. (3) one notes that $A \rightarrow \rho$. Also, if the atmosphere becomes optically very thick, i.e. as $\tau_o \rightarrow \infty$ the albedo becomes

$$A = \frac{(1 - \eta) \omega_o}{1 - \eta \omega_o + \sqrt{(1 - \omega_o) (1 + \omega_o - 2\eta \omega_o)}} \quad (4)$$

2.3 Energy Conservation Relations

Using Eqs. (1) and (2) we get the following relation:

$$A + (1 - \rho) \tilde{F}_- + (1 - \omega_o) F_\ell = 1 \quad (5)$$

The first term is the albedo, the second term represents the energy lost through the surface, and the third term represents the energy absorbed by the atmosphere. Any state of the Earth-Atmospheric system can be represented by a point inside of an equilateral triangle in which the length of each perpendicular is equal to one of the quantities in Eq. (5). For a non absorbing atmosphere a similar relationship is the following:

$$A + (1 - \rho) F_d + (1 - \rho) F_- = 1 \quad (6)$$

where the second term represents the loss of direct solar radiation through the surface and the third term represents the loss of the diffusely scattered sky radiation. The conservation relation can be illustrated as in Figure 1. States with low surface reflectances are near the lower part of the triangle whereas states of high reflectance are near the top. As one goes from conditions of very clear atmospheres to conditions of haze or fog, points representative of

of the state of the system proceed from the right to the left part of the triangle. Hence, points which cluster along the left edge of the diagram represent turbid atmospheres. If the direct solar and the diffuse sky components are measured at the surface and the reflectance is known then the albedo can be calculated using Eq. (6). An example of the dependence of the albedo on the sky radiance measured in a vertical direction is illustrated in Figure 2. As we progress from a Rayleigh atmosphere to a hazy atmosphere the sky radiance increases but the albedo decreases because the scattering by the aerosols which constitute the haze is anisotropic. With an increase in the haze, however, the sky radiance increases and also relatively more radiation is back-scattered, giving rise to an increase in the albedo. Finally, for a very hazy condition the less radiation is able to penetrate the atmosphere and is instead reflected giving rise to a large albedo. The whole effect is less noticeable for highly reflecting surfaces because of greater amount of radiation reflected by the surface as compared to the amount reflected by the atmosphere.

3.0 Conclusions

In this paper we have investigated the relationship between albedo and easily measurable radiometric quantities. If the sky radiance, path radiance and irradiances are measured from the surface or from a satellite then it is possible to deduce the albedo of the entire Earth-Atmosphere system provided one knows other geometrical parameters which define the measurement conditions. It was also found that any planetary state can be represented in a unique way by a point in an energy conservation diagram.

4.0 References

1. R. E. Turner, Atmospheric Effects in Remote Sensing, *Remote Sensing of Earth Resources*, Vol. II., F. Shahrokhi, Ed., 1973.
2. R. E. Turner, Contaminated Atmospheres and Remote Sensing, *Remote Sensing of Earth Resources*, Vol. III., F. Shahrokhi, Ed., 1974.
3. Robert E. Turner, Investigation of Earth's Albedo Using Skylab Data, Final Report, ERIM 102200-20-F, Environmental Research Institute of Michigan, 1976.

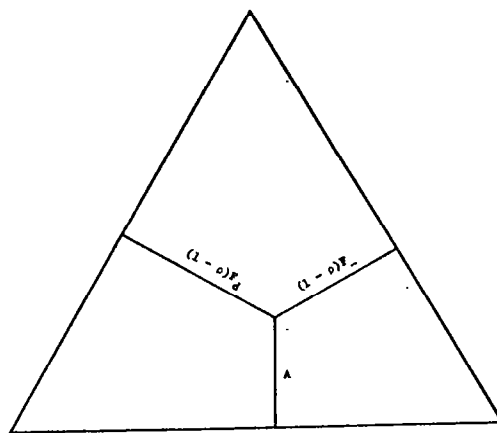
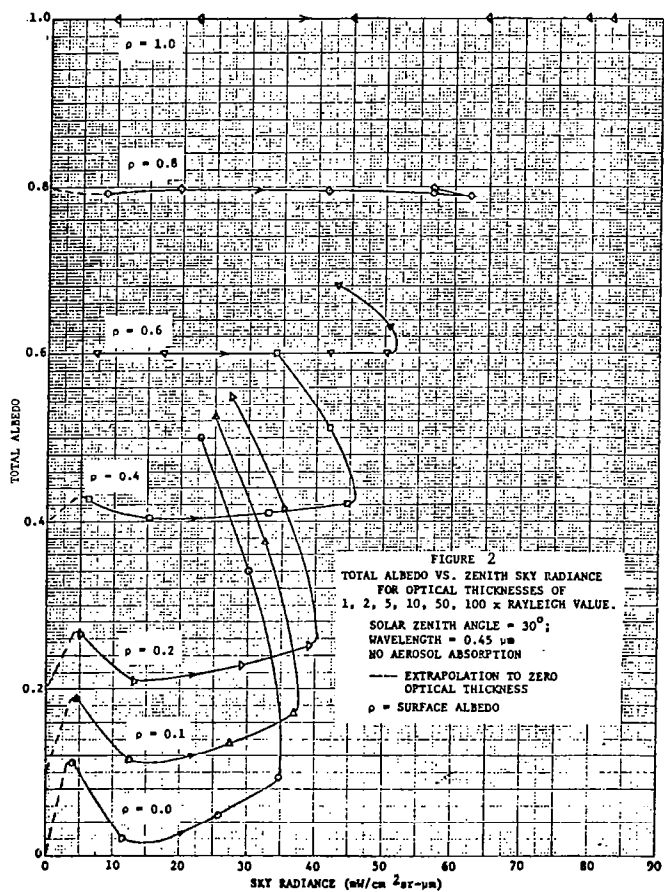


FIGURE 1
ENERGY CONSERVATION RELATION FOR
A NON-ABSORBING PLANETARY
ATMOSPHERE

$A \sim$ Total Albedo
 $(1 - \rho)F_d \sim$ Direct Flux Loss
 $(1 - \rho)F_d \sim$ Diffuse Flux Loss



**ANALYSIS OF RADIATIVE PROPERTIES OF
WARM CLOUDS AT INFRARED WAVELENGTHS**

Richard D. H. Low and Richard B. Gomez
Atmospheric Sciences Laboratory
White Sands Missile Range, New Mexico 88002

Satellite technology has improved so markedly in recent years that the most serious problem in the utilization of this new technology to meteorological applications is the proper interpretation of the satellite data. Perhaps the most difficult aspect of this problem relates to clouds. In this paper we examine under what microphysical conditions a cloud may be unmistakeably regarded as a blackbody radiator and what this implies in the determination of cloud-top heights and in the retrieval of atmospheric temperature by satellite. The spectral region of interest here is the 9-12.5 μm band which approximates the bandwidth of infrared radiometers in current use. To treat the radiative transfer process in clouds as is applicable to these satellite problems, we used the Gauss-Seidel iteration technique.^{1,2} As input data to these radiance calculations, we used the statistical cloud parameters^{3,4,5} presented in Table 1 and assumed the cloud particles are spherical water droplets. The symbols N , b , and NA are the parameters of the Khrgian-Mazin distribution function, $T(\text{°C})$ is the cloud temperature, $r(\mu\text{m})$ is the droplet radius, and $LWC(\text{g m}^{-3})$ is the liquid water content.

TABLE 1
CLOUD TYPES, TEMPERATURES, AND STATISTICAL PARAMETERS
(Surface Temperature = 32°C)

Type	T	r_{min}	r_{avg}	r_{max}	LWC	N	b	NA
Stratus	5	1	4	20	0.12	200	0.750	42.18750
Cumulus (continental)	1	2	5	25	0.20	170	0.600	18.36000
Cumulus (maritime)	3	2.5	8	30	0.40	85	0.375	2.24121
Cumulus (fairly strong)	0	3	10	40	0.60	65	0.300	0.87750

In this short presentation, we offer our findings in three figures. Figure 1 was prepared on the basis of radiation flux calculations, as is usually found in the literature on cloud studies.^{6,7} The cloud having a greater water

droplet number concentration or liquid water content attains blackbody radiation at a smaller thickness than one having a smaller amount.

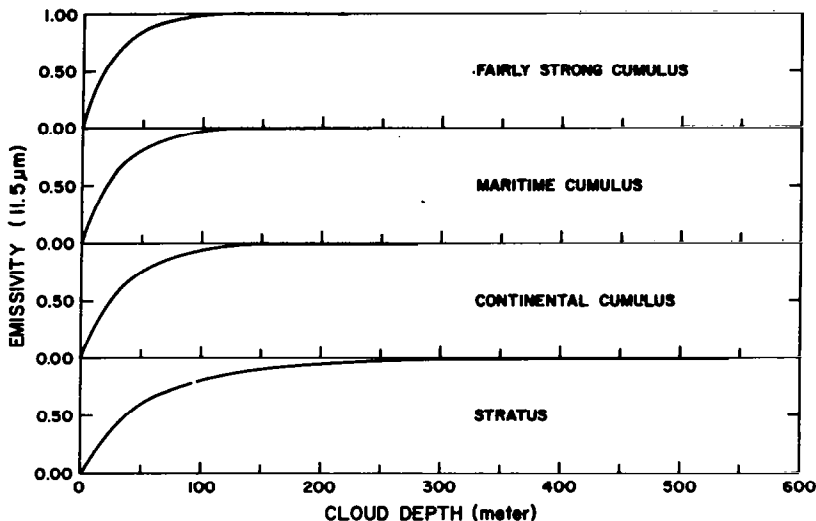


Figure 1. The emissivities of four cloud models at the $11.5\mu\text{m}$ wavelength as a function of cloud depth. The end points of the curves signify the depths required in each case for blackbody radiation.

The satellite radiometer measures upwelling radiance, not radiation flux. Moreover, when the cloud reaches such a thickness as to behave like a blackbody radiator, the upwelling radiance from its top becomes very nearly isotropic, except near the limbs.^{6,7,8} Therefore, we display in the next two figures only the upwelling radiance emerging at the zenith for each of the cloud types considered. We assumed the radiometer viewing angle is near zenith and that its field of view is covered by cloud tops.

Figure 2 illustrates the stratus model case. When the curves meet in one straight line, cloud emissivity assumes unity. Above this line, emissivity is greater than 1, and below this line is smaller than 1. The insert is an amplification of the segment of interest to us. An isolated cloud without ground radiation becomes a blackbody radiator when it reaches about 650 meters in thickness, different from our flux calculations by approximately 300 meters. A cloud illuminated by ground radiation does not become a blackbody radiator until it attains a depth of over 900 meters, a difference of more than 250 meters. Below this depth, the cloud appears warmer than it actually is, with an emissivity greater than unity.

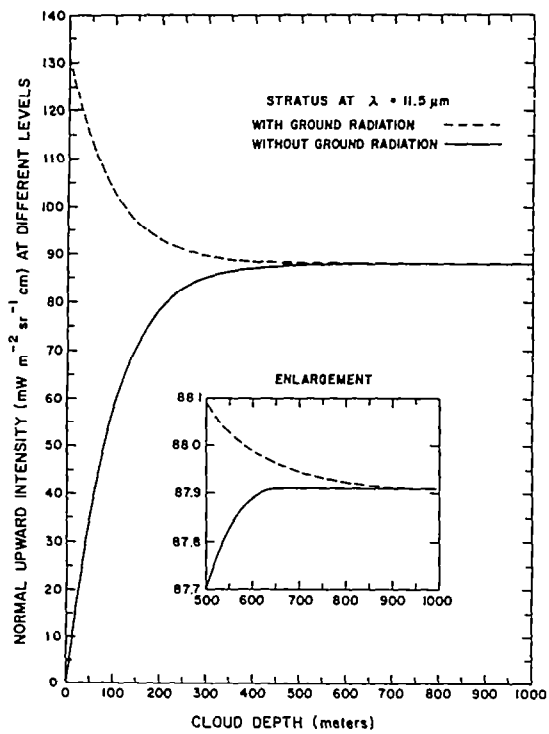


Figure 2. Upwelling radiation at the zenith in the $11.5\mu\text{m}$ window as a function of cloud depth. At a cloud depth where the curve becomes a straight line signifies the beginning of blackbody radiation at that depth.

The results obtained for the three other cloud models are shown in Figure 3. As the cloud gains in liquid water content, the difference between the two cases diminishes. Nevertheless, it is important that if cloud emissivity is to be used in the interpretation of satellite radiometric measurements it be based upon radiance calculations.

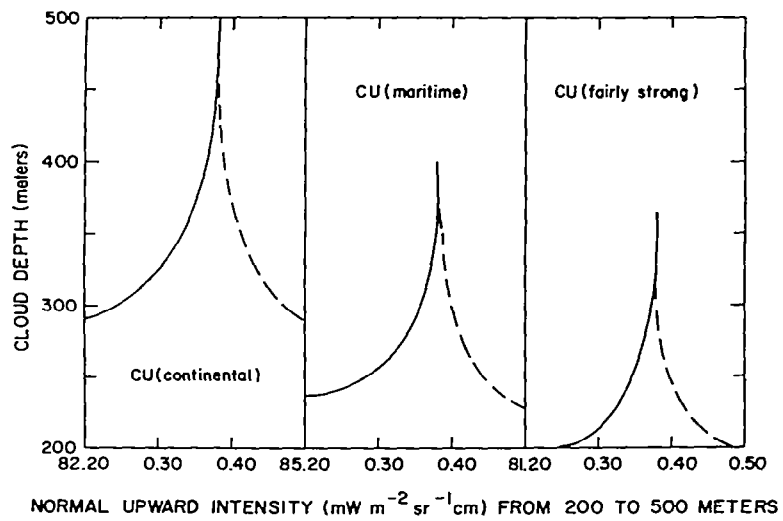


Figure 3. Upwelling radiation at the zenith in the $11.5\mu\text{m}$ window as a function of cloud depth, similar to Figure 2.

These and other similar calculations for clouds of varying thickness show that, given the microphysical parameters tabulated in Table 1, for all clouds of thickness greater than 1 km the radiometer looks upon the cloud as a blackbody. Moreover, the thickness at which a given cloud approaches the property of a blackbody varies with wavelength. In the spectral band 9-12.5 μ m, a given cloud type appears the "blackest" in the 11-12.5 μ m region; this implies that the thickness required for it to radiate like a blackbody is at the minimum in this region. In order to examine the internal radiation in some detail, we divided the cloud into 50 sublayers. However, this is unnecessary in practice if only the upwelling radiance emerging from the cloud top is of interest. In our test runs, the upwelling radiation was found to vary within 0.2% whether there were 10 sublayers of 100 m each or 50 of 20 m each.

Of course, no cloud is ever isolated, nor is ever any cloud, except the fogs, in immediate contact with the ground surface without some intervening water vapor and temperature distributions, as are assumed in our present investigation as well as in the studies of others.^{6,8} Nevertheless, the observations made here as elsewhere about the gross optical properties of clouds are by no means invalid and, indeed, represent a first step toward a better understanding of radiative transfer in clouds as is applicable to satellite problems.

REFERENCES

1. James, M. L., G. M. Smith and J. C. Wolford, Applied Numerical Methods, International Textbook, Scranton, 1967.
2. Herman, B. M. and S. R. Browning, J. Atmospheric Sci., 22, 559, (1965).
3. Fletcher, N. H., The Physics of Rainclouds, Cambridge Press, Cambridge, 1962.
4. Borovikov, A. M. and A. Kh. Khrgian, Cloud Physics, Israel Program for Scientific Translation, Jerusalem, 1963.
5. Mason, B. J., The Physics of Clouds, Clarendon Press, Oxford, 1971.
6. Yamamoto, G., M. Tanaka, and K. Kamitani, J. Atmospheric Sci., 23, 305, (1966).
7. Hunt, G. E., Quart. J. Roy. Meteorol. Soc., 99, 346, (1973).
8. Zdunkowski, W. G., and I. Choronenko, Beitr. Atmospheric Phys., 42, 206, (1969).

KEY TO AUTHORS AND PAPERS

Acquista, Charles - MC13
Ahlquist, N. C. - TuA4
Alkezweeny, A. J., and N. S. Laulainen - MA5
Anderson, R. J. - MC2
Baker, M. B. - WB5
Box, Michael A., and Shui-yin Lo - WA9
Box, Michael A., and Bruce H. J. McKellar - WA11
Bright, David S., Natasha K. Neihart, and Ilan Chabay - TuA2
Brouwer, William - TuC6
Bruce, C. W., and R. G. Pinnick - MC4
Bullrich, K., and G. Hänel - MA1
Bullrich, K., and Reiner Eiden - WB4
Buser, R. G. - TuA6
Byrne, Dale M. - MA4, TuC3
Byrne, Dale M., and Michael D. King - TuB5
Carlson, T. N. - MB1
Carswell, A. I., J. S. Ryan, and S. R. Pal - TuC7
Castleman, A. W., Jr. - MC1
Chabay, Ilan - TuA2
Chang, James J. C. - MB3
Charlson, R. J., A. H. Vanderpol, A. P. Waggoner, D. S. Covert, and M. B. Baker - MC6
Charlson, R. J. - TuA4, WB5
Chýlek, Petr - MC8
Chu, W. P. - MB7
Chu, W. P., T. J. Swissler, and M. P. McCormick WA6
Cosden, Thomas H. - MA6
Covert, D. S. - MC6, WB5
Crumbly, K. H., R. J. Sentell, R. W. Storey, Jr., and D. C. Woods - MB5
Dearborn, Frank K. - MB6
Deepak, Adarsh - WA8, WB6
Drake, Ronald L. - WA1
Ebersole, John F., David M. Mann, and Conrad M. Gozewski - TuA9
Edwards, H. B. - TuB2
Eiden, Reiner - WB4
Eversole, R. A. - MC7
Farmer, W. M., and J. O. Hornkohl - TuA7
Fernald, F. G. - MB8
Fiocco, G. - WB1
Fishburne, E. S. - TuC5
Fowler, Bruce W. - WC6
Fraser, Alistair B. - WA12
Fuller, W. H., Swissler, T. J., and M. P. McCormick - TuC2
Gerber, H. E., R. K. Stilling, R. G. Buser, and R. S. Rohde - TuA6
Gillette, D. A. - MC3
Gomez, Richard B. - MB2, WC8
Gozewski, Conrad M. - TuA9
Grams, G. W., G. Fiocco, and A. Mugnai - WB1
Grams, G. W., and E. M. Patterson - TuA5
Gravatt, C. C. - TuA3
Grether, D. F., A. J. Hunt, M. Wahlig - TuC11
Hagard, Arne, Bertil Nilsson, Hans Ottersten, and Ove Steinwall - WB7
Hamill, Patrick - WA2, WA4
Hänel, G. - MA1
Harris, Franklin S., Jr. - MC11

Harris, Franklin S., Jr., and James M. Rosen - MA2

Herman, Benjamin M. - MA4, TuC3, WC5

Hindman, Edward E. - TuC10

Hinds, Bobby D. - MB2

Hoffman, D. J. - WA5

Hoidale, Glenn B., Richard B. Gomez, and Bobby D. Hinds - MB2

Holland, A. C. - WA14

Hornkohl, J. O. - TuA7

Hunt, A. J. - TuC11

Jennings, S. G. - MB4

Johnson, G. - MC15

Katz, U. - MC2

King, Michael D. - TuB5, TuC3

King, Michael D., Dale M. Byrne, Benjamin M. Herman, and John A. Reagan - MA4

Koepke, P., and Heinrich Quenzel - MA3, TuB3

Kuhn, P. M. - MC5

Laulainen, N. S. - MA5

Lenoble, Jacqueline - WC2

Lo, Shui-yin - WA9

Lovill, James E. - TuB1

Low, Richard D. H., and Richard B. Gomez - WC8

Lundgren, Dale A. - TuA1

Mack, E. J., U. Katz, R. J. Pillié, and R. J. Anderson - MC2

Mangano, J. J. - MC7

Mann, David M. - TuA9

Matloff, Gregory L. - WA7

Mauldin, L. E., III. - TuB2

McCormick, M. P., H. B. Edwards, L. E. Mauldin, III, and L. R. McMaster - TuB2

McCormick, M. P., T. J. Swissler, and W. P. Chu - MB7

McCormick, M. P. - TuC2, WA6

McKellar, Bruce H. J. - WALL

McMaster, L. R. - TuB2

Medor, W. E., and W. R. Weaver - WC4

Miranda, Henry A., and Frank K. Dearborn - MB6

Motycka, Jiri - Tuc8

Mugnai, A. - WB1

Neihart, Natasha K. - TuA2

Neer, M. E., G. Sandri, and E. S. Fishburne - TuC5

Nees, R. T. - MB1

Nilsson, Bertil - WB7

Northam, G. Burton - TuC4

Novakov, T. - TuA8

Ottersten, Hans - WB7

Pal, S. R. - TuC7

Patterson, E. M. - TuA5

Patterson, E. M., D. A. Gillette, and E. H. Stockton - MC3

Pearce, William A. - WA14

Pearce, W. A. and R. W. L. Thomas - WA10

Pillié, R. J. - MC2

Pinnick, R. G. - MC4

Pollack, James B. - WB3

Porch, William M., and James E. Lovill - TuB1

Post, M. J. and R. L. Schwiesow - TuC9

Prospero, J. M., T. N. Carlson, D. Savoie, and R. T. Nees - MB1

Pueschel, R. F., and P. M. Kuhn - MC5

Quenzel, Heinrich - MA3, TuB3

Reagan, John A. - MA4

Reagan, John A., Dale M. Byrne, Benjamin M. Herman, and Michael D. King - TuC3

Reck, Ruth A. - WB2

Reich, Michael - WA10

Reiss, N. M., R. A. Eversole, and J. J. Mangano - MC7

Remsberg, Ellis E., and G. Burton Northam - TuC4

Rohde, R. S. - TuA6

Rosen, H., and T. Novakov - TuA8

Rosen, James M. - MA2

Rosen, J. M., D. J. Hoffman, and P. Singh - WA5

Russell, Philip B., and Edward E. Uthe - WB8

Ryan, J. S. - TuC7

Sandri, G. - TuC5

Savoie, D. - WB1

Schwehm, Gerhard - MC12

Schwiesow, R. L. - TuC9

Sentell, R. J. - MB5

Sentell, Ronald J., Richard W. Storey, and James J. C. Chang - MB3

Shettle, Eric P. - WA15

Shettle, Eric P., and F. E. Volz - MC14

Shuler, Marion - TuC6

Singh, P. - WA5

Spinhirne, James - TuC1

Stein, David and Gray Ward - MC9

Steinwall, Ove - WB7

Stewart, Harold, William Brouwer, and Marion Shuler - TuC6

Stilling, R. K. - TuA6

Stockton, E. H. - MC3

Storey, R. W., Jr. - MB5

Storey, R. W., Jr. - MB3

Stowe, L. L. - WA13

Swissler, T. J. - MB7, TuC2, WA6

Swissler, T. J., and Franklin S. Harris, Jr. MC11

Thomas, R. W. L. - WA10

Thomas, Robert W. L., William A. Pearce, A. C. Holland - WA14

Thorsell, D. - WB5

Tingey, David L. - TuB4

Toon, O. B. - WA4

Toon, O. B., and James B. Pollack - WB3

Trusty, Gary L., and Thomas H. Cosden - MA6

Turco, R. P. - WA3

Turco, R. P., P. Hamill, O. B. Toon, and R. C. Whitten - WA4

Turner, Robert E. - WC7

Uthe, Edward E. - WB8

van de Hulst, H. C. - WC1

Vanderpol, A. H. - MC6

Volz, Frederic E. - MB9, MC14

Waggoner, A. P. - MC6, WB5

Waggoner, A. P., N. C. Ahlquist, and R. J. Charlson - TuA4

Wahlig, M. - TuC11

Ward, Gray - MC9

Wark, D. Q., and L. L. Stowe - WA13

Weaver, W. R. - WC4

Weiss, K. - MC10

Weiss, R. E., R. J. Charlson, A. P. Waggoner, M. B. Baker, D. S. Covert, D. Thorsell, and S. Yuen - WB5

Whitney, Cynthia - WC3

Whitten, R. C. - WA4

Whitten, R. C., and R. P. Turco - WA3

Woods, D. C. - MB5

Wright, M. L., and G. Johnson - MC15

Yuen, S. - WB5

Zerull, R. H., and K. Weiss - MC10